DEVELOPMENT OF A DETECTOR FOR CHARGE MOBILITY MEASUREMENTS IN TMBI

Tim Engling
t_engl01@uni-muenster.de
BACHELORTHESIS IN THE DEPARTMENT OF PHYSICS
OF THE WWU MÜNSTER

Examiner: Prof. Dr. C. Weinheimer
Coexaminer: Prof. Dr. Rer. Medic. K. P. Schäfers
April 23, 2021

Abstract

This work aims at characterizing a detector, that was developed to investigate certain properties of TriMethylBismuth (TMBi).

The main component of the detector is a system of an anode and a photocathode in combination with an UV-LED. The capacitance of the detector cell is an important characteristic of the detector, since it influences detector noise and can be used to determine the gap distance between the anode and photocathode inside the detector. The capacitance was measured to be $C_{\mathrm{detector}} = (1.2969 \pm 0.0002)\mathrm{e}{-13}\,\mathrm{F}$. The distance between anode and photocathode was calculated from the capacitance measurement and the detector geometry $d_{\mathrm{anode-cathode}} = (1.34 \pm 0.02)\,\mathrm{mm}$. This measurement enables further simulations for the electromagnetic field inside the detector and the detector geometry.

Using a FEMTO DDPCA-300 current amplifier with a pre-resistor and a charge-sensitive amplifier connected to the detector by a BNC T-piece, simultaneous measurement of the charge pulses and electrical current $I_{\mathrm{UV-LED}}$ generated by the photocathode in conjunction with the pulsed UV-LED was possible. The relationship between electrical current I_{pulse} inside the detector generated by the UV-LED pulses and the pulse width of the UV-LED pulses were in good agreement with a linear fitting function $I_{\mathrm{pulse}} = m_{\mathrm{pulse}} \cdot \mathrm{width}$. The fitting parameter was $m_{\mathrm{pulse}} = (-2.110 \pm 0.006)\mathrm{e}{-7}\,\frac{\mathrm{A}}{\mathrm{s}}$. However the relationship between the current I_{pulse} inside the detector and the electrical power of the pulses through the UV-LED seemed to be non linear.

In a simultaneous measurement of the electrical charge and the electrical current in the detector, the charge signal did not seem to be in a linear relation to the pulse width of the UV-LED. One reason could be a too small shaping time of the spectroscopy amplifier used in the measurement. Further measurements with an analog-to-digital converter might be necessary to acquire the understanding required to enable measuring the electron mobility and the free ion yield with the detector.

Contents

1 Introduction

Positron Emission Tomography (PET) is an imaging technology used e.g. in the detection of cancerous cells in biologically active material. For this imaging technology Trimethylbismuth (TMBi), an organometallic compound with a high atomic number and low electronegativity, is currently being researched as a novel material used in modern PET detectors [1]. TMBi exists in a liquid state at room temperature negating the need for a cooling system integrated into the PET detector. A thorough understanding of material properties such as the electron mobility or the free ion yield G_{fi} is necessary to use TMBi in developing a detector for PET applications.

This work describes a new detector designed to measure the electron mobility, free ion yield and relative permittivity of TMBi while at the same time function as a purity monitor in the purification loop of TMBi. In this work the capacitance of the anode-photocathode pair inside the detector as well as the distance between the anode surface and the photocathode is measured.

Additional measurements are conducted using a pulsed UV-LED to induce an electrical current inside the detector. Using a pulsed UV-LED to introduce excess electrons from a photocathode into the liquid introduces an electrical current flowing to the anode. This electrical current as well as the charge signal can be measured. The relationship between the current and charge signal inside the detector and the pulse width and power of the UV-LED are examined. These measurements could be the start of further studies to acquire more detector properties such as the electron yield from the photocathode.

2 Positron Emission Tomography

Positron Emission Tomography (PET) is a versatile imaging technology used e.g. in the detection and imaging of cancerous cells in humans or animals. The basic principle of a PET scan makes use of the reaction between a positron e^+ and an electron e^- forming the instable positronium which then decays under emission of photons γ with the e^- and e^+ annihilating [2]. The e^+ particle stems from a β^+ decay. The principle of a β^+ decay is shown in formula 1 and the reaction to positronium and the following decay is shown in formula 2 [2].

$$^{A}_{Z}C \rightarrow ^{A}_{Z-1} C^* + e^+ + \nu_e \tag{1}$$

$$e^+ + e^- \rightarrow e^-e^+ \rightarrow 2\gamma \tag{2}$$

There are two states of positronium, orthopositronium and parapositronium. While orthopositronium has a total spin of 1 with the electron and positron spin having the same value, parapositronium has a total spin of 0 with the electron and positron having spins in opposite directions. Because of spin conservation parapositronium decays under emission of an even number of photons, most commonly two, orthopositronium emits an odd number of photons during its decay, at least three because of impulse conservation [2]. Parapositronium has a decay rate of $\lambda_p = (7990.9 \pm 1.7)\,\mu\text{s}^{-1}$ [3] while orthopositronium has a decay rate of $\lambda_o = (7.0404 \pm 0.0010)\,\mu\text{s}^{-1}$ [4]. Both states of positronium can transform into one another through interactions with ambient electrons changing the spin of the onium. Due to the decay rate of parapositronium being 1135.0 ± 0.3 times higher than the decay rate of orthopositronium the decay path of parapositronium is observed to a much higher degree.

If the parapositronium had no impulse before the decay the two photons are emitted back to back due to impulse conservation. If the parapositronium had an impulse the two photons are not emitted exactly back to back resulting in non colinear emitted photons. Both photons together carry the mass energy of the e^- and e^+ particle so each of the photons has an energy of $(0.51099895000 \pm 0.00000000015)\,\text{MeV}$ [5] which is approximately 511 keV.

In cancer detection a β^+ emitting tracer is introduced into the body. For this application Fluorodeoxyglucose (FDG) is one of the most commonly used tracers. It is a glucose molecule with the 2-hydroxyl group replaced by ^{18}F which acts as a β^+ emitter. Inside the human and animal metabolism FDG acts very similar to glucose. Since cancerous cells act at an increased metabolic rate FDG accumulates inside those cells [6] [7]. A chemical drawing of FDG is shown in figure 1.

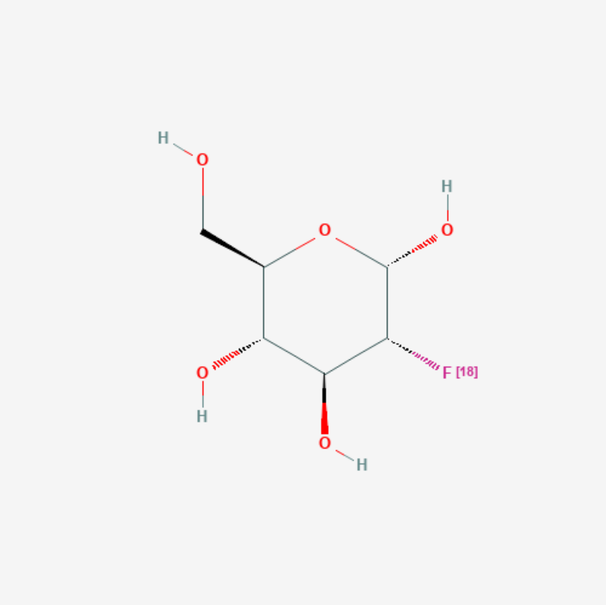

Figure 1: Fluorodeoxyglucose F18, a compound often used in PET. Similar to glucose with one HO group at the 2 position substituted by ^{18}F. The fluorine isotope acts as a positron emitter, while the molecule acts similarly to glucose in the metabolism. [8]

The two γ quanta from the annihilation of the positronium following the β^+-decay of ^{18}F are then detected by the detector cells which are placed around the subject. A line drawn between two detectors that measured two seperate 511 keV photons within a coincidence time window is called line of response (LOR) with a decay event assigned to this line [2]. Due to the fact that positrons have a finite range within the tissue the intersection points of all detected lines gives a good approximation of the position of the cancer cell. If the timing resolution is high enough it is possible to determine a more accurate position on the line of response by the time difference between the detection of one γ quant and the corresponding one.

Various materials have been used for the γ detection in the detector cells. Common are Lutetium based scintillation crystals using the scintillation light for the γ detection. Another detector concept uses liquid Xenon in which scintillation light is detected as well as ionization signals [1]. The CaLIPSO project presented by Yvon et al. in [1] uses liquid Trimethylbismuth (TMBi) for the detection of the 511 keV photons using the photoelectric effect. As described in [2] the cross section of the photoelectric effect is proportional to Z^5, with Z being the atomic number. Bismuth has an atomic number of 86. Since TMBi involves no primary compound of high electronegativity nor unavoidable contaminants with such properties, it promises to enable a high mobility for free electrons [1]. In contrast to liquid Xenon no additional cooling apparatus is required, increasing ease of use, detector volume while also reducing cost.

A schematic drawing of one of the planned detector modules in the CaLIPSO project is shown in figure 3. The 511 keV γ quanta from the positronium annihilation ionize the bismuth in the TMBi molecule by way of the photoelectric effect, creating a free electron inside the

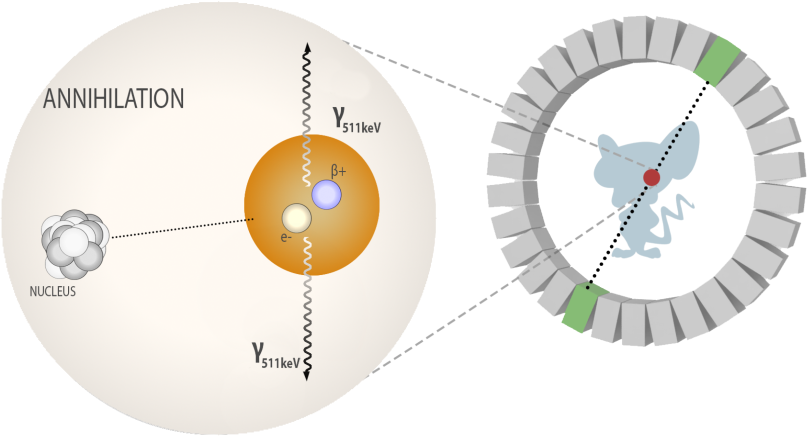

Figure 2: This is a schematic figure showing the detection process in positron emission tomography. A β^+ source is injected into the subject. Fluorodeoxyglucose (FDG) is an often used source which acts similar to glucose and accumulates in metabolicaly active cells, for example cancer cells [6] [7]. The annihilation photons are detected and the location of the positron annihilation is determined from spacial and timing information. [9]

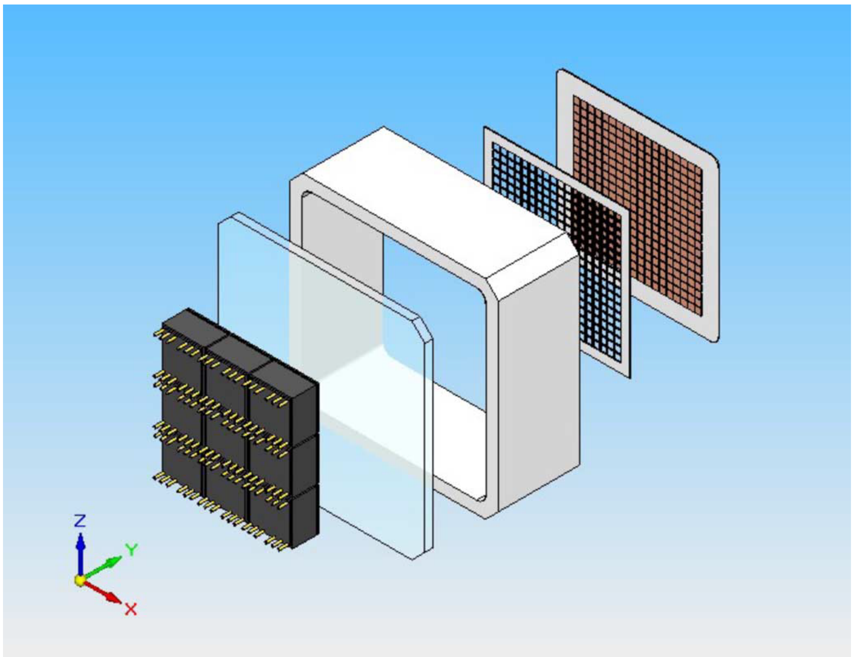

Figure 3: CAD drawing [1] of the CaLIPSO detector. The detector volume is filled with liquid TMBi. The black cubes are photomultiplier tubes detecting cherenkov light signals. A pixelated charge detector (brown) collects the ionization signal behind a frisch-grid (black). The goal is to reconstruct the point of annihilation of the positronium from the spacial and timing information of the ionizing 511 keV photon. [1]

detector material. Due to the high refractive index of TMBi the emitted electron propagates faster than light in TMBi, creating cherenkov light in the process [1]. The charges created from ionization events then drift to a segmented anode behind a frisch-grid creating a charge signal that can be detected using a pixelized anode. This charge signal provides x and y spacial information. A frisch-grid shields the segmented anode from the ionisation volume. Charge signals from electrons are only measured at the anode once they passed the frisch-grid. The frisch-grid allows for a measurement of the electron drift speed since all electrons measured at the segmented anode have the same starting point in the frisch-grid. Additionally it allows for shorter rise times in the charge signal and higher pulses, increasing the resolution [10][2].

The cherenkov light is detected by a photomultiplier tube multiplying and detecting the cherenkov photons or in more recent designs microchannelplates (MCP) [11]. Therefore the photon detection provides timing information for the γ detection. The time difference between charge signal and photomultiplier signal can be used in conjunction with the drift velocity of the electrons to calculate the z spacial information. From this data the path of the initial electron can be recreated. Our objective is to reach an accuracy of $1\,\mathrm{mm}^3$ in the localization of the first ionization caused by the 511 keV photon in the detector [1].

Because of the high atomic number Z = 86 of bismuth the photoelectric effect outweighs the Compton effect as the mechanism for energy transfer between the 511 keV photon and TMBi due to the fact that the cross-section of the photoelectric effect is $\sim \mathrm{Z}^5$ while the cross-section for Compton-scattering is $\sim$ Z [2]. This should allow the identification of 511 keV photons since all of the energy is transmitted in the interaction and these events can be distinguished from Compton scattering events. The low oxidation numbers in TMBi also decreases the tendency to trap electrons [1].

The detector described in this work aims to measure various material properties of TMBi in the context of use in a PET detector. Some characteristics of TMBi that are going to be investigated in the future are the relative permittivity ϵ_r, the free ion yield G_{fi} and the electron mobility in TMBi. The relative permittivity influences the capacitance of the anode-cathode system inside the detector, thus might influence the design of the electronics needed for a functioning detector. The free ion yield G_{fi} is quantified as the number of ion pairs detected per 100 eV energy absorbed [1] and can be used to identify the 511 keV photons. A higher value of G_{fi} should result in a higher energy resolution due to more ion pairs generated per amount of energy. Knowledge of the electron mobility inside TMBi enables measuring the position of the ionization in the z-plane, orthogonal to the frisch-grid. The position in the z-plane can be calculated using the electron mobility in TMBi and the time difference between the cherenkov light signal and the frish-grid signal.

In this work the detector is characterized under vacuum. This allows to investigate the differences in behavior between the detector under vacuum and the detector filled with TMBi in future measurements.

3 Charge mobility detector design

The detector described in this work was designed by Simon-Nis Peters and the technical drawing was done by Christian Huhmann. This detector consists of an anode surrounded by a guard ring and a gold coated glass layer that serves as a photocathode, which can be illuminated by an UV-LED. The guard ring and anode are on the same potential. The guard ring supports homogeneity of the electrical field between the photocathode and the anode reducing the inhomogeneity of the electrical field near the edge of the anode area. Additionally it allows for a more defined detector volume. The photocathode in combination with the UV-LED enables the injection of electrons into the detector volume in pulses. A constant potential gradient between the photocathode and the anode accelerates the electrons from the photocathode to the anode. Using a FEMTO DDPCA-300 as a current amplifier the electrical current inside the detector can be measured at the anode side. A charge-sensitive-amplifier (CSA) is connected to the anode side of the electron mobility detector to measure the charge signal.

The detector is constructed in a way, that TMBi can flow through the detector between anode and anode guard ring, passing through the volume between the anode and photocathode in a continuous stream. This ensures that when TMBi is circulated through the system the active detector volume is always replaced with new TMBi.

A cross-section of the detector insides is shown in figure 4 while figure 5 shows a 3D render of the anode, ceramic tube and the guard ring.

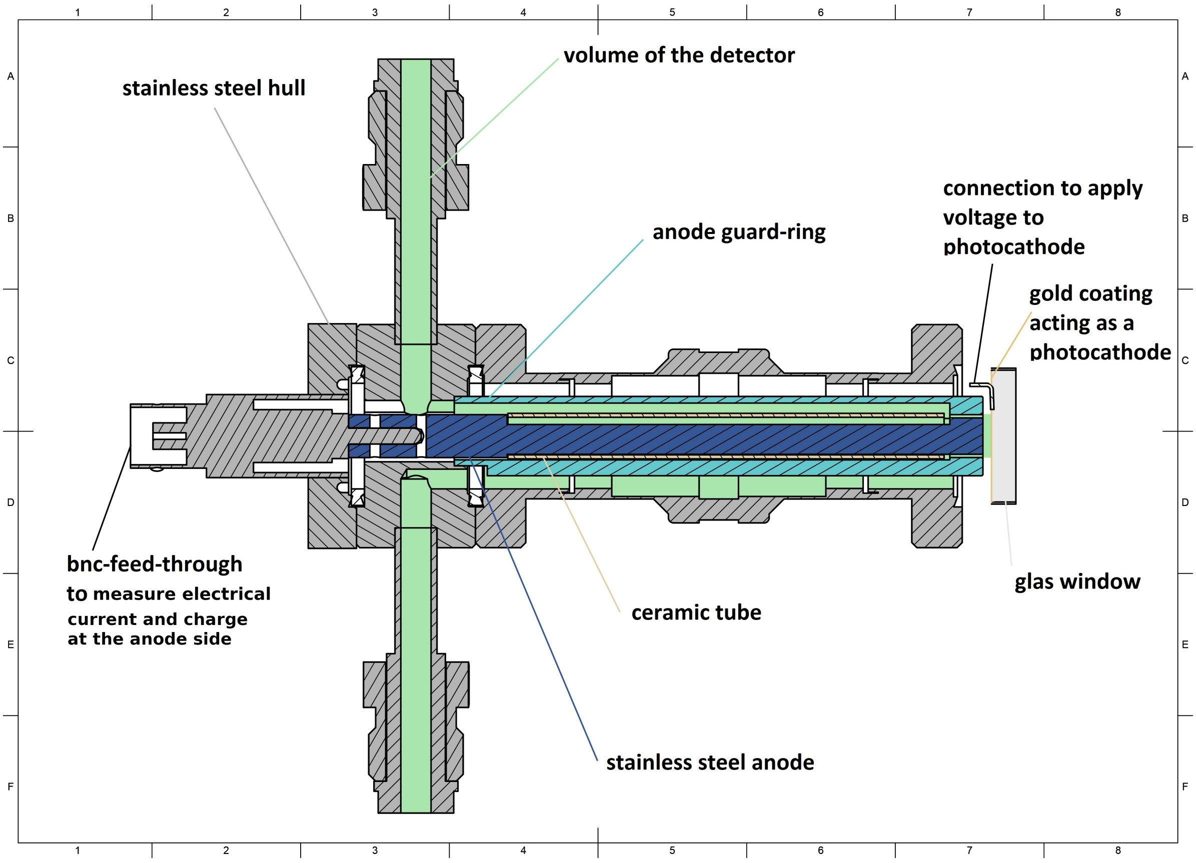

Figure 4: This figure shows a cross-section of the insides of the charge mobility detector. The drawing was derived from the CAD created by Christian Huhmann.

To ensure an even and clean surface the stainless steel parts were electro-polished by submerging them in a bath of copper(II)sulfate ($CuSO_4$) with an electrical current inside the bath of approximately 6.2 A. To reduce the influence of impurities on the measurements all detector parts have been cleaned with Almeco cleaning solution in an ultrasound bath for approximately 15 minutes. Afterwards all parts were cleaned with deionized water to get rid of any residue of the cleaning solution, as any residue could dilute into the TMBi resulting in a deterioration of the purity. The ceramic tube surrounding the anode was cleaned using acetone and a ultrasound bath. The detector was assembled in a clean room to avoid contamination with dust particles. During assembly the screws compressing the copper gaskets between detector parts were tightened. This introduces an uncertainty which will be discussed in chapter 4. The UV-LED was placed in front of the gold-layered window using a 3d-printed attachment designed by Simon-Nis

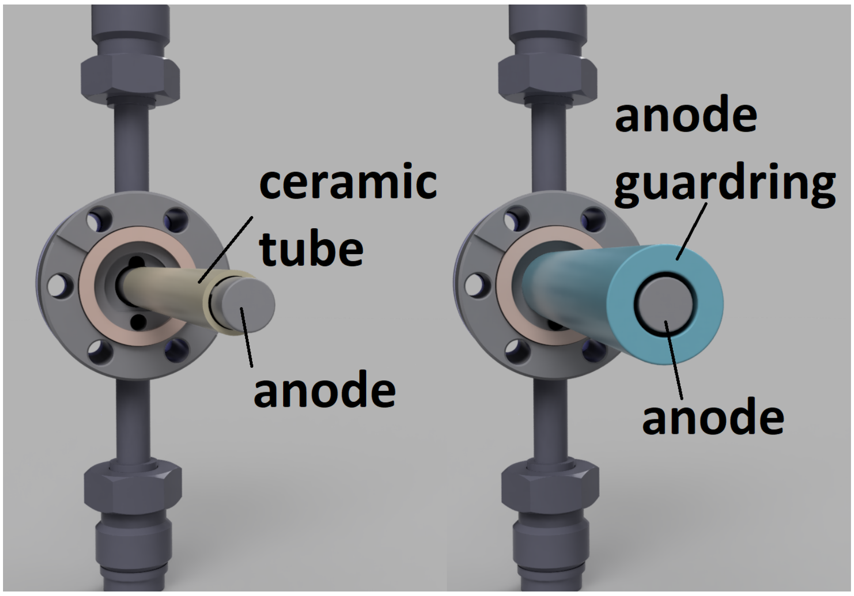

Figure 5: This figure shows a 3D render of the insides of the charge mobility detector showing the spacing of the anode, the ceramic tube and the guard ring inside the detector. The rendering was created from the CAD drawing of the detector provided by Christian Huhmann and Simonnis Peters.

Peters.

One application of this detector would be to analyze the charge answer to a UV-LED pulse injecting electrons into the detector volume filled with TMBi which could lead to a measurement of the electron mobility of TMBi.

The free ion yield G_{fi} could be measured by introducing ionizing radiation of a known energy into the detector volume filled with TMBi and measuring the electrical current answer as a way of measuring the amount of created ion pairs.

Additionally it could serve as a purity measuring device for electronegative impurities in TMBi. The free electrons from the photoelectric reaction can themselves ionize electronegative impurities in TMBi creating free ions in the material. By combining measurements of the electric current and the charge signals in TMBi in response to a defined pulse from the UV-LED it should be possible to decouple the electronic signal from the ionic signal allowing for an evaluation of electronegative impurities in TMBi. Since the FEMTO DDPCA-300 integrates over a larger time frame in the electrical current measurement than the charge measurement ionic signals should still contribute to the electrical current measured. Due to the ions being slower in TMBi than free electrons, because of their size, the amplitude of the charge peak measured in response to the UV-LED pulse should be anti-proportional to the amount of ions in TMBi. Therefore the amplitude of the charge signal is expected to decrease with an increase in electronegative impurities.

The specificities of these potential measurements exceed the scope of this work and could be researched in future studies. For these and other future measurements the capacitance of the detector and the distance between anode and photocathode might be needed and the measurement of these parameters will be described in the following chapter 4. To characterize the system consisting of photocathode and UV-LED, which might be used in future measurements to introduce free electrons into the detector volume, several measurements regarding the current induced in the detector by a pulsed UV-LED were conducted and are described in chapter 5.

4 Capacitance measurement of the capacitor plates inside the detector

For measurements of the relative permittivity and electron mobility of TMBi in the detector, it is important to know the capacitance of the system consisting of the photocathode and the anode as well as the distance between anode and cathode. A rough estimate could be produced from the data in the CAD drawing, which was used to build the detector. Using the standard formula for a plate capacitor in conjunction with the lengths from the CAD drawing of the detector resulted in a capacitance of $C_{\mathrm{plate,CAD}} = (1.3 \pm 0.5)\mathrm{e}{-13}\,\mathrm{F}$ with the distance in the CAD drawing being $d_{\mathrm{anode-cathode,CAD}} = (1.3 \pm 0.5)\,\mathrm{mm}$

Tightening the screws during assembly compresses the copper gaskets thus sealing the detector. This process introduces an additional uncertainty to the distance between anode and photocathode. By measuring the capacitance of the capacitor inside the detector the distance between anode and cathode can be determined using the known area of the anode. For the capacitance measurement the voltage between the anode and cathode was changed at a constant rate. By measuring the current resulting from the changing voltage the capacitance could be determined. This measurement resulted in a capacitance of $C_{\mathrm{detector}} = (1.2969 \pm 0.0002)\mathrm{e} - 13\,\mathrm{F}$ and a distance of $d_{\mathrm{anode-cathode}} = (1.34 \pm 0.02)\,\mathrm{mm}$

To acquire a more thorough understanding of the detector and a more accurate measurement of the distance between anode and cathode simulations could be conducted in future works, using the measured capacitance and the detector geometry from the CAD drawing.

4.1 Method of the capacitance measurement

Figure 6 shows a cross section of the inside area near the photocathode and the anode with the lengths derived from the CAD drawing. According to [12] (page 21) the capacitance C of a plate capacitor under vacuum is:

$$C = \frac{\epsilon_0 \cdot A}{d} \tag{3}$$

With A being the area of the opposing plates and d being the distance between them. ϵ_0 is the vacuum electric permittivity. This formula leads to a capacitance between the anode and the photocathode of:

$$C_{\mathrm{plate,CAD}} = (1.3 \pm 0.5)\mathrm{e}{-13}\,\mathrm{F} \tag{4}$$

Because of uncertainties in the distance between anode and cathode resulting from the assembly these values can only serve as a rough estimate. To obtain a more precise value additional measurements of the capacitance were conducted.

A FLUKE digital multimeter was used to acquire a first measurement of the capacitance inside the detector. Since the capacitance meter could not be attached directly to the anode and cathode, several measurements had to be conducted. The measurement setup is shown in figure 7. The FLUKE handheld capacitance meter was first used to determine the capacitance of the plug connected to the red cable and the plug connected to the blue cable. These measurements produced:

$$C_{\mathrm{plug+cable_{blue}}} = (50.760 \pm 0.003)\mathrm{e}{-12}\,\mathrm{F} \tag{5}$$

$$C_{\mathrm{plug+cable_{red}}} = (26.730 \pm 0.003)\mathrm{e}{-12}\,\mathrm{F} \tag{6}$$

Afterwards the cables were attached to points 1 and 2 respectively as shown in figure 7. This resulted in a measurement of :

$$C_1 = (88.720 \pm 0.003)\mathrm{e}{-12}\,\mathrm{F} \tag{7}$$

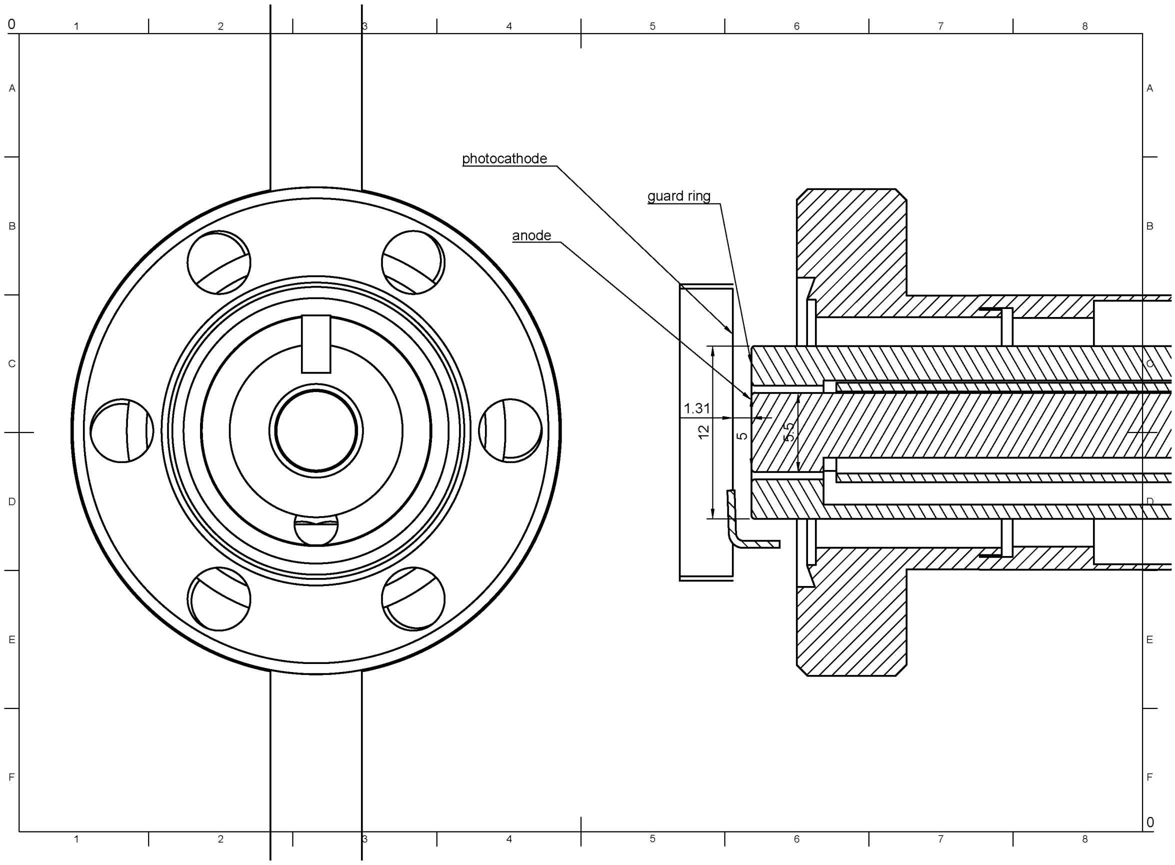

Figure 6: This figure shows a cross-section of the detector in the area of the photocathode and anode. The dimensions of the detector were derived from the CAD drawing and are given in mm. The distance between anode and photocathode is $d_{\mathrm{anode-cathode,CAD}} = (1.3 \pm 0.5)$ mm. The inner diameter of the anode is $2r_{\mathrm{anode,inner}} = (5.00 \pm 0.10)$ mm . The outer diameter of the guard ring is $2r_{\mathrm{anode,inner}} = (12.00 \pm 0.10)$ mm. The estimated capacity of this plate capacitor under vacuum is $C_{\mathrm{plate,CAD}} = (1.3 \pm 0.5)\mathrm{e}{-13}\,\mathrm{F}$ [12]. The CAD drawing was created by Christian Huhmann and Simon-nis Peters.

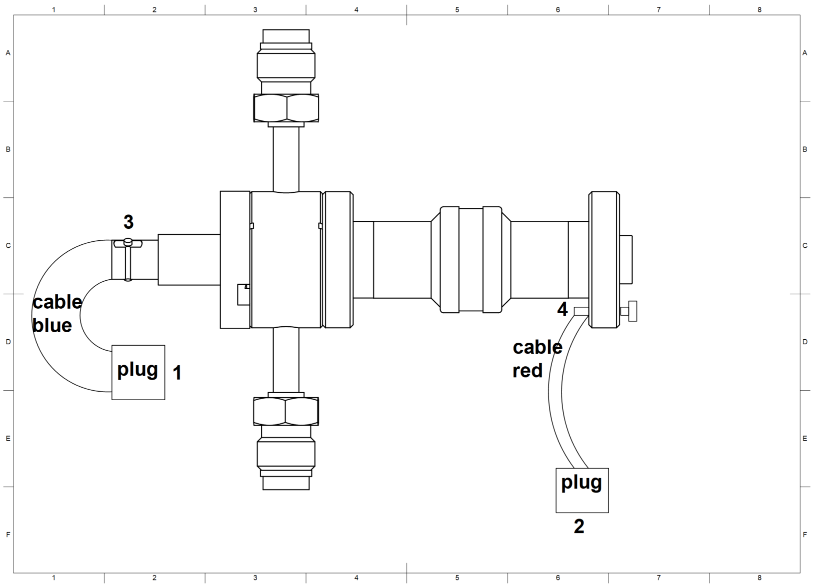

Figure 7: This figure shows a sketch of the setup for the capacitance measurement using the handheld FLUKE capacitance meter. Measurements were conducted at the points 1 and 2, as well as measurements of the plug attached to the blue cable and the plug attached to the red cable. Since the cable connection used a bnc-cable, point 1 and 2 respectively could be understood as a parallel connection of the capacitor at point 3 and the blue cable and plug or the capacitor at point 4 and the red cable and the plug. Since 3 is connected to the anode and 4 is connected to the photocathode, both should measure the same capacitance. The result of the measurement was $C_3 = (3.7960 \pm 0.0004)\mathrm{e}{-11}\,\mathrm{F}$ and $C_4 = (1.497 \pm 0.0004)\mathrm{e}{-11}\,\mathrm{F}$.

$$C_2 = (41.700 \pm 0.003)\mathrm{e}{-12}\,\mathrm{F} \tag{8}$$

The connection between the cables and the anode respectively the cathode was using a bnc-feedthrough. So the capacitor inside the detector could be interpreted as being parallel to the cable-plug system. According to [12] (page 22) the capacitance of a parallel system of capacitors is equal to their sum

$$C_{\text{total}} = \sum_i C_i \tag{9}$$

For the capacitance at 3 and 4 this formula 9 gives:

$$C_3 = (3.7960 \pm 0.0004)\mathrm{e}{-11}\,\mathrm{F} \tag{10}$$

$$C_4 = (1.4970 \pm 0.0004)\mathrm{e}{-11}\,\mathrm{F} \tag{11}$$

This measurement is several magnitudes larger than the rough estimate from the detector geometry $C_{\text{plate,CAD}} = (1.3 \pm 0.5)\mathrm{e}{-13}\,\mathrm{F}$ in formula 4. This deviation might be caused by the isolation between the anode and the guard ring. The FLUKE multimeter is battery powered, thus does not share the common ground of the guard-ring and the anode. Due to this isolation the capacitance between the anode and cathode in addition to the capacitance between the anode and the guard ring might be measured by the FLUKE multimeter. Since point 3 is connected to the anode inside the detector and point 4 in figure 7 is connected to the photocathode both should have the same capacitance, which is not the case. A reason for this could be, that the FLUKE multimeter measures a different amount of the capacitance between the anode and the guard ring depending on the connection point. Nevertheless the measurement with the FLUKE multimeter proved to be unsuitable to determine the capacitance between the anode and the photocathode, which is why additional measurements were conducted.

To obtain a more precise measurement of the capacity of the detector, the electrical current in response to a changing voltage was measured. The capacitance of a capacitor can be calculated with the formula

$$C = \frac{Q}{U} \tag{12}$$

from [12]. Q is the amount of charge stored in the capacitor plates and U is the voltage between the plates. Using the time derivative of both sides under the assumption, that the capacitance of the detector is not dependent on the time, results in:

$$\frac{\mathrm{d}}{\mathrm{d}t} Q = C \cdot \frac{\mathrm{d}}{\mathrm{d}t} U \tag{13}$$

$$I = C \cdot \frac{\mathrm{d}}{\mathrm{d}t} U \tag{14}$$

This correlation was used as the basis for the measurement of the capacitance of the charge mobility detector.

All measurements were performed with the detector being under vacuum. A high voltage source was connected to the cathode, while the anode and the guard ring were on ground potential. Using an ISEG NHQ-high voltage module, the voltage applied to the cathode could be controlled. The ISEG NHQ-high voltage module was connected to a laboratory computer. A LabView program was designed by Tim Engling, using parts of an earlier program from Simon-nis Peters to change the applied voltage. Ramping up the voltage on the cathode with a constant ramping speed while simultaneously measuring the electrical current induced in the anode allows measuring the capacitance of the anode-photocathode system. Since the guard ring is on the same potential as the anode and galvanically separated from the anode, no current flowing through the guard ring is measured in the capacitance measurement.

The electrical current was expected to be in the magnitude of pA. Therefore a FEMTO DDPCA-300 electrical current amplifier was used behind the anode to measure the current. The FEMTO DDPCA-300 generates an output voltage proportional to the electrical current measured and in combination with the amplification level it allows measurements of electrical currents in the magnitude of fA. For the measurement the FEMTO DDPCA-300 was attached to the anode and the laboratory computer and the amplification level was controlled by the LabView program. The LabView program ramped up the voltage from 10 V to 1010 V keeping the ramping speed constant during each ramping process. The program conducts several measurement cycles using various constant speeds for each ramping process.

To shield the detector from electromagnetic radiation a Faraday cage surrounding the detector was installed. This cage also served as protection from touching the high-voltage cathode. Earlier measurements have shown that the setup was susceptible to microphonic noise. Especially movement surrounding the detector and vibrations inside the laboratory resulted in spikes in the current measurement. A rigid mounting structure reduced the noise introduced by vibrations. Figure 8 shows a photograph of the detector setup during the capacity measurement.

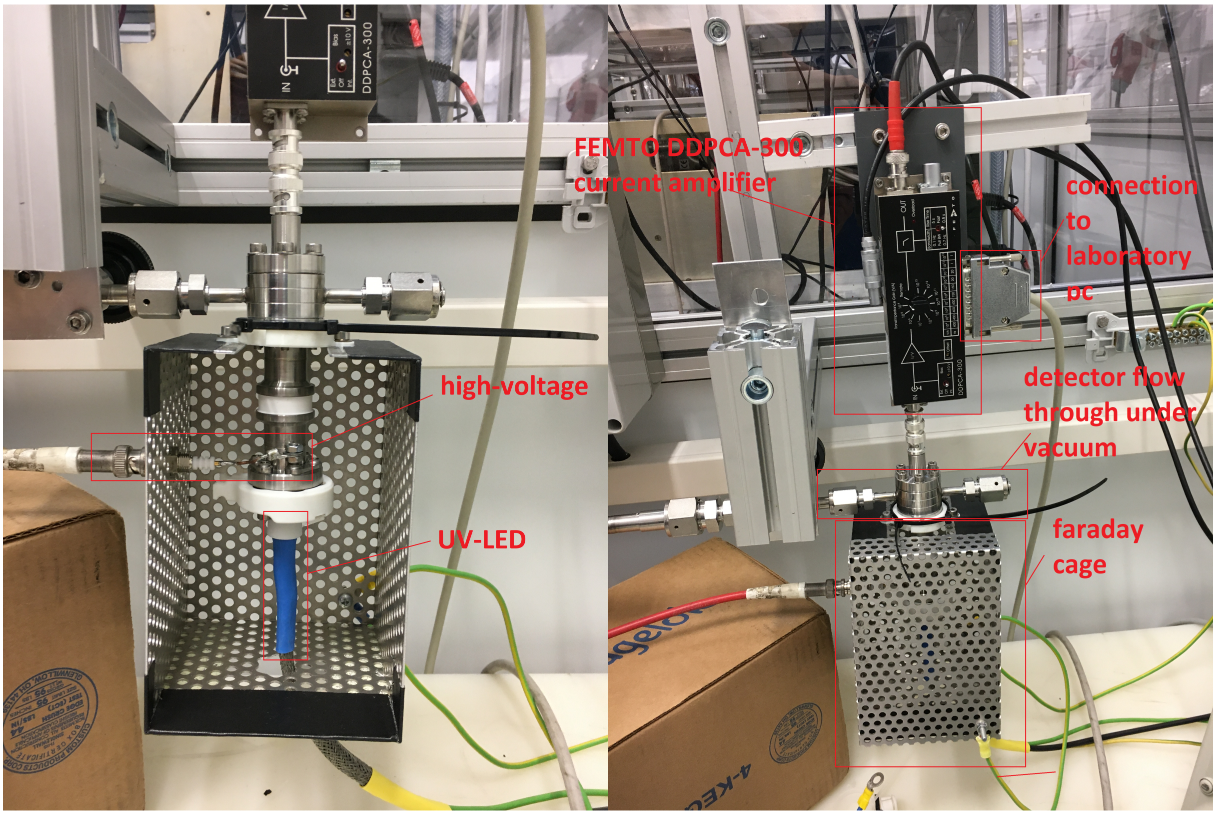

Figure 8: This photograph shows the setup during the capacitance measurement. The detector is inside the grounded Faraday cage. The measurement was performed under vacuum conditions. Using a ISEG NHQ-high voltage source controlled a LabView program, the voltage inside the detector is increased and decreased using a constant ramping speed. During the measurement the electrical current I is measured using the FEMTO DDPCA-300 current amplifier.

4.2 Capacitance measurement and results

The python script used for data analysis has been written by Tim Engling. Parts of the code regarding uncertainties of fitting functions as described in [13] were modeled after code from Daniel Săvoiu and Günter Quast which was provided by Dr. Volker Hannen. To correctly determine the current I during changing voltages the background current was analyzed first to correct the data by the background fitting function. Figure 9 shows the data of the capacitance measurement. The electrical current correlates to the changing voltage in the detector. In accordance with formula 14 under the assumption of a constant capacitance a constant electrical current I is expected in response to changing voltage with a constant $\frac{\mathrm{d}U}{\mathrm{d}t}$. At first glance this behavior could be measured. The absolute of the electrical current is higher for higher absolute voltage ramp speeds.

A change in value of the amplification level of the FEMTO DDPCA-300 lead to a spike in the measured electrical current. Since these features occurred regularly during periods of switching amplification levels they might be caused by the electronics of the FEMTO DDPCA-300 current amplifier, with the change in amplification level influencing the measured current. Investigating the cause of these spikes would exceed the scope of this work. For this reason data points shortly before and after such a change in amplification level have been selected and removed automatically by a python script.

Additional spikes in the electrical current were recognized after parsing the background part of the measurement. Since these spikes seem to appear several times before and after the ramping process of the measurement they might be connected to internal workings of the ISEG NHQ-high voltage source. The electrical current readout detects currents in a magnitude smaller than pA so even small changes in voltage are recognized. For the capacitance measurement the background part of the measurement is only used to correct the data to assess the electrical current during ramping segments more precisely. For this reason analyzing the spikes in the background measurement was deemed to be not significant for the capacitance measurement and the data points were removed.

Figure 10 shows the data during absolute ramping speeds of 60 $\frac{\mathrm{V}}{\mathrm{s}}$. Figure 11 shows the data of the capacitance measurement for ramping speeds of 15 $\frac{\mathrm{V}}{\mathrm{s}}$. The regular occurrence of the spikes in the background part of the data, as well as during the beginning and end of each ramp process can be observed. The selection of the datapoints were similar for the other ramping speeds in the capacitance measurement. The corresponding figures can be found in the appendix, chapter 10.

An exponential decay was used to describe the background current. The datapoints of the background were fitted to:

$$f_{\mathrm{bg}}(x) = bg + amp \cdot e^{\frac{-x}{\tau}} \tag{15}$$

with x being the time data of the measurement.

Values for the peak-to-peak noise of the current measurement were derived from the datasheet of the FEMTO DDPCA-300 current amplifier [14] and used as a starting point for the uncertainty of the electrical current. Since no further information was given on the way the noise relates to the standard uncertainty a rectangular distribution was assumed and the peak-to-peak noise value was used as the width of the rectangular shape. The uncertainty was calculated using the formula 36 with the given peak-to-peak noise for the amplification level.

A first fit of the background current resulted in a reduced $\chi^2_{\mathrm{red.}} = 2.02 \pm 0.02$. However not all sources of noise are numerically known for the uncertainty of the electrical current measurement. Early measurements already showed that the measurement setup is susceptible to microphonic noise. To rectify this the background fit was used to get a better estimate for the standard uncertainty of the electrical current. Formula 16 was used to correct the uncertainty of the

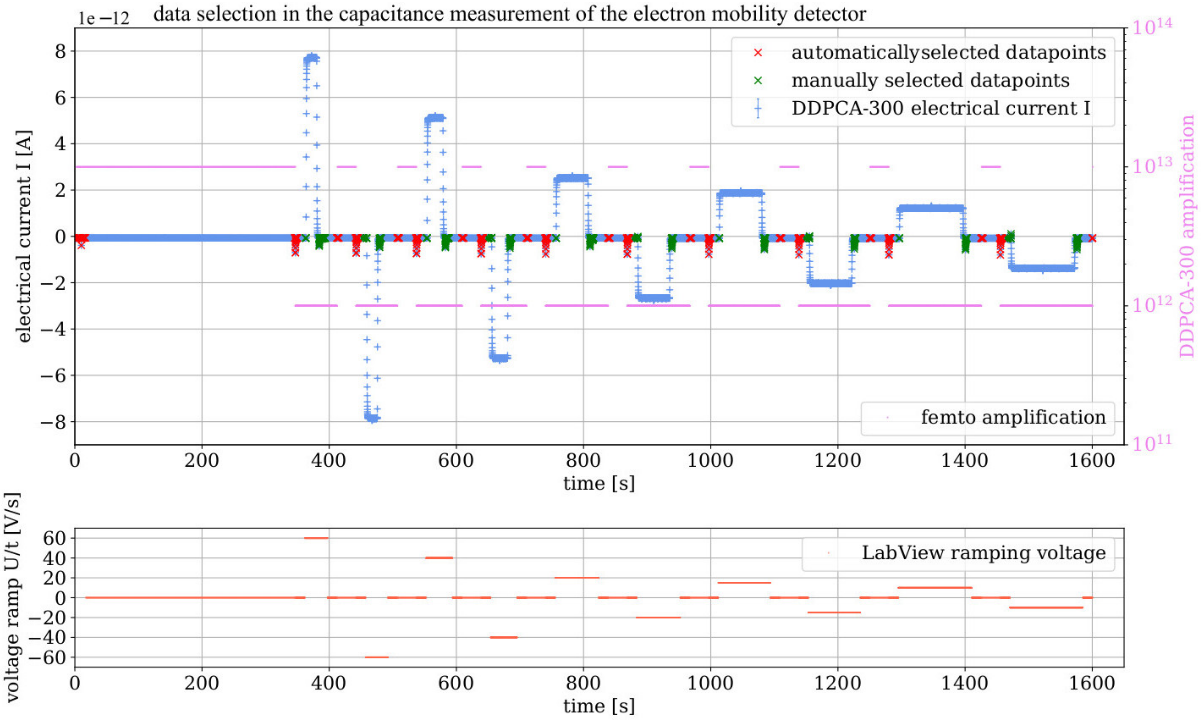

Figure 9: This graph shows the data selection in the capacitance measurement. The electrical current is shown over the time of the measurement. The ramping speed is shown as well as the FEMTO DDPCA-300 amplification level. Several datapoints of the measurement were removed. One reason for the selection was the spike in electrical current near changing FEMTO DDPCA-300 amplification levels. Since these features occurred regularly during periods of switching amplification levels, they are probably a feature of the current amplifier and not an effect within the detector which is why they were removed. Additionally regular spikes could be seen during the background parts of the measurement and at the beginning and end of ramping processes. These spikes might be caused by the voltage source. For the capacitance measurement only the current during ramping voltage is used and the background part of the measurement is used to correct the data. Therefore analyzing these spikes in the background part was deemed not significant for the capacitance measurement and the data points were removed.

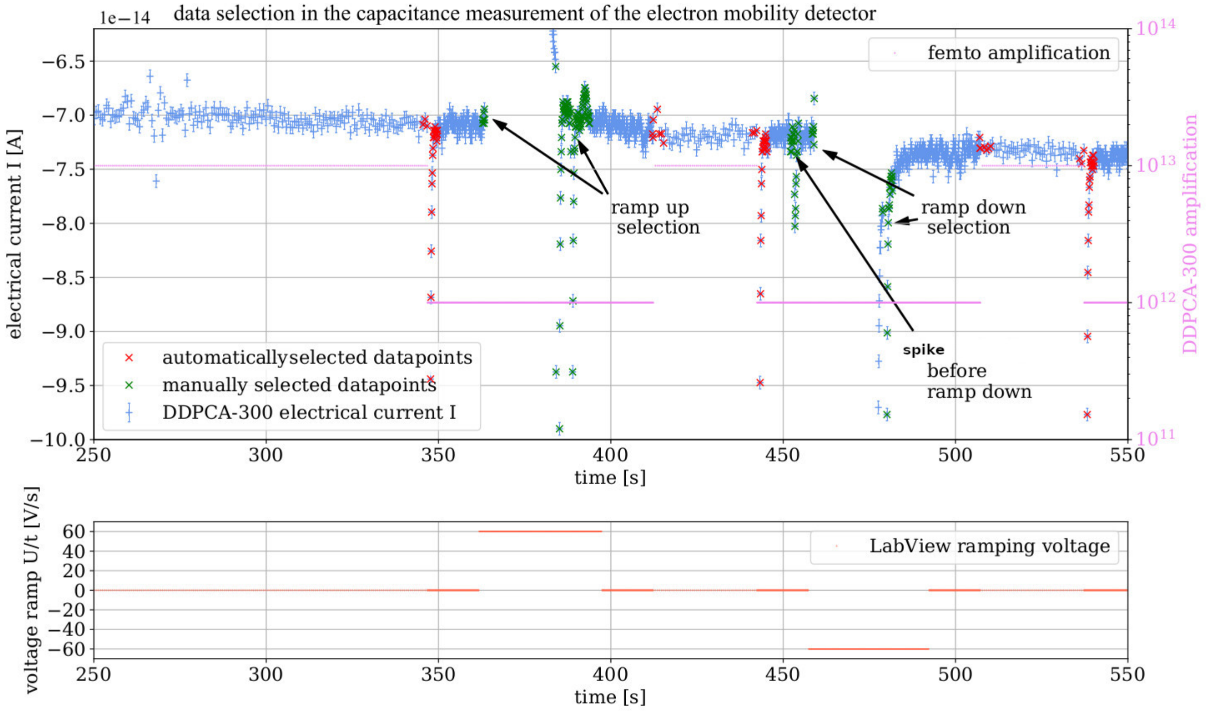

Figure 10: This graph shows the data of the capacitance measurement during the ramping processes with a ramping speed of 60 $\frac{\text{V}}{\text{s}}$ and the datapoints that were removed for the further analysis. Datapoints that have been automatically selected due to changing FEMTO DDPCA-300 amplification level as well as the manually selected spikes in the electrical current are marked.

electrical current in a way, that the fit to the exponential decay yields a reduced $\chi^2_{\text{red.}} = 1$. This correction of the uncertainty was applied to the whole measurement, under the assumption, that noise during constant voltages would influence the electrical current during ramping voltages as well.

$$\sigma_{\text{corr.}}(I) = \sqrt{\sigma(I)^2 \cdot \chi^2_{\text{red.}}} \tag{16}$$

The fit for the background current together with the measured electrical current including the corrected uncertainty is displayed in figure 12. To calculate the uncertainty of the fit function [13] gives the following formula:

$$\sigma_f^2 = g^{\mathrm{T}} V g \tag{17}$$

σ_f is the standard uncertainty of the function, with V being the covariance of the function parameters β and the vector g consisting of enries $\frac{\delta f}{\delta \beta_i}$ [13]. Formula 17 was used to calculate the uncertainty. With V being the covariance matrix of the fitting parameters attained from iminuit. The background current I and the fit function, as well as the $1\sigma_{f_{\text{bg}}}$ interval of the fit function are shown in the figure 13. The background fit function f_{bg} and the uncertainty of the fit function was used to correct the electrical current during the whole measurement.

$$I_{\text{corr.}}(t) = I_{\text{meas.}}(t) - f_{\text{bg}}(t) \tag{18}$$

$$\sigma(I_{\text{corr.}}) = \sqrt{\sigma(I_{\text{meas.}})^2 + \sigma^2_{f_{\text{bg}}}} \tag{19}$$

To calculate the capacitance, the current flowing to the anode induced by the changing voltage had to be determined. The electrical current during each ramping process was fitted to:

$$f_{\text{peak}}(x) = A \cdot (1 - e^{-\frac{x - x_l}{\tau}}) \cdot \left(\Theta(x - x_l) \cdot \Theta(-x + x_r) + \Theta(x - x_r) \cdot e^{-\frac{x - x_r}{\tau}}\right) \tag{20}$$

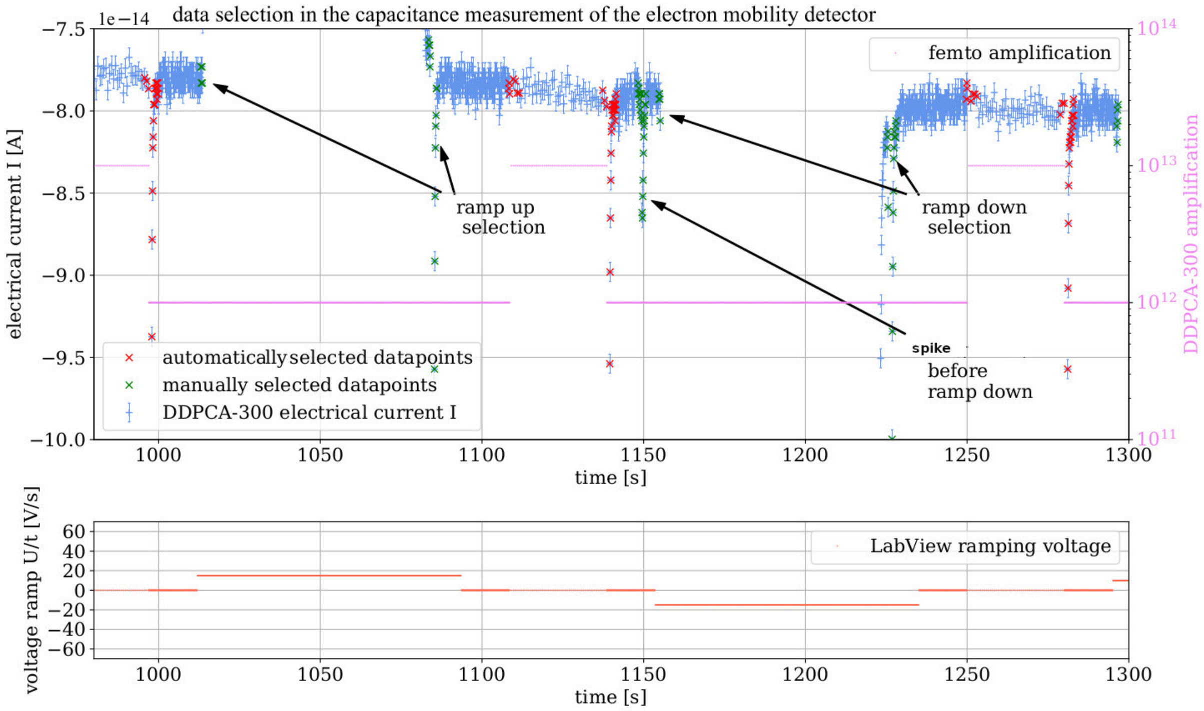

Figure 11: This graph shows the data of the capacitance measurement during the ramping processes with a ramping speed of 15 $\frac{\mathrm{V}}{\mathrm{s}}$ and the datapoints that were removed for the further analysis. Datapoints that have been automatically selected due to changing FEMTO DDPCA-300 amplification level as well as datapoints that were manually selected are marked.

This function consists of a capacitor charge function and a capacitor discharge function. The capacitor charge function starts at x_l and is later multiplied by the discharge function for $x \geq x_r$. For x values with $x_l << x < x_r$ the value of the electrical current is sufficiently close to a constant value of A before the capacitor discharges as soon as the voltage remains constant and after the discharge no electrical current except for the background current is measured. The value of A will later be used to determine the capacitance C of the detector. It represents the constant electrical current I that is induced in the detector as a result of the changing voltage with a constant rate of change.

The background corrected data of the electrical current was fitted using the formula 20. The value $\chi^2_{\mathrm{red}} = 2535.49 \pm 0.09$ is several magnitudes higher than the expected value of 1 for a good fit. So either the value of the uncertainty of the electrical current data is too small or the fit does not describe the data. Since the value of A seems to describe the data during the phase of constant current sufficiently, the uncertainty of the current was corrected with formula 16. This way the uncertainty of the fitting parameters would not be set at a too small value.

In figure 14 the data with the corrected values of uncertainty is shown, for the ramping speed of $\frac{U}{t} = 60.0\,\frac{\mathrm{V}}{\mathrm{s}}$. The value of the current was $A = (7.786 \pm 0.003)\mathrm{e}{-12}\,\mathrm{A}$. The uncertainty of the fitting function has been calculated, following the formula 17 from [13]. The 1σ uncertainty interval has been included in the figure 15. All the other ramping processes have been analyzed in a similar fashion, and the corresponding graphs are included in the appendix chapter 10.

Using the formula

$$I = C \cdot \frac{\mathrm{d}}{\mathrm{d}t} U \tag{21}$$

the capacitance can be determined from a linear fit of the constant current I during ramping

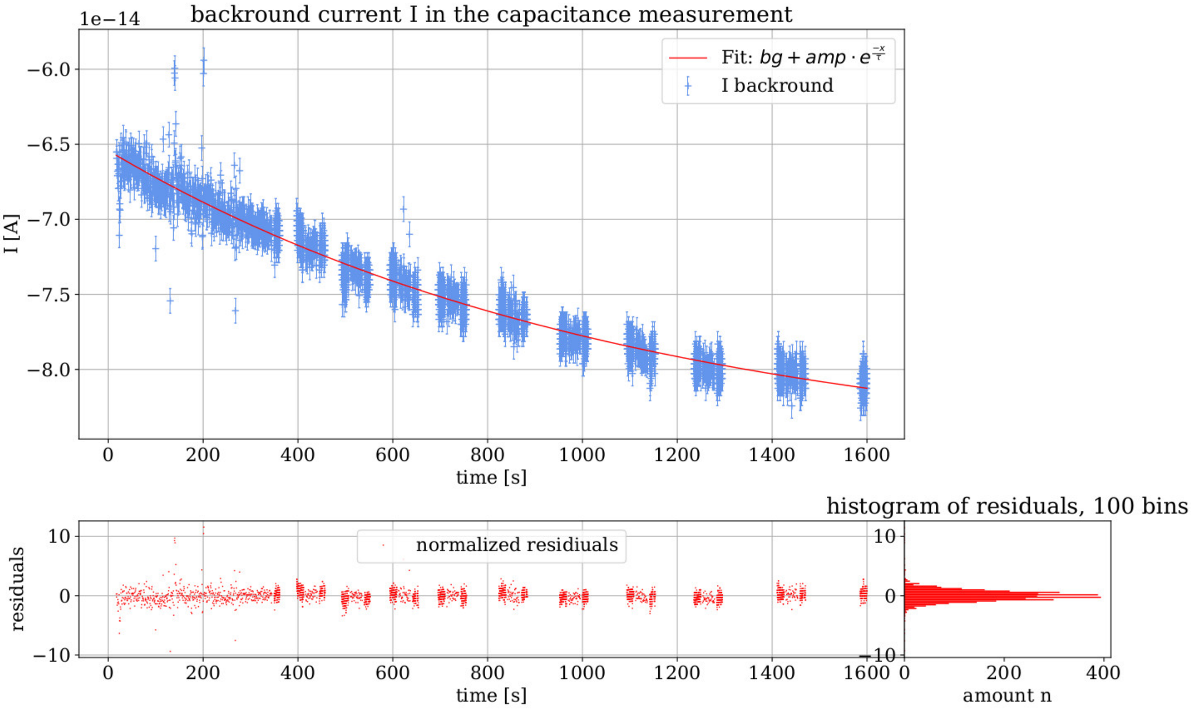

Figure 12: This graph shows the data of the capacitance measurement during the background parts of the measurement with constant voltage after the uncertainty was corrected using the exponential decay fit. Fitting parameters: $bg = (-86.040 \pm 0.012)\mathrm{e}{-15}\,\mathrm{A}$, $amp = (20.6 \pm 0.3)\mathrm{e}{-15}\,\mathrm{A}$, $\tau = (1100 \pm 30)\,\mathrm{s}$. The reduced $\chi^2_{\mathrm{red.}} = (1.00 \pm 0.02)$. Additionally the normalized residuals between the fit function and the measured electrical current is displayed.

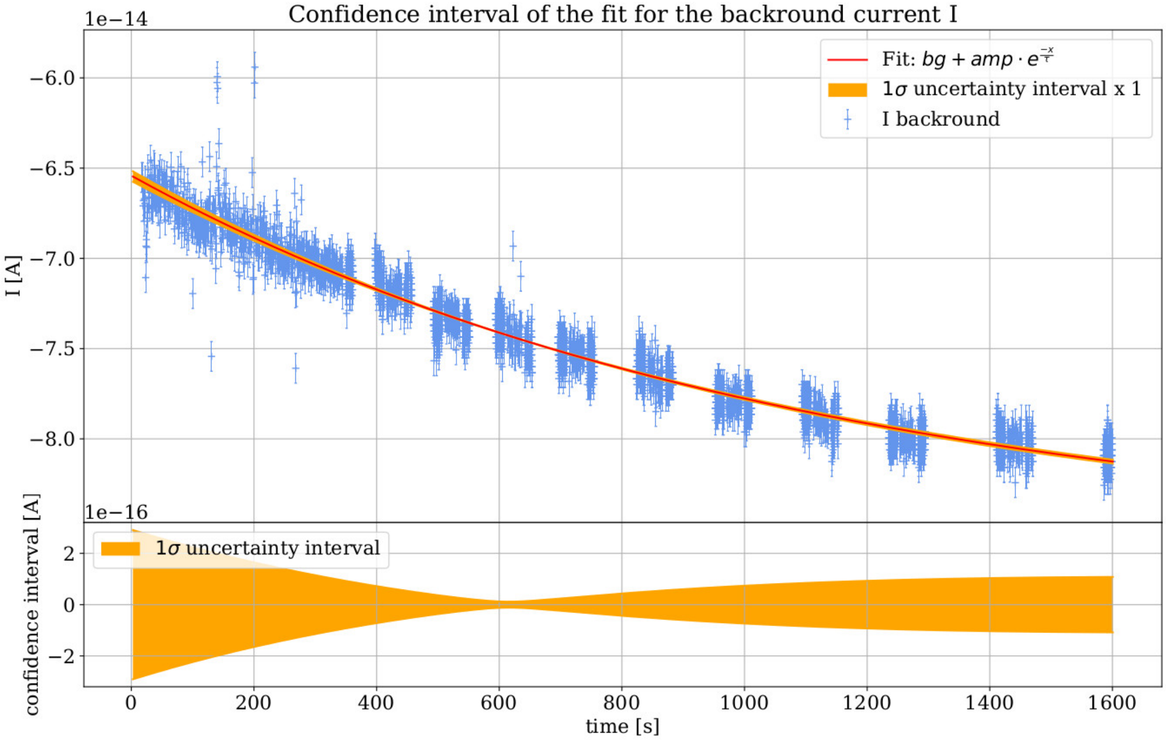

Figure 13: This graph shows the background current I during the capacitance measurement, as well as the fit function used to describe the background current. Additionally the $1\sigma_{f_{\mathrm{bg}}}$ interval of the fitting function is shown. Fitting parameters: $bg = (-86.040 \pm 0.012)\mathrm{e}{-15}\,\mathrm{A}$, $amp = (20.6 \pm 0.3)\mathrm{e}{-15}\,\mathrm{A}$, $\tau = (1100 \pm 30)\,\mathrm{s}$. The reduced $\chi^2_{\mathrm{red.}} = (1.00 \pm 0.02)$.

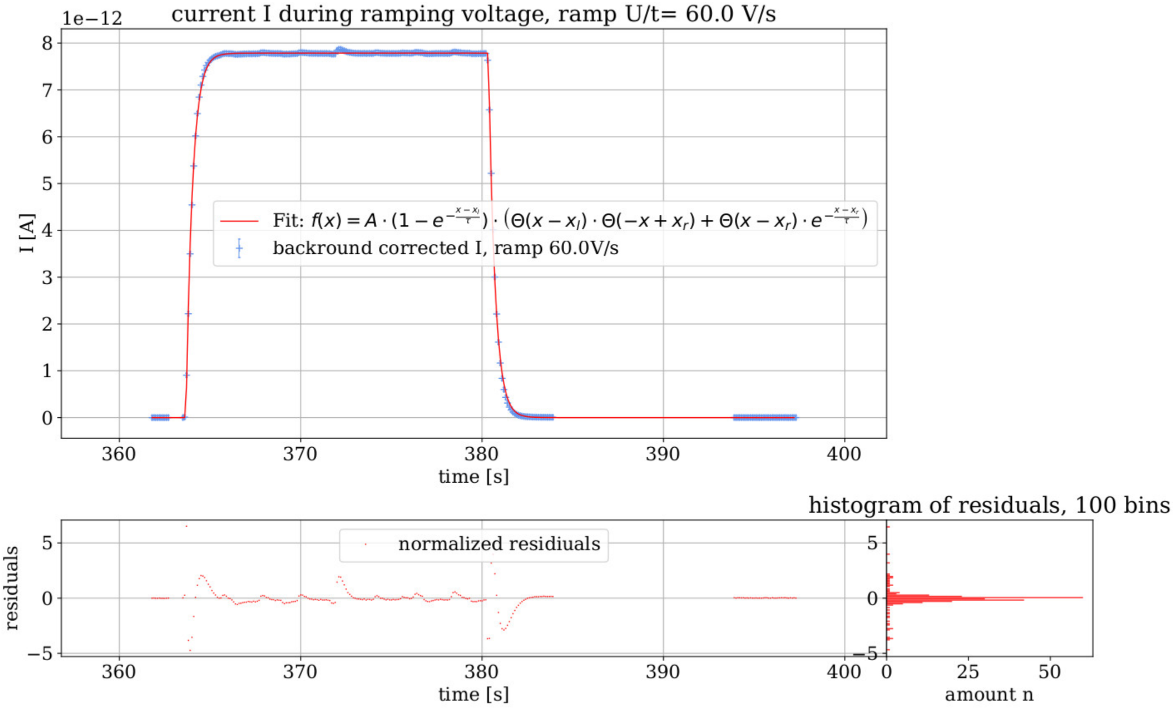

Figure 14: This graph shows the electrical current measured during the ramp up process from 10 V to 1010 V with a constant ramping speed of $\frac{U}{t} = 60.0\,\frac{\mathrm{V}}{\mathrm{s}}$ after the uncertainties of the electrical current I have been modified in a way, that the fit has a $\chi^2_{\mathrm{red}} = 1.00 \pm 0.09$. Fit parameters: $A = (7.786 \pm 0.003)\mathrm{e}{-12}\,\mathrm{A}$, $\tau = (358 \pm 2)\mathrm{e}{-3}\,\mathrm{s}$, $x_l = (363.673 \pm 0.002)\,\mathrm{s}$, $x_r = (380.35 \pm 0.002)\,\mathrm{s}$.

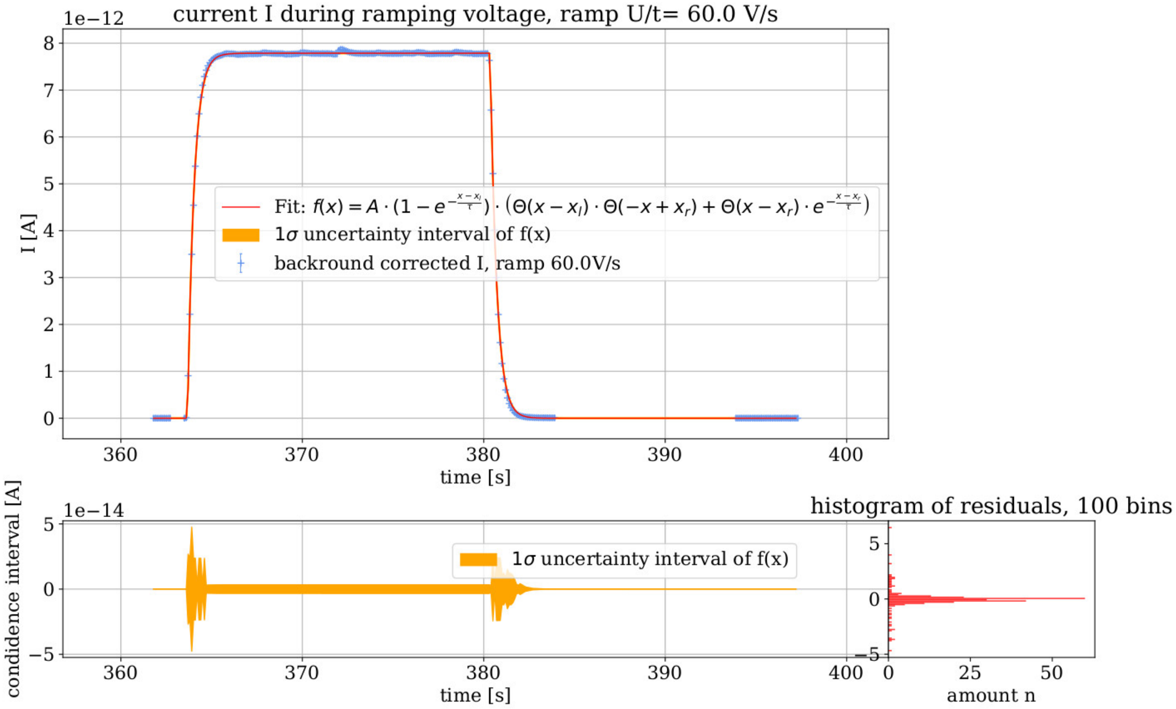

Figure 15: This graph shows the electrical current measured during the ramp up process from 10 V to 1010 V with a constant ramping speed of $\frac{U}{t} = 60.0\,\frac{\mathrm{V}}{\mathrm{s}}$. The uncertainties have been modified so that the fit has a $\chi^2_{\text{red.}} = 1.00 \pm 0.09$. Fit parameters: $A = (7.786 \pm 0.003)\text{e}{-12}\,\mathrm{A}$, $\tau = (358 \pm 2)\text{e}{-3}\,\mathrm{s}$, $x_l = (363.673 \pm 0.002)\,\mathrm{s}$, $x_r = (380.35 \pm 0.002)\,\mathrm{s}$.

processes over the corresponding ramping speed. In figure 16 the fitting parameters for the electrical current were put in relation to the ramping speed $\frac{U}{t}$ and fitted to a linear function. The uncertainties of the resulting fitting parameters were modified to result in a $\chi^2_{\text{red.}} = (1.0 \pm 0.5)$ to not underestimate the uncertainty of the fit. The capacitance measurement yielded a result of:

$$C_{\text{detector}} = (1.2969 \pm 0.0002)\text{e}{-13}\,\text{F}) \tag{22}$$

This result was used to determine the distance between the anode and the photocathode using the formula:

$$d = \epsilon_0 \cdot \frac{A}{C} \tag{23}$$

With the area of the anode of $A_{\text{anode}} = (19.6 \pm 0.3)\,\text{mm}^2$ leads to a distance:

$$d_{\text{anode}-\text{cathode}} = (1.34 \pm 0.02)\,\text{mm} \tag{24}$$

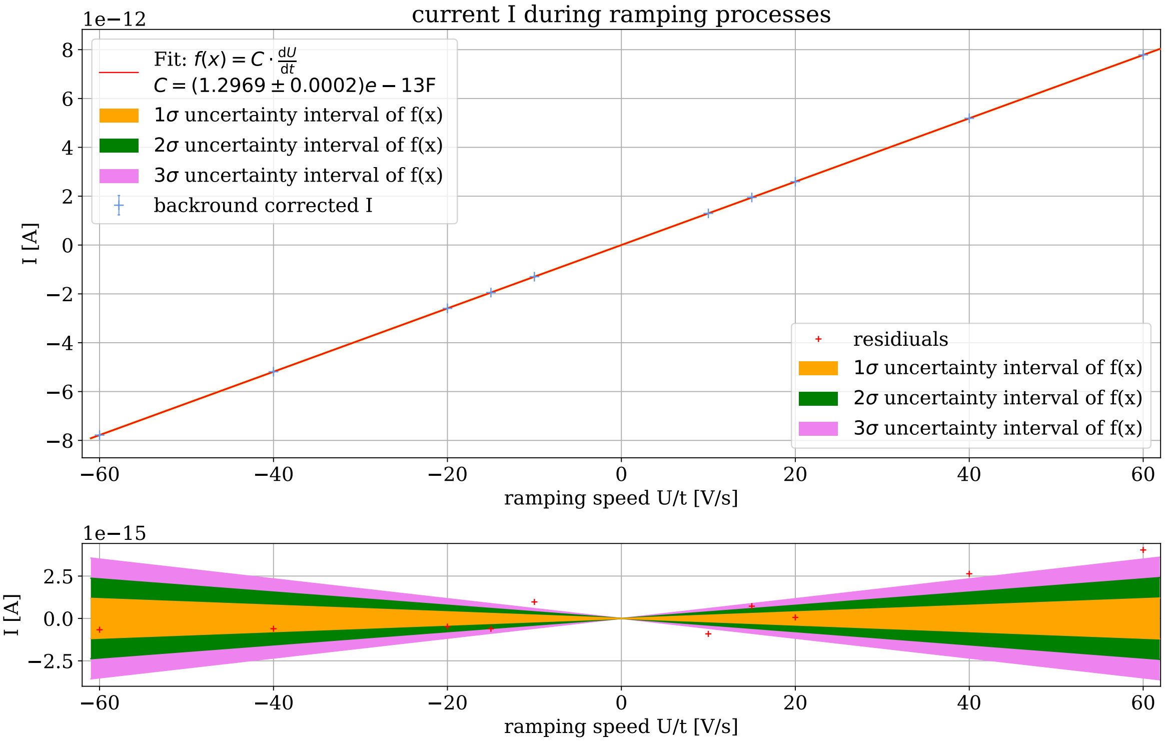

Figure 16: This graph shows the electrical currents acquired from the fitting parameters for the varying ramping speeds. Using the formula $I = C \cdot \frac{\text{d}}{\text{d}t}U$, the capacitance C can be acquired by fitting the data to a linear growth. This resulted in a capacitance of $C_{\text{detector}} = (1.2969 \pm 0.0002)\text{e}{-13}\,\text{F}$. The uncertainty of the value has been modified to produce $\chi^2_{\text{red.}} = (1.0 \pm 0.5)$.

4.3 Conclusion of the capacitance measurement

The FLUKE multimeter seemed to be unable to properly measure the capacitance of the system consisting of cathode and anode. The measurement of the capacitance of the detector with the

FLUKE multimeter yielded two different results of $C_3 = (3.7960 \pm 0.0004)\mathrm{e}{-11}\,\mathrm{F}$ and $C_4 = (1.497 \pm 0.0004)\mathrm{e}{-11}\,\mathrm{F}$ which are both several magnitudes larger than the rough estimate from the detector geometry as well as the value acquired by the measurement using the ramping voltage. It seems to be the case, that the FLUKE multimeter measures not only the capacitance between anode and cathode but also between anode and guard ring.

Measuring the current flowing through the anode induced by a changing voltage resulted in a capacitance of $C_{\mathrm{detector}} = (1.2969 \pm 0.0002)\mathrm{e}{-13}\,\mathrm{F}$ which differs by $0.0031\mathrm{e}{-13}\,\mathrm{F}$ from the value derived from the geometrical properties in the CAD drawing $C_{\mathrm{plate,CAD}} = (1.3 \pm 0.5)\mathrm{e}{-13}\,\mathrm{F}$. The difference might be caused by the difference in distance between anode and cathode in the actual detector versus the CAD drawing. This difference may be caused by two influences. First the length of the anode had to be modified to fit into the detector changing the measurements. Second the distance between anode and cathode can be influenced by tightening the screws during assembly and therefore compressing the copper gaskets resulting in a high uncertainty of the distance between anode and cathode.

With this capacitance measurement a value of $d_{\mathrm{anode-cathode}} = (1.34 \pm 0.02)\,\mathrm{mm}$ was measured for the distance between cathode and anode using the capacitance C_{detector} and the area of the anode from the CAD drawing. It is recommended to use the value of $C_{\mathrm{detector}} = (1.2969 \pm 0.0002)\mathrm{e}{-13}\,\mathrm{F}$ for future work with the electron mobility detector. This value could be the basis for future simulations with the detector to get a better understanding of the electromagnetic field inside the detector volume. Comparing the simulation with the measurement data could lead to an additional method to determine the distance $d_{\mathrm{anode-cathode}}$. These simulations could also be used to verify the interpretation of the FLUKE multimeter data.

Future measurements could be improved by measuring the voltage applied to the photocathode directly to get a measurement of the voltage for each data point. Then the ramping speed could be determined from the voltage measurement. The uncertainty of the distance measurement could be improved by an additional measurement of the area of the anode with a smaller uncertainty.

With this data future measurements can be conducted to determine the G_{fi}, ϵ_r and the electron mobility of TMBi. In future measurements with TMBi, knowledge of the exact distance between anode and cathode will help to improve simulations needed for measurements of material properties such as the free ion yield G_{fi}. Exact simulations are needed to verify the measurements done in [15].

5 Measurement of the electrical current inside the detector induced by a UV-LED pulse for different measurement setups

It is planned for future measurements to use simultaneous measurement of the electrical current and the charge generated inside the detector by a pulsed UV-LED and the photocathode. The UV-LED used had a wavelength of 250 nm to 270 nm [16]. Therefore it was necessary to proof that simultaneous charge measurement does not influence the current measurement in a way that invalidates the data. A comparative measurement of the electrical current was conducted changing the setup from the current measurement of previous measurements to the setup for simultaneous current and charge measurement step by step, followed by a current measurement in between each step.

These measurements showed that the current measurements with and without simultaneous charge measurement seem to be in agreement with each other, even though a comparison by a functional relationship remains to be done in future work.

It may be advantageous for future measurements to modify the current generated inside the detector by the pulsed UV-LED in conjunction with the photocathode. This can be achieved by modifying the pulse used to power the UV-LED. For this reason the relationship between the current inside the detector I_{pulse} and the peak electrical power $P_{\text{UV-LED}}$ of the UV-LED for pulses of $f = 2\,\text{kHz}$ and width $= 50\,\mu\text{s}$ was investigated. The relationship between the two seemed to be non-linear but the determination of the functional relationship has to be part of future works. Therefore it is recommended to keep the amplitude of the pulse powering the UV-LED constant until the functional relationship is clarified.

The relationship between the current I_{pulse} and the pulse width of a rectangular pulse powering the UV-LED with $f = 1\,\text{kHz}$ and a peak power $P_{\text{UV-LED}} = (0.419 \pm 0.010)\,\text{W}$ was investigated and a linear relationship was used to fit the measured current I_{pulse} to the corresponding pulse width. The fit parameter was $m_{\text{pulse}} = (-2.110 \pm 0.006)\text{e}{-7}\,\frac{\text{A}}{\text{s}}$ with $I_{\text{pulse}} = m_{\text{pulse}} \cdot \text{width}$. Because of this linear relationship it is recommended to modify the pulse width rather than the power of the UV-LED $P_{\text{UV-LED}}$ to modify the amount of electrons introduced into the detector volume by the UV-LED and the photocathode.

5.1 Comparative measurement of the electrical current inside the detector for different measurement setups and varying $P_{\text{UV-LED}}$

The first part of this measurement consisted of the comparative measurement between the 3 different measurement setups. For each setup the current I_{pulse} inside the detector was measured for varying pulse amplitudes.

5.1.1 Method of the comparative current measurement for different measurement setups

To measure the electrical current generated by the UV-LED, the UV-LED was connected to a Tektronix AFG3102 pulse generator, with a resistor of $R_{\text{preUV-LED}} = (100.00 \pm 0.01)\,\Omega$ in between. This resistor was placed to monitor the voltage before and after the resistor to control the voltage going into the UV-LED as well as the current $I_{\text{UV-LED}}$ flowing through the UV-LED. In doing so the maximum voltage and current could be monitored as to not exceed the given maximum value in the datasheet of the UV-LED [16]. The UV-LED was positioned in front of the gold coated window acting as the photocathode. The voltage amplitude of the pulse was monitored using a Tektronix MSG 4054 oscilloscope. The voltage applied to the detector cathode was kept at a constant value of $-20\,\text{V}$. Since the aim was to measure the generated electrical current as well as the charge pulse inside the detector a charge-sensitive preamplifier was connected to the anode side of the detector. To ensure that this change in setup does not change the electrical current I measured by the FEMTO DDPCA-300 current amplifier a comparative measurement was conducted.

Flowcharts of the three setups are shown in figure 17. Since the final measurement setup for the simultaneous charge and current measurement will be using a similar setup to setup 3 each individual change of the measurement setup had to be evaluated. This process was conducted to ensure that the change in measurement setup does not change the measured electrical current in a major way.

For the comparative measurement, the pulsewidth was kept at a constant width $= 50\,\mu\text{s}$ while the frequency was kept at $f = 2\,\text{kHz}$. The voltage before and after the resistor between Tektronix AFG3102 pulse generator and the UV-LED was measured with a Tektronix MSG 4054 oscilloscope and the electrical current flowing through the UV-LED was calculated using formula 25:

$$I = \frac{U}{R} \tag{25}$$

The electrical power of the pulse was calculated using the voltage measured after the resistor

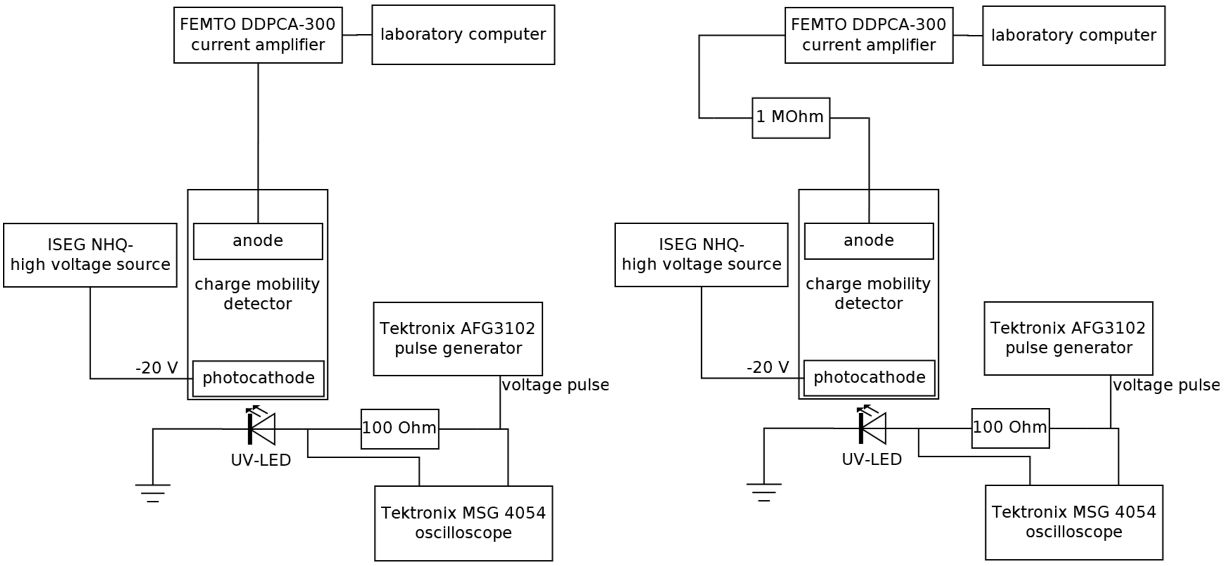

(a) setup 1

(b) setup 2

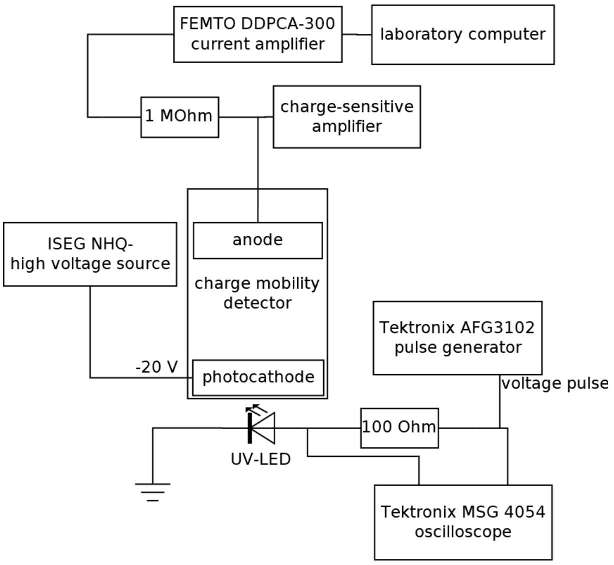

(c) setup 3

Figure 17: This figure shows flowcharts of the 3 setups for the comparative measurement with the pulsed UV-LED. The UV-LED is positioned infront of the photocathode and is powered by the Tektronix AFG3102 pulse generator. The Tektronix MSG 4054 oscilloscope is used to readout the voltages of the pulse before and after the $100\,\Omega$ resistor. (a) in setup 1 the FEMTO DDPCA-300 current amplifier is connected directly to the anode (b) setup 2 differs from setup 1 by the resistor in between the anode and the FEMTO DDPCA-300. (c) setup 3 includes the charge-sensitive-preamplifier attached to a splitter in between the resistor and the anode.

and the current flowing through the UV-LED using formula 26.

$$P = U \cdot I \tag{26}$$

5.1.2 Results of the comparative measurement of I_{pulse} for different $P_{\text{UV-LED}}$ using differing measurement setups

Measurements of the electrical current inside the detector have been conducted for varying $I_{\text{UV-LED}}$ respectively $P_{\text{UV-LED}}$. With $I_{\text{UV-LED}}$ being the current flowing through the UV-LED during the pulse peaks and $P_{\text{UV-LED}}$ being the power calculated from $I_{\text{UV-LED}}$ and the voltage measured after $R_{\text{preUV-LED}}$ using formula 26 . Similar to the capacitance measurement in section 4.2 datapoints around times of changing amplification levels in the FEMTO DDPCA-300 current amplifier have been removed. Additionally datapoints during switch on and switch off periods of the pulse generator Tektronix AFG3102 have been removed, because the measured voltages from the oscilloscope Tektronix MSG 4054 were recorded manually, invalidating datapoints around periods of changing pulse properties. The measurement data for setup 3 as well as the removed datapoints are shown in figure 18 as an example.

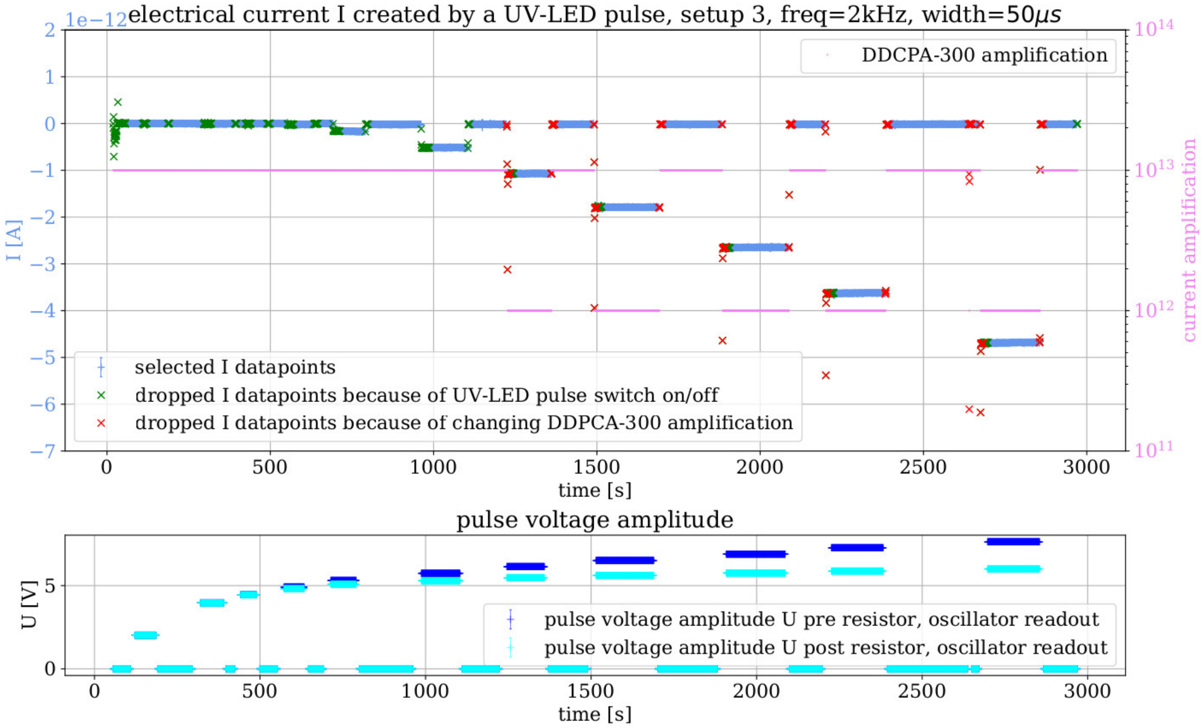

Figure 18: This graph shows the electrical current inside the detector generated by a pulsed UV-LED for varying pulse voltages for the measurement setup 3. The voltage measured before and after the pre-resistor is shown in the lower graph. The data selection process is illustrated as an example for the selection process for all three setups.

To describe the background current of the measurement, the current before and after each pulsed measurement has been used as the basis of a fit:

$$f_{\text{bg,pulse}}(x) = bg + amp \cdot e^{\frac{-(x-t_0)}{\tau}} \tag{27}$$

The $\chi^2_{\text{red.}}$ of the fit has been used to determine the uncertainties in the current I data of the measurement according to formula 16. Figure 19 shows the background current while the

UV-LED current was set to $I_{\mathrm{UV-LED}} = (0.0045 \pm 0.0002)\,\mathrm{A}$ which corresponds to a power of $P_{\mathrm{UV-LED}} = (0.0238 \pm 0.0011)\,\mathrm{W}$. The uncertainty of the measured current I inside the charge mobility detector has already been corrected using the fitting function as described in formula 16. In figure 20 the 1 σ confidence interval of the fit is displayed. The uncertainty of the fit was calculated using formula 17.

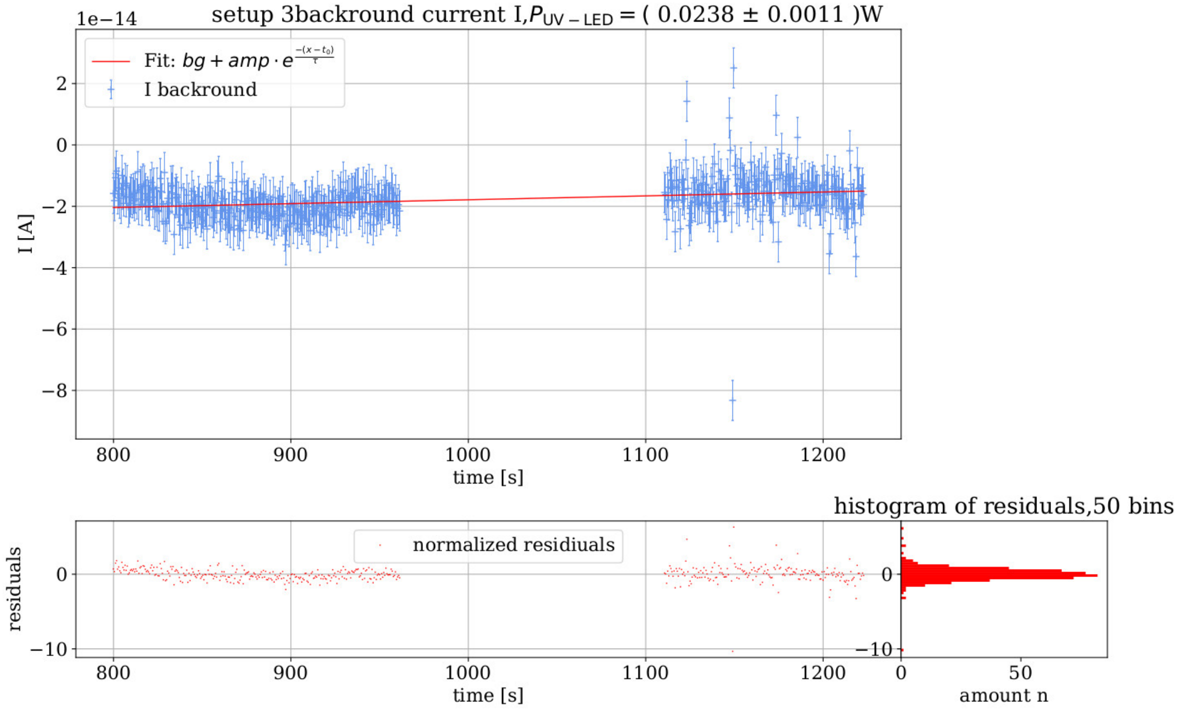

Figure 19: setup 3: background current I for $P_{\mathrm{UV-LED}} = (0.0238 \pm 0.0011)\,\mathrm{W}$. Fit parameters: $bg = (320.802 \pm 0.004)\mathrm{e}{-12}\,\mathrm{A}$, $amp = (-308.905 \pm 0.004)\mathrm{e}{-12}\,\mathrm{A}$, $t_0 = (961.0 \pm 0.3)\mathrm{e}3\,\mathrm{s}$, $\tau = (25.366 \pm 0.009)\mathrm{e}6\,\mathrm{s}$. $\chi^2_{\mathrm{red.}} = 1.00 \pm 0.07$. This fit has already been used to modify the uncertainties of the measured current I to produce a $\chi^2_{\mathrm{red.}} = 1.00$ using formula 16.

Analogously to the background correction described in 4.2 this background fit has been used to correct the data of the current I during the pulse. In the electrical current measurement the FEMTO DDPCA-300 integrates the data with a rise/fall time of 350 ms for the amplification levels used [14]. This is much higher then the pulse width which is why the response function was expected to be a constant current during the UV-LED pulses. The fit to a constant value I_{pulse} for $P_{\mathrm{UV-LED}} = (0.0238 \pm 0.0011)\,\mathrm{W}$ is shown in figure 21.

The data for all 3 setups and all $P_{\mathrm{UV-LED}}$ pulse peaks have been analyzed analogously and are shown in figure 22. The measured I_{pulse} for the different setups seem sufficiently close to justify using setup 3 to measure both current I and the charge Q simultaneously.

5.1.3 Conclusion for the comparative measurement of I_{pulse} for different $P_{\mathrm{UV-LED}}$ using differing measurement setups

The current I_{pulse} in the detector induced by the pulsed UV-LED was measured for various $P_{\mathrm{UV-LED}}$. The relationship seems to be non linear. Future measurements could improve on this

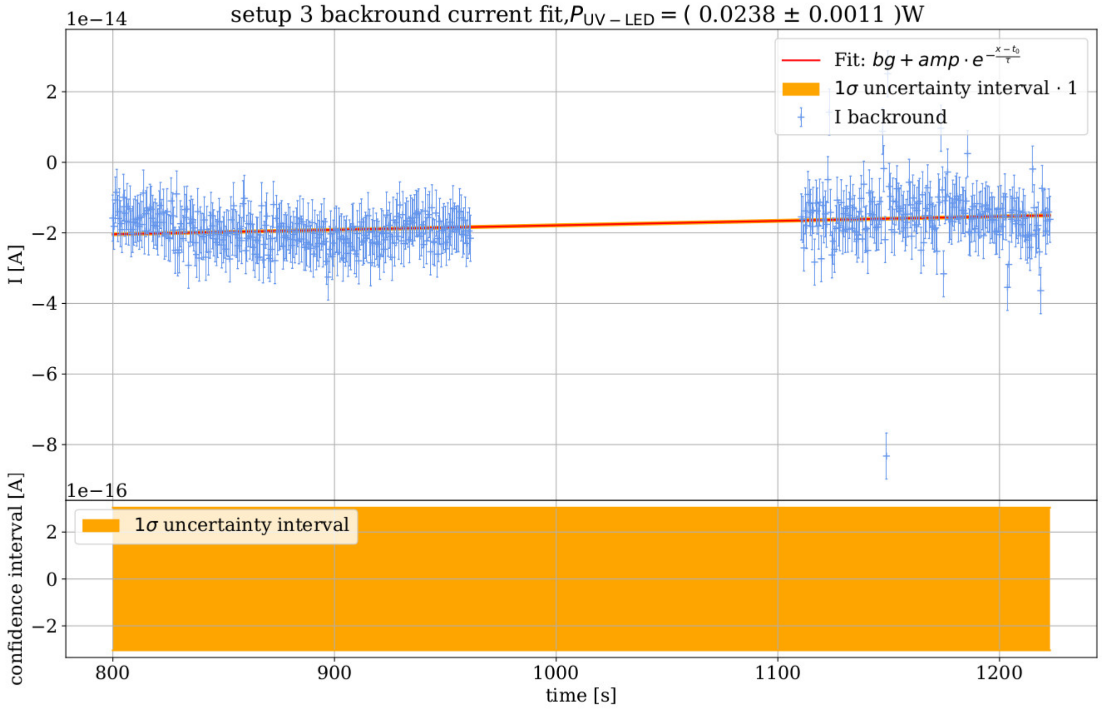

Figure 20: setup 3: background current I for $P_{\mathrm{UV-LED}} = (0.0238 \pm 0.0011)\,\mathrm{W}$. 1 σ confidence of the background fit function. Fit parameters: $bg = (320.802 \pm 0.004)\mathrm{e}{-12}\,\mathrm{A}$, $amp = (-308.905 \pm 0.004)\mathrm{e}{-12}\,\mathrm{A}$, $t_0 = (961.0 \pm 0.3)\mathrm{e}3\,\mathrm{s}$, $\tau = (25.366 \pm 0.009)\mathrm{e}6\,\mathrm{s}$. $\chi^2_{\mathrm{red.}} = 1.00 \pm 0.07$.

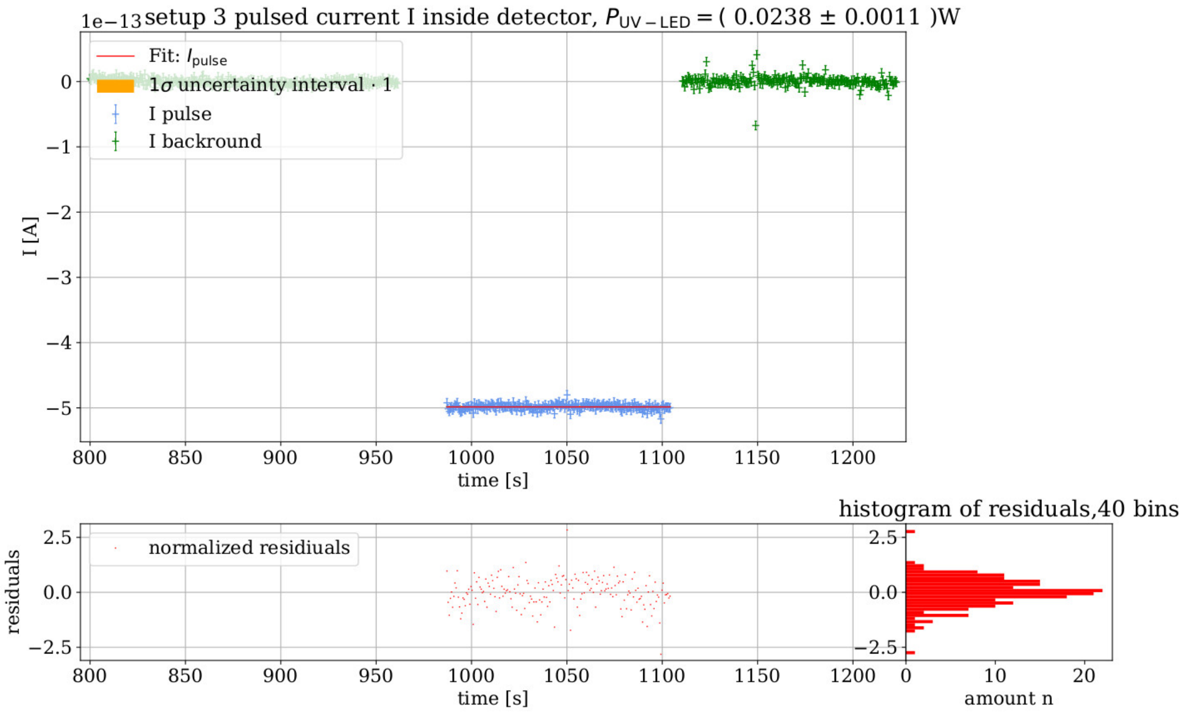

Figure 21: setup 3: background corrected data for the pulse current I_{pulse} with $P_{\text{UV−LED}} = (0.0238 \pm 0.0011)$ A. Fit parameters: $I_{\text{pulse}} = (-498.6 \pm 0.3)\text{e}{-15}$ A. $\chi^2_{\text{red.}} = 0.4 \pm 0.1$. The uncertainty of the fit parameters was modified by $\sigma(I_{\text{pulse}}) = \sqrt{\sigma(I_{\text{pulse}})^2 \cdot \chi^2_{\text{red.}}}$ so that the uncertainty value is not misrepresented.

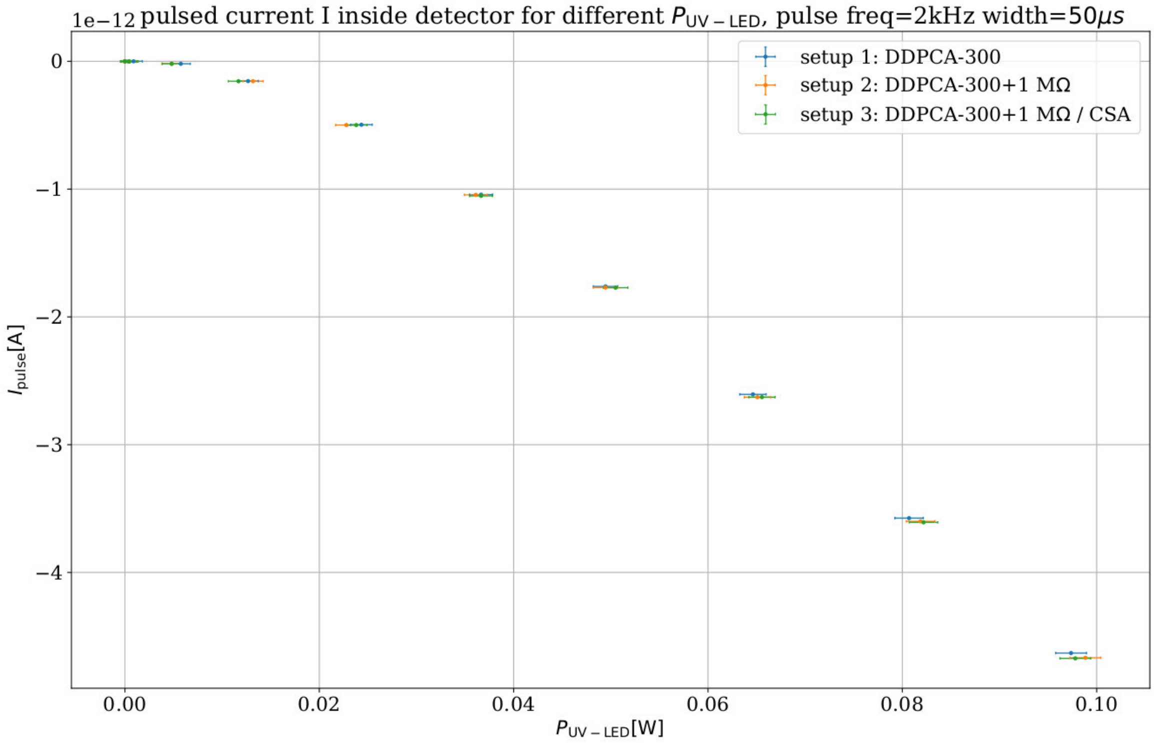

Figure 22: Comparison of I_{pulse} for various $P_{\text{UV−LED}}$ in the three the different measurement setups. I_{pulse} doesn't follow a linear progression for all measurement setups. Also the measured I_{pulse} seem to be sufficiently close to justify using setup 3 to measure the current I at the same time as the charge Q in the detector.

work by using even smaller steps in $P_{\mathrm{UV-LED}}$ to evaluate the functional relationship and further compare the three different setups. For now it is recommended to use pulses with a constant amplitude when measuring with the UV-LED.

For the 3 measurement setups the values were sufficiently close to justify using setup 3 for further measurements, to simultaneously measure the charge and the current inside the detector.

5.2 Measurement of the current I_{pulse} for varying pulse widths

To determine the relationship between the pulsewidth of the UV-LED pulse and the induced current I_{pulse}, the measurement setup shown in figure 24 was used to measure the electrical current inside the detector created by the UV-LED and the photocathode. The current was measured with the FEMTO DDPCA-300 while the generated charge was measured using a charge-sensitive amplifier. This data was measured with an electrical power in the UV-LED during the pulse peaks of $P_{\mathrm{UV-LED}} = (0.419 \pm 0.010)\,\mathrm{W}$ and pulse frequency of $f = 1\,\mathrm{kHz}$ for varying pulse widths of a rectangular pulse.

The relationship between the induced current I_{pulse} and the pulsewidth seem to be in agreement with a linear relationship. For $I_{\mathrm{pulse}} = m_{\mathrm{pulse}} \cdot \mathrm{width}$, a proportionality constant of $m_{\mathrm{pulse}} = (-2.110 \pm 0.006)\mathrm{e}{-7}\,\frac{\mathrm{A}}{\mathrm{s}}$ was determined using a linear fit.

5.2.1 Measurement setup for the simultaneous measurement of the current I_{pulse} and the charge signal

Since it is planned to use the charge mobility detector for future measurements in a continuous cleaning cycle for TMBi, the measurement setup shown in figure 24 was connected to the electric cleaning setup, which was subsequently put under vacuum. A photograph of the measurement setup is shown in the figure 23

Using the Tektronix AFG3102 pulse generator rectangular pulses of a constant amplitude and frequency but varying pulse widths were used to power the UV-LED. A resistor of $R_{\mathrm{preUV-LED}} = (100.00 \pm 0.01)\,\Omega$ was installed between the Tektronix AFG3102 and the UV-LED. The Tektronix MSG 4054 oscilloscope was used to control the pulse voltages before and after the resistor in front of the UV-LED and subsequently the current $I_{\mathrm{UV-LED}}$ was calculated using formula 25. From the current $I_{\mathrm{UV-LED}}$ and the voltage measured before the UV-LED the power $P_{\mathrm{UV-LED}}$ during the peak of the pulses was calculated using formula 26. The FEMTO DDPCA-300 was then used to measure the current I_{pulse} inside the detector for various pulse widths, while the charge-sensitive-amplifier was used to measure the generated charge. To achieve this the charge-sensitive-amplifier was attached to a spectroscopy amplifier with a shaping time of $6\,\mu\mathrm{s}$ and an amplification level of 1000. Additionally the data from the spectroscopy amplifier was filtered by a gating pulse from the Tektronix AFG3102 pulse generator which was synchronous to the pulse used to power the UV-LED. To properly filter the charge signal the gating pulse was delayed to overlap with the measured charge pulse. The filtered data from the spectroscopy amplifier was then converted by an analog-to-digital converter and compiled by the MAESTRO software on the laboratory computer. A flowchart of the setup is shown in figure 24.

5.2.2 Measurement results for the relationship between pulse width and pulse current I_{pulse} inside the detector

Similar to previous measurements the datapoints surrounding points where the amplification level of the FEMTO DDPCA-300 current amplifier changed were removed. Analogously to chapter 5.1.2 datapoints surrounding points of pulse switch on and switch off have been removed as well. This data selection is shown in figure 25. The electrical power of the UV-LED pulses was $P_{\mathrm{UV-LED}} = (0.419 \pm 0.010)\,\mathrm{W}$.

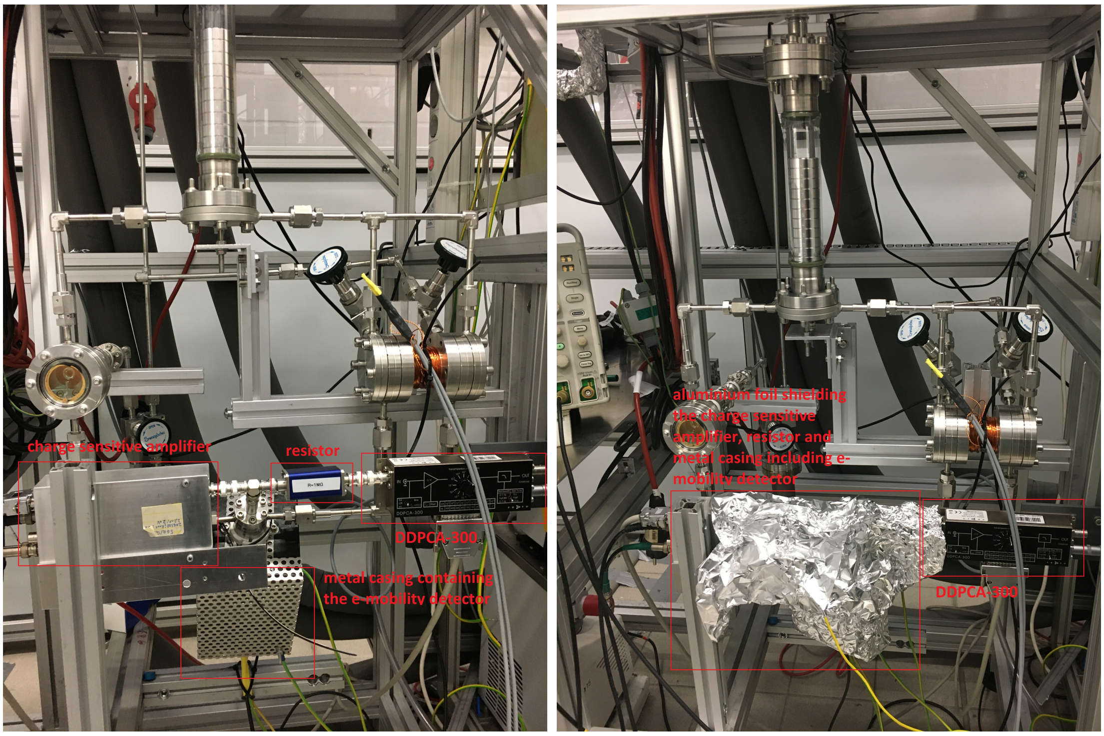

(a) measurement setup inside the cleaning setup

(b) measurement setup inside the cleaning setup wrapped in aluminum foil

Figure 23: This photograph shows the measurement setup for the simultaneous measurement of the charge and the electric current inside the detector for varying pulse widths. The setup consisted of the charge mobility detector inside its metal casing with the anode side connected to a charge sensitive amplifier and the FEMTO DDPCA-300 current amplifier behind a resistor of 1 MΩ. The FEMTO DDPCA-300 was connected to a computer with a LabView program managing the amplification level and data readout. The detector was attached to a ISEG NHQ-high voltage source, which was controlled by a LabView program. The charge-sensitive-amplifier was connected to a spectroscopy amplifier, the data of which was filtered by a gating pulse from the Tektronix AFG3102 pulse generator. The filtered data from the spectroscopy amplifier was then converted by an analog-to-digital converter. The data from the analog-to-digital converter was read out by the MAESTRO software. For the measurement the setup was wrapped in aluminum foil to reduce the noise.

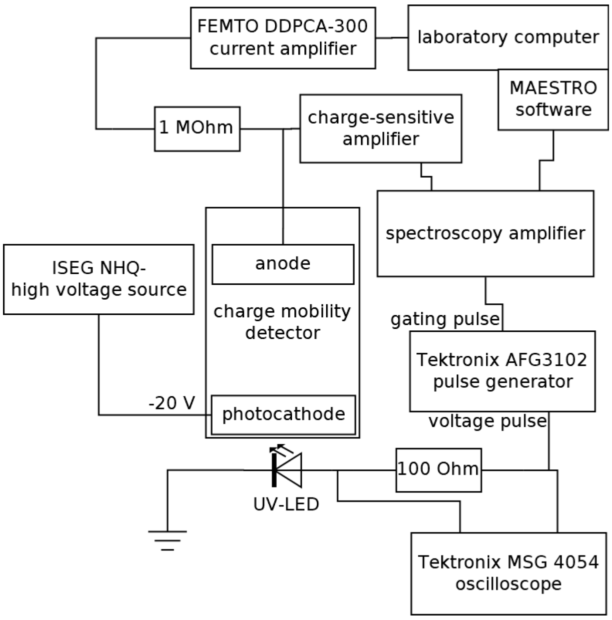

Figure 24: Flowchart of the setup for the simultaneous measurement of the charge and the electric current inside the detector generated by UV-LED pulses of varying pulse widths. The UV-LED is powered by pulses from the Tektronix AFG3102. A Tektronix MSG 4054 oscilloscope is used to measure and control the voltage of the pulses. The electrical current is measured by a FEMTO DDPCA-300 current amplifier and the charge is measured with a charge-sensitive amplifier. The data from the charge-sensitive amplifier is analyzed using a spectroscopy amplifier with a gating pulse from the Tektronix AFG3102 and afterwards recorded by the MAESTRO software on the laboratory computer.

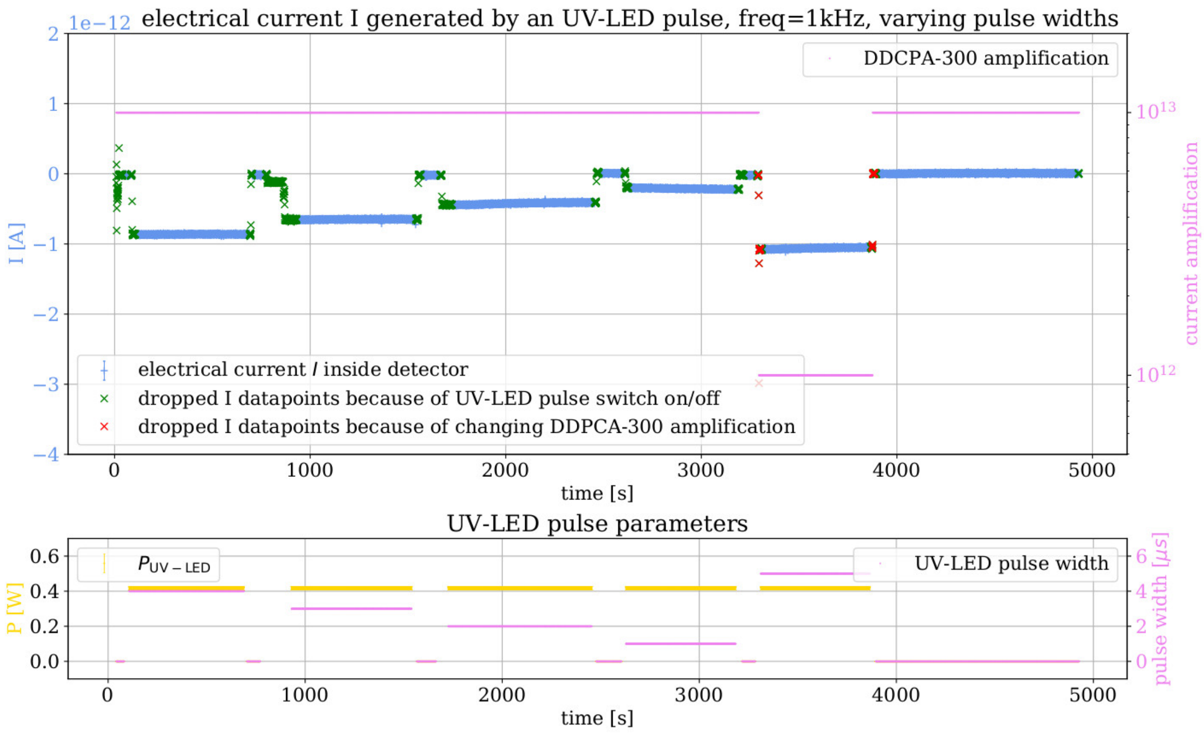

Figure 25: Data selection for the current measurement in the detector generated by UV-LED pulses of varying pulse width.

As described in 5.1.2 the background parts of the data for each pulse width were fitted to formula 27. This fit is shown for a pulse width of $5\,\mu$s in figure 26 and in figure 27 with the 1σ confidence interval of the fitting function calculated using 17. Similarly to previous data analysis the background fit has been used to modify the uncertainties of the current measurement. The measured current I was corrected by the data of the background fit. The corrected data of the current I was fitted to a constant value under the assumption, that the FEMTO DDPCA-300 integrates over a large enough time frame, that the UV-LED pulses will only be detected as a constant current. This current and the fit to I_{pulse} for the pulse width $5\,\mu$s is shown in figure 28

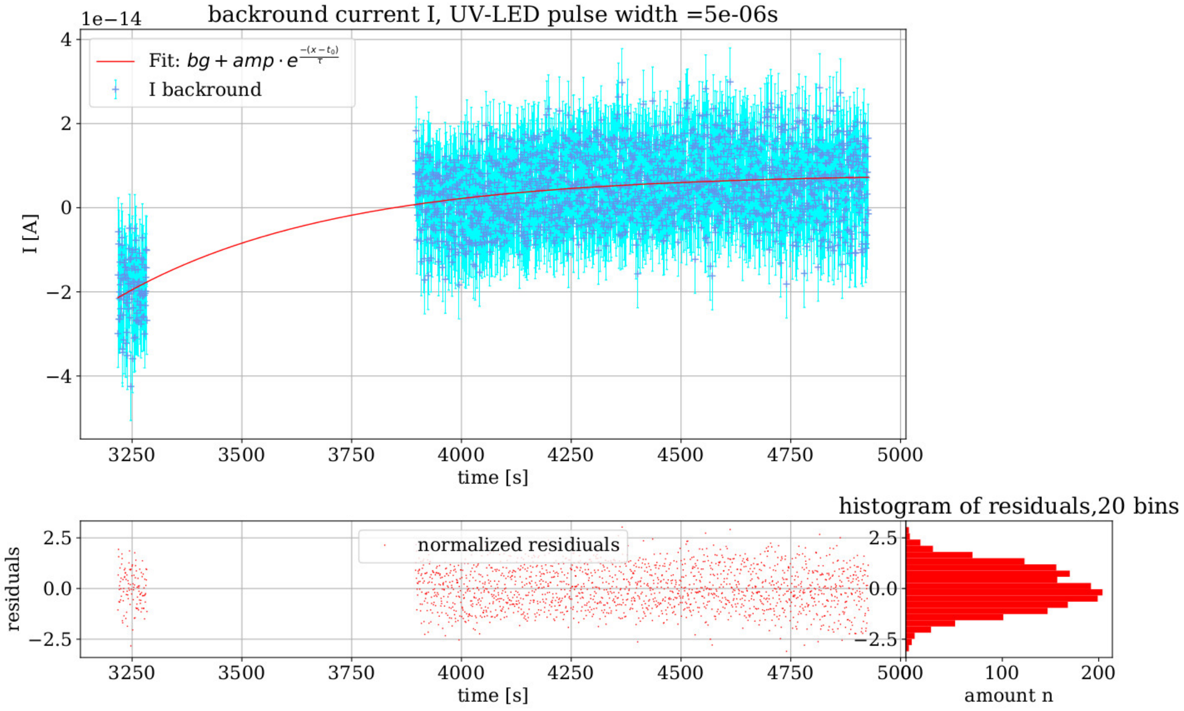

Figure 26: Background current for a pulse width of 5e−6 s. Fit parameters: $bg = (8.1 \pm 0.3)\mathrm{e}{-15}\,\mathrm{A}$, $amp = (-0.11 \pm 0.03)\mathrm{e}{-6}\,\mathrm{A}$, $t_0 = (-4.1 \pm 0.2)\mathrm{e}3\,\mathrm{s}$, $\tau = (488 \pm 11)\,\mathrm{s}$. $\chi^2_{\text{red.}} = 1.00 \pm 0.03$.

This process was conducted all pulse widths. The fit parameters I_{pulse} for the different pulse widths are shown in relationship to the pulse widths in figure 29. This data was fitted to a linear function:

$$I_{\text{pulse}} = m_{\text{pulse}} \cdot \text{width} \tag{28}$$

With $m_{\text{pulse}} = (-2.110 \pm 0.006)e - 7\,\frac{\mathrm{A}}{\mathrm{s}}$.

5.2.3 Conclusion for the measurement regarding the relationship between I_{pulse} inside the detector and the pulsewidth of the UV-LED

The relationship between the pulsewidth of the UV-LED pulse and the induced current I_{pulse} seems to be linear with $I_{\text{pulse}} = m_{\text{pulse}} \cdot \text{width}$.

The proportionality factor is $m_{\text{pulse}} = (-2.110 \pm 0.006)e - 7\,\frac{\mathrm{A}}{\mathrm{s}}$. Therefore it is recommended to modify the current inside the detector by modifying the pulse width rather than $I_{\text{UV-LED}}$ or

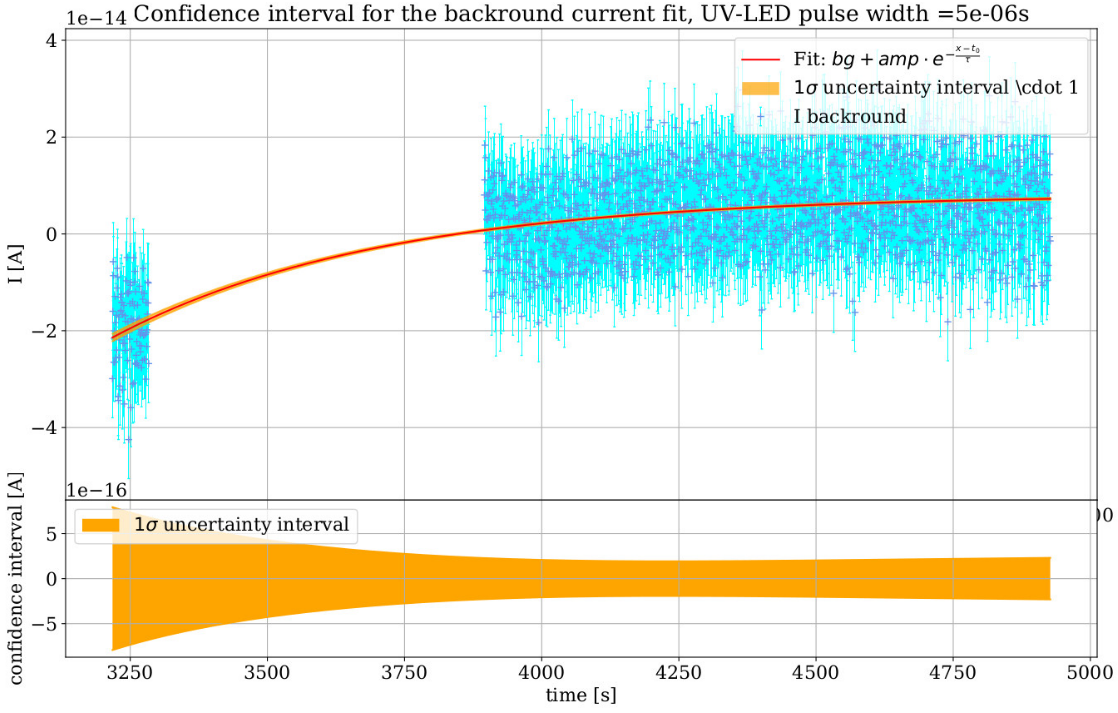

Figure 27: 1σ confidence interval of the background current fit for a pulse width of 5e−6 s. Fit parameters: $bg = (8.1 \pm 0.3)$e−15 A , $amp = (-0.11 \pm 0.03)$e−6 A , $t_0 = (-4.1 \pm 0.2)$e3 s , $\tau = (488 \pm 11)$ s . $\chi^2_{\mathrm{red.}} = 1.00 \pm 0.03$.

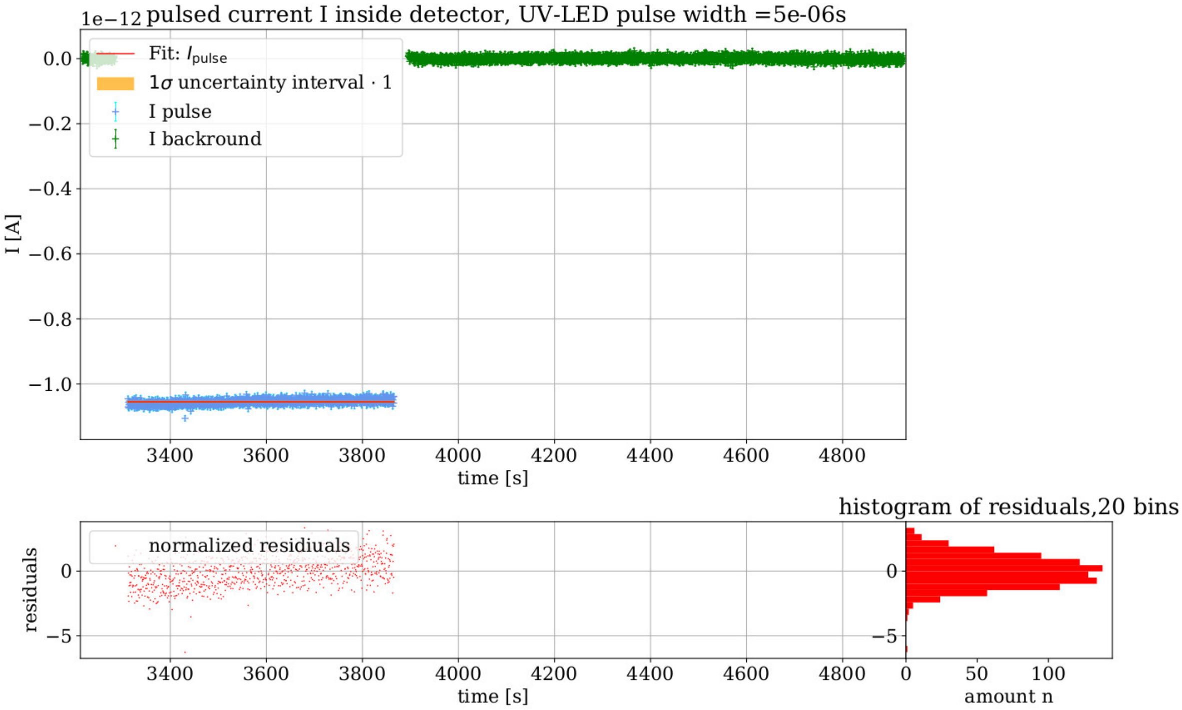

Figure 28: Current I during UV-LED pulses with a pulsewidth of 5e−6 s. Fit parameters: $I_{\text{pulse}} = (-1.0550 \pm 0.0003)\text{e}{-12}\,\text{A}$. The uncertainty of I_{pulse} has been modified according to formula 16 to accommodate for the slightly higher $\chi^2_{\text{red.}} = 1.34 \pm 0.05$.

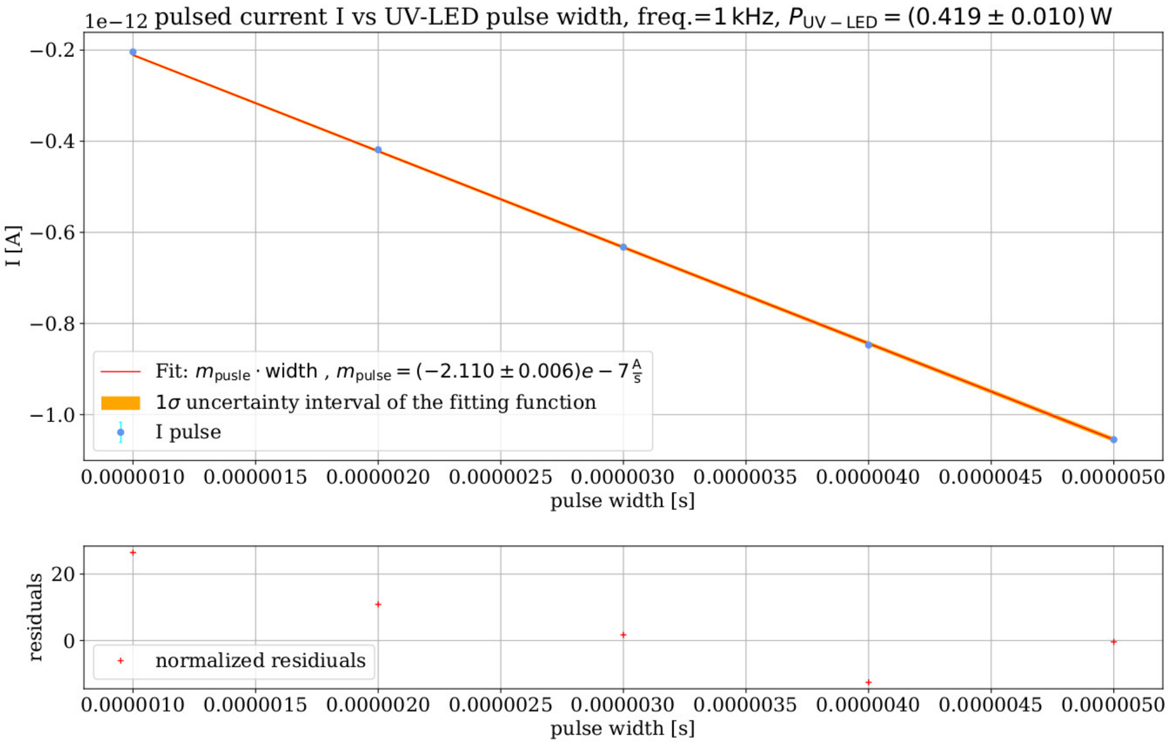

Figure 29: Current I_{pulse} in relationship to the pulse widths of an UV-LED pulse. Fit parameters: $m_{\mathrm{pulse}} = (-2.110 \pm 0.006)e - 7\,\frac{\mathrm{A}}{\mathrm{s}}$. The uncertainty of m_{pulse} has been modified according to formula 16 to accommodate for the high $\chi^2_{\mathrm{red.}} = 244.9 \pm 0.7$.

$P_{\mathrm{UV-LED}}$.

Future measurements could expand on this by measuring a wider variety of pulse widths and also modifying the frequency of the pulse. It is assumed that the parameter linearly connected to the induced current is the duty cycle, this could be confirmed in future studies.

5.3 Charge measurement for UV-LED pulses of varying pulse widths

Since measurements of electron mobility and free ion yield require a differentiation between electronic and ionic signal inside the detector, the charge and the current had to be measured simultaneously. The charge measurement only measures a charge signal for the charged particles that move quickly through the detector. This enables a lot of interesting measurements by comparing the charge signal to the current signal which also detects slow moving particles like ions. By comparing the electric current to the charge signal it might be possible to decouple the ionic and electronic signal. This comparison might serve as an indicator of purity of TMBi in regards to electronegative pollution. Electronegative particles should be easier to ionize, reducing the quick charge signal but still contributing to the current signal. Since the effectiveness of TMBi as a PET material depends on ionizing electrons moving through TMBi it is important to use TMBi of a high purity. Therefore it might be possible to use the charge mobility detector described in this work as a purity monitor in a continuous purification cycle.

However, this application of the detector as a purity monitor is only possible if the charge measurement is successful. During the current measurement with varying pulse widths, described in chapter 5.2, the charge inside the detector was measured as well using an analog-to-digital converter and the MAESTRO software.

While the electrical current behaved linearly with the pulse width, the charge signal was not in good agreement with a linear progression. One reason for this could be the small shaping time of $6\,\mu$s which was only slightly larger then the highest pulse width used ($5\,\mu$s). This could result in a faulty analysis of the charge-pulse.

5.3.1 Method of the charge measurement for UV-LED pulses of varying pulse widths

To measure the charge inside the detector the setup shown in figure 24 was used. The charge-sensitive-amplifier was attached to a spectroscopy amplifier with a shaping time of $6\,\mu$s and an amplification level of 1000. Additionally the data from the spectroscopy amplifier was filtered by a gating pulse from the Tektronix AFG3102 pulse generator. This gating pulse was synchronous to the pulse used to power the UV-LED but delayed as to properly filter the charge signal measured by the spectroscopy amplifier. The filtered data from the spectroscopy amplifier was then converted by an analog-to-digital converter (ADC) and compiled by the MAESTRO software on the laboratory computer.

5.3.2 Results of the charge measurement for UV-LED pulses of varying pulse widths

The spectroscopy datasets for the various pulse widths were first re-binned, with the counts of 4 channels put together and the channel number being the average of the 4 channels. All data with a channel number > 8000 was excluded, since the overflow of the measurement was saved in these channels. Because the aim was to fit a Gaussian function added to an exponential decay to the spectroscopy data, all channels with a count number of 0 after the re-binning were excluded from the data so to not overfit the data. The electrical power of the UV-LED pulses was $P_{\mathrm{UV-LED}} = (0.419 \pm 0.010)\,\mathrm{W}$. The charge measurement data for the different pulse widths

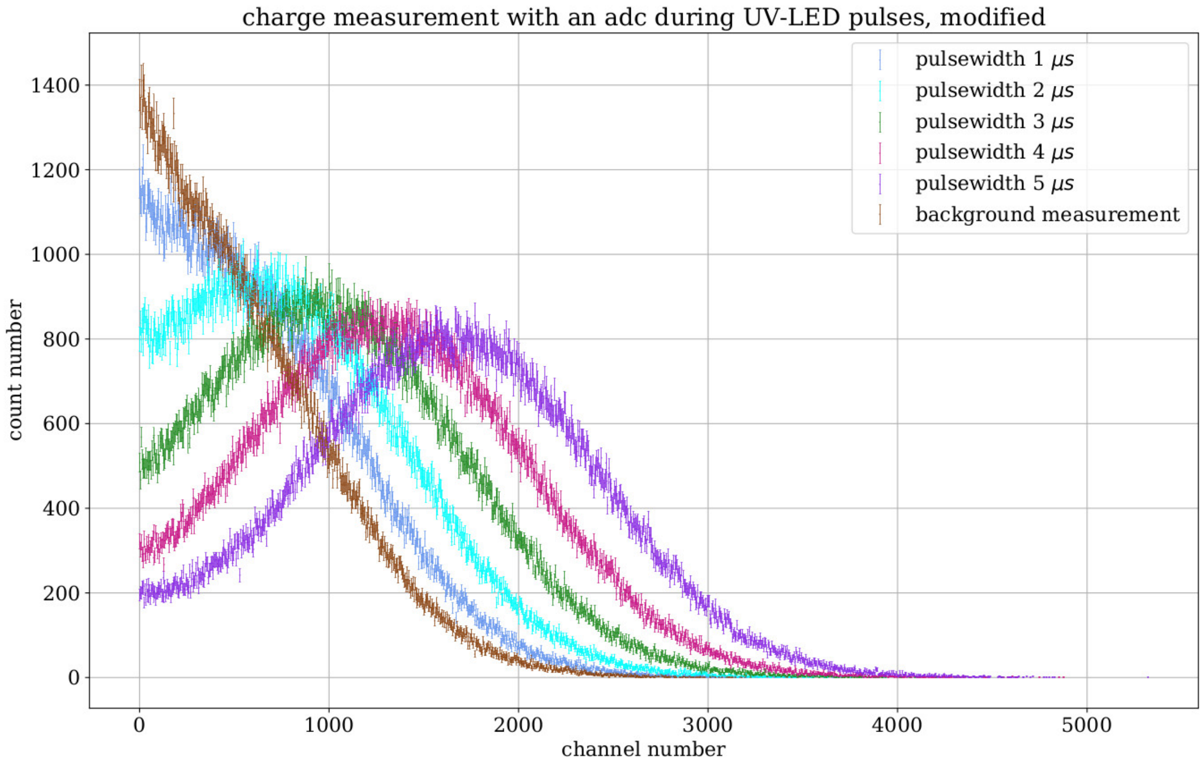

Figure 30: ADC data for the charge measurement for varying pulse widths. UV-LED pulses of $P_{\mathrm{UV-LED}} = (0.419 \pm 0.010)\,\mathrm{W}$ and pulse frequency of $f = 1\,\mathrm{kHz}$.

are shown in figure 30. The data was fitted to:

$$f(x) = A_{bg} \cdot e^{-\frac{x}{\tau_{bg}}} + A_p \cdot e^{-\frac{(x-\mu_p)^2}{2\sigma_p^2}} \tag{29}$$

This fitting function consists of an exponential decay to model the background signal and a Gaussian peak for the charge value from the charge sensitive amplifier. The spectroscopy amplifier sends data that correlates to the size of the charge pulse generated by each UV-LED pulse. This fit for a pulse width of $5\,\mu\mathrm{s}$ is shown in figure 31 with the residuals of the fit. Figure 32 shows the fit with the 1σ uncertainty interval of the fitting function

This process was conducted for all pulse widths and a measurement without any UV-LED pulse. The channel numbers of the peak position of the Gaussian part of the fitting function in formula 29 are shown in figure 33 for the corresponding pulse widths. The data was fitted to a linear growth under the assumption that it would behave similarly to the relationship between current I_{pulse} and pulse width. This seemed to not be the case as seen in figure 33.

5.3.3 Conclusion of the charge measurement for UV-LED pulses of varying pulse widths

There seems to be a disconnect between the measured current I_{pulse} and the measured charge Q, since the relationship between I_{pulse} and the pulse width seemed to be linear, while the relationship between the charge and the pulse width was not properly described by a linear fit. This could be explained by the shaping time of the spectroscopy amplifier which was $6\,\mu\mathrm{s}$ and therefore only slightly higher than $5\,\mu\mathrm{s}$.

The width of the Gaussian peaks in the analog-to-digital-converter measurement is rather large which could result in a reduced energy resolution of the charge measurement.

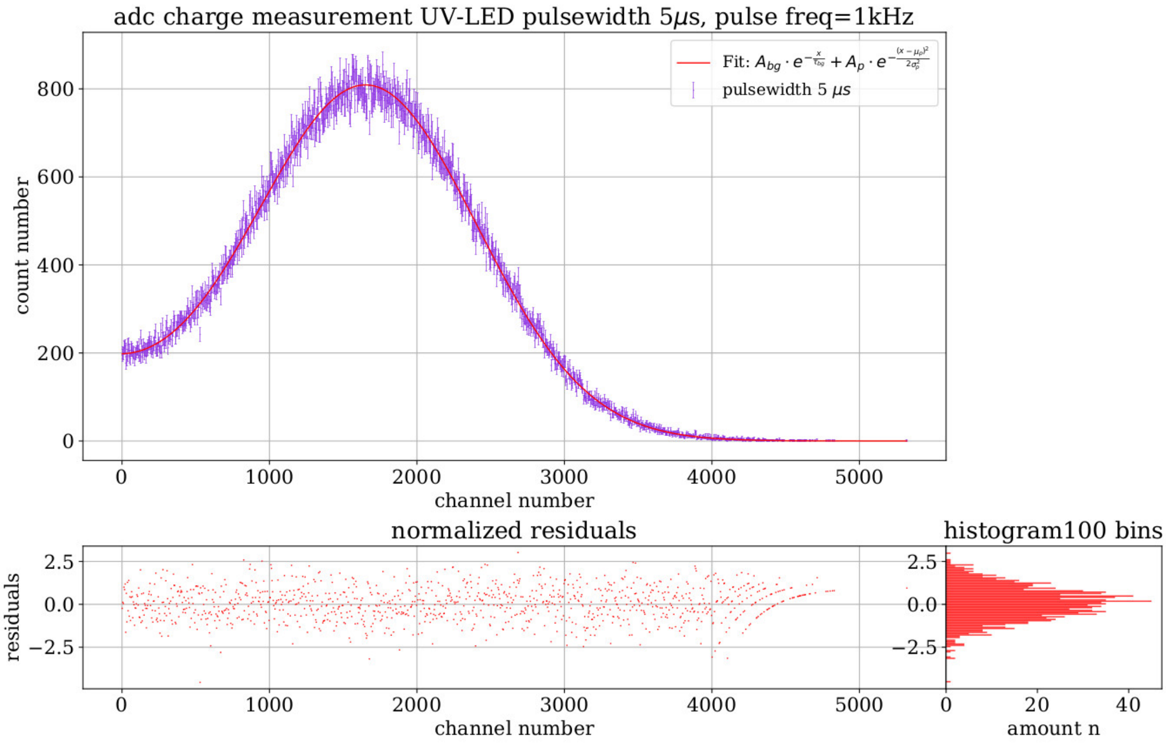

Figure 31: ADC data for the charge measurement for a pulse width of $5e-6$ s. UV-LED pulses of $P_{\mathrm{UV-LED}} = (0.419 \pm 0.010)$ W and pulse frequency of $f = 1$ kHz. Fit parameters: $A_{bg} = (131 \pm 3)$, $\tau_{bg} = (670 \pm 70)$, $A_p = (798 \pm 3)$, $\mu_p = (1663 \pm 4)$, $\sigma_p = (748 \pm 3)$. $\chi^2_{\mathrm{red.}} = 0.96 \pm 0.04$.

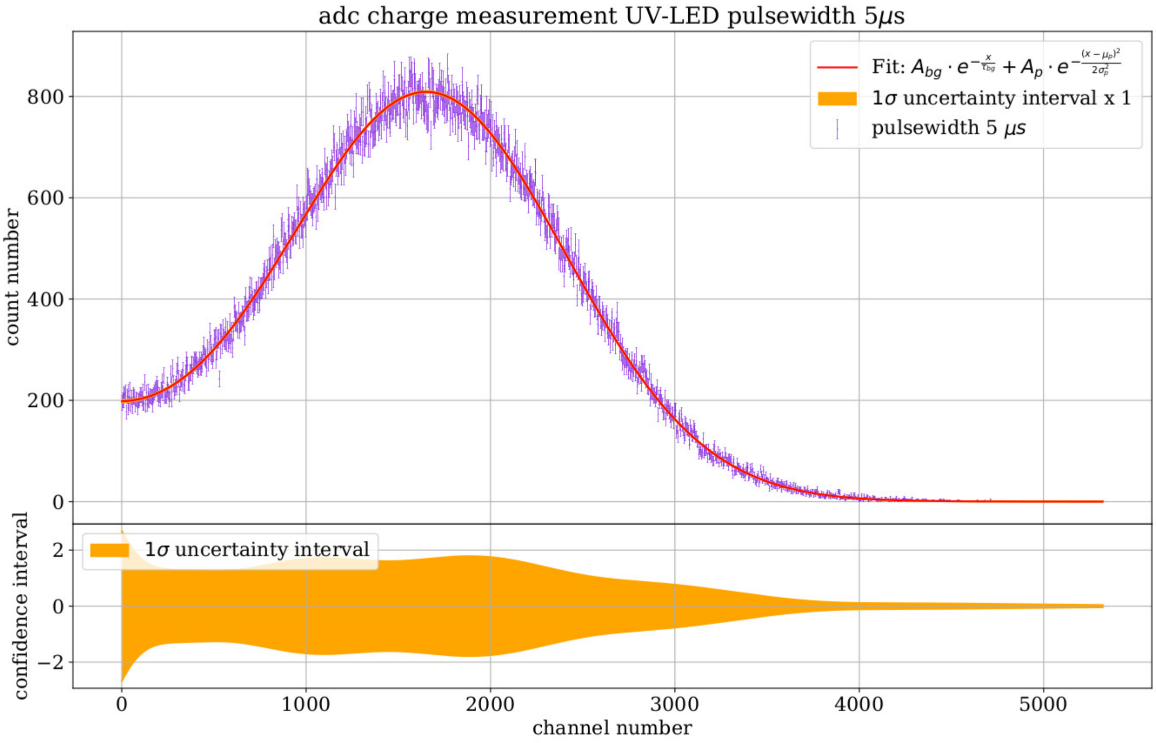

Figure 32: ADC data for the charge measurement for a pulse width of $5e-6$ s. UV-LED pulses of $P_{\mathrm{UV-LED}} = (0.419 \pm 0.010)$ W and pulse frequency of $f = 1$ kHz and 1σ confidence interval of the fitting function. Fit parameters: $A_{bg} = (131 \pm 3)$, $\tau_{bg} = (670 \pm 70)$, $A_p = (798 \pm 3)$, $\mu_p = (1663 \pm 4)$, $\sigma_p = (748 \pm 3)$. $\chi^2_{\mathrm{red.}} = 0.96 \pm 0.04$.

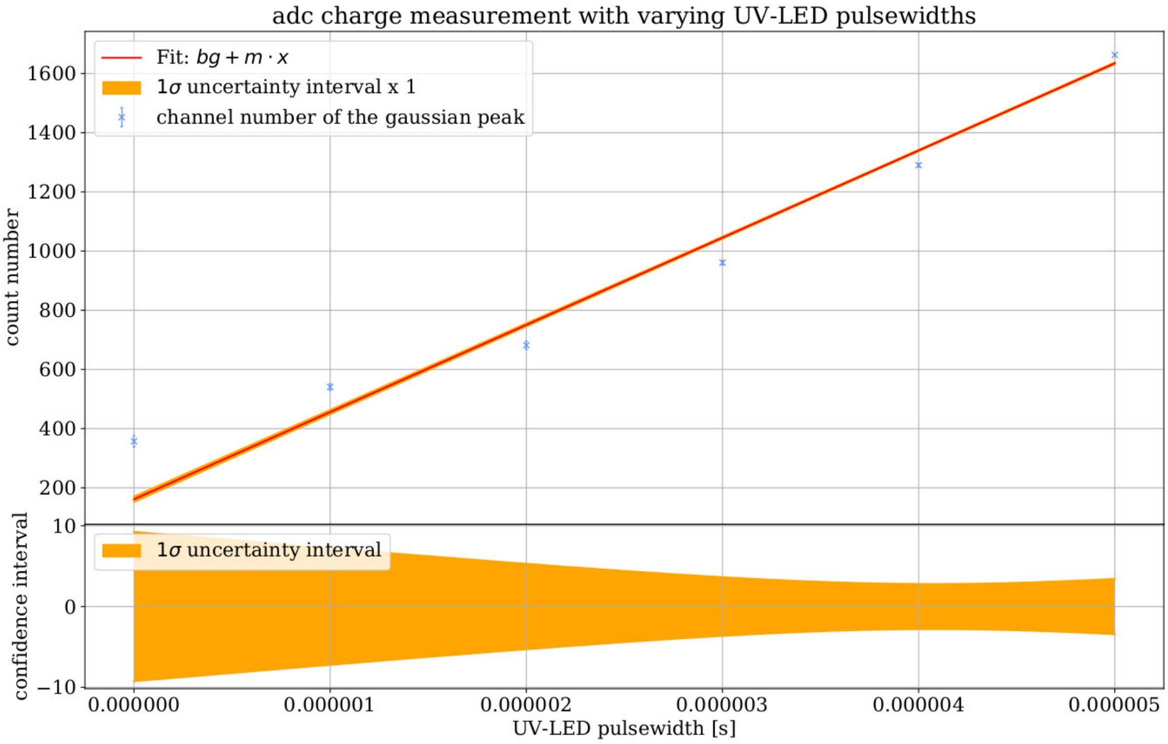

Figure 33: ADC data for the charge measurement for various pulse widths. UV-LED pulses of $P_{\mathrm{UV-LED}} = (0.419 \pm 0.010)\,\mathrm{W}$ and pulse frequency of $f = 1\,\mathrm{kHz}$. Shows the peak positions of the Gaussian functions for the fitting functions for various pulse widths in relationship to the pulsewidths. The data was fitted to a linear growth but it was not a good fit. Fit parameters: $bg = (161 \pm 9)$, $m = (295 \pm 2)\mathrm{e}6\,\frac{1}{\mathrm{s}}$. $\chi^2_{\mathrm{red.}} = 104.8 \pm 0.7$

It might still be possible to use the detector as a purity monitor by monitoring the current and the charge signal during the purification cycle and looking for a change which only affects the charge signal with the current signal remaining the same. Otherwise further measurements might be necessary with different spectroscopy amplifier settings. Also a calibration of the analog-to-digital converter with a source of known activity might be useful to compare the energy values of the charge to the measured current. One possibility for calibration would be using an americium source with known activity and a silicon-lithium detector but this has to be done in future studies.

6 Conclusion and outlook

To use TMBi in future PET technology it is important to understand material properties such as electron mobility, free ion yield and relative permittivity. Purity of the compound is a big concern as well. The detector discussed in this work could be used to measure these material properties and be used as a purity monitor for electronegative impurities.

Future measurements require a thorough understanding of the detector and its properties. The capacitance of the anode-photocathode system was measured to be $C_{\text{detector}} = (1.2969 \pm 0.0002)\text{e}{-13}\,\text{F}$, using a changing voltage with a constant ramping speed while measuring the current induced in the detector. From the capacitance and the geometry of the detector the distance of $d_{\text{anode-cathode}} = (1.34 \pm 0.02)\,\text{mm}$ between the anode and cathode was calculated. Both these properties are important parts for permittivity, free ion yield or electron mobility measurements and lay the foundation for future studies using this detector.

The capacitance can be used in simulations to understand the electromagnetic fields inside the detector or to acquire another measurement of the distance between anode and cathode using the simulation. The distance between the anode and the cathode can be used in electron mobility measurements in conjunction with the timing information of a pulsed signal and the charge answer.

The capabilities for simultaneous charge and electric current measurement were tested using a pulsed UV-LED signal to inject electrons into the detector volume. It was possible to measure the electric current at the same time as the charge signal in response to the UV-LED pulses. The relationship between the current inside the detector I_{pulse} and the power of the pulse $P_{\text{UV-LED}}$ used to power the UV-LED seemed to be non linear. The relationship between the current I_{pulse} to the pulse widths of the UV-LED pulses seemed to be linear following $I_{\text{pulse}} = m_{\text{pulse}} \cdot \text{width}$ with $m_{\text{pulse}} = (-2.110 \pm 0.006)\text{e}{-7}\,\frac{\text{A}}{\text{s}}$. Therefore to modify the electric current in the detector in response to UV-LED pulses it is recommended to modify the pulse width rather than the electrical power.

Further measurements will be necessary to understand the relationship between the measured electric current and the measured charge signal inside the detector. While the electric current seemed to be linear in relation to the pulse width, the charge signal was not in good agreement with a linear function between charge signal and pulse width. This behavior might be the subject of future studies.

7 Uncertainties

The uncertainty of the relation between the decay rate λ_p and λ_o of the two states of positronium was calculated using Gaussian uncertainty propagation.

$$\sigma\left(\frac{\lambda_p}{\lambda_o}\right) = \sqrt{\left(\frac{\sigma(\lambda_p)}{\lambda_o}\right)^2 + \left(\frac{\sigma(\lambda_o)\lambda_p}{\lambda_o^2}\right)^2} \tag{30}$$

The precision of the manufacturing process of the detector parts was assumed to be $\sigma_{\mathrm{rel}}(s) = 0.1\,\mathrm{mm}$.

Since the distance between anode and cathode was influenced by the tightening of the screws compressing the copper gaskets the uncertainty of the distance was estimated to be:

$$\sigma(d_{\mathrm{CAD}}) = 0.5\,\mathrm{mm} \tag{31}$$

The uncertainty of the plate area was calculated using Gaussian uncertainty propagation:

$$\sigma(A) = \sqrt{(\sigma(r) \cdot 2 \cdot \pi \cdot r)^2} \tag{32}$$

The capacitance $C_{\mathrm{plate,CAD}}$ was derived from the measurements given in the CAD drawing using the formula 3. This leads to a uncertainty of $C_{\mathrm{plate,CAD}}$ according to Gaussian uncertainty propagation:

$$\sigma(C_{\mathrm{plate,CAD}}) = \sqrt{\left(\sigma(\epsilon_0) \cdot \frac{A}{d}\right)^2 + \left(\sigma(A) \cdot \epsilon_0 \frac{1}{d}\right)^2 + \left(\sigma(d) \cdot \epsilon_0 \frac{-A}{d^2}\right)^2} \tag{33}$$

There was no value given for the relative uncertainty of the hand held capacitance device. The digital display rounded to 0.01e−12 F. The rounding error results in a Gaussian standard deviation of:

$$\sigma(C_{\mathrm{Handheld}}) = \frac{0.01\mathrm{e}{-12}\,\mathrm{F}}{2\sqrt{3}} = 0.003\mathrm{e}{-12}\,\mathrm{F} \tag{34}$$

The capacitance of the hand held measurement was calculated using the formula 9. The Gaussian uncertainty propagation results in a combined uncertainty according to:

$$\sigma(C_{\mathrm{total}}) = \sqrt{\sum_i \sigma(C_i)^2} \tag{35}$$

A peak-to-peak noise value was given for different amplification levels in the FEMTO DDPCA-300 current amplifier. As a starting point for the uncertainty of the electrical current measurement the value for the peak-to-peak noise was used as a basis for a rectangular distribution. The standard uncertainty of this distribution was calculated using:

$$\sigma_{\mathrm{rect}}(I) = \frac{\mathrm{ptp} - \mathrm{noise}}{2\sqrt{3}} \tag{36}$$

The uncertainty of the data after fitting to a function was modified by:

$$\sigma_{\mathrm{corr.}}(I) = \sqrt{\sigma(I)^2 \cdot \chi^2_{\mathrm{red.}}} \tag{37}$$

to accommodate for a $\chi^2_{\mathrm{red.}}$ that differs from 1. This procedure is used, since all sources of uncertainty in the measurement are not numerically known.

The uncertainty of all functions using the fitting parameters are calculated by:

$$\sigma_f^2 = g^{\mathrm{T}} V g \tag{38}$$

as described in [13].

To determine the uncertainty of the data after subtracting the background current fitting function from the data the following formula was used:

$$\sigma(I_{\mathrm{corr.}}) = \sqrt{\sigma(I_{\mathrm{meas.}})^2 + \sigma^2_{f_{\mathrm{bg}}}} \tag{39}$$

Since the distance between the anode and the cathode was calculated using $d = \epsilon_0 \cdot \frac{A}{C}$ the uncertainty of d was calculated using Gaussian uncertainty propagation:

$$\sigma(d_{\text{anode-cathode}}) = \sqrt{\left(\sigma(\epsilon_0) \cdot \frac{A}{C}\right)^2 + \left(\epsilon_0 \cdot \frac{\sigma(A)}{C}\right)^2 + \left(\epsilon_0 \cdot \frac{A \cdot \sigma(C)}{C^2}\right)^2} \tag{40}$$

The voltage amplitude of the pulse used to power the UV-LED was measured using a Tektronix MSG 4054 oscilloscope. The voltage was read from the display of the oscilloscope. Since the value of the voltage was subject to noise, for each measured value the maximum range of deviation was estimated from the varying voltage measured. From this range the uncertainty of the voltage was derived using a rectangular distribution using the range of the value as the width of the rectangle.

$$\sigma(U_{\text{oscilloscope}}) = \frac{\text{range}_{U_{\text{oscilloscope}}}}{2 \cdot \sqrt{3}} \tag{41}$$

The uncertainty of the resistance of the 100Ω resistor was specified by the color code on the resistor.

$$\sigma(R_{\text{preUV-LED}}) = 0.01\,\Omega \tag{42}$$

The voltage drop at the 100Ω resistor before the UV-LED was calculated from the voltage measured before and after the resistor. The uncertainty of the difference between the voltage before the resistor $U_{\text{pre-resistor}}$ and the voltage after the resistor $U_{\text{post-resistor}}$ was calculated using Gaussian uncertainty propagation.

$$\sigma(U_{100\Omega}) = \sqrt{(\sigma(U_{\text{pre-resistor}}))^2 + (\sigma(U_{\text{post-resistor}}))^2} \tag{43}$$

The current flowing through the UV-LED that was in line with the 100Ω resistor was calculated with $I = \frac{U}{R}$. Thus the uncertainty of the electrical current $I_{\text{UV-LED}}$ flowing through the UV-LED was calculated using Gaussian uncertainty propagation.

$$\sigma(I_{\text{UV-LED}}) = \sqrt{\left(\frac{\sigma(U_{100\Omega})}{R_{\text{preUV-LED}}}\right)^2 + \left(\frac{U_{100\Omega} \cdot \sigma(U_{100\Omega})}{R^2_{\text{preUV-LED}}}\right)^2} \tag{44}$$

The electrical power of the pulse amplitude was calculated from the voltage $U_{\text{post-resistor}}$ and the electrical current $I_{\text{UV-LED}}$ with $P = U \cdot I$. The uncertainty of the power was calculated according to Gaussian uncertainty propagation.

$$\sigma(P_{\text{UV-LED}}) = \sqrt{(\sigma(U_{\text{post-resistor}}) \cdot I_{\text{UV-LED}})^2 + (\sigma(I_{\text{UV-LED}}) \cdot U_{\text{post-resistor}})^2} \tag{45}$$

The values for the frequency from the Tektronix AFG3102 pulse generator were read from its display. The last digit to which the values were rounded was used to estimate the uncertainty of the values using a rectangular distribution. The width of the rectangle was 1 times 10 to the power of $-n$ with n being the amount of digits after the comma.

The values of the pulse width were read from the display of the AFG3102 pulse generator. According to [17] the resolution of the pulse width for a pulse wave is 5 digits.

The uncertainty of the MAESTRO measurements were approximated by a Poisson distribution with:

$$\sigma(N) = \sqrt{N} \tag{46}$$

8 Constants and formulas

According to [18] the dielectric constant ϵ_0 is:

$$\epsilon_0 = (8.8541878128 \pm 0.0000000013)\text{e}{-12}\,\text{Fm}^{-1} \tag{47}$$

Bibliography

[1] D. Yvon, J. Ph Renault, G. Tauzin, P. Verrecchia, C. Flouzat, S. Sharyy, E. Ramos, J. P. Bard, Y. Bulbul, J. P. Mols, P. Starzynski, D. Desforge, A. Marcel, J. M. Reymond, S. Jan, C. Comtat, and R. Trebossen. CaLIPSO: An novel detector concept for PET imaging. *IEEE Transactions on Nuclear Science*, 61(1):60–66, 2014. ISSN 00189499. doi: 10.1109/TNS.2013.2291971.

[2] Klaus Bethge, Gertrud Walter, and Bernhard Wiedemann. *Kernphysik.* Springer-Lehrbuch. Springer Berlin Heidelberg, Berlin, Heidelberg, 3 edition, 2008. ISBN 978-3-540-74566-2. doi: 10.1007/978-3-540-74567-9. URL `http://link.springer.com/10.1007/978-3-540-74567-9`.

[3] A. H. Al-Ramadhan and D. W. Gidley. New precision measurement of the decay rate of singlet positronium. *Physical Review Letters*, 72(11):1632–1635, mar 1994. ISSN 00319007. doi: 10.1103/PhysRevLett.72.1632. URL `https://journals.aps.org/prl/abstract/10.1103/PhysRevLett.72.1632`.

[4] R. S. Vallery, P. W. Zitzewitz, and D. W. Gidley. Resolution of the Orthopositronium-Lifetime Puzzle. *Physical Review Letters*, 90(20):4, may 2003. ISSN 10797114. doi: 10.1103/PhysRevLett.90.203402. URL `https://journals.aps.org/prl/abstract/10.1103/PhysRevLett.90.203402`.

[5] Committee on Data for Science and Technology. CODATA Value: electron mass energy equivalent in MeV. URL `https://physics.nist.gov/cgi-bin/cuu/Value?mec2mev`.

[6] P. Som, H. L. Atkins, D. Bandoypadhyay, J. S. Fowler, R. R. MacGregor, K. Matsui, Z. H. Oster, D. F. Sacker, C. Y. Shiue, H. Turner, C. N. Wan, A. P. Wolf, and S. V. Zabinski. A fluorinated glucose analog, 2-fluoro-2-deoxy-D-glucose (F-18): Nontoxic tracer for rapid tumor detection. *Journal of Nuclear Medicine*, 21(7):670–675, 1980. ISSN 01615505. doi: 10.1097/00004728-198012000-00045. URL `https://pubmed.ncbi.nlm.nih.gov/7391842/`.

[7] Gary J. Kelloff, John M. Hoffman, Bruce Johnson, Howard I. Scher, Barry A. Siegel, Edward Y. Cheng, Bruce D. Cheson, Joyce O'Shaughnessy, Kathryn Z. Guyton, David A. Mankoff, Lalitha Shankar, Steven M. Larson, Caroline C. Sigman, Richard L. Schilsky, and Daniel C. Sullivan. Progress and promise of FDG-PET imaging for cancer patient management and oncologic drug development. *Clinical Cancer Research*, 11(8):2785–2808, apr 2005. ISSN 10780432. doi: 10.1158/1078-0432.CCR-04-2626. URL `www.aacrjournals.org`.

[8] National Center for Biotechnology Information; PubChem [Internet]. Bethesda (MD): National Library of Medicine (US). Fludeoxyglucose F18 | C6H11FO5 - PubChem, 2004. URL `https://pubchem.ncbi.nlm.nih.gov/compound/Fludeoxyglucose-F18`.

[9] Simon-nis Peters. Set Up of a Purification and Measurement System for Organometallic Liquids for a Future PET Detector and Test Measurements with Tetramethylsilane. 2019.

[10] The Frisch grid. URL `https://rtsd.tistory.com/7`.

[11] C Canot, M Alokhina, P Abbon, J P Bard, D Breton, E Delagnes, J Maalmi, G Tauzin, D Yvon, and V Sharyy. Fast and Efficient Detection of 511 keV Photons using Cherenkov Light in PbF 2 Crystal, coupled to a MCP-PMT and SAMPIC Digitization Module. Technical report, 2019.

[12] W Demtröder. *Experimentalphysik 2: Elektrizität und Optik.* Springer, 2008.

[13] Joel Tellinghuisen. Statistical error propagation. *Journal of Physical Chemistry A*, 105(15): 3917–3921, 2001. ISSN 10895639. doi: 10.1021/jp003484u.

[14] FEMTO® Messtechnik GmbH. Datasheet DDPCA-300 Variable Gain Sub Femto Ampere Current Amplifier. Technical report. URL `https://www.femto.de/images/pdf-dokumente/de-ddpca-300.pdf`.

[15] M Farradèche, G Tauzin, J-Ph Mols, J-P Dognon, V Dauvois, V Sharyy, J-P Bard, X Mancardi, P Verrecchia, and D Yvon. Free ion yield of Trimethyl Bismuth used as sensitive medium for high-energy photon detection. Technical report, 2018.

[16] Greenergy. 2018 new TO39 250nm 260nm deep uv leds datasheet, 2018.

[17] Tektronix. Arbitrary/Function Generator AFG3000 Series (replaced by AFG3000C) | Tektronix. URL `https://de.tek.com/datasheet/afg3000-series`.

[18] Committee on Data for Science and Technology. CODATA Value: vacuum electric permittivity, 2018. URL `https://physics.nist.gov/cgi-bin/cuu/Value?ep0`.

9 Declaration of Academic Integrity

I hereby confirm that this thesis on Development of a detector for charge mobility measurements in TMBi is solely my own work and that I have used no sources or aids other than the ones stated. All passages in my thesis for which other sources, including electronic media, have been used, be it direct quotes or content references, have been acknowledged as such and the sources cited.

(Münster, 23.04.2021)

I agree to have my thesis checked in order to rule out potential similarities with other works and to have my thesis stored in a database for this purpose.

(Münster, 23.04.2021)

10 Appendix

This chapter shows additional figures of the measured and analyzed data for the various measurements.

10.1 Additional figures for the capacitance measurement

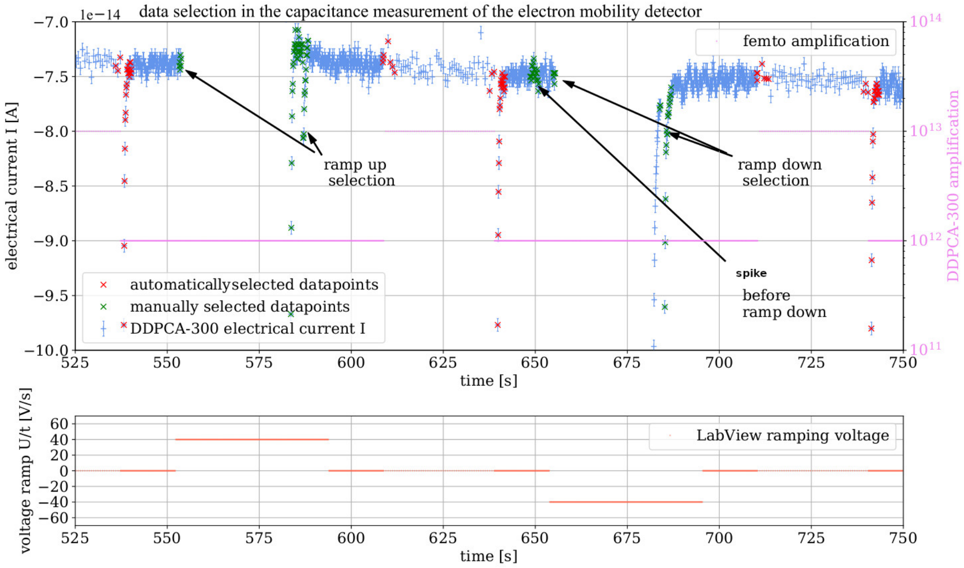

Figure 34: This graph shows the data of the capacitance measurement during the ramping processes with a ramping speed of $40\,\frac{\mathrm{V}}{\mathrm{s}}$ and the datapoints that were removed for the further analysis. Datapoints that have been automatically selected due to changing FEMTO DDPCA-300 amplification level as well as the manually selected spikes in the electrical current are marked.

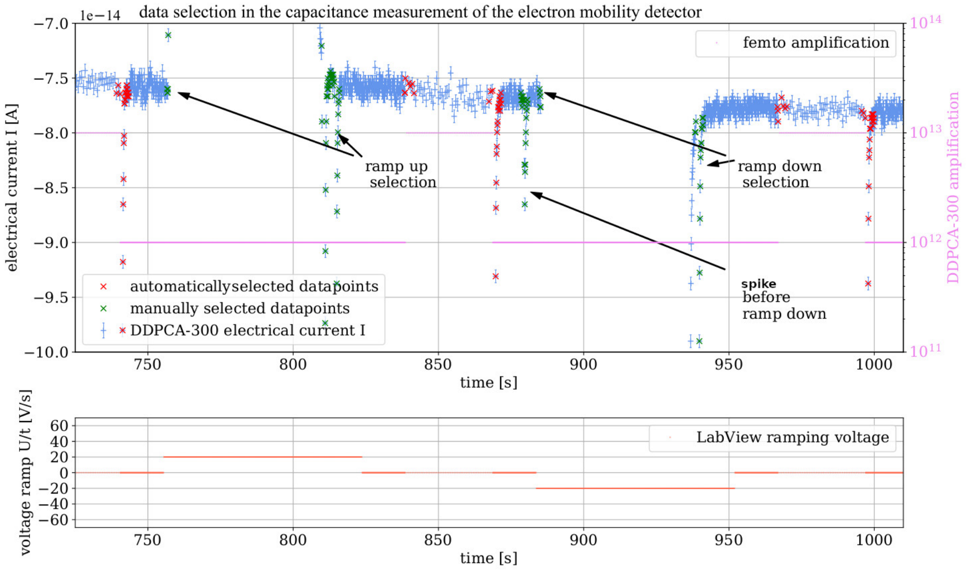

Figure 35: This graph shows the data of the capacitance measurement during the ramping processes with a ramping speed of 20 $\frac{\text{V}}{\text{s}}$ and the datapoints that were removed for the further analysis. Datapoints that have been automatically selected due to changing FEMTO DDPCA-300 amplification level as well as the manually selected spikes in the electrical current are marked.

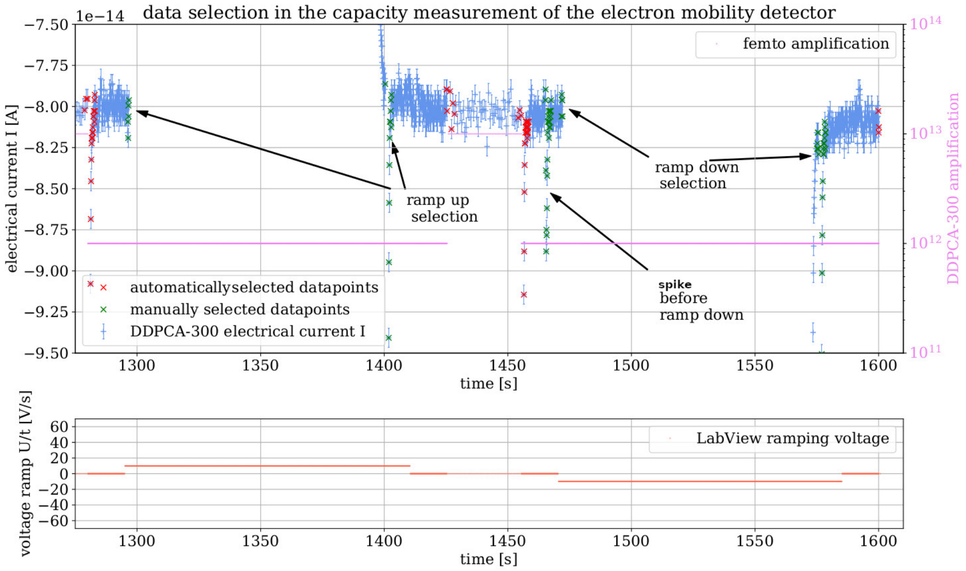

Figure 36: This graph shows the data of the capacitance measurement during the ramping processes with a ramping speed of 10 $\frac{\text{V}}{\text{s}}$ and the datapoints that were removed for the further analysis. Datapoints that have been automatically selected due to changing FEMTO DDPCA-300 amplification level as well as the manually selected spikes in the electrical current are marked.

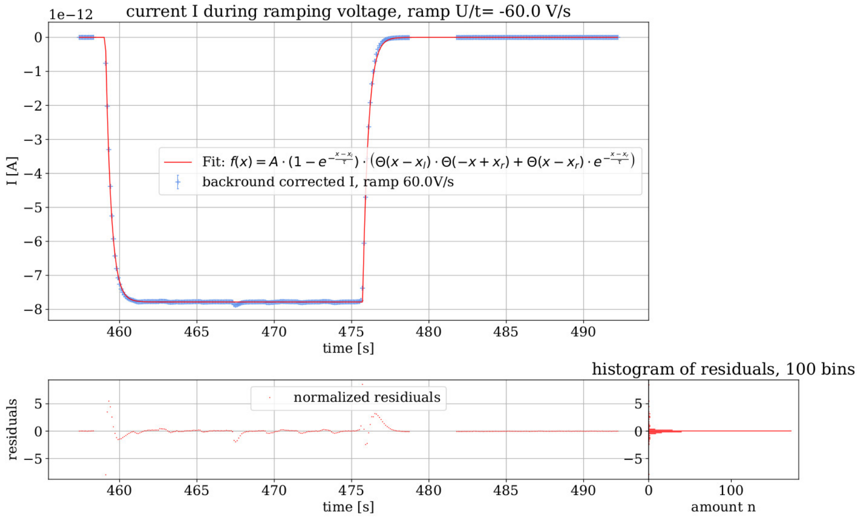

Figure 37: This graph shows the electrical current measured during the ramp up process from 1010 V to 10 V with a constant ramping speed of $\frac{U}{t} = -60.0\,\frac{\mathrm{V}}{\mathrm{s}}$ after the uncertainties of the electrical current I have been modified in a way, that the fit has a $\chi^2_{\mathrm{red}} = 1.00 \pm 0.08$. Fit parameters: $A = (-7.782 \pm 0.004)\mathrm{e}{-12}\,\mathrm{A}$, $\tau = (356 \pm 2)\mathrm{e}{-3}\,\mathrm{s}$, $x_l = (459.086 \pm 0.002)\,\mathrm{s}$, $x_r = (475.716 \pm 0.002)\,\mathrm{s}$.

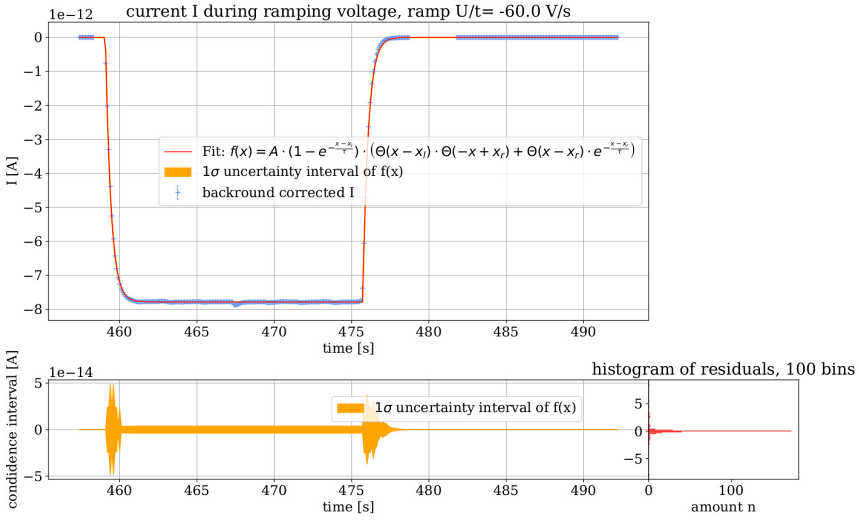

Figure 38: This graph shows the electrical current measured during the ramp up process from 1010 V to 10 V with a constant ramping speed of $\frac{U}{t} = -60.0\,\frac{\mathrm{V}}{\mathrm{s}}$. The uncertainties have been modified so that the fit has a $\chi^2_{\mathrm{red.}} = 1.00 \pm 0.08$. Fit parameters: $A = (-7.782 \pm 0.004)\mathrm{e}{-12}\,\mathrm{A}$, $\tau = (356 \pm 2)\mathrm{e}{-3}\,\mathrm{s}$, $x_l = (459.086 \pm 0.002)\,\mathrm{s}$, $x_r = (475.716 \pm 0.002)\,\mathrm{s}$. Also shows the 1σ uncertainty interval of the fit.

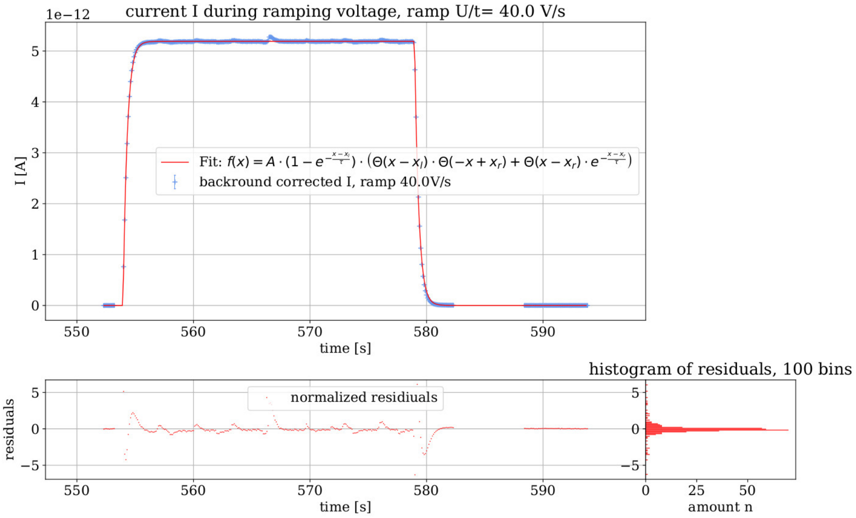

Figure 39: This graph shows the electrical current measured during the ramp up process from 10 V to 1010 V with a constant ramping speed of $\frac{U}{t} = 40.0\,\frac{\text{V}}{\text{s}}$ after the uncertainties of the electrical current I have been modified in a way, that the fit has a $\chi^2_{\text{red}} = 1.00 \pm 0.08$. Fit parameters: $A = (5.190 \pm 0.002)\text{e}{-12}\,\text{A}$, $\tau = (352 \pm 2)\text{e}{-3}\,\text{s}$, $x_l = (553.958 \pm 0.002)\,\text{s}$, $x_r = (578.9753 \pm 0.0014)\,\text{s}$.

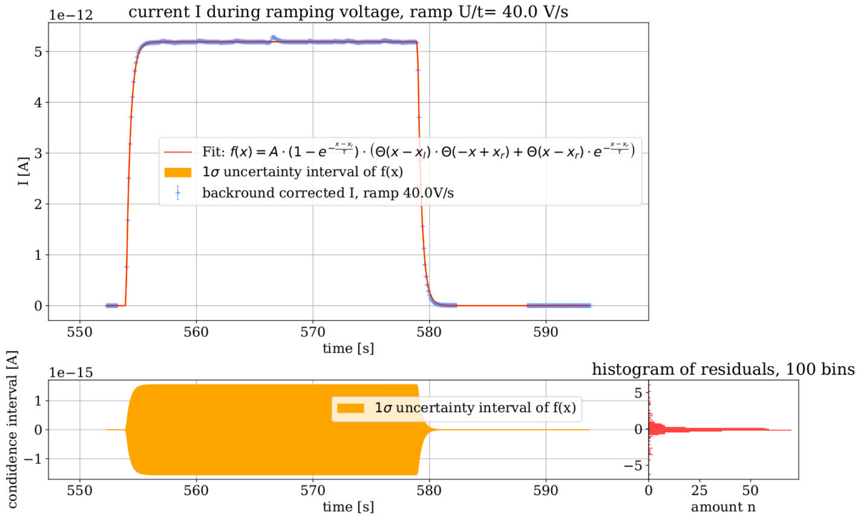

Figure 40: This graph shows the electrical current measured during the ramp up process from 10 V to 1010 V with a constant ramping speed of $\frac{U}{t} = 40.0\,\frac{\mathrm{V}}{\mathrm{s}}$. The uncertainties have been modified so that the fit has a $\chi^2_{\mathrm{red.}} = 1.00 \pm 0.08$. Fit parameters: $A = (5.190 \pm 0.002)\mathrm{e}{-12}\,\mathrm{A}$, $\tau = (352 \pm 2)\mathrm{e}{-3}\,\mathrm{s}$, $x_l = (553.958 \pm 0.002)\,\mathrm{s}$, $x_r = (578.9753 \pm 0.0014)\,\mathrm{s}$. Also shows the 1σ uncertainty interval of the fit.

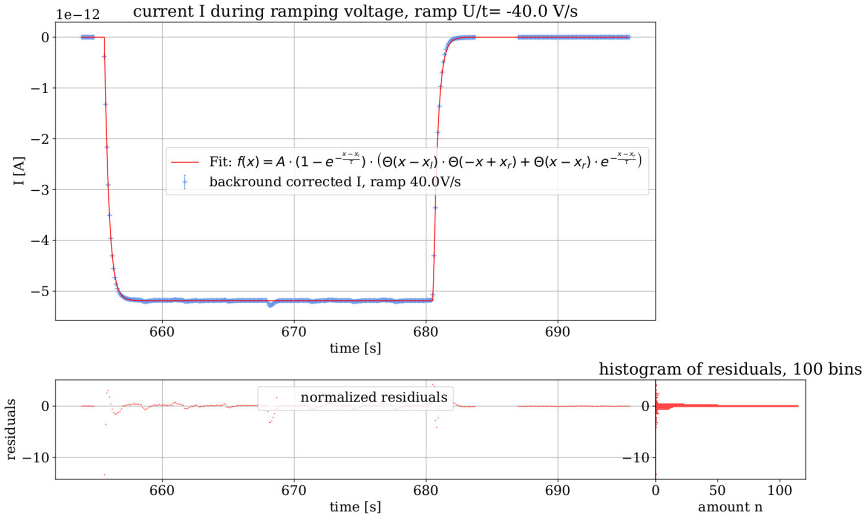

Figure 41: This graph shows the electrical current measured during the ramp up process from 1010 V to 10 V with a constant ramping speed of $\frac{U}{t} = -40.0\,\frac{\mathrm{V}}{\mathrm{s}}$ after the uncertainties of the electrical current I have been modified in a way, that the fit has a $\chi^2_{\mathrm{red}} = 1.00 \pm 0.07$. Fit parameters: $A = (-5.188 \pm 0.002)\mathrm{e}{-12}\,\mathrm{A}$, $\tau = (337 \pm 2)\mathrm{e}{-3}\,\mathrm{s}$, $x_l = (655.614 \pm 0.002)\,\mathrm{s}$, $x_r = (680.550 \pm 0.002)\,\mathrm{s}$.

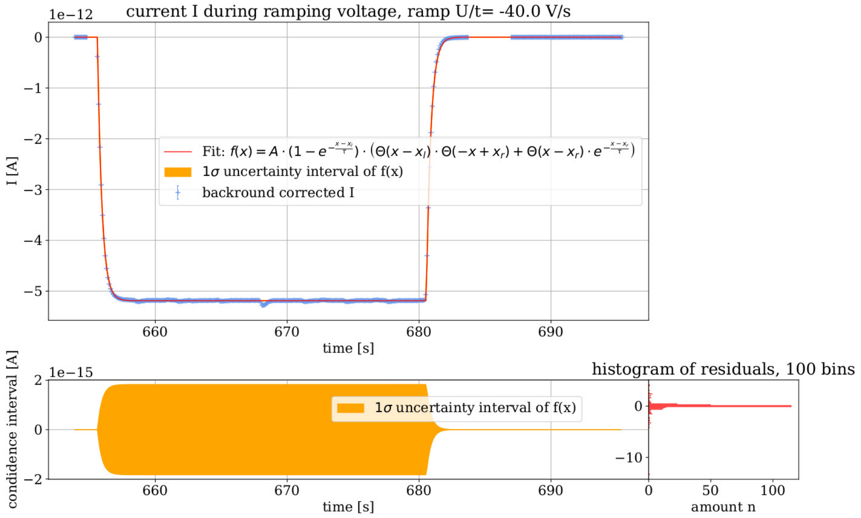

Figure 42: This graph shows the electrical current measured during the ramp up process from 1010 V to 10 V with a constant ramping speed of $\frac{U}{t} = -40.0\,\frac{\mathrm{V}}{\mathrm{s}}$. The uncertainties have been modified so that the fit has a $\chi^2_{\text{red.}} = 1.00 \pm 0.07$. Fit parameters: $A = (-5.188 \pm 0.002)\text{e}{-12}\,\mathrm{A}$, $\tau = (337 \pm 2)\text{e}{-3}\,\mathrm{s}$, $x_l = (655.614 \pm 0.002)\,\mathrm{s}$, $x_r = (680.550 \pm 0.002)\,\mathrm{s}$. Also shows the 1σ uncertainty interval of the fit.

10.2 Additional figures of the comparative current measurement

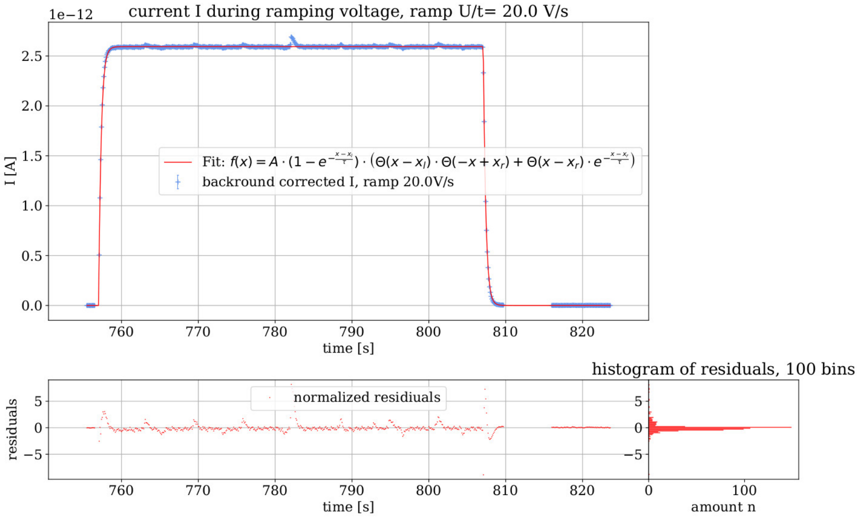

Figure 43: This graph shows the electrical current measured during the ramp up process from 10 V to 1010 V with a constant ramping speed of $\frac{U}{t} = 20.0\,\frac{\mathrm{V}}{\mathrm{s}}$ after the uncertainties of the electrical current I have been modified in a way, that the fit has a $\chi^2_{\mathrm{red}} = 1.00 \pm 0.06$. Fit parameters: $A = (2.5939 \pm 0.0005)\mathrm{e}{-12}\,\mathrm{A}$, $\tau = (328 \pm 2)\mathrm{e}{-3}\,\mathrm{s}$, $x_l = (757.028 \pm 0.002)\,\mathrm{s}$, $x_r = (807.0836 \pm 0.0013)\,\mathrm{s}$.

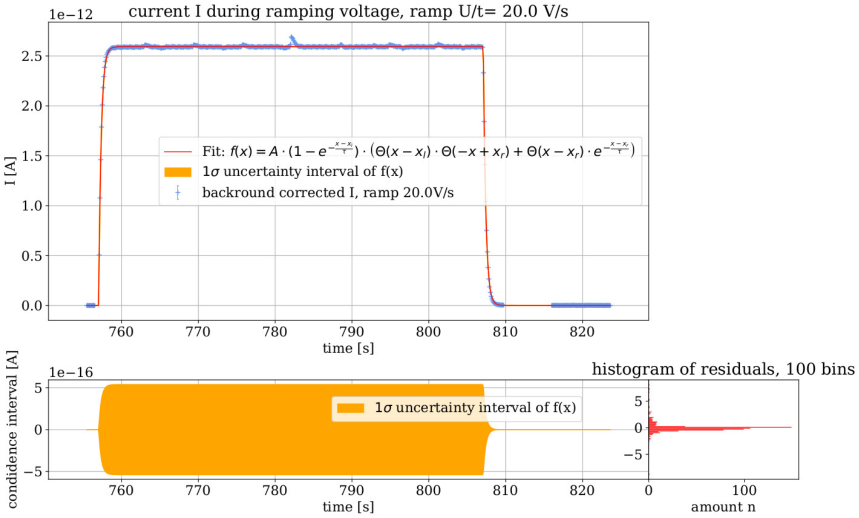

Figure 44: This graph shows the electrical current measured during the ramp up process from 10 V to 1010 V with a constant ramping speed of $\frac{U}{t} = 20.0\,\frac{\mathrm{V}}{\mathrm{s}}$. The uncertainties have been modified so that the fit has a $\chi^2_{\mathrm{red.}} = 1.00 \pm 0.06$. Fit parameters: $A = (2.5939 \pm 0.0005)\mathrm{e}{-12}\,\mathrm{A}$, $\tau = (328 \pm 2)\mathrm{e}{-3}\,\mathrm{s}$, $x_l = (757.028 \pm 0.002)\,\mathrm{s}$, $x_r = (807.0836 \pm 0.0013)\,\mathrm{s}$. Also shows the 1σ uncertainty interval of the fit.

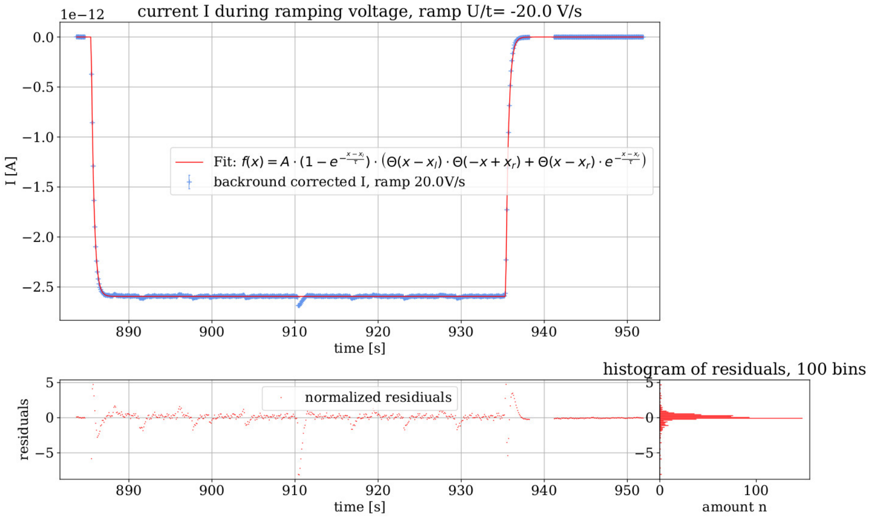

Figure 45: This graph shows the electrical current measured during the ramp up process from 1010 V to 10 V with a constant ramping speed of $\frac{U}{t} = -20.0\,\frac{\mathrm{V}}{\mathrm{s}}$ after the uncertainties of the electrical current I have been modified in a way, that the fit has a $\chi^2_{\text{red}} = 1.00 \pm 0.06$. Fit parameters: $A = (-2.5944 \pm 0.0005)\text{e}{-12}\,\mathrm{A}$, $\tau = (312 \pm 2)\text{e}{-3}\,\mathrm{s}$, $x_l = (885.4623 \pm 0.0013)\,\mathrm{s}$, $x_r = (935.3616 \pm 0.0013)\,\mathrm{s}$.

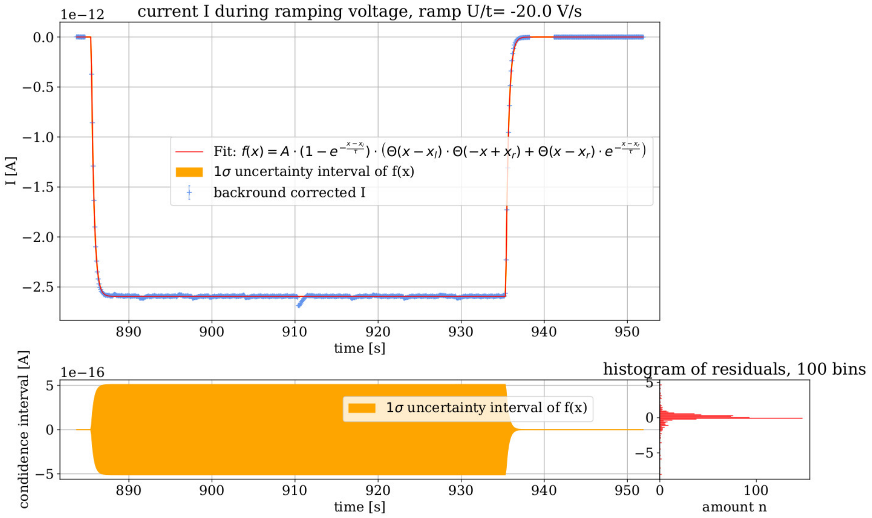

Figure 46: This graph shows the electrical current measured during the ramp up process from 1010 V to 10 V with a constant ramping speed of $\frac{U}{t} = -20.0\,\frac{\mathrm{V}}{\mathrm{s}}$. The uncertainties have been modified so that the fit has a $\chi^2_{\text{red}} = 1.00 \pm 0.06$. Fit parameters: $A = (-2.5944 \pm 0.0005)\text{e}{-12}\,\mathrm{A}$, $\tau = (312 \pm 2)\text{e}{-3}\,\mathrm{s}$, $x_l = (885.4623 \pm 0.0013)\,\mathrm{s}$, $x_r = (935.3616 \pm 0.0013)\,\mathrm{s}$. Also shows the 1σ uncertainty interval of the fit.

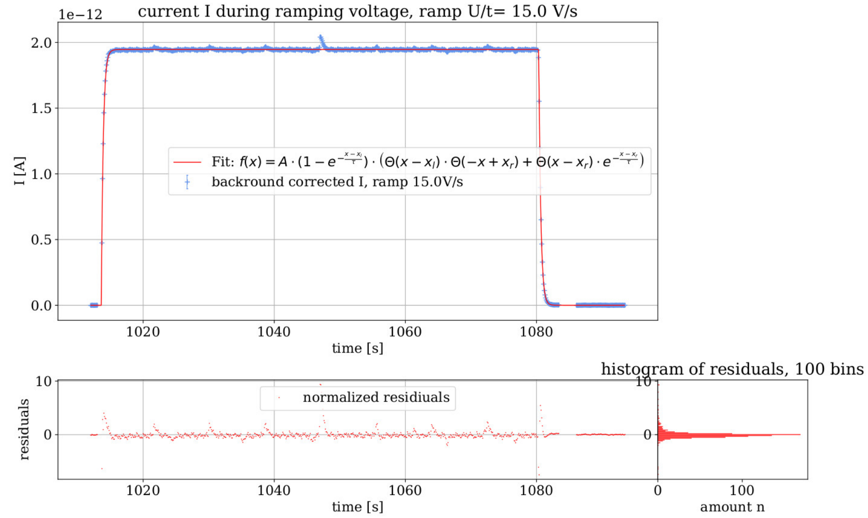

Figure 47: This graph shows the electrical current measured during the ramp up process from 10 V to 1010 V with a constant ramping speed of $\frac{U}{t} = 15.0\,\frac{\mathrm{V}}{\mathrm{s}}$ after the uncertainties of the electrical current I have been modified in a way, that the fit has a $\chi^2_{\mathrm{red}} = 1.00 \pm 0.05$. Fit parameters: $A = (1.9461 \pm 0.0004)\mathrm{e}{-12}\,\mathrm{A}$, $\tau = (303 \pm 2)\mathrm{e}{-3}\,\mathrm{s}$, $x_l = (1013.606 \pm 0.002)\,\mathrm{s}$, $x_r = (1080.35 \pm 0.002)\,\mathrm{s}$.

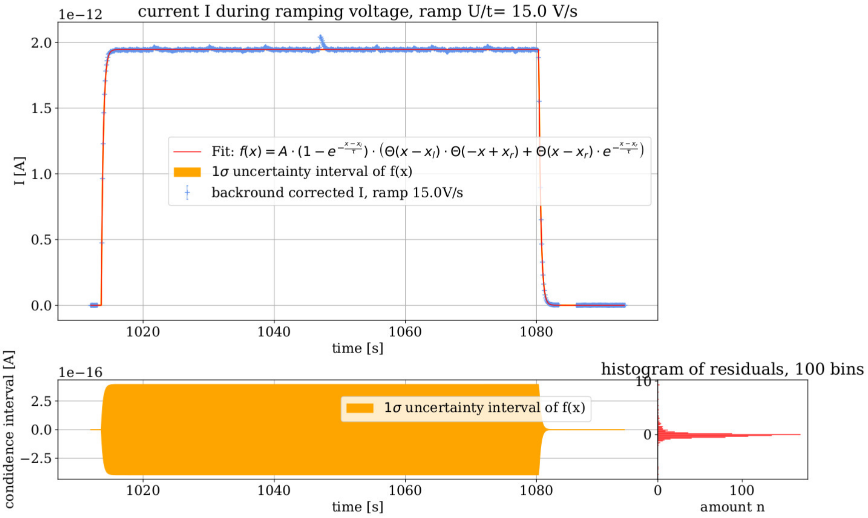

Figure 48: This graph shows the electrical current measured during the ramp up process from 10 V to 1010 V with a constant ramping speed of $\frac{U}{t} = 15.0\,\frac{\mathrm{V}}{\mathrm{s}}$. The uncertainties have been modified so that the fit has a $\chi^2_{\mathrm{red}} = 1.00 \pm 0.05$. Fit parameters: $A = (1.9461 \pm 0.0004)\mathrm{e}{-12}\,\mathrm{A}$, $\tau = (303 \pm 2)\mathrm{e}{-3}\,\mathrm{s}$, $x_l = (1013.606 \pm 0.002)\,\mathrm{s}$, $x_r = (1080.35 \pm 0.002)\,\mathrm{s}$. Also shows the 1σ uncertainty interval of the fit.

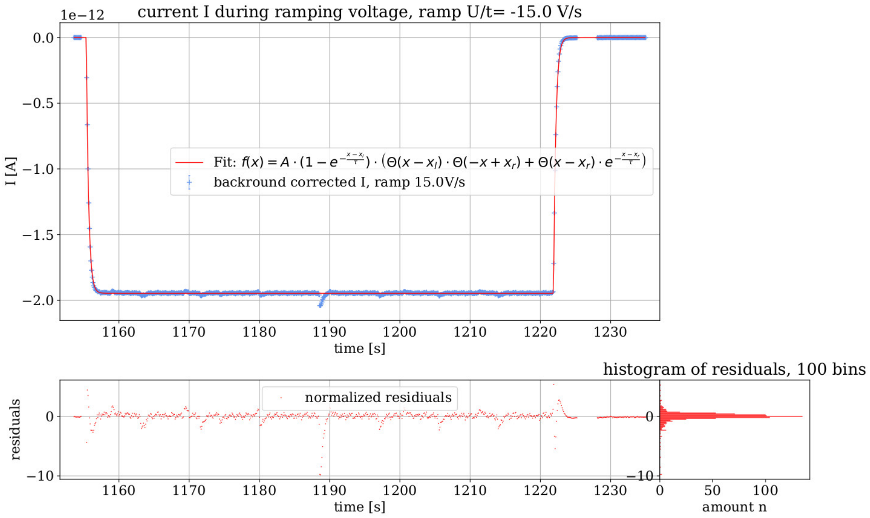

Figure 49: This graph shows the electrical current measured during the ramp up process from 1010 V to 10 V with a constant ramping speed of $\frac{U}{t} = -15.0\,\frac{\mathrm{V}}{\mathrm{s}}$ after the uncertainties of the electrical current I have been modified in a way, that the fit has a $\chi^2_{\mathrm{red}} = 1.00 \pm 0.05$. Fit parameters: $A = (-1.9460 \pm 0.0005)\mathrm{e}{-12}\,\mathrm{A}$, $\tau = (327 \pm 2)\mathrm{e}{-3}\,\mathrm{s}$, $x_l = (1155.357 \pm 0.002)\,\mathrm{s}$, $x_r = (1221.8730 \pm 0.0014)\,\mathrm{s}$.

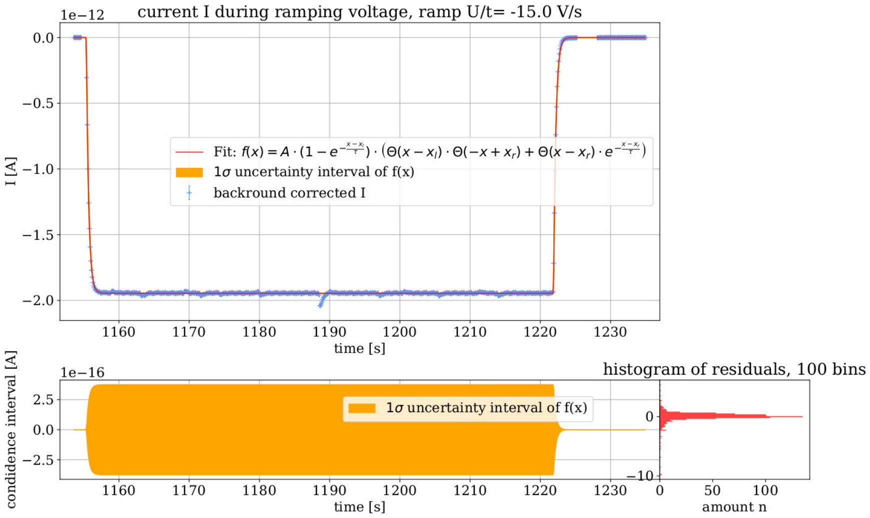

Figure 50: This graph shows the electrical current measured during the ramp up process from 1010 V to 10 V with a constant ramping speed of $\frac{U}{t} = -15.0\,\frac{\mathrm{V}}{\mathrm{s}}$. The uncertainties have been modified so that the fit has a $\chi^2_{\mathrm{red}} = 1.00 \pm 0.05$. Fit parameters: $A = (-1.9460 \pm 0.0005)\mathrm{e}{-12}\,\mathrm{A}$, $\tau = (327 \pm 2)\mathrm{e}{-3}\,\mathrm{s}$, $x_l = (1155.357 \pm 0.002)\,\mathrm{s}$, $x_r = (1221.8730 \pm 0.0014)\,\mathrm{s}$. Also shows the 1σ uncertainty interval of the fit.

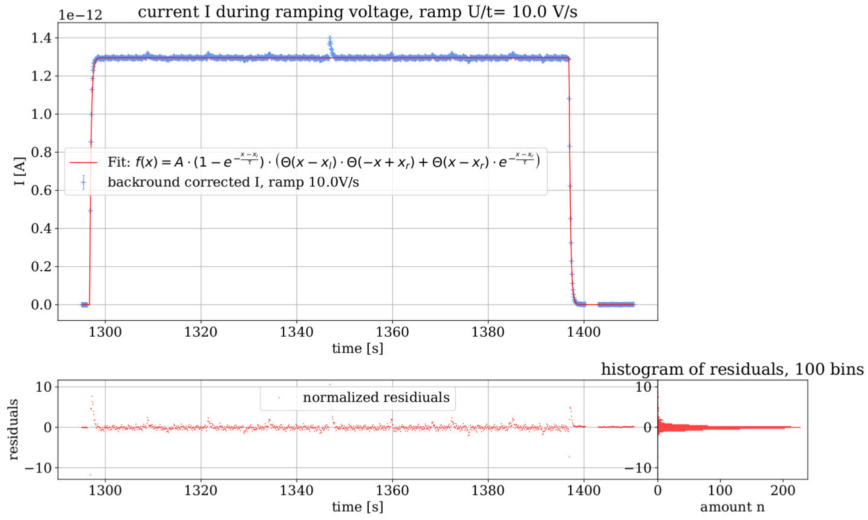

Figure 51: This graph shows the electrical current measured during the ramp up process from 10 V to 1010 V with a constant ramping speed of $\frac{U}{t} = 10.0\,\frac{\mathrm{V}}{\mathrm{s}}$ after the uncertainties of the electrical current I have been modified in a way, that the fit has a $\chi^2_{\mathrm{red}} = 1.00 \pm 0.04$. Fit parameters: $A = (1.2960 \pm 0.0003)\mathrm{e}{-12}\,\mathrm{A}$, $\tau = (287 \pm 3)\mathrm{e}{-3}\,\mathrm{s}$, $x_l = (1296.722 \pm 0.004)\,\mathrm{s}$, $x_r = (1396.870 \pm 0.002)\,\mathrm{s}$.

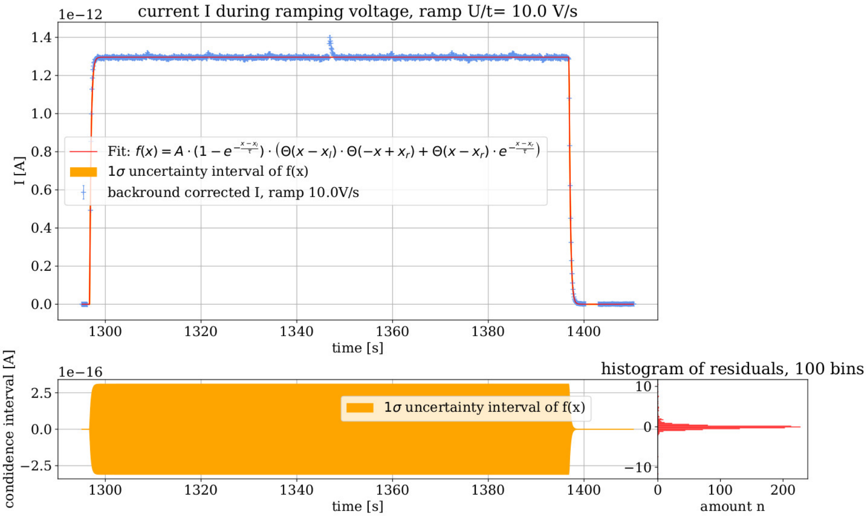

Figure 52: This graph shows the electrical current measured during the ramp up process from 10 V to 1010 V with a constant ramping speed of $\frac{U}{t} = 10.0\,\frac{\mathrm{V}}{\mathrm{s}}$. The uncertainties have been modified so that the fit has a $\chi^2_{\mathrm{red}} = 1.00 \pm 0.04$. Fit parameters: $A = (1.2960 \pm 0.0003)\mathrm{e}{-12}\,\mathrm{A}$, $\tau = (287 \pm 3)\mathrm{e}{-3}\,\mathrm{s}$, $x_l = (1296.722 \pm 0.004)\,\mathrm{s}$, $x_r = (1396.870 \pm 0.002)\,\mathrm{s}$. Also shows the 1σ uncertainty interval of the fit.

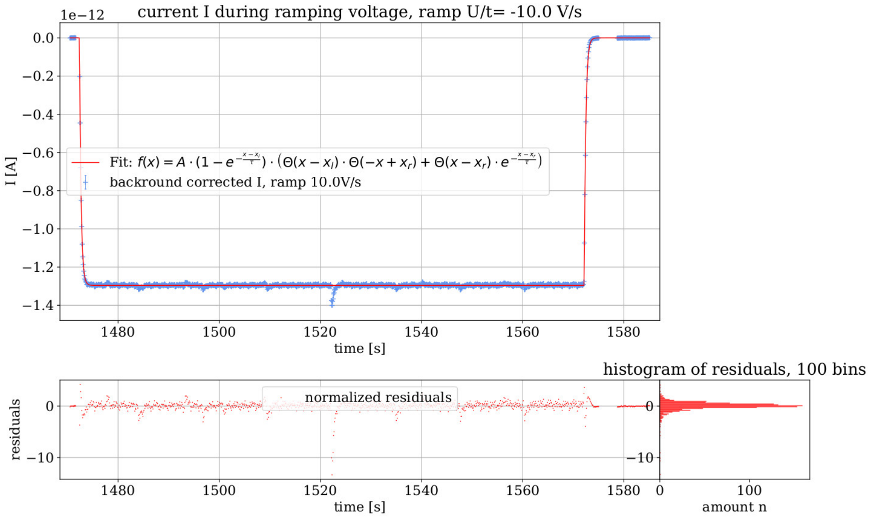

Figure 53: This graph shows the electrical current measured during the ramp up process from 1010 V to 10 V with a constant ramping speed of $\frac{U}{t} = -10.0\,\frac{\mathrm{V}}{\mathrm{s}}$ after the uncertainties of the electrical current I have been modified in a way, that the fit has a $\chi^2_{\mathrm{red}} = 1.00 \pm 0.04$. Fit parameters: $A = (-1.2960 \pm 0.0003)\mathrm{e}{-12}\,\mathrm{A}$, $\tau = (315 \pm 2)\mathrm{e}{-3}\,\mathrm{s}$, $x_l = (1472.359 \pm 0.002)\,\mathrm{s}$, $x_r = (1572.153 \pm 0.002)\,\mathrm{s}$.

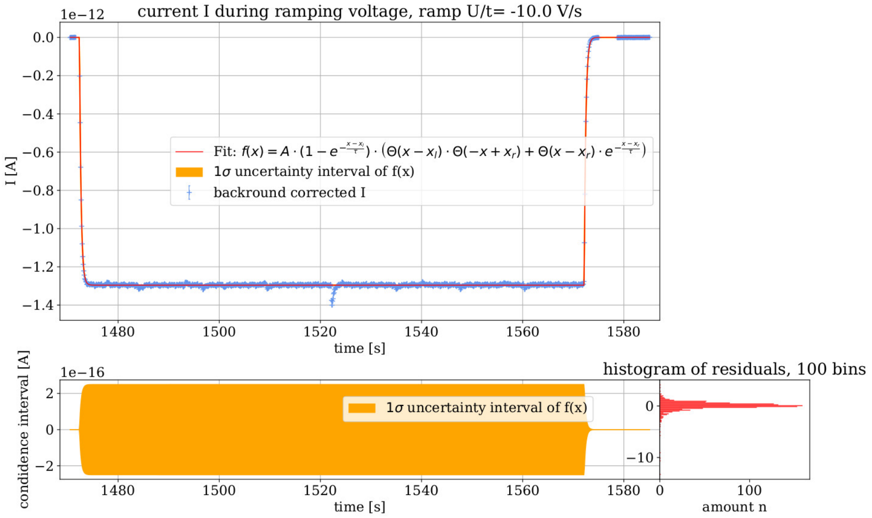

Figure 54: This graph shows the electrical current measured during the ramp up process from 1010 V to 10 V with a constant ramping speed of $\frac{U}{t} = -10.0\,\frac{\mathrm{V}}{\mathrm{s}}$. The uncertainties have been modified so that the fit has a $\chi^2_{\mathrm{red}} = 1.00 \pm 0.04$. Fit parameters: $A = (-1.2960 \pm 0.0003)\mathrm{e}{-12}\,\mathrm{A}$, $\tau = (315 \pm 2)\mathrm{e}{-3}\,\mathrm{s}$, $x_l = (1472.359 \pm 0.002)\,\mathrm{s}$, $x_r = (1572.153 \pm 0.002)\,\mathrm{s}$. Also shows the 1σ uncertainty interval of the fit.

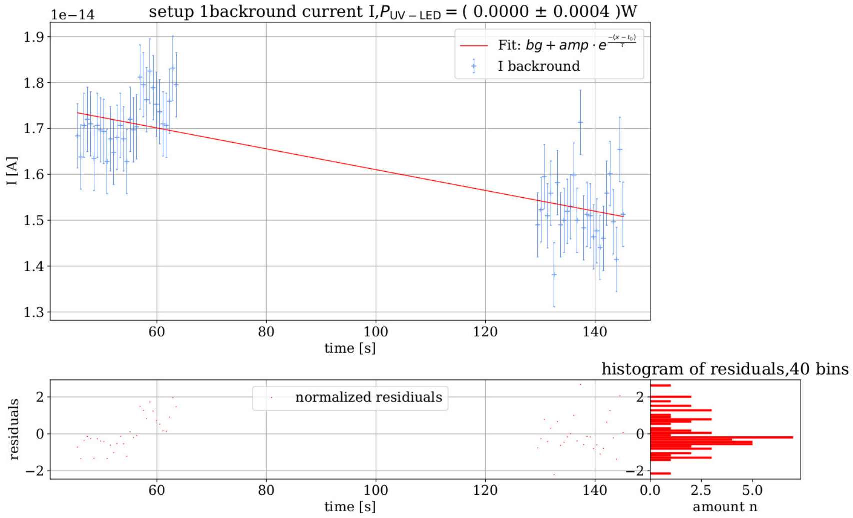

Figure 55: setup 1: background current I for $P_{\mathrm{UV-LED}} = (0.0000 \pm 0.0004)\,\mathrm{W}$. Fit parameters: $bg = (-192.5 \pm 0.2)\mathrm{e}{-15}\,\mathrm{A}$, $amp = (214.6 \pm 1.1)\mathrm{e}{-15}\,\mathrm{A}$, $t_0 = (-160 \pm 31)\,\mathrm{s}$, $\tau = (9.2 \pm 1.0)\mathrm{e}3\,\mathrm{s}$. $\chi^2_{\mathrm{red.}} = 1.0 \pm 0.2$. This fit has already been used to modify the uncertainties of the measured current I to produce a $\chi^2_{\mathrm{red.}} = 1.0$ using formula 16.

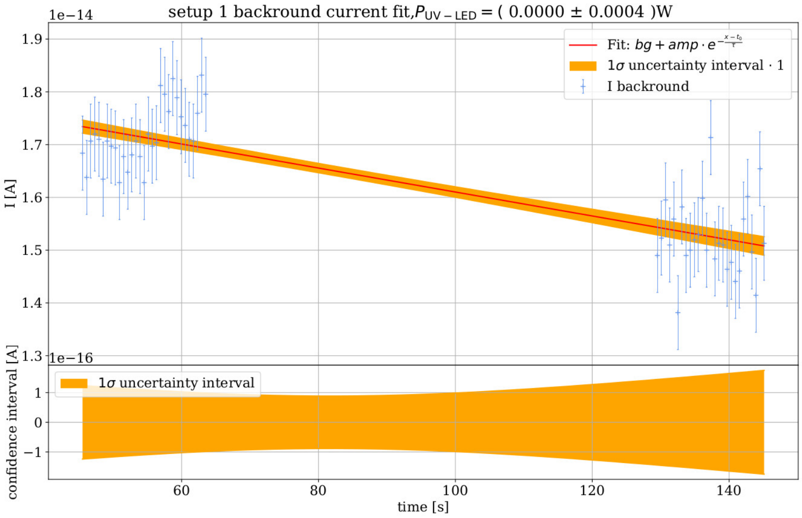

Figure 56: setup 1: background current I for $P_{\mathrm{UV-LED}} = (0.0000 \pm 0.0004)\,\mathrm{W}$. 1 σ confidence of the background fit function. Fit parameters: $bg = (-192.5 \pm 0.2)\mathrm{e}{-15}\,\mathrm{A}$, $amp = (214.6 \pm 1.1)\mathrm{e}{-15}\,\mathrm{A}$, $t_0 = (-160 \pm 31)\,\mathrm{s}$, $\tau = (9.2 \pm 1.0)\mathrm{e}3\,\mathrm{s}$. $\chi^2_{\mathrm{red.}} = 1.0 \pm 0.2$.

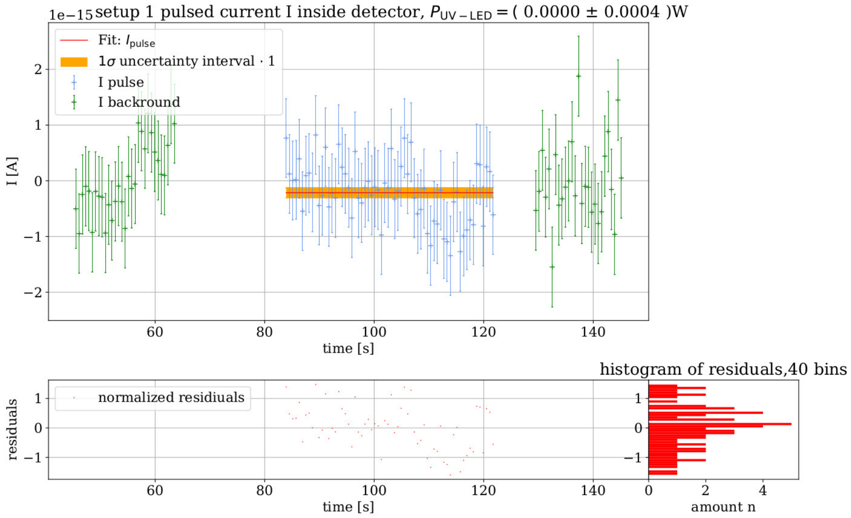

Figure 57: setup 1: background corrected data for the pulse current I_{pulse} with $P_{\text{UV}-\text{LED}} = (0.0000 \pm 0.0004)\,\text{A}$. Fit parameters: $I_{\text{pulse}} = (-0.22 \pm 0.07)\text{e}{-15}\,\text{A}$. $\chi^2_{\text{red.}} = 0.6 \pm 0.2$. The uncertainty of the fit parameters was modified by $\sigma(I_{\text{pulse}}) = \sqrt{\sigma(I_{\text{pulse}})^2 \cdot \chi^2_{\text{red.}}}$ so that the uncertainty value is not misrepresented.

10.3 Additional figures for the relationship between pulsewidth of the UV-LED and I_{pulse}

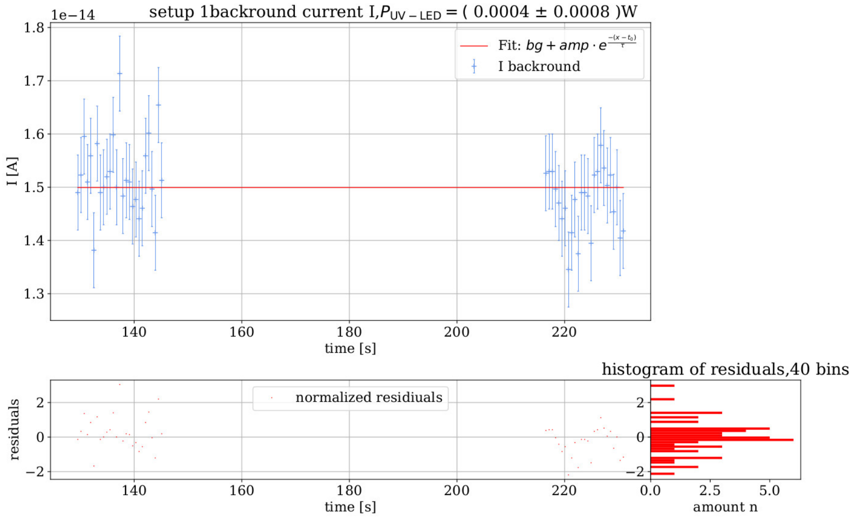

Figure 58: setup 1: background current I for $P_{\mathrm{UV-LED}} = (0.0004 \pm 0.0008)\,\mathrm{W}$. Fit parameters: $bg = (-76.60 \pm 0.14)\mathrm{e}{-15}\,\mathrm{A}$, $amp = (91.6 \pm 1.2)\mathrm{e}{-15}\,\mathrm{A}$, $t_0 = (-0 \pm 1.2)\mathrm{e}6\,\mathrm{s}$, $\tau = (-0 \pm 1.6)\mathrm{e}9\,\mathrm{s}$. $\chi^2_{\mathrm{red.}} = 1.0 \pm 0.2$. This fit has already been used to modify the uncertainties of the measured current I to produce a $\chi^2_{\mathrm{red.}} = 1.0$ using formula 16.

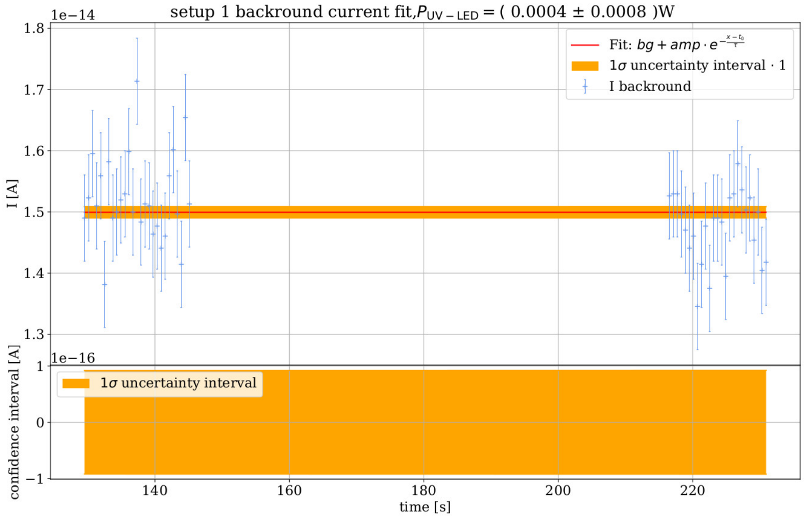

Figure 59: setup 1: background current I for $P_{\mathrm{UV-LED}} = (0.0004 \pm 0.0008)\,\mathrm{W}$. 1 σ confidence of the background fit function. Fit parameters: $bg = (-76.60 \pm 0.14)\mathrm{e}{-15}\,\mathrm{A}$, $amp = (91.6 \pm 1.2)\mathrm{e}{-15}\,\mathrm{A}$, $t_0 = (-0 \pm 1.2)\mathrm{e}6\,\mathrm{s}$, $\tau = (-0 \pm 1.6)\mathrm{e}9\,\mathrm{s}$. $\chi^2_{\mathrm{red.}} = 1.0 \pm 0.2$.

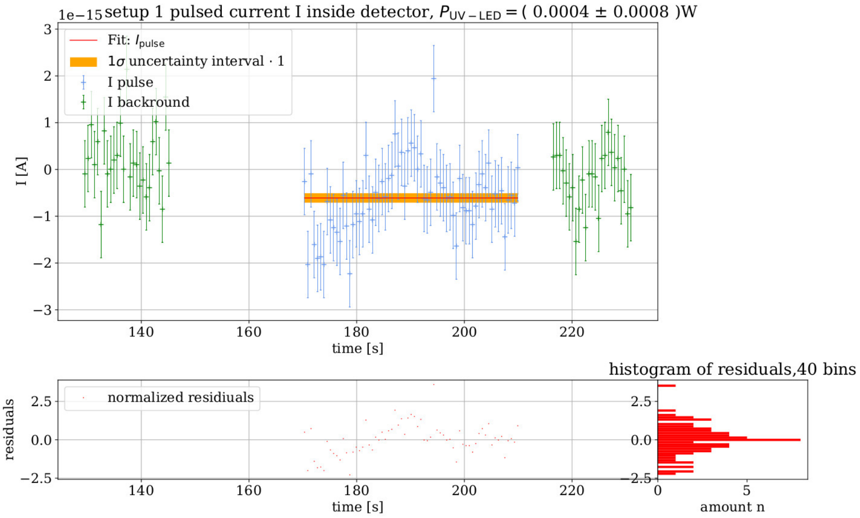

Figure 60: setup 1: background corrected data for the pulse current I_{pulse} with $P_{\text{UV-LED}} = (0.0004 \pm 0.0008)\,\text{A}$. Fit parameters: $I_{\text{pulse}} = (-0.61 \pm 0.09)\text{e}{-15}\,\text{A}$. $\chi^2_{\text{red.}} = 1.1 \pm 0.2$. The uncertainty of the fit parameters was modified by $\sigma(I_{\text{pulse}}) = \sqrt{\sigma(I_{\text{pulse}})^2 \cdot \chi^2_{\text{red.}}}$ so that the uncertainty value is not misrepresented.

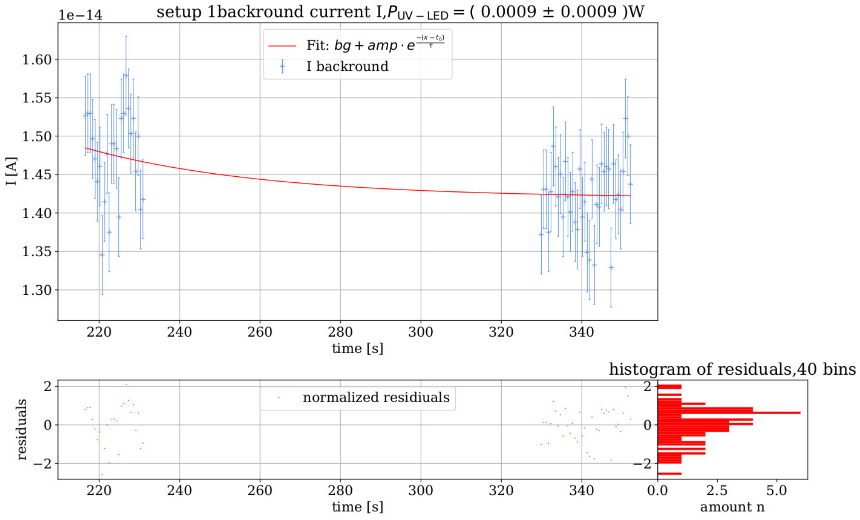

Figure 61: setup 1: background current I for $P_{\text{UV-LED}} = (0.0009 \pm 0.0009)\,\text{W}$. Fit parameters: $bg = (14.194 \pm 0.010)\text{e}{-15}\,\text{A}$, $amp = (1.0 \pm 0.6)\text{e}{-15}\,\text{A}$, $t_0 = (200 \pm 20)\,\text{s}$, $\tau = (40 \pm 30)\,\text{s}$. $\chi^2_{\text{red.}} = 1.0 \pm 0.2$. This fit has already been used to modify the uncertainties of the measured current I to produce a $\chi^2_{\text{red.}} = 1.0$ using formula 16.

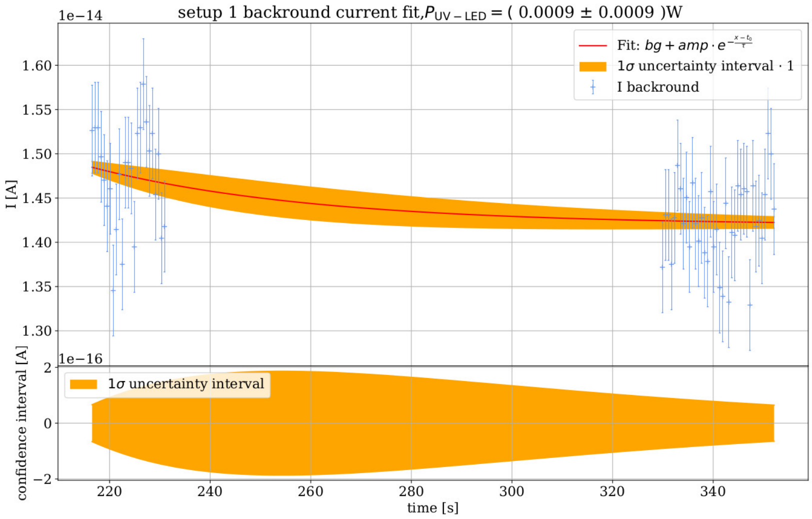

Figure 62: setup 1: background current I for $P_{\mathrm{UV-LED}} = (0.0009 \pm 0.0009)\,\mathrm{W}$. 1 σ confidence of the background fit function. Fit parameters: $bg = (14.194 \pm 0.010)\mathrm{e}{-15}\,\mathrm{A}$, $amp = (1.0 \pm 0.6)\mathrm{e}{-15}\,\mathrm{A}$, $t_0 = (200 \pm 20)\,\mathrm{s}$, $\tau = (40 \pm 30)\,\mathrm{s}$. $\chi^2_{\mathrm{red.}} = 1.0 \pm 0.2$.

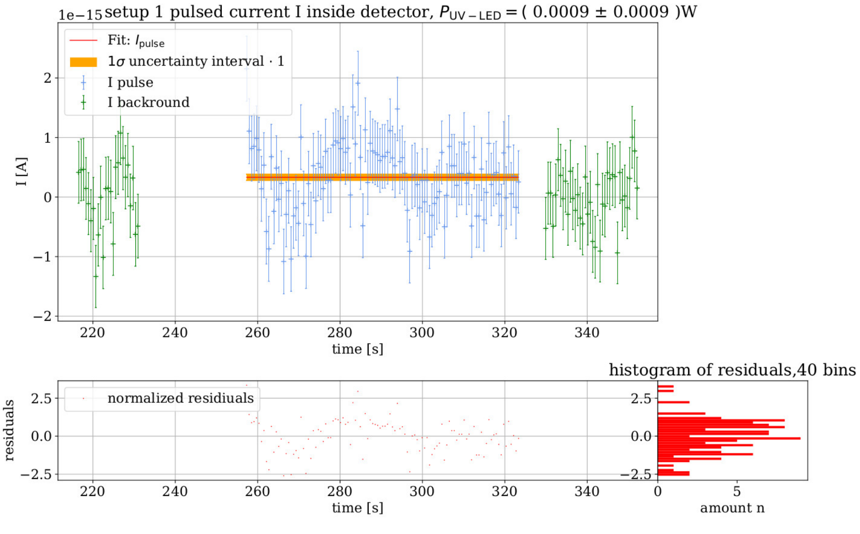

Figure 63: setup 1: background corrected data for the pulse current I_{pulse} with $P_{\mathrm{UV-LED}} = (0.0009 \pm 0.0009)\,\mathrm{A}$. Fit parameters: $I_{\mathrm{pulse}} = (0.33 \pm 0.06)\mathrm{e}{-15}\,\mathrm{A}$. $\chi^2_{\mathrm{red.}} = 1.21 \pm 0.13$. The uncertainty of the fit parameters was modified by $\sigma(I_{\mathrm{pulse}}) = \sqrt{\sigma(I_{\mathrm{pulse}})^2 \cdot \chi^2_{\mathrm{red.}}}$ so that the uncertainty value is not misrepresented.

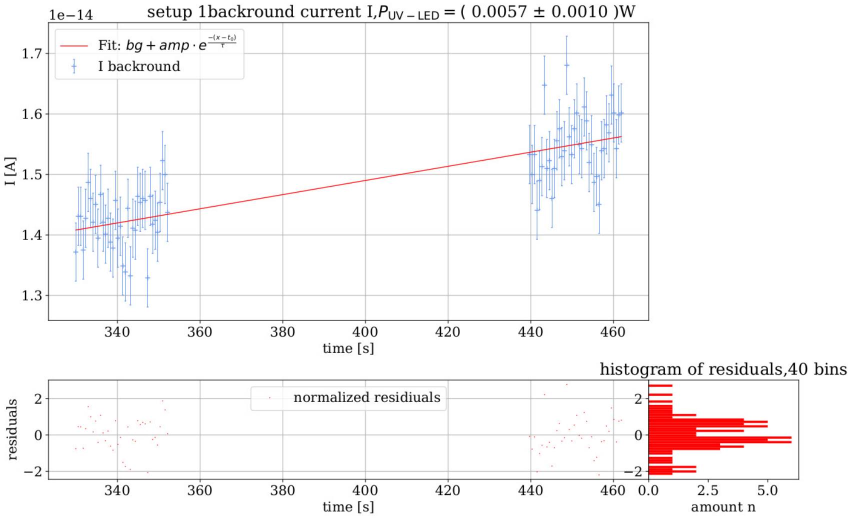

Figure 64: setup 1: background current I for $P_{\mathrm{UV-LED}} = (0.0057 \pm 0.0010)\,\mathrm{W}$. Fit parameters: $bg = (2.0179 \pm 0.0007)\mathrm{e}{-12}\,\mathrm{A}$, $amp = (-1.2671 \pm 0.0003)\mathrm{e}{-12}\,\mathrm{A}$, $t_0 = (78.77 \pm 0.04)\mathrm{e}3\,\mathrm{s}$, $\tau = (171.16 \pm 0.08)\mathrm{e}3\,\mathrm{s}$. $\chi^2_{\mathrm{red.}} = 1.0 \pm 0.2$. This fit has already been used to modify the uncertainties of the measured current I to produce a $\chi^2_{\mathrm{red.}} = 1.0$ using formula 16.

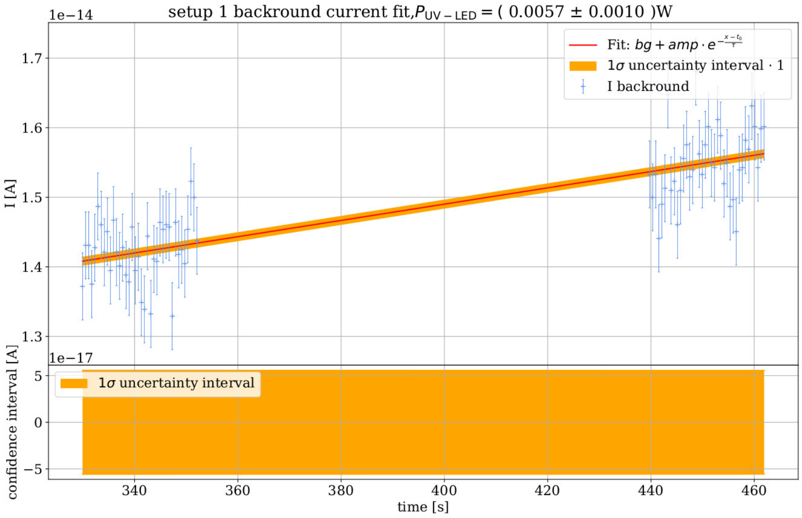

Figure 65: setup 1: background current I for $P_{\mathrm{UV-LED}} = (0.0057 \pm 0.0010)\,\mathrm{W}$. 1 σ confidence of the background fit function.Fit parameters: $bg = (2.0179 \pm 0.0007)\mathrm{e}{-12}\,\mathrm{A}$, $amp = (-1.2671 \pm 0.0003)\mathrm{e}{-12}\,\mathrm{A}$, $t_0 = (78.77 \pm 0.04)\mathrm{e}3\,\mathrm{s}$, $\tau = (171.16 \pm 0.08)\mathrm{e}3\,\mathrm{s}$. $\chi^2_{\mathrm{red.}} = 1.0 \pm 0.2$

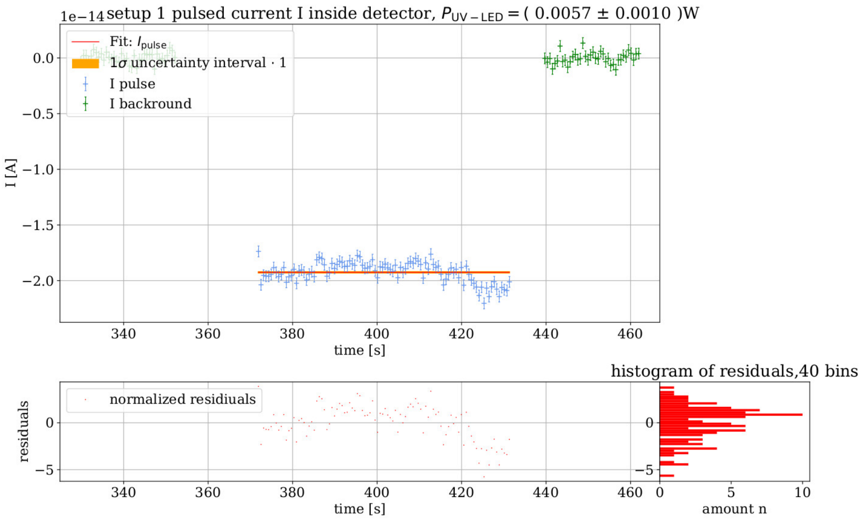

Figure 66: setup 1: background corrected data for the pulse current I_{pulse} with $P_{\text{UV-LED}} = (0.0057 \pm 0.0010)$ A. Fit parameters: $I_{\text{pulse}} = (-19.25 \pm 0.09)\text{e}{-15}$ A. $\chi^2_{\text{red.}} = 3.59 \pm 0.14$. The uncertainty of the fit parameters was modified by $\sigma(I_{\text{pulse}}) = \sqrt{\sigma(I_{\text{pulse}})^2 \cdot \chi^2_{\text{red.}}}$ so that the uncertainty value is not misrepresented.

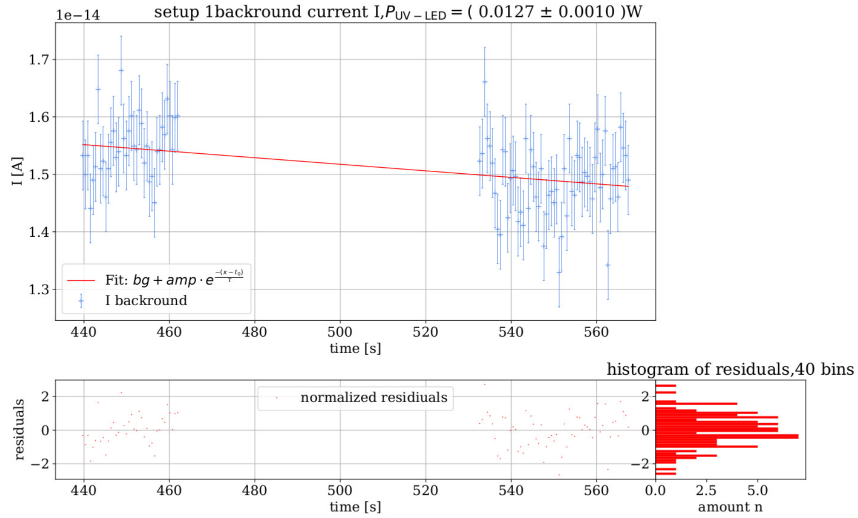

Figure 67: setup 1: background current I for $P_{\text{UV-LED}} = (0.0127 \pm 0.0010)$ W. Fit parameters: $bg = (-83.11 \pm 0.12)\text{e}{-15}$ A, $amp = (100.5 \pm 0.7)\text{e}{-15}$ A, $t_0 = (110 \pm 80)$ s, $\tau = (17 \pm 3)\text{e}3$ s. $\chi^2_{\text{red.}} = 1.00 \pm 0.15$. This fit has already been used to modify the uncertainties of the measured current I to produce a $\chi^2_{\text{red.}} = 1.00$ using formula 16.

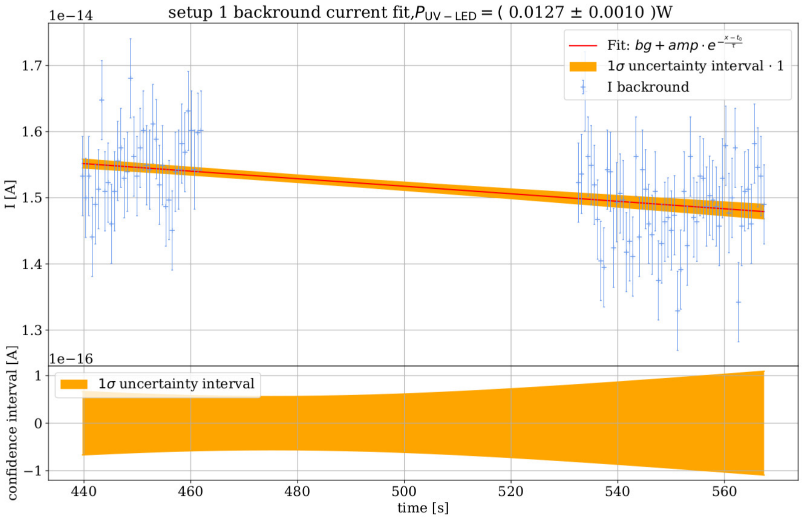

Figure 68: setup 1: background current I for $P_{\mathrm{UV-LED}} = (0.0127 \pm 0.0010)\,\mathrm{W}$. 1 σ confidence of the background fit function.Fit parameters: $bg = (-83.11 \pm 0.12)\mathrm{e}{-15}\,\mathrm{A}$, $amp = (100.5 \pm 0.7)\mathrm{e}{-15}\,\mathrm{A}$, $t_0 = (110 \pm 80)\,\mathrm{s}$, $\tau = (17 \pm 3)\mathrm{e}3\,\mathrm{s}$. $\chi^2_{\mathrm{red.}} = 1.00 \pm 0.15$.

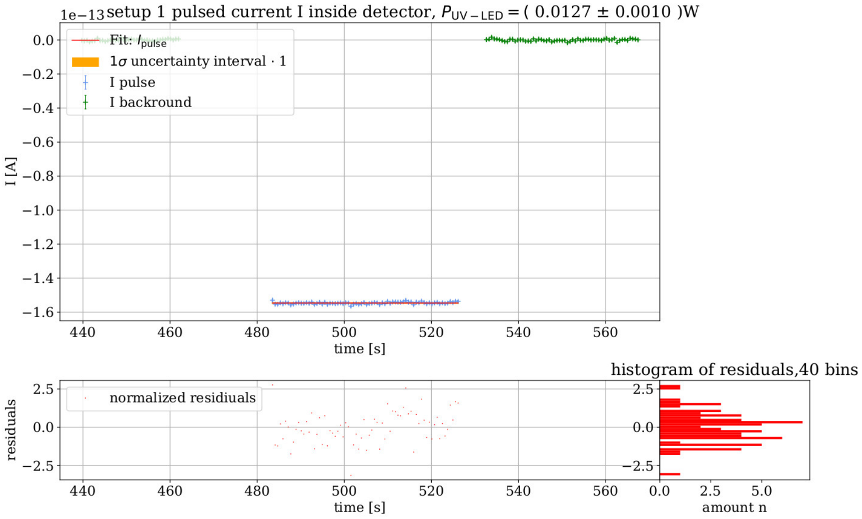

Figure 69: setup 1: background corrected data for the pulse current I_{pulse} with $P_{\mathrm{UV-LED}} = (0.0127 \pm 0.0010)\,\mathrm{A}$. Fit parameters: $I_{\mathrm{pulse}} = (-154.61 \pm 0.07)\mathrm{e}{-15}\,\mathrm{A}$. $\chi^2_{\mathrm{red.}} = 1.1 \pm 0.2$. The uncertainty of the fit parameters was modified by $\sigma(I_{\mathrm{pulse}}) = \sqrt{\sigma(I_{\mathrm{pulse}})^2 \cdot \chi^2_{\mathrm{red.}}}$ so that the uncertainty value is not misrepresented.

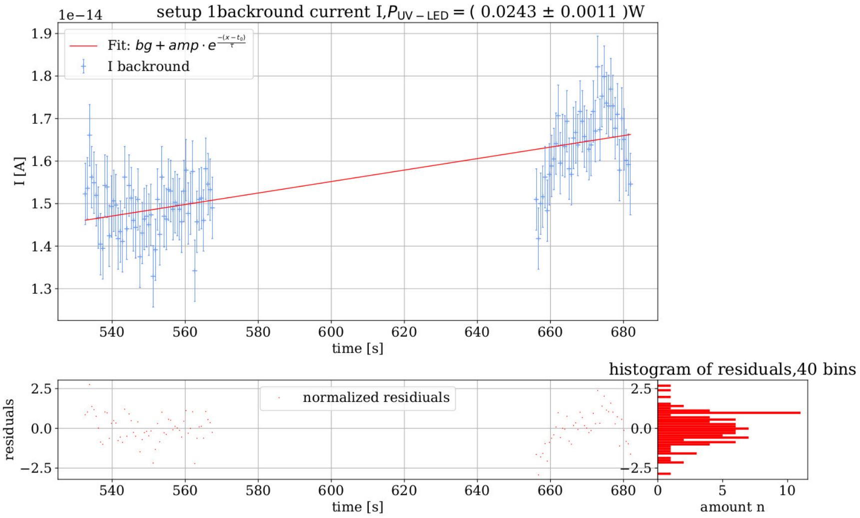

Figure 70: setup 1: background current I for $P_{\mathrm{UV-LED}} = (0.0243 \pm 0.0011)\,\mathrm{W}$. Fit parameters: $bg = (9.9272 \pm 0.0010)\mathrm{e}{-12}\,\mathrm{A}$, $amp = (-8.9062 \pm 0.0006)\mathrm{e}{-12}\,\mathrm{A}$, $t_0 = (79.14 \pm 0.06)\mathrm{e}3\,\mathrm{s}$, $\tau = (734.2 \pm 0.6)\mathrm{e}3\,\mathrm{s}$. $\chi^2_{\mathrm{red.}} = 1.00 \pm 0.14$. This fit has already been used to modify the uncertainties of the measured current I to produce a $\chi^2_{\mathrm{red.}} = 1.00$ using formula 16.

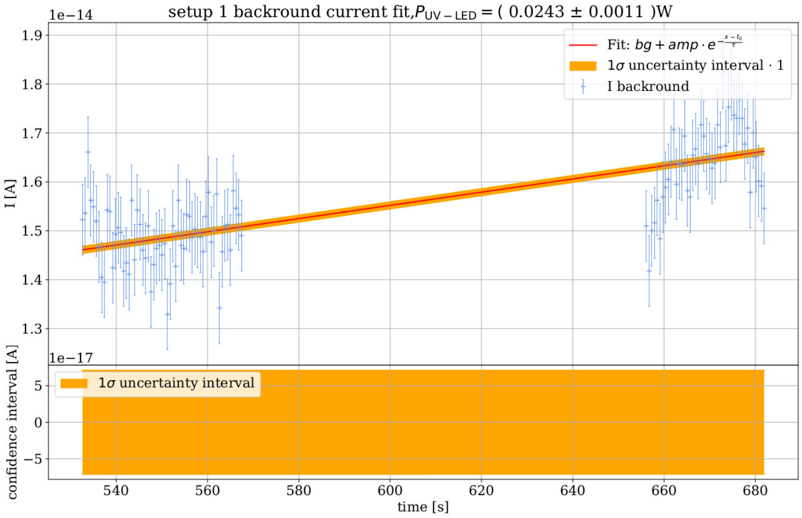

Figure 71: setup 1: background current I for $P_{\mathrm{UV-LED}} = (0.0243 \pm 0.0011)\,\mathrm{W}$. 1 σ confidence of the background fit function. Fit parameters: $bg = (9.9272 \pm 0.0010)\mathrm{e}{-12}\,\mathrm{A}$, $amp = (-8.9062 \pm 0.0006)\mathrm{e}{-12}\,\mathrm{A}$, $t_0 = (79.14 \pm 0.06)\mathrm{e}3\,\mathrm{s}$, $\tau = (734.2 \pm 0.6)\mathrm{e}3\,\mathrm{s}$. $\chi^2_{\mathrm{red.}} = 1.00 \pm 0.14$.

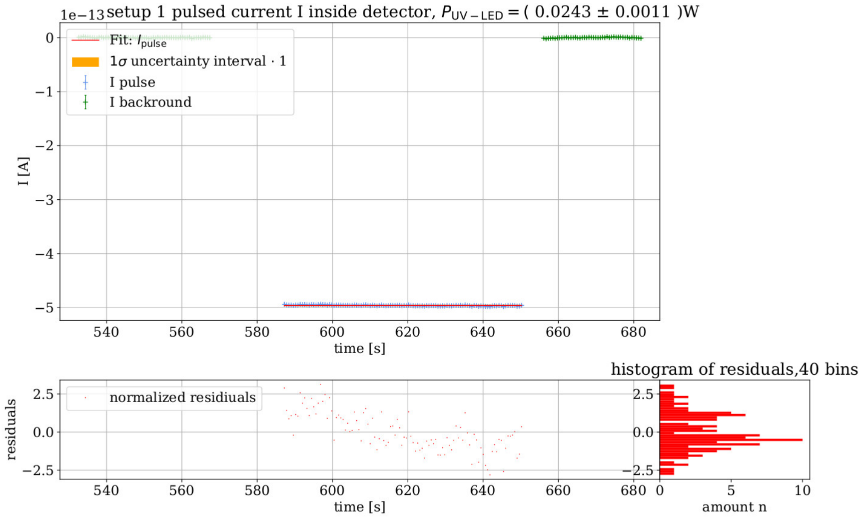

Figure 72: setup 1: background corrected data for the pulse current I_{pulse} with $P_{\text{UV-LED}} = (0.0243 \pm 0.0011)\,\text{A}$. Fit parameters: $I_{\text{pulse}} = (-495.98 \pm 0.09)\text{e}{-15}\,\text{A}$. $\chi^2_{\text{red.}} = 1.59 \pm 0.14$. The uncertainty of the fit parameters was modified by $\sigma(I_{\text{pulse}}) = \sqrt{\sigma(I_{\text{pulse}})^2 \cdot \chi^2_{\text{red.}}}$ so that the uncertainty value is not misrepresented.

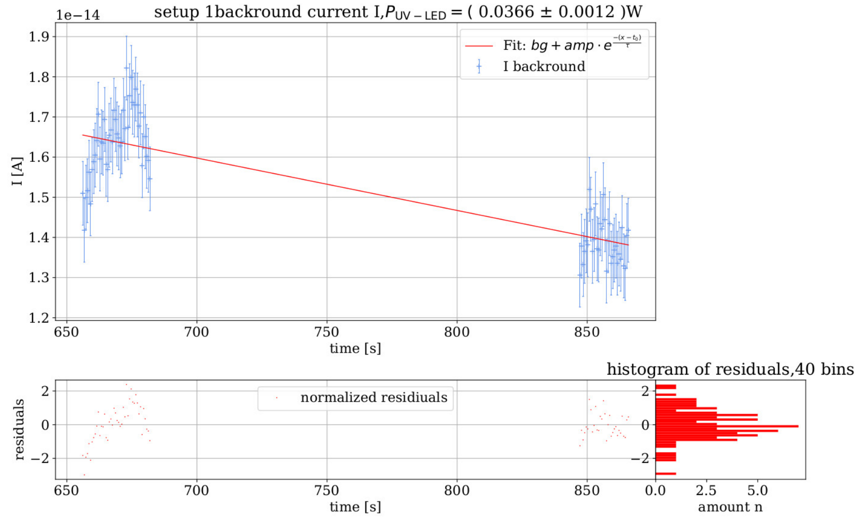

Figure 73: setup 1: background current I for $P_{\text{UV-LED}} = (0.0366 \pm 0.0012)\,\text{W}$. Fit parameters: $bg = (-110.7915 \pm 0.0012)\text{e}{-12}\,\text{A}$, $amp = (70.7671 \pm 0.0008)\text{e}{-12}\,\text{A}$, $t_0 = (3.80772 \pm 0.00009)\text{e}6\,\text{s}$, $\tau = (8.4902 \pm 0.0002)\text{e}6\,\text{s}$. $\chi^2_{\text{red.}} = 1.0 \pm 0.2$. This fit has already been used to modify the uncertainties of the measured current I to produce a $\chi^2_{\text{red.}} = 1.0$ using formula 16.

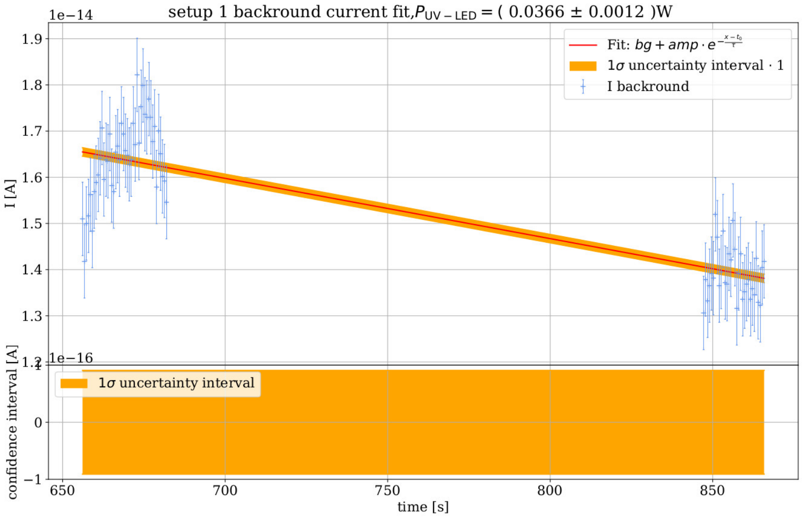

Figure 74: setup 1: background current I for $P_{\mathrm{UV-LED}} = (0.0366 \pm 0.0012)\,\mathrm{W}$. 1 σ confidence of the background fit function. Fit parameters: $bg = (-110.7915 \pm 0.0012)\mathrm{e}{-12}\,\mathrm{A}$, $amp = (70.7671 \pm 0.0008)\mathrm{e}{-12}\,\mathrm{A}$, $t_0 = (3.80772 \pm 0.00009)\mathrm{e}6\,\mathrm{s}$, $\tau = (8.4902 \pm 0.0002)\mathrm{e}6\,\mathrm{s}$. $\chi^2_{\mathrm{red.}} = 1.0 \pm 0.2$.

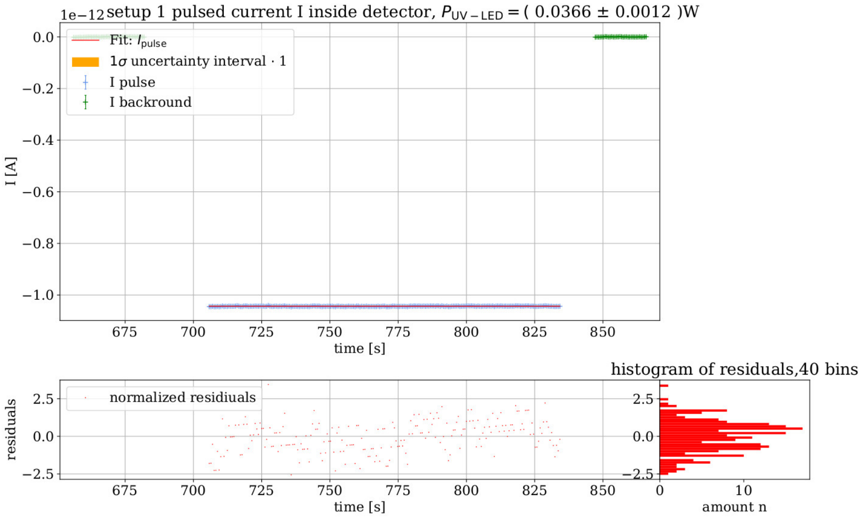

Figure 75: setup 1: background corrected data for the pulse current I_{pulse} with $P_{\mathrm{UV-LED}} = (0.0366 \pm 0.0012)\,\mathrm{A}$. Fit parameters: $I_{\mathrm{pulse}} = (-1.04336 \pm 0.00006)\mathrm{e}{-12}\,\mathrm{A}$. $\chi^2_{\mathrm{red.}} = 1.11 \pm 0.10$. The uncertainty of the fit parameters was modified by $\sigma(I_{\mathrm{pulse}}) = \sqrt{\sigma(I_{\mathrm{pulse}})^2 \cdot \chi^2_{\mathrm{red.}}}$ so that the uncertainty value is not misrepresented.

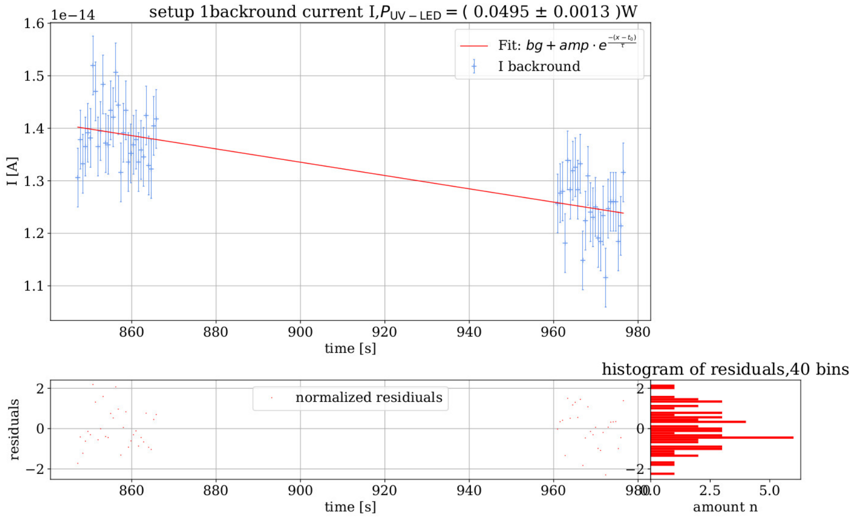

Figure 76: setup 1: background current I for $P_{\mathrm{UV-LED}} = (0.0495 \pm 0.0013)\,\mathrm{W}$. Fit parameters: $bg = (-1.2333 \pm 0.0003)\mathrm{e}{-12}\,\mathrm{A}$, $amp = (862.5 \pm 0.6)\mathrm{e}{-15}\,\mathrm{A}$, $t_0 = (37.14 \pm 0.04)\mathrm{e}3\,\mathrm{s}$, $\tau = (98.40 \pm 0.12)\mathrm{e}3\,\mathrm{s}$. $\chi^2_{\mathrm{red.}} = 1.0 \pm 0.2$. This fit has already been used to modify the uncertainties of the measured current I to produce a $\chi^2_{\mathrm{red.}} = 1.0$ using formula 16.

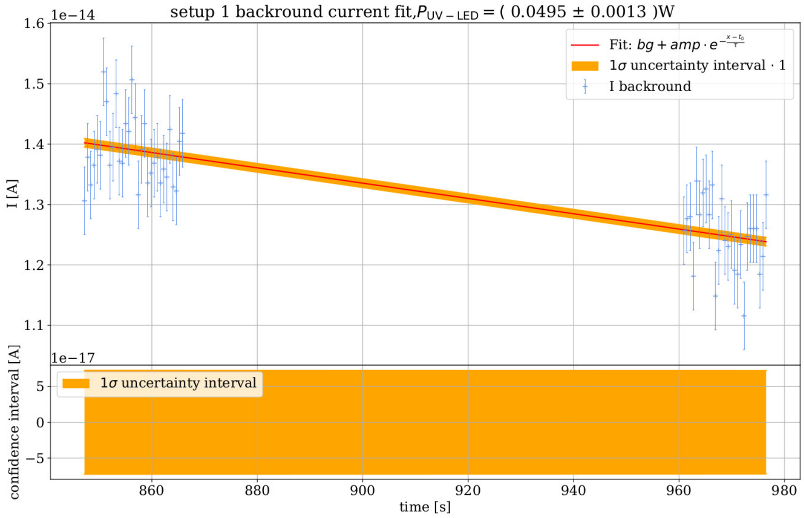

Figure 77: setup 1: background current I for $P_{\mathrm{UV-LED}} = (0.0495 \pm 0.0013)\,\mathrm{W}$. 1 σ confidence of the background fit function. Fit parameters: $bg = (-1.2333 \pm 0.0003)\mathrm{e}{-12}\,\mathrm{A}$, $amp = (862.5 \pm 0.6)\mathrm{e}{-15}\,\mathrm{A}$, $t_0 = (37.14 \pm 0.04)\mathrm{e}3\,\mathrm{s}$, $\tau = (98.40 \pm 0.12)\mathrm{e}3\,\mathrm{s}$. $\chi^2_{\mathrm{red.}} = 1.0 \pm 0.2$.

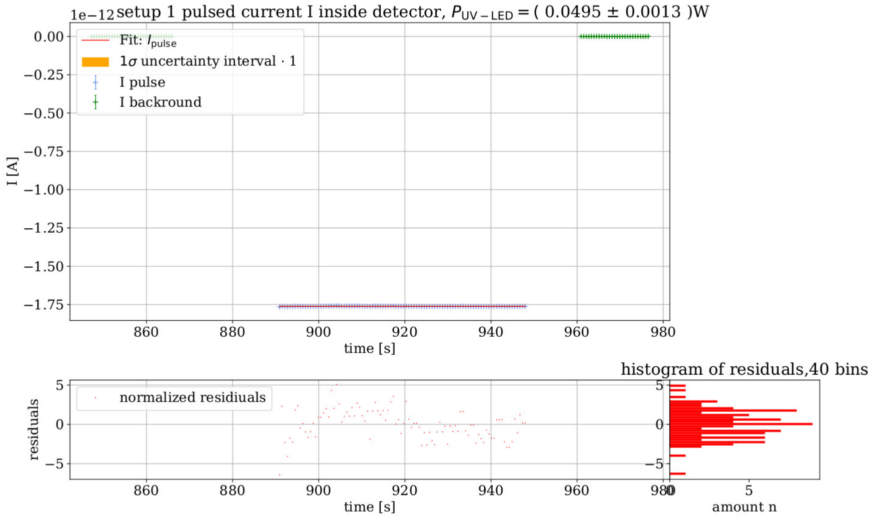

Figure 78: setup 1: background corrected data for the pulse current I_{pulse} with $P_{\mathrm{UV-LED}} = (0.0495 \pm 0.0013)\,\mathrm{A}$. Fit parameters: $I_{\mathrm{pulse}} = (-1.76145 \pm 0.00011)\mathrm{e}{-12}\,\mathrm{A}$. $\chi^2_{\mathrm{red.}} = 3.58 \pm 0.15$. The uncertainty of the fit parameters was modified by $\sigma(I_{\mathrm{pulse}}) = \sqrt{\sigma(I_{\mathrm{pulse}})^2 \cdot \chi^2_{\mathrm{red.}}}$ so that the uncertainty value is not misrepresented.

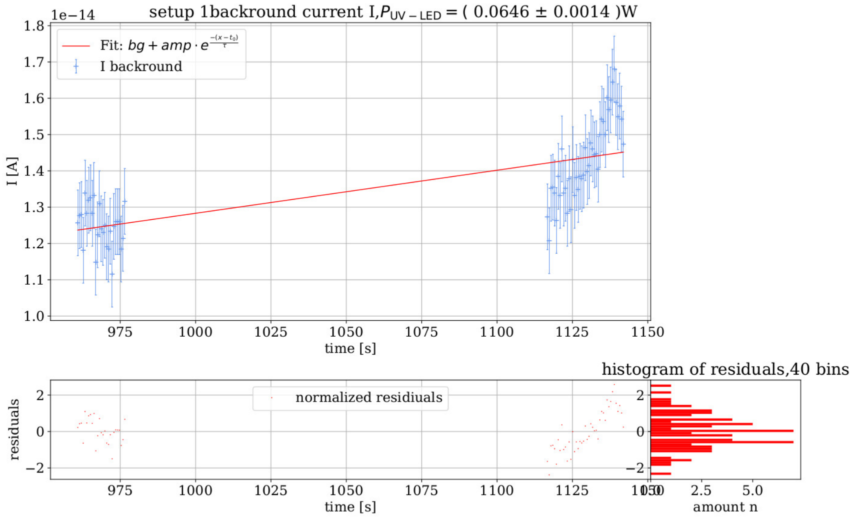

Figure 79: setup 1: background current I for $P_{\mathrm{UV-LED}} = (0.0646 \pm 0.0014)\,\mathrm{W}$. Fit parameters: $bg = (15.3994 \pm 0.0015)\mathrm{e}{-12}\,\mathrm{A}$, $amp = (-9.1687 \pm 0.0007)\mathrm{e}{-12}\,\mathrm{A}$, $t_0 = (672.63 \pm 0.10)\mathrm{e}3\,\mathrm{s}$, $\tau = (1.2973 \pm 0.0002)\mathrm{e}6\,\mathrm{s}$. $\chi^2_{\mathrm{red.}} = 1.0 \pm 0.2$. This fit has already been used to modify the uncertainties of the measured current I to produce a $\chi^2_{\mathrm{red.}} = 1.0$ using formula 16.

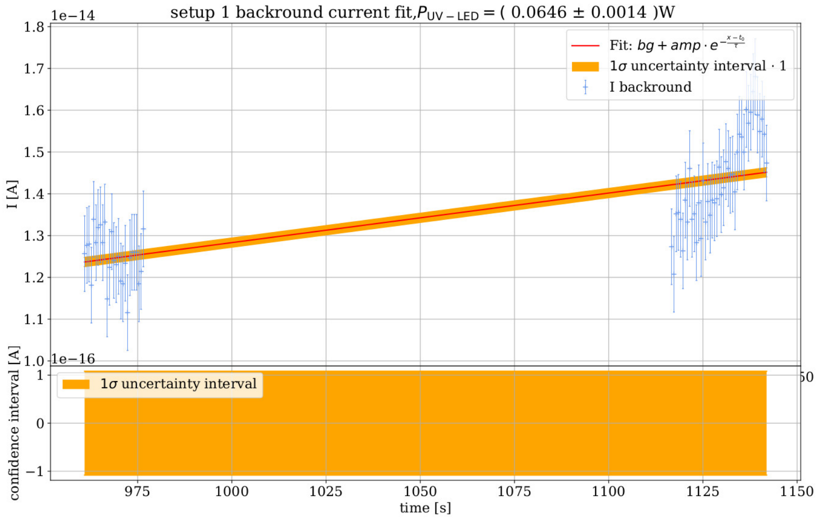

Figure 80: setup 1: background current I for $P_{\mathrm{UV-LED}} = (0.0646 \pm 0.0014)$ W. 1 σ confidence of the background fit function. Fit parameters: $bg = (15.3994 \pm 0.0015)e-12$ A, $amp = (-9.1687 \pm 0.0007)e-12$ A, $t_0 = (672.63 \pm 0.10)$e3 s, $\tau = (1.2973 \pm 0.0002)$e6 s. $\chi^2_{\mathrm{red.}} = 1.0 \pm 0.2$.

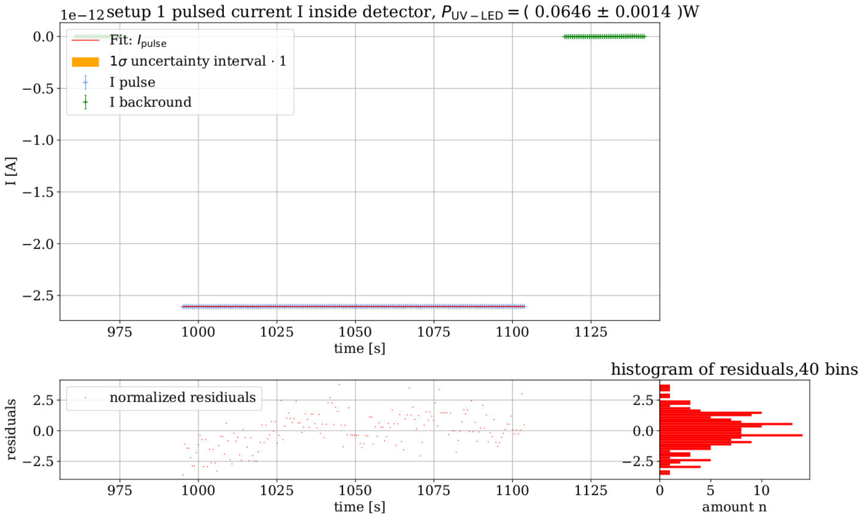

Figure 81: setup 1: background corrected data for the pulse current I_{pulse} with $P_{\mathrm{UV-LED}} = (0.0646 \pm 0.0014)$ A. Fit parameters: $I_{\mathrm{pulse}} = (-2.60629 \pm 0.00009)e-12$ A. $\chi^2_{\mathrm{red.}} = 1.95 \pm 0.11$. The uncertainty of the fit parameters was modified by $\sigma(I_{\mathrm{pulse}}) = \sqrt{\sigma(I_{\mathrm{pulse}})^2 \cdot \chi^2_{\mathrm{red.}}}$ so that the uncertainty value is not misrepresented.

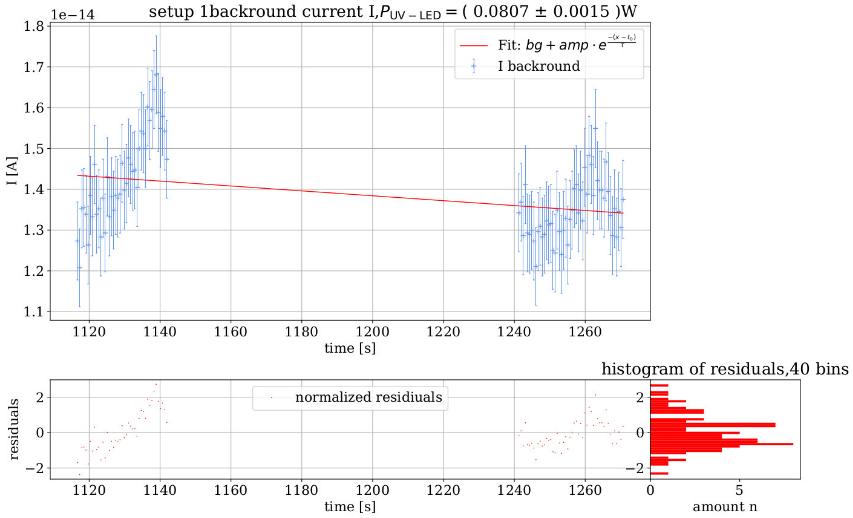

Figure 82: setup 1: background current I for $P_{\mathrm{UV-LED}} = (0.0807 \pm 0.0015)\,\mathrm{W}$. Fit parameters: $bg = (-3.0660 \pm 0.0007)\mathrm{e}{-12}\,\mathrm{A}$, $amp = (4.300 \pm 0.002)\mathrm{e}{-12}\,\mathrm{A}$, $t_0 = (-170.1 \pm 0.2)\mathrm{e}3\,\mathrm{s}$, $\tau = (513.1 \pm 0.5)\mathrm{e}3\,\mathrm{s}$. $\chi^2_{\mathrm{red.}} = 1.0 \pm 0.15$. This fit has already been used to modify the uncertainties of the measured current I to produce a $\chi^2_{\mathrm{red.}} = 1.0$ using formula 16.

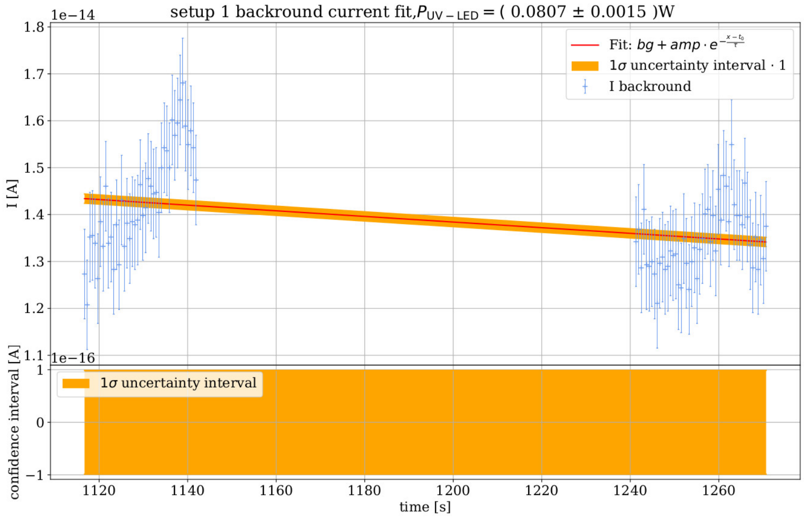

Figure 83: setup 1: background current I for $P_{\mathrm{UV-LED}} = (0.0807 \pm 0.0015)\,\mathrm{W}$. 1 σ confidence of the background fit function. Fit parameters: $bg = (-3.0660 \pm 0.0007)\mathrm{e}{-12}\,\mathrm{A}$, $amp = (4.300 \pm 0.002)\mathrm{e}{-12}\,\mathrm{A}$, $t_0 = (-170.1 \pm 0.2)\mathrm{e}3\,\mathrm{s}$, $\tau = (513.1 \pm 0.5)\mathrm{e}3\,\mathrm{s}$. $\chi^2_{\mathrm{red.}} = 1.00 \pm 0.15$.

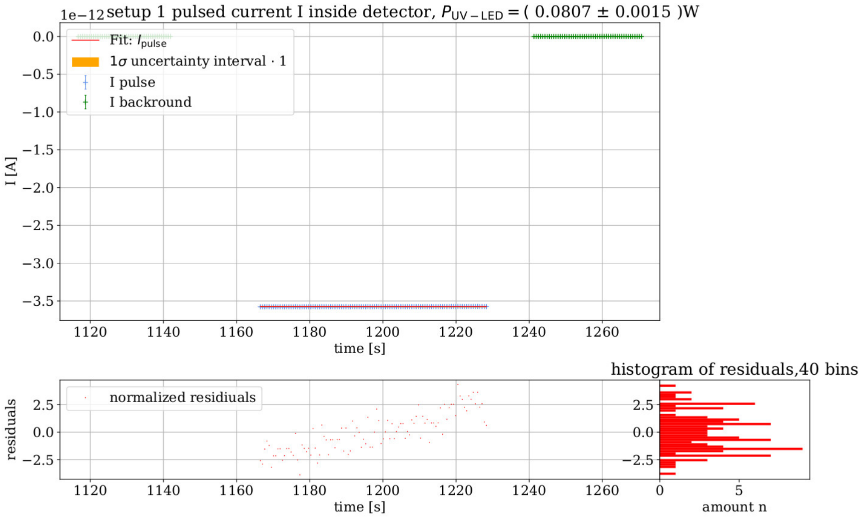

Figure 84: setup 1: background corrected data for the pulse current I_{pulse} with $P_{\mathrm{UV-LED}} = (0.0807 \pm 0.0015)\,\mathrm{A}$. Fit parameters: $I_{\mathrm{pulse}} = (-3.5748 \pm 0.0002)\mathrm{e}{-12}\,\mathrm{A}$. $\chi^2_{\mathrm{red.}} = 3.10 \pm 0.14$. The uncertainty of the fit parameters was modified by $\sigma(I_{\mathrm{pulse}}) = \sqrt{\sigma(I_{\mathrm{pulse}})^2 \cdot \chi^2_{\mathrm{red.}}}$ so that the uncertainty value is not misrepresented.

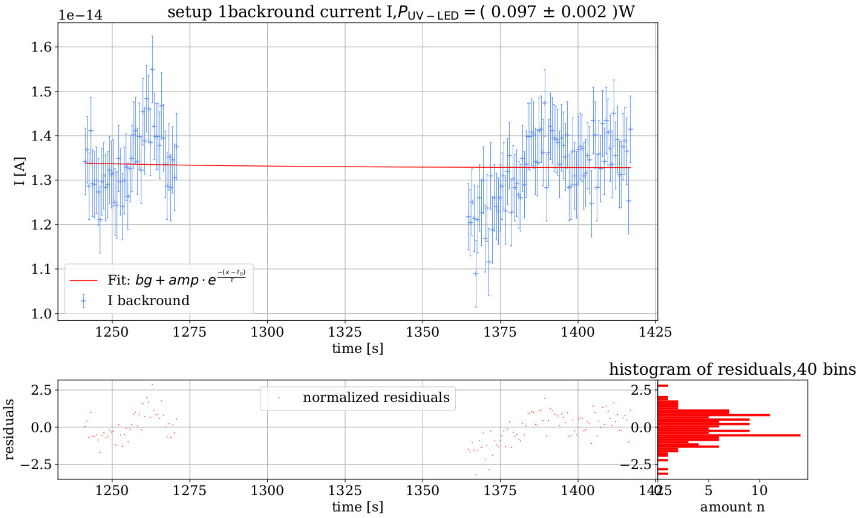

Figure 85: setup 1: background current I for $P_{\mathrm{UV-LED}} = (0.097 \pm 0.002)\,\mathrm{W}$. Fit parameters: $bg = (13.28 \pm 0.09)\mathrm{e}{-15}\,\mathrm{A}$, $amp = (0 \pm 2)\mathrm{e}{-12}\,\mathrm{A}$, $t_0 = (0.8 \pm 0.5)\mathrm{e}3\,\mathrm{s}$, $\tau = (60 \pm 70)\,\mathrm{s}$. $\chi^2_{\mathrm{red.}} = 1.0 \pm 0.12$. This fit has already been used to modify the uncertainties of the measured current I to produce a $\chi^2_{\mathrm{red.}} = 1.0$ using formula 16.

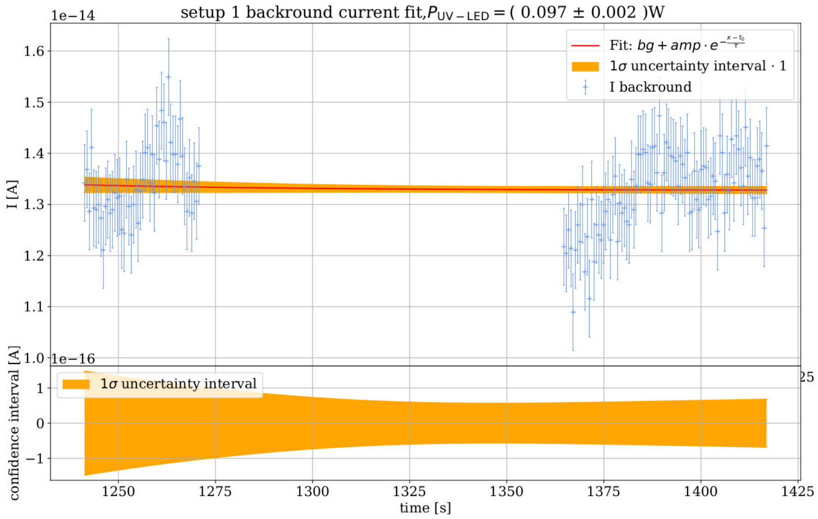

Figure 86: setup 1: background current I for $P_{\mathrm{UV-LED}} = (0.097 \pm 0.002)\,\mathrm{W}$. 1 σ confidence of the background fit function. Fit parameters: $bg = (13.28 \pm 0.09)\mathrm{e}{-15}\,\mathrm{A}$, $amp = (0 \pm 2)\mathrm{e}{-12}\,\mathrm{A}$, $t_0 = (0.8 \pm 0.5)\mathrm{e}3\,\mathrm{s}$, $\tau = (60 \pm 70)\,\mathrm{s}$. $\chi^2_{\mathrm{red.}} = 1.0 \pm 0.12$.

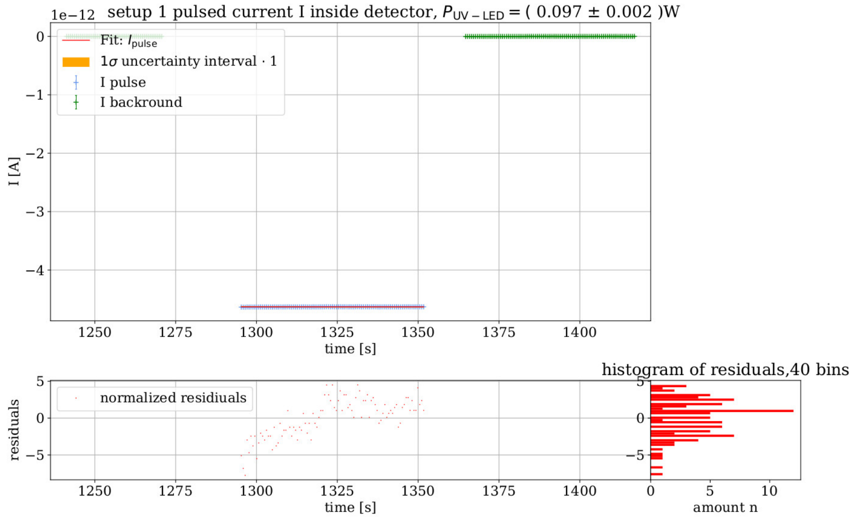

Figure 87: setup 1: background corrected data for the pulse current I_{pulse} with $P_{\mathrm{UV-LED}} = (0.097 \pm 0.002)\,\mathrm{A}$. Fit parameters: $I_{\mathrm{pulse}} = (-4.6307 \pm 0.0002)\mathrm{e}{-12}\,\mathrm{A}$. $\chi^2_{\mathrm{red.}} = 6.75 \pm 0.15$. The uncertainty of the fit parameters was modified by $\sigma(I_{\mathrm{pulse}}) = \sqrt{\sigma(I_{\mathrm{pulse}})^2 \cdot \chi^2_{\mathrm{red.}}}$ so that the uncertainty value is not misrepresented.

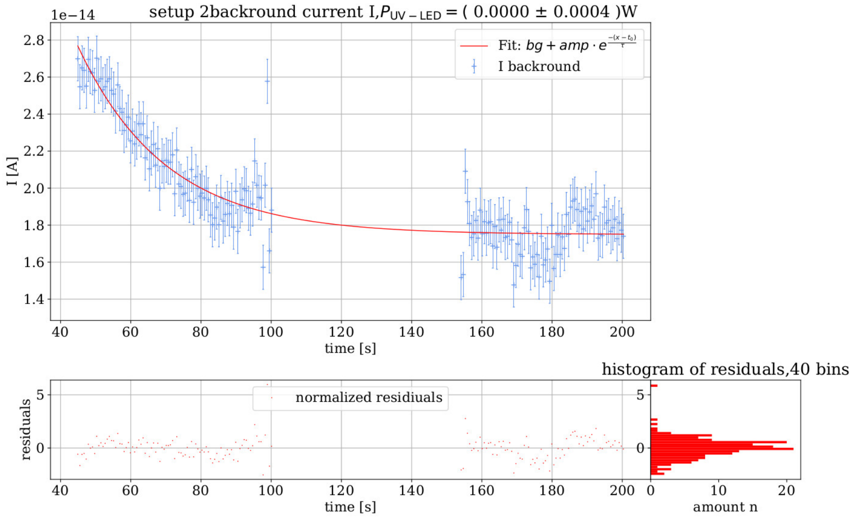

Figure 88: setup 2: background current I for $P_{\mathrm{UV-LED}} = (0.0000 \pm 0.0004)\,\mathrm{W}$. Fit parameters: $bg = (17.49{\pm}0.05)\mathrm{e}{-15}\,\mathrm{A}$, $amp = (8{\pm}2)\mathrm{e}{-15}\,\mathrm{A}$, $t_0 = (51{\pm}5)\,\mathrm{s}$, $\tau = (25{\pm}4)\,\mathrm{s}$. $\chi^2_{\mathrm{red.}} = 1.00{\pm}0.11$. This fit has already been used to modify the uncertainties of the measured current I to produce a $\chi^2_{\mathrm{red.}} = 1.0$ using formula 16.

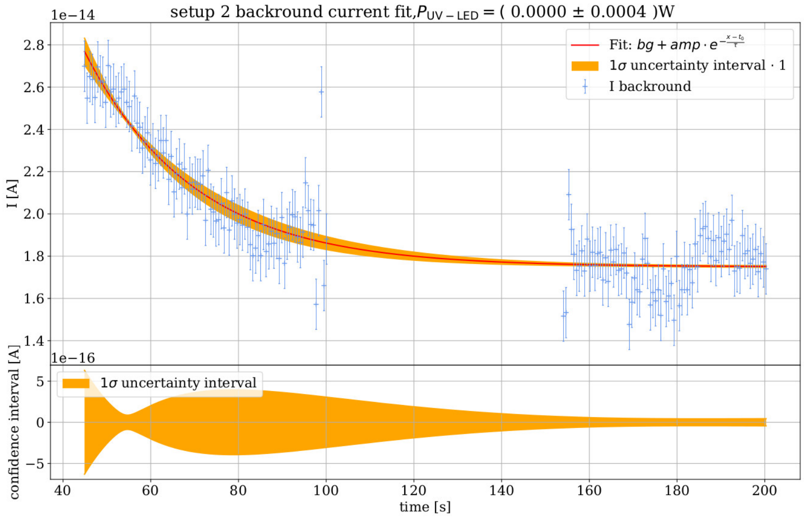

Figure 89: setup 2: background current I for $P_{\mathrm{UV-LED}} = (0.0000 \pm 0.0004)\,\mathrm{W}$. 1 σ confidence of the background fit function. Fit parameters: $bg = (17.49 \pm 0.05)\mathrm{e}{-15}\,\mathrm{A}$, $amp = (8 \pm 2)\mathrm{e}{-15}\,\mathrm{A}$, $t_0 = (51 \pm 5)\,\mathrm{s}$, $\tau = (25 \pm 4)\,\mathrm{s}$. $\chi^2_{\mathrm{red.}} = 1.00 \pm 0.11$.

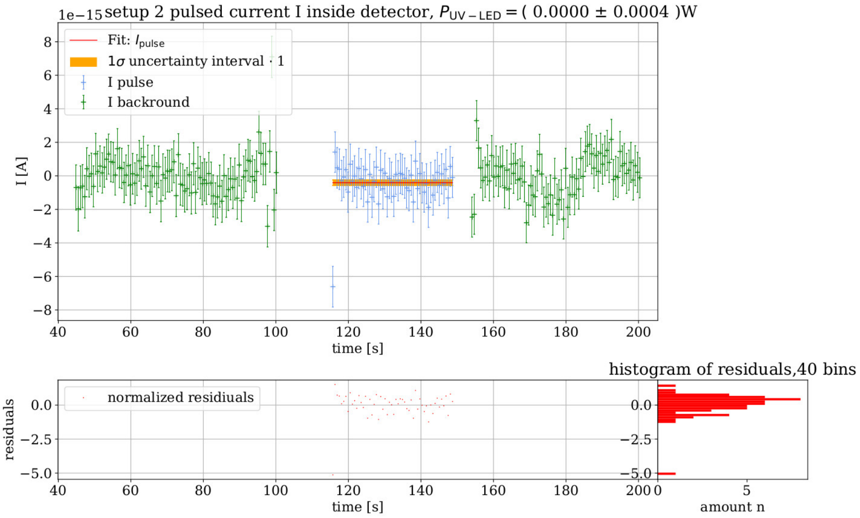

Figure 90: setup 2: background corrected data for the pulse current I_{pulse} with $P_{\text{UV-LED}} = (0.0000 \pm 0.0004)\,\text{A}$. Fit parameters: $I_{\text{pulse}} = (-0.41 \pm 0.14)\text{e}{-15}\,\text{A}$. $\chi^2_{\text{red.}} = 0.8 \pm 0.2$. The uncertainty of the fit parameters was modified by $\sigma(I_{\text{pulse}}) = \sqrt{\sigma(I_{\text{pulse}})^2 \cdot \chi^2_{\text{red.}}}$ so that the uncertainty value is not misrepresented.

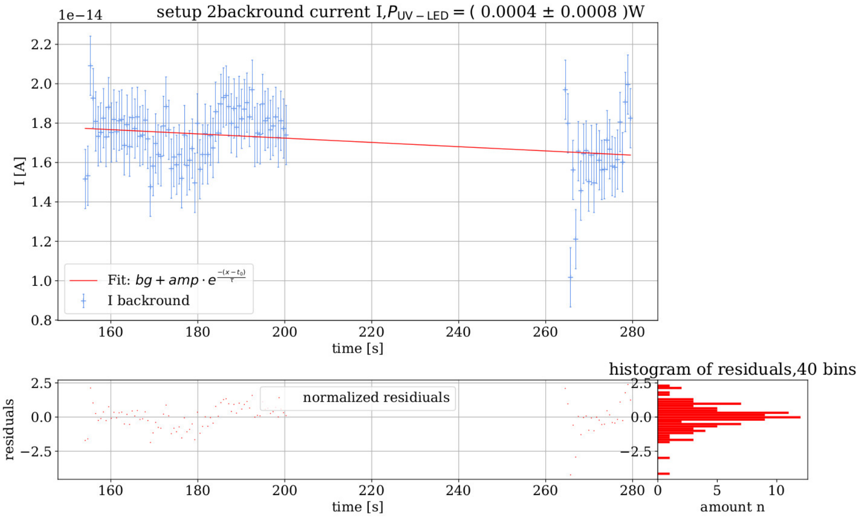

Figure 91: setup 2: background current I for $P_{\text{UV-LED}} = (0.0004 \pm 0.0008)\,\text{W}$. Fit parameters: $bg = (-83.4 \pm 0.2)\text{e}{-15}\,\text{A}$, $amp = (101 \pm 2)\text{e}{-15}\,\text{A}$, $t_0 = (0.2 \pm 0.2)\text{e}3\,\text{s}$, $\tau = (9 \pm 3)\text{e}3\,\text{s}$. $\chi^2_{\text{red.}} = 1.00 \pm 0.14$. This fit has already been used to modify the uncertainties of the measured current I to produce a $\chi^2_{\text{red.}} = 1.00$ using formula 16.

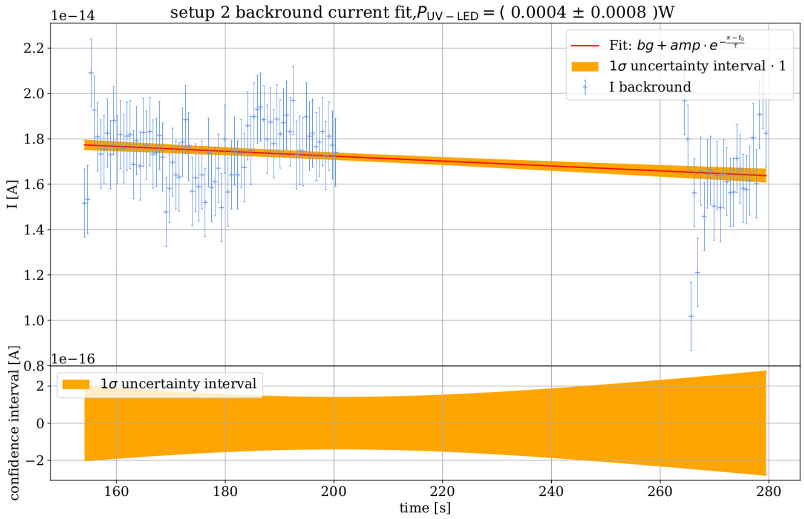

Figure 92: setup 2: background current I for $P_{\mathrm{UV-LED}} = (0.0004 \pm 0.0008)\,\mathrm{W}$. 1 σ confidence of the background fit function. Fit parameters: $bg = (-83.4 \pm 0.2)\mathrm{e}{-15}\,\mathrm{A}$, $amp = (101 \pm 2)\mathrm{e}{-15}\,\mathrm{A}$, $t_0 = (0.2 \pm 0.2)\mathrm{e}3\,\mathrm{s}$, $\tau = (9 \pm 3)\mathrm{e}3\,\mathrm{s}$. $\chi^2_{\mathrm{red.}} = 1.00 \pm 0.14$.

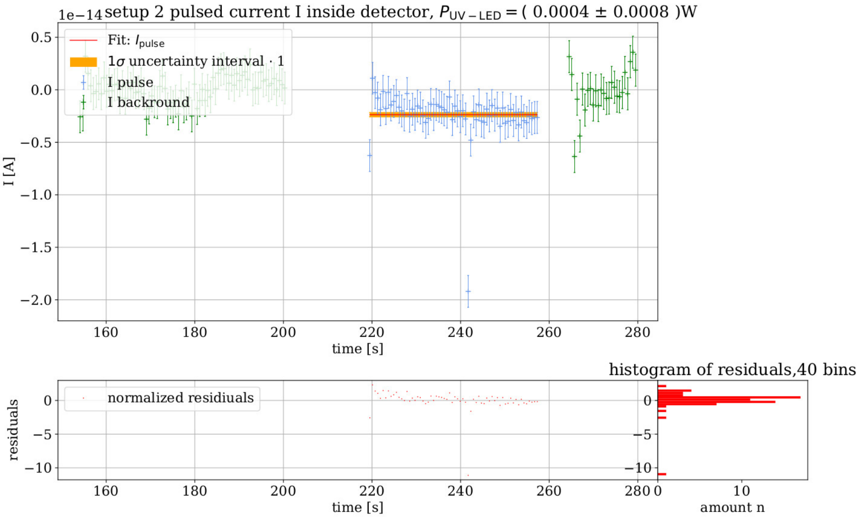

Figure 93: setup 2: background corrected data for the pulse current I_{pulse} with $P_{\mathrm{UV-LED}} = (0.0004 \pm 0.0008)\,\mathrm{A}$. Fit parameters: $I_{\mathrm{pulse}} = (-2.4 \pm 0.3)\mathrm{e}{-15}\,\mathrm{A}$. $\chi^2_{\mathrm{red.}} = 2.5 \pm 0.2$. The uncertainty of the fit parameters was modified by $\sigma(I_{\mathrm{pulse}}) = \sqrt{\sigma(I_{\mathrm{pulse}})^2 \cdot \chi^2_{\mathrm{red.}}}$ so that the uncertainty value is not misrepresented.

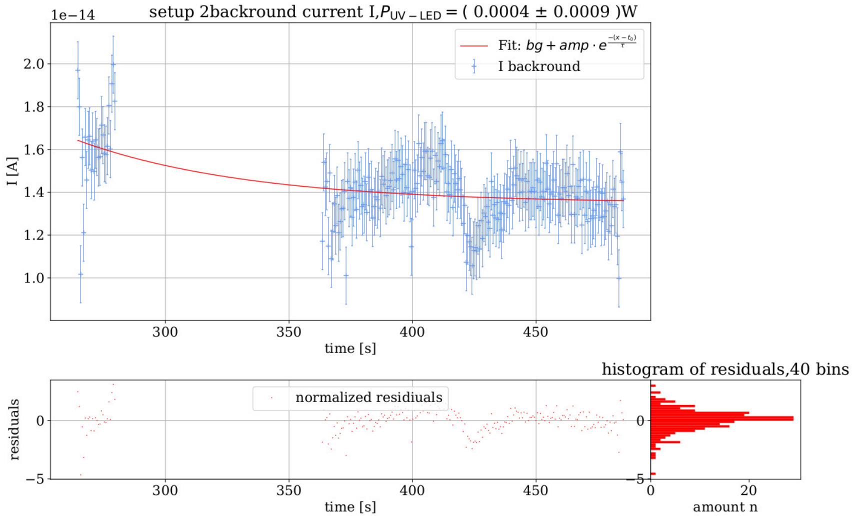

Figure 94: setup 2: background current I for $P_{\mathrm{UV-LED}} = (0.0004 \pm 0.0009)\,\mathrm{W}$. Fit parameters: $bg = (13.48 \pm 0.02)\mathrm{e}{-15}\,\mathrm{A}$, $amp = (1.4 \pm 0.6)\mathrm{e}{-15}\,\mathrm{A}$, $t_0 = (320 \pm 30)\,\mathrm{s}$, $\tau = (70 \pm 20)\,\mathrm{s}$. $\chi^2_{\mathrm{red.}} = 1.00 \pm 0.09$. This fit has already been used to modify the uncertainties of the measured current I to produce a $\chi^2_{\mathrm{red.}} = 1.00$ using formula 16.

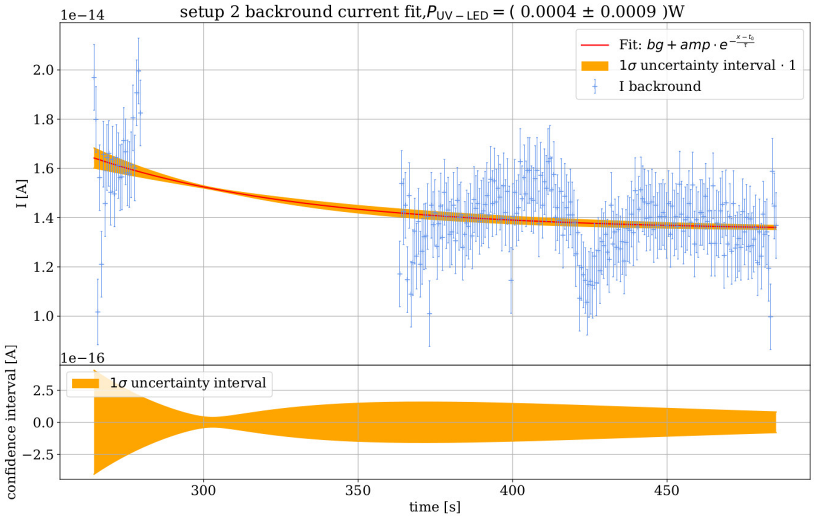

Figure 95: setup 2: background current I for $P_{\mathrm{UV-LED}} = (0.0004 \pm 0.0009)\,\mathrm{W}$. 1 σ confidence of the background fit function. Fit parameters: $bg = (13.48 \pm 0.02)\mathrm{e}{-15}\,\mathrm{A}$, $amp = (1.4 \pm 0.6)\mathrm{e}{-15}\,\mathrm{A}$, $t_0 = (320 \pm 30)\,\mathrm{s}$, $\tau = (70 \pm 20)\,\mathrm{s}$. $\chi^2_{\mathrm{red.}} = 1.00 \pm 0.09$.

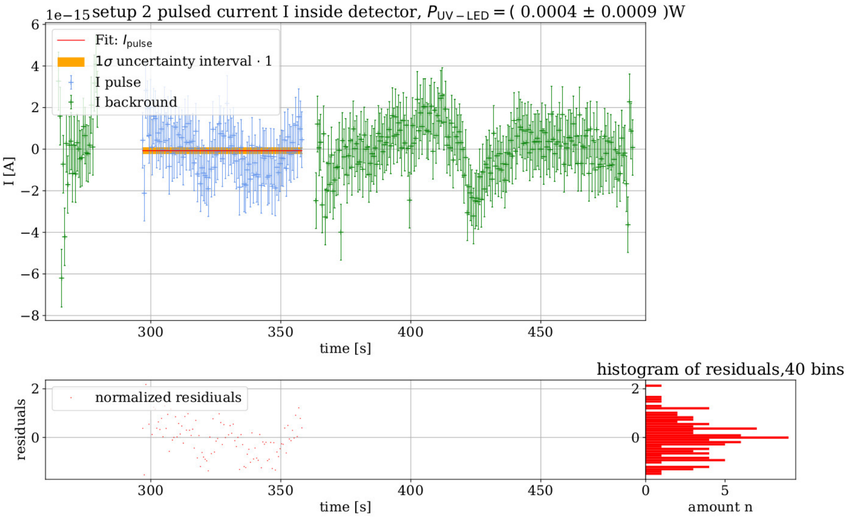

Figure 96: setup 2: background corrected data for the pulse current I_{pulse} with $P_{\text{UV−LED}} = (0.0004 \pm 0.0009)$ A. Fit parameters: $I_{\text{pulse}} = (-0.07 \pm 0.10)\text{e}{-15}$ A. $\chi^2_{\text{red.}} = 0.59 \pm 0.14$. The uncertainty of the fit parameters was modified by $\sigma(I_{\text{pulse}}) = \sqrt{\sigma(I_{\text{pulse}})^2 \cdot \chi^2_{\text{red.}}}$ so that the uncertainty value is not misrepresented.

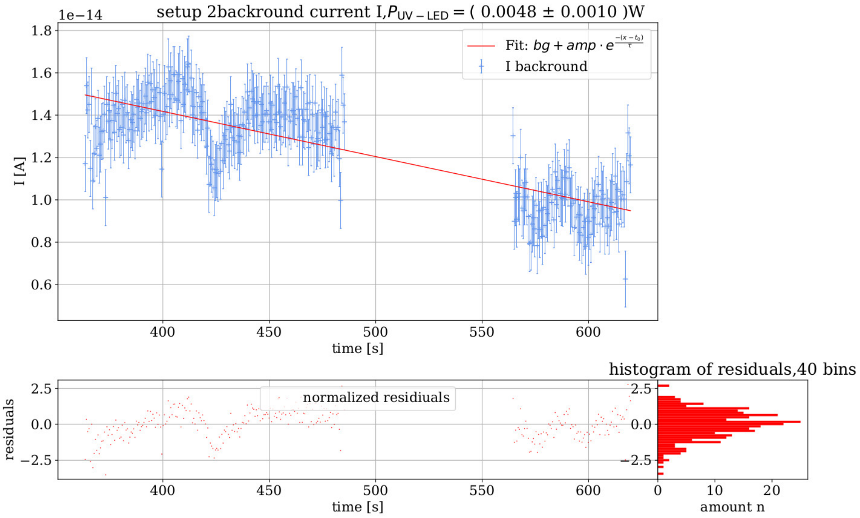

Figure 97: setup 2: background current I for $P_{\text{UV−LED}} = (0.0048 \pm 0.0010)$ W. Fit parameters: $bg = (-252.2255 \pm 0.0010)\text{e}{-12}$ A, $amp = (211.0191 \pm 0.0009)\text{e}{-12}$ A, $t_0 = (2.10895 \pm 0.00005)\text{e}6$ s, $\tau = (11.8172 \pm 0.0003)\text{e}6$ s. $\chi^2_{\text{red.}} = 1.00 \pm 0.08$. This fit has already been used to modify the uncertainties of the measured current I to produce a $\chi^2_{\text{red.}} = 1.00$ using formula 16.

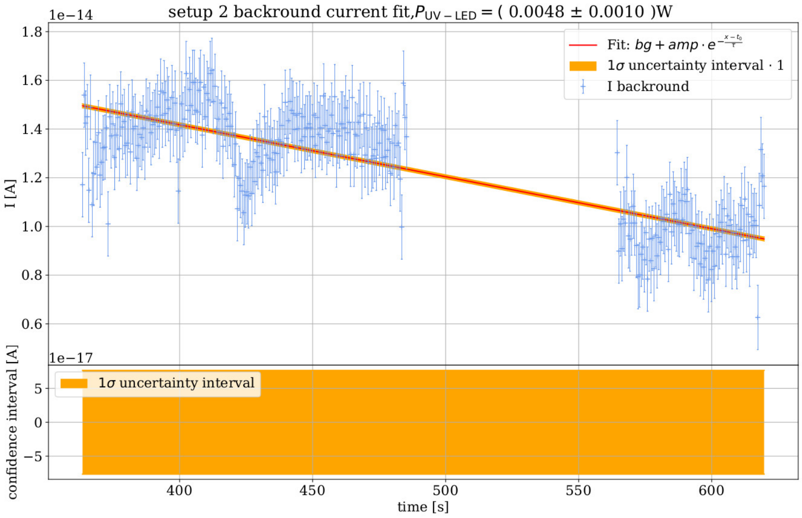

Figure 98: setup 2: background current I for $P_{\mathrm{UV-LED}} = (0.0048 \pm 0.0010)\,\mathrm{W}$. 1 σ confidence of the background fit function. Fit parameters: $bg = (-252.2255 \pm 0.0010)\mathrm{e}{-12}\,\mathrm{A}$, $amp = (211.0191 \pm 0.0009)\mathrm{e}{-12}\,\mathrm{A}$, $t_0 = (2.10895 \pm 0.00005)\mathrm{e}6\,\mathrm{s}$, $\tau = (11.8172 \pm 0.0003)\mathrm{e}6\,\mathrm{s}$. $\chi^2_{\mathrm{red.}} = 1.00 \pm 0.08$.

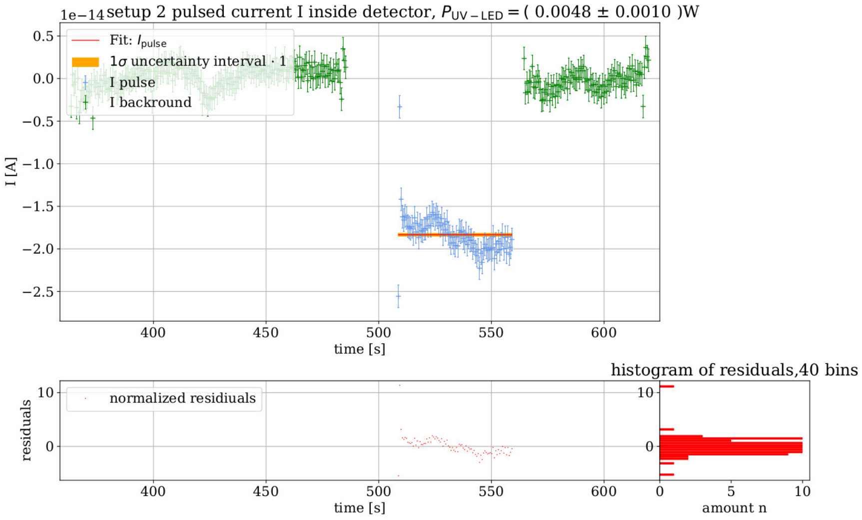

Figure 99: setup 2: background corrected data for the pulse current I_{pulse} with $P_{\mathrm{UV-LED}} = (0.0048 \pm 0.0010)\,\mathrm{A}$. Fit parameters: $I_{\mathrm{pulse}} = (-18.3 \pm 0.3)\mathrm{e}{-15}\,\mathrm{A}$. $\chi^2_{\mathrm{red.}} = 3.3 \pm 0.2$. The uncertainty of the fit parameters was modified by $\sigma(I_{\mathrm{pulse}}) = \sqrt{\sigma(I_{\mathrm{pulse}})^2 \cdot \chi^2_{\mathrm{red.}}}$ so that the uncertainty value is not misrepresented.

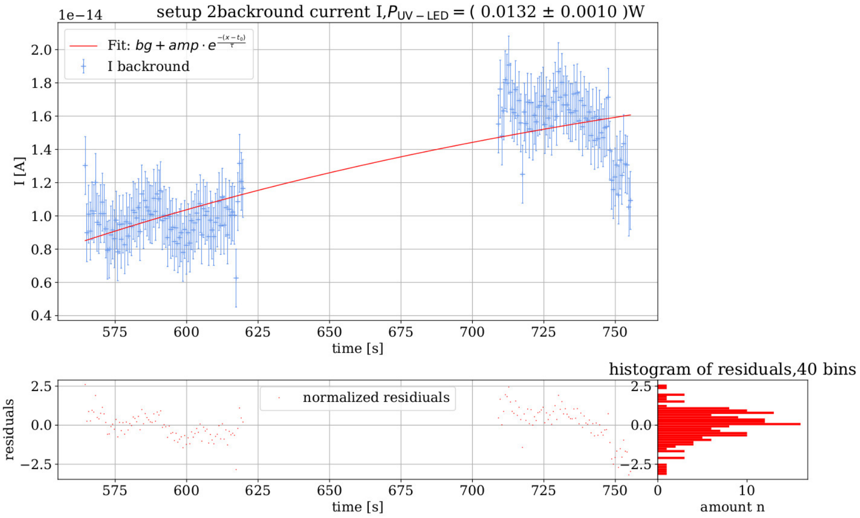

Figure 100: setup 2: background current I for $P_{\mathrm{UV-LED}} = (0.0132 \pm 0.0010)$ W. Fit parameters: $bg = (23.0 \pm 0.4)\mathrm{e}{-15}$ A, $amp = (-5.4 \pm 0.5)\mathrm{e}{-15}$ A, $t_0 = (820 \pm 20)$ s, $\tau = (260 \pm 20)$ s. $\chi^2_{\mathrm{red.}} = 1.00 \pm 0.11$. This fit has already been used to modify the uncertainties of the measured current I to produce a $\chi^2_{\mathrm{red.}} = 1.00$ using formula 16.

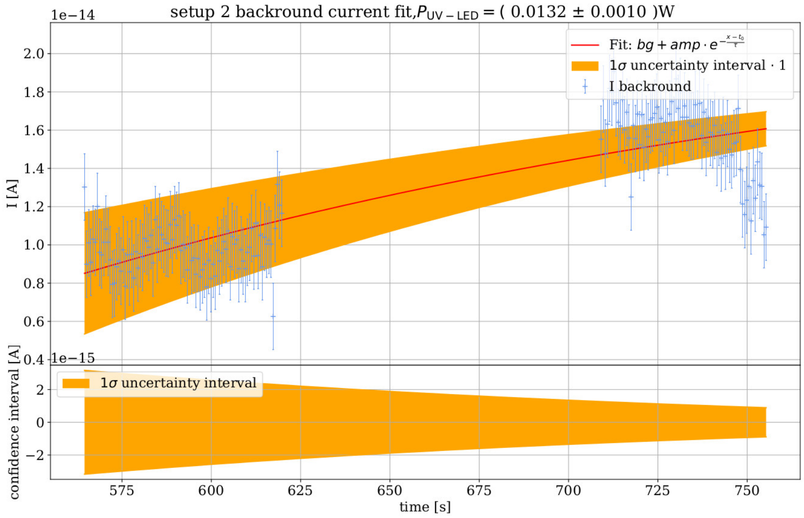

Figure 101: setup 2: background current I for $P_{\mathrm{UV-LED}} = (0.0132 \pm 0.0010)$ W. 1 σ confidence of the background fit function. Fit parameters: $bg = (23.0 \pm 0.4)\mathrm{e}{-15}$ A, $amp = (-5.4 \pm 0.5)\mathrm{e}{-15}$ A, $t_0 = (820 \pm 20)$ s, $\tau = (260 \pm 20)$ s. $\chi^2_{\mathrm{red.}} = 1.00 \pm 0.11$.

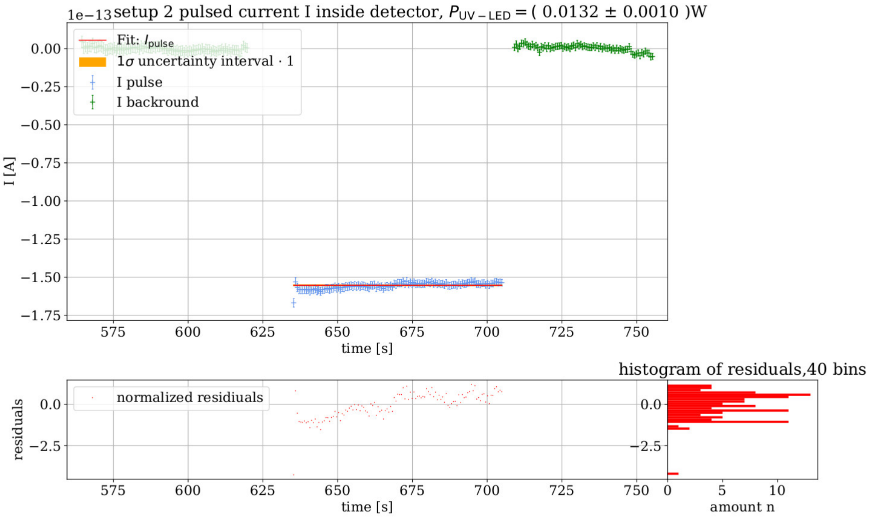

Figure 102: setup 2: background corrected data for the pulse current I_{pulse} with $P_{\text{UV-LED}} = (0.0132 \pm 0.0010)\,\text{A}$. Fit parameters: $I_{\text{pulse}} = (-155.3 \pm 0.2)\text{e}{-15}\,\text{A}$. $\chi^2_{\text{red.}} = 0.61 \pm 0.13$. The uncertainty of the fit parameters was modified by $\sigma(I_{\text{pulse}}) = \sqrt{\sigma(I_{\text{pulse}})^2 \cdot \chi^2_{\text{red.}}}$ so that the uncertainty value is not misrepresented.

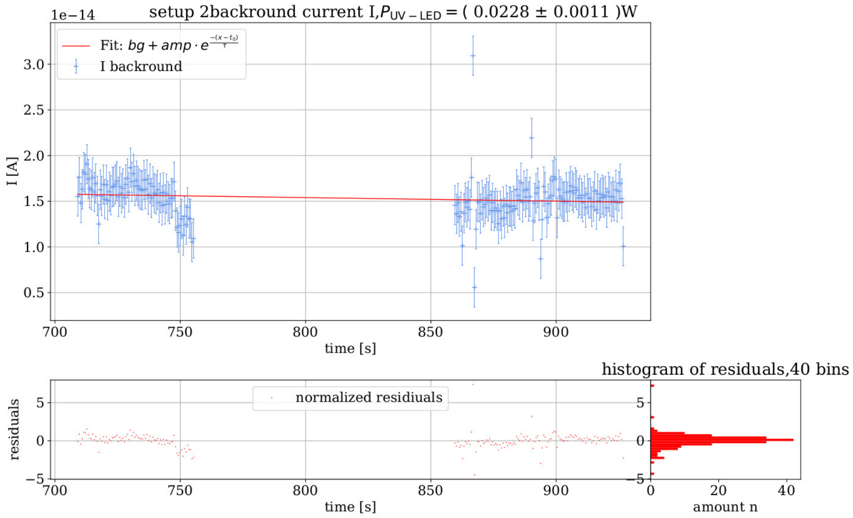

Figure 103: setup 2: background current I for $P_{\text{UV-LED}} = (0.0228 \pm 0.0011)\,\text{W}$. Fit parameters: $bg = (-257.2 \pm 0.5)\text{e}{-15}\,\text{A}$, $amp = (516 \pm 4)\text{e}{-15}\,\text{A}$, $t_0 = (-43.9 \pm 0.3)\text{e}3\,\text{s}$, $\tau = (70.1 \pm 0.5)\text{e}3\,\text{s}$. $\chi^2_{\text{red.}} = 1.00 \pm 0.10$. This fit has already been used to modify the uncertainties of the measured current I to produce a $\chi^2_{\text{red.}} = 1.00$ using formula 16.

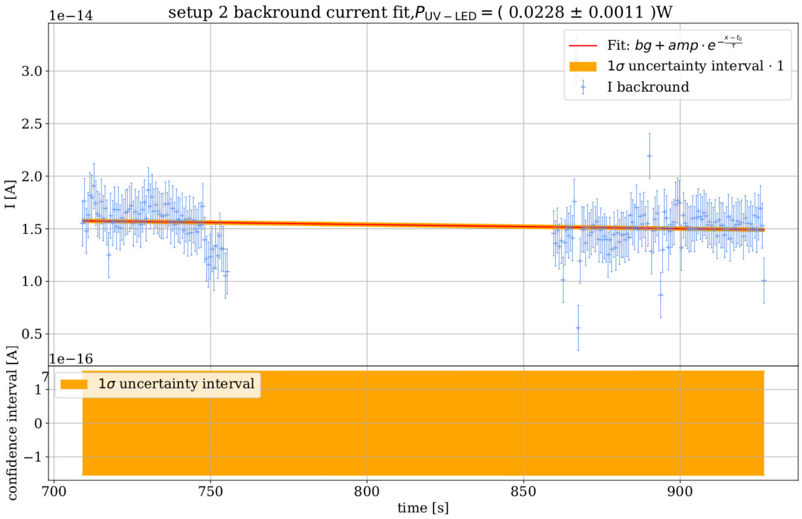

Figure 104: setup 2: background current I for $P_{\mathrm{UV-LED}} = (0.0228 \pm 0.0011)\,\mathrm{W}$. 1 σ confidence of the background fit function. Fit parameters: $bg = (-257.2 \pm 0.5)\mathrm{e}{-15}\,\mathrm{A}$, $amp = (516 \pm 4)\mathrm{e}{-15}\,\mathrm{A}$, $t_0 = (-43.9 \pm 0.3)\mathrm{e}3\,\mathrm{s}$, $\tau = (70.1 \pm 0.5)\mathrm{e}3\,\mathrm{s}$. $\chi^2_{\mathrm{red.}} = 1.00 \pm 0.10$.

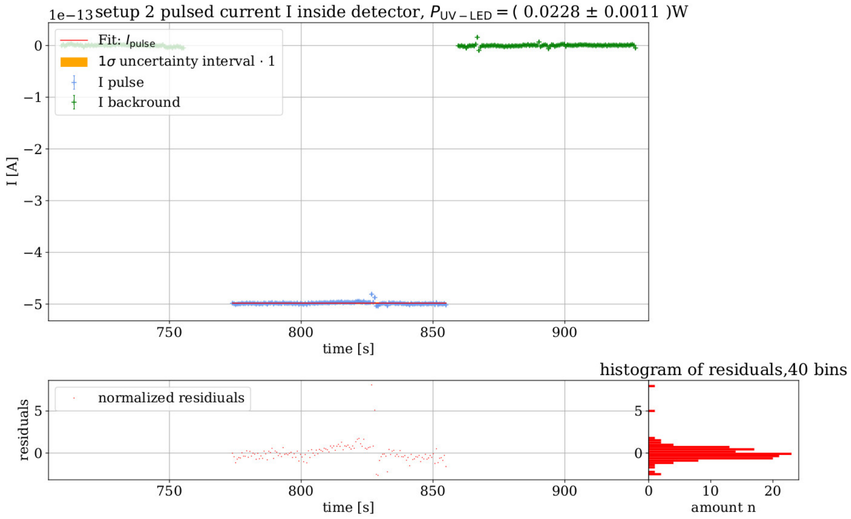

Figure 105: setup 2: background corrected data for the pulse current I_{pulse} with $P_{\mathrm{UV-LED}} = (0.0228 \pm 0.0011)\,\mathrm{A}$. Fit parameters: $I_{\mathrm{pulse}} = (-498.3 \pm 0.2)\mathrm{e}{-15}\,\mathrm{A}$. $\chi^2_{\mathrm{red.}} = 1.22 \pm 0.12$. The uncertainty of the fit parameters was modified by $\sigma(I_{\mathrm{pulse}}) = \sqrt{\sigma(I_{\mathrm{pulse}})^2 \cdot \chi^2_{\mathrm{red.}}}$ so that the uncertainty value is not misrepresented.

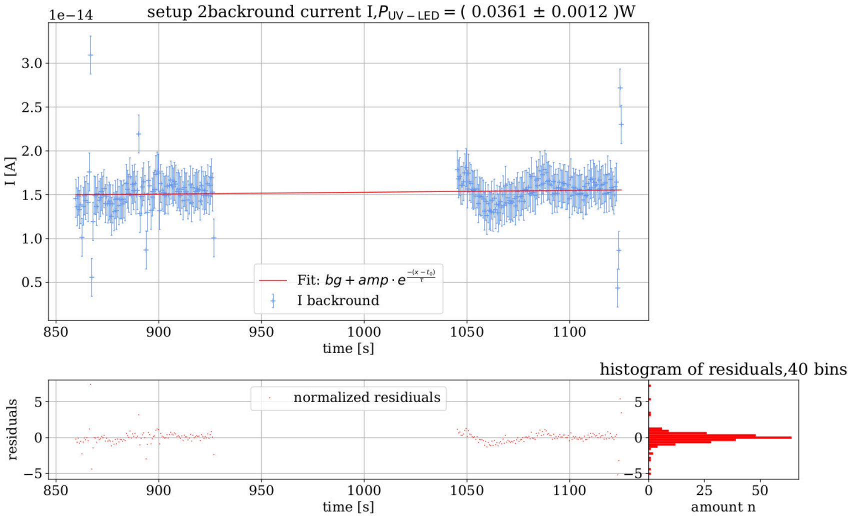

Figure 106: setup 2: background current I for $P_{\mathrm{UV-LED}} = (0.0361 \pm 0.0012)$ W. Fit parameters: $bg = (11.860 \pm 0.002)\mathrm{e}{-12}$ A, $amp = (-22.558 \pm 0.003)\mathrm{e}{-12}$ A, $t_0 = (-3.6823 \pm 0.0008)\mathrm{e}6$ s, $\tau = (5.7174 \pm 0.0013)\mathrm{e}6$ s. $\chi^2_{\mathrm{red.}} = 1.00 \pm 0.09$. This fit has already been used to modify the uncertainties of the measured current I to produce a $\chi^2_{\mathrm{red.}} = 1.00$ using formula 16.

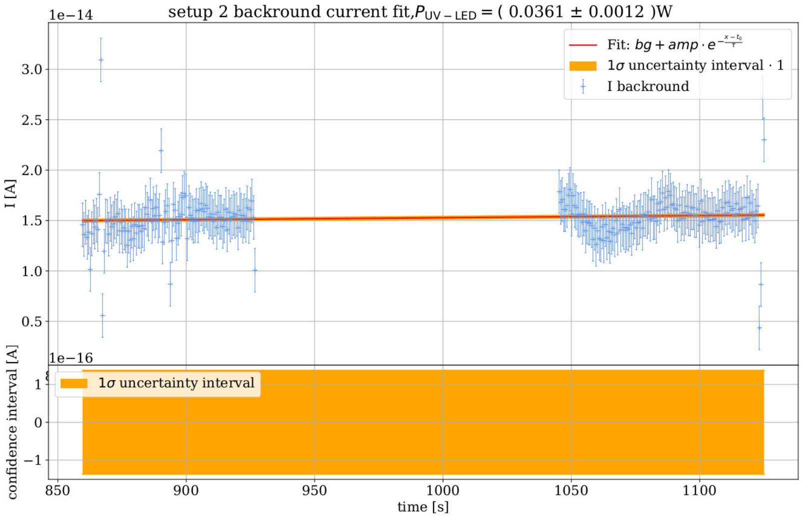

Figure 107: setup 2: background current I for $P_{\mathrm{UV-LED}} = (0.0361 \pm 0.0012)$ W. 1 σ confidence of the background fit function. Fit parameters: $bg = (11.860 \pm 0.002)\mathrm{e}{-12}$ A, $amp = (-22.558 \pm 0.003)\mathrm{e}{-12}$ A, $t_0 = (-3.6823 \pm 0.0008)\mathrm{e}6$ s, $\tau = (5.7174 \pm 0.0013)\mathrm{e}6$ s. $\chi^2_{\mathrm{red.}} = 1.00 \pm 0.09$.

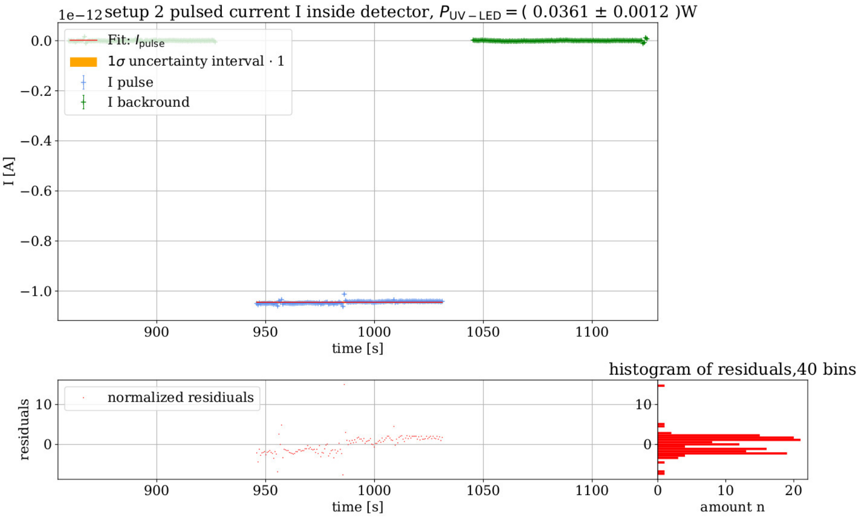

Figure 108: setup 2: background corrected data for the pulse current I_{pulse} with $P_{\text{UV−LED}} = (0.0361 \pm 0.0012)\,\text{A}$. Fit parameters: $I_{\text{pulse}} = (-1.0448 \pm 0.0004)\text{e}{-12}\,\text{A}$. $\chi^2_{\text{red.}} = 5.46 \pm 0.12$. The uncertainty of the fit parameters was modified by $\sigma(I_{\text{pulse}}) = \sqrt{\sigma(I_{\text{pulse}})^2 \cdot \chi^2_{\text{red.}}}$ so that the uncertainty value is not misrepresented.

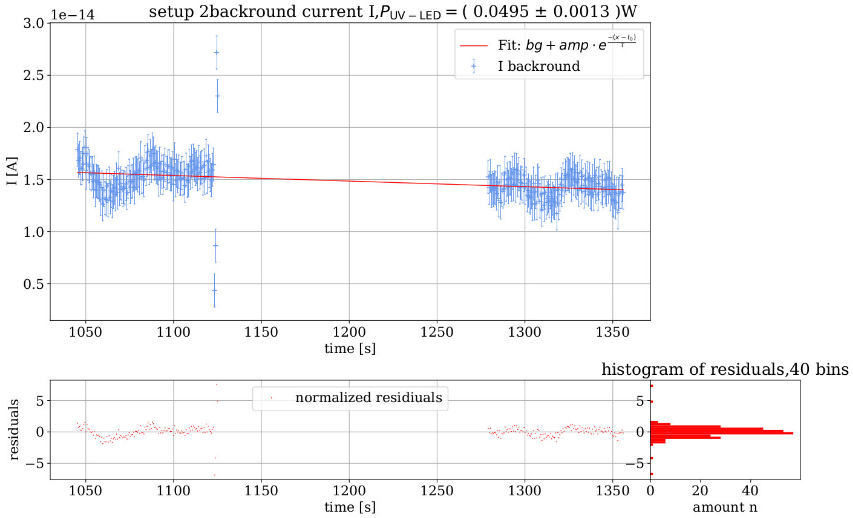

Figure 109: setup 2: background current I for $P_{\text{UV−LED}} = (0.0495 \pm 0.0013)\,\text{W}$. Fit parameters: $bg = (-6.9411 \pm 0.0006)\text{e}{-12}\,\text{A}$, $amp = (2.6121 \pm 0.0005)\text{e}{-12}\,\text{A}$, $t_0 = (1.2748 \pm 0.0002)\text{e}6\,\text{s}$, $\tau = (1.3003 \pm 0.0002)\text{e}6\,\text{s}$. $\chi^2_{\text{red.}} = 1.00 \pm 0.09$. This fit has already been used to modify the uncertainties of the measured current I to produce a $\chi^2_{\text{red.}} = 1.00$ using formula 16.

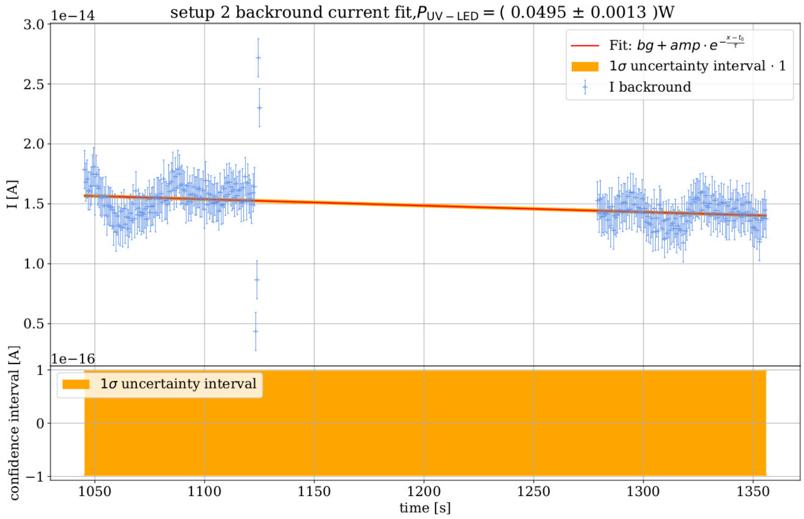

Figure 110: setup 2: background current I for $P_{\mathrm{UV-LED}} = (0.0495 \pm 0.0013)\,\mathrm{W}$. 1 σ confidence of the background fit function. Fit parameters: $bg = (-6.9411 \pm 0.0006)\mathrm{e}{-12}\,\mathrm{A}$, $amp = (2.6121 \pm 0.0005)\mathrm{e}{-12}\,\mathrm{A}$, $t_0 = (1.2748 \pm 0.0002)\mathrm{e}6\,\mathrm{s}$, $\tau = (1.3003 \pm 0.0002)\mathrm{e}6\,\mathrm{s}$. $\chi^2_{\mathrm{red.}} = 1.00 \pm 0.09$.

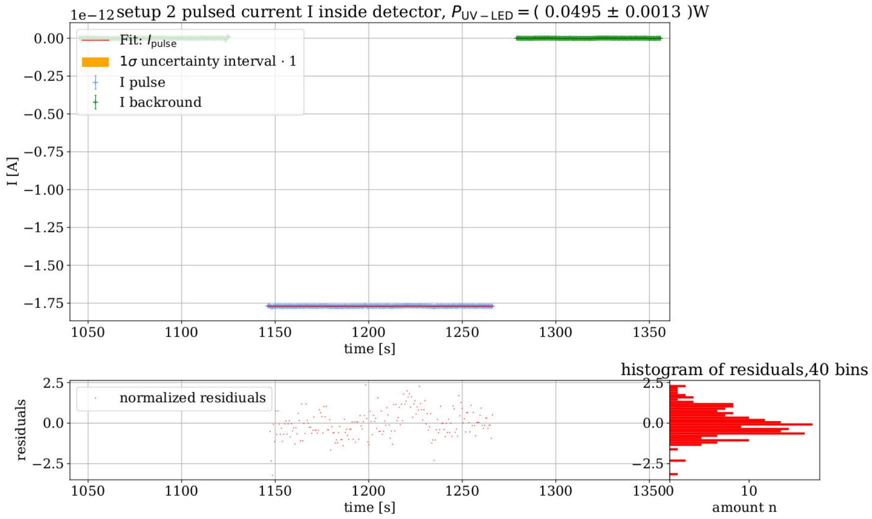

Figure 111: setup 2: background corrected data for the pulse current I_{pulse} with $P_{\mathrm{UV-LED}} = (0.0495 \pm 0.0013)\,\mathrm{A}$. Fit parameters: $I_{\mathrm{pulse}} = (-1.77051 \pm 0.00010)\mathrm{e}{-12}\,\mathrm{A}$. $\chi^2_{\mathrm{red.}} = 0.7 \pm 0.1$. The uncertainty of the fit parameters was modified by $\sigma(I_{\mathrm{pulse}}) = \sqrt{\sigma(I_{\mathrm{pulse}})^2 \cdot \chi^2_{\mathrm{red.}}}$ so that the uncertainty value is not misrepresented.

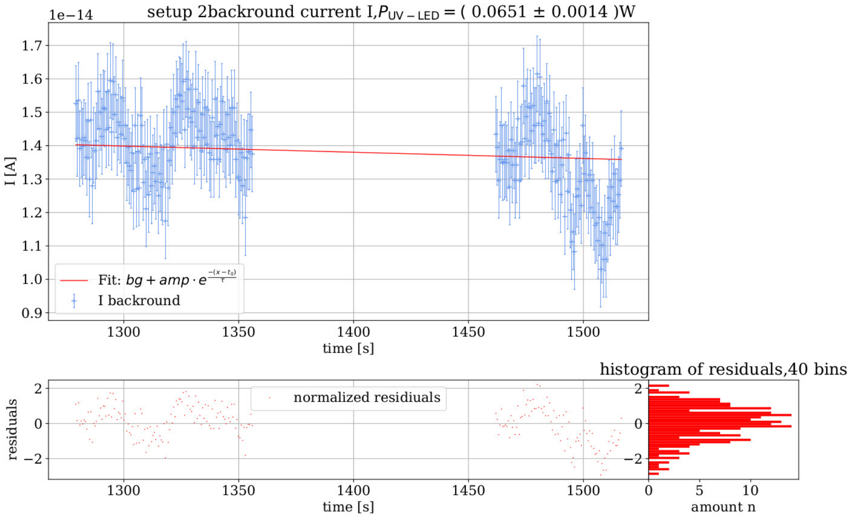

Figure 112: setup 2: background current I for $P_{\mathrm{UV-LED}} = (0.0651 \pm 0.0014)\,\mathrm{W}$. Fit parameters: $bg = (-51.0974 \pm 0.0010)\mathrm{e}{-12}\,\mathrm{A}$, $amp = (99.050 \pm 0.002)\mathrm{e}{-12}\,\mathrm{A}$, $t_0 = (-18.2103 \pm 0.0005)\mathrm{e}6\,\mathrm{s}$, $\tau = (27.5258 \pm 0.0008)\mathrm{e}6\,\mathrm{s}$. $\chi^2_{\mathrm{red.}} = 1.00 \pm 0.10$. This fit has already been used to modify the uncertainties of the measured current I to produce a $\chi^2_{\mathrm{red.}} = 1.00$ using formula 16.

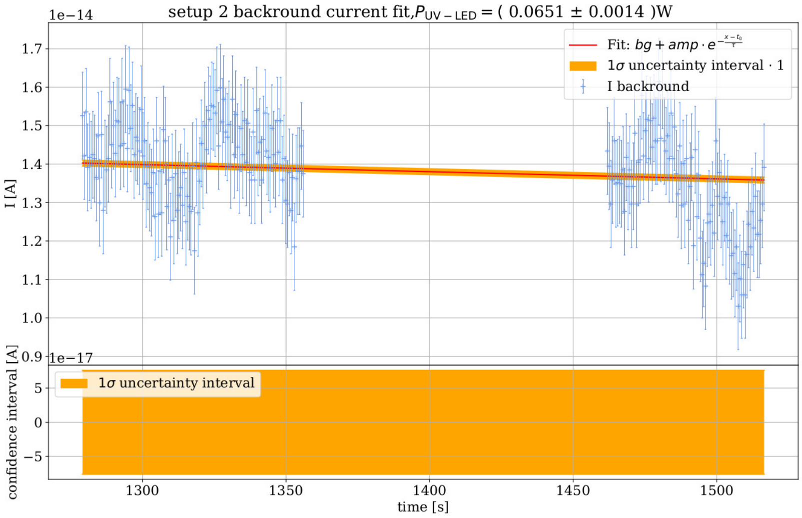

Figure 113: setup 2: background current I for $P_{\mathrm{UV-LED}} = (0.0651 \pm 0.0014)\,\mathrm{W}$. 1 σ confidence of the background fit function. Fit parameters: $bg = (-51.0974 \pm 0.0010)\mathrm{e}{-12}\,\mathrm{A}$, $amp = (99.050 \pm 0.002)\mathrm{e}{-12}\,\mathrm{A}$, $t_0 = (-18.2103 \pm 0.0005)\mathrm{e}6\,\mathrm{s}$, $\tau = (27.5258 \pm 0.0008)\mathrm{e}6\,\mathrm{s}$. $\chi^2_{\mathrm{red.}} = 1.00 \pm 0.10$.

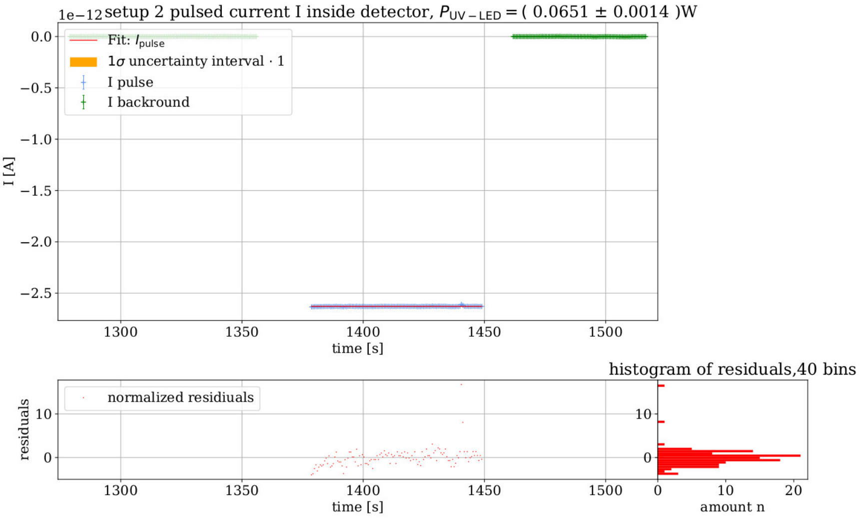

Figure 114: setup 2: background corrected data for the pulse current I_{pulse} with $P_{\text{UV-LED}} = (0.0651 \pm 0.0014)$ A. Fit parameters: $I_{\text{pulse}} = (-2.6285 \pm 0.0002)\text{e}{-12}$ A. $\chi^2_{\text{red.}} = 4.79 \pm 0.13$. The uncertainty of the fit parameters was modified by $\sigma(I_{\text{pulse}}) = \sqrt{\sigma(I_{\text{pulse}})^2 \cdot \chi^2_{\text{red.}}}$ so that the uncertainty value is not misrepresented.

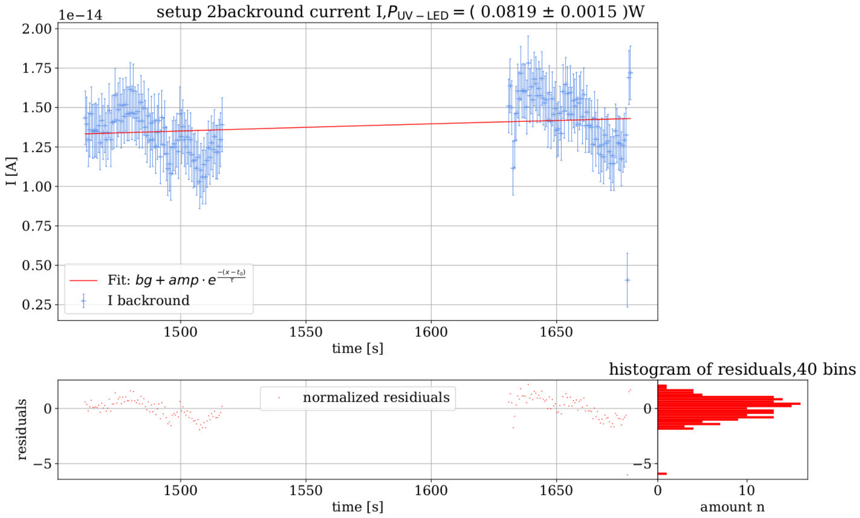

Figure 115: setup 2: background current I for $P_{\text{UV-LED}} = (0.0819 \pm 0.0015)$ W. Fit parameters: $bg = (19 \pm 2)\text{e}{-15}$ A, $amp = (-0.12 \pm 0.02)\text{e}{-12}$ A, $t_0 = (-1.87 \pm 0.13)\text{e}3$ s, $\tau = (1.08 \pm 0.04)\text{e}3$ s. $\chi^2_{\text{red.}} = 1.00 \pm 0.11$. This fit has already been used to modify the uncertainties of the measured current I to produce a $\chi^2_{\text{red.}} = 1.00$ using formula 16.

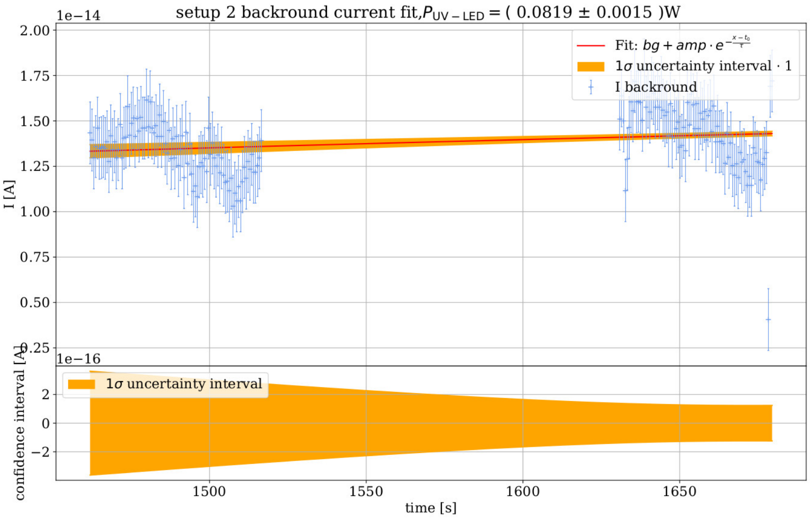

Figure 116: setup 2: background current I for $P_{\mathrm{UV-LED}} = (0.0819 \pm 0.0015)$ W. 1 σ confidence of the background fit function. Fit parameters: $bg = (19 \pm 2)\mathrm{e}{-15}$ A, $amp = (-0.12 \pm 0.02)\mathrm{e}{-12}$ A, $t_0 = (-1.87 \pm 0.13)\mathrm{e}3$ s, $\tau = (1.08 \pm 0.04)\mathrm{e}3$ s. $\chi^2_{\mathrm{red.}} = 1.00 \pm 0.11$.

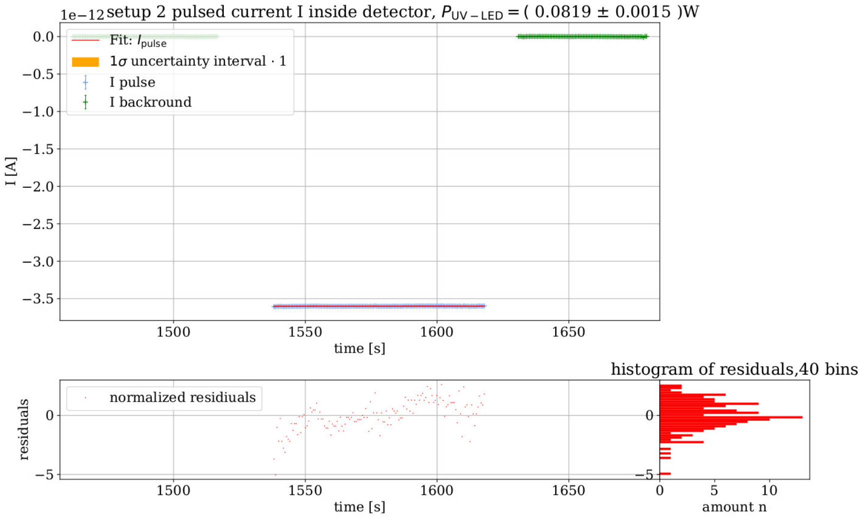

Figure 117: setup 2: background corrected data for the pulse current I_{pulse} with $P_{\mathrm{UV-LED}} = (0.0819 \pm 0.0015)$ A. Fit parameters: $I_{\mathrm{pulse}} = (-3.6001 \pm 0.0002)\mathrm{e}{-12}$ A. $\chi^2_{\mathrm{red.}} = 1.61 \pm 0.12$. The uncertainty of the fit parameters was modified by $\sigma(I_{\mathrm{pulse}}) = \sqrt{\sigma(I_{\mathrm{pulse}})^2 \cdot \chi^2_{\mathrm{red.}}}$ so that the uncertainty value is not misrepresented.

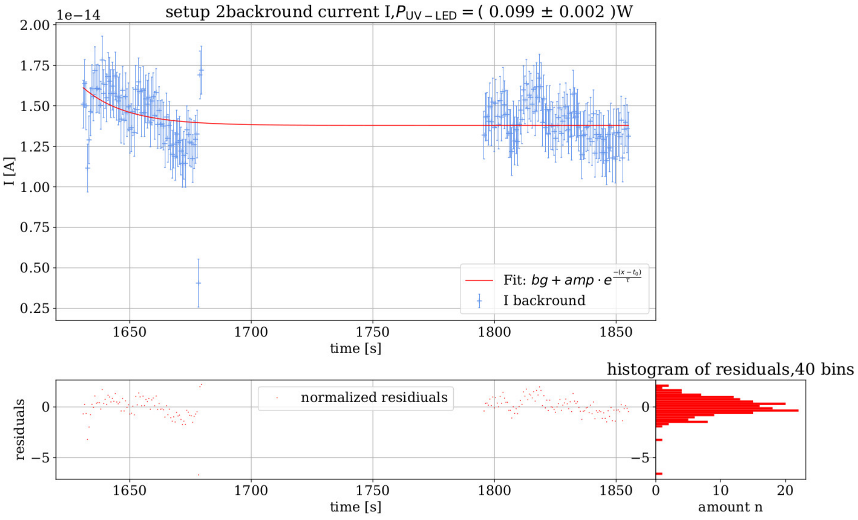

Figure 118: setup 2: background current I for $P_{\mathrm{UV-LED}} = (0.099 \pm 0.002)\,\mathrm{W}$. Fit parameters: $bg = (13.79 \pm 0.03)\mathrm{e}{-15}\,\mathrm{A}$, $amp = (3 \pm 3)\mathrm{e}{-15}\,\mathrm{A}$, $t_0 = (1.625 \pm 0.014)\mathrm{e}3\,\mathrm{s}$, $\tau = (18 \pm 10)\,\mathrm{s}$. $\chi^2_{\mathrm{red.}} = 1.00 \pm 0.11$. This fit has already been used to modify the uncertainties of the measured current I to produce a $\chi^2_{\mathrm{red.}} = 1.00$ using formula 16.

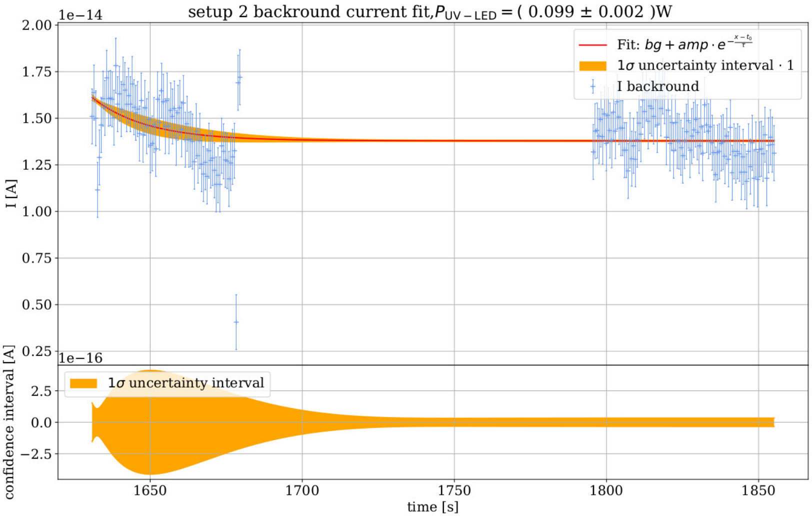

Figure 119: setup 2: background current I for $P_{\mathrm{UV-LED}} = (0.099 \pm 0.002)\,\mathrm{W}$. 1 σ confidence of the background fit function.Fit parameters: $bg = (13.79 \pm 0.03)\mathrm{e}{-15}\,\mathrm{A}$, $amp = (3 \pm 3)\mathrm{e}{-15}\,\mathrm{A}$, $t_0 = (1.625 \pm 0.014)\mathrm{e}3\,\mathrm{s}$, $\tau = (18 \pm 10)\,\mathrm{s}$. $\chi^2_{\mathrm{red.}} = 1.00 \pm 0.11$.

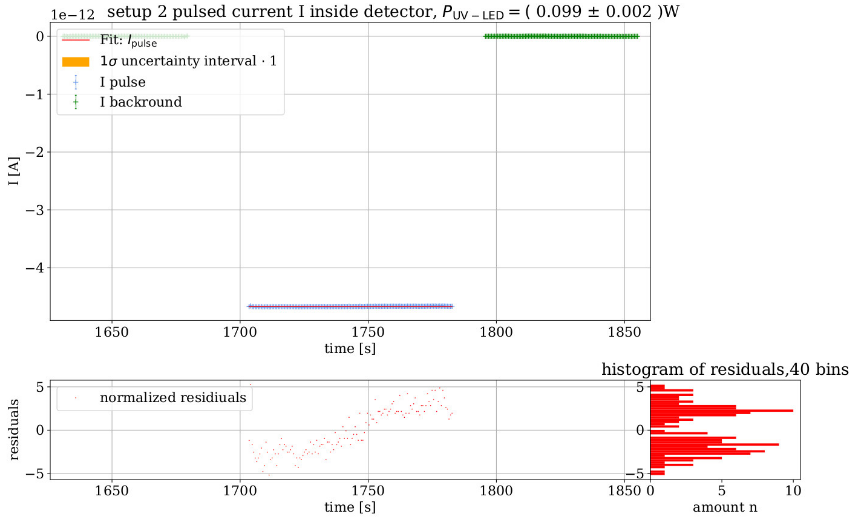

Figure 120: setup 2: background corrected data for the pulse current I_{pulse} with $P_{\text{UV-LED}} = (0.099 \pm 0.002)$ A. Fit parameters: $I_{\text{pulse}} = (-4.6678 \pm 0.0003)\text{e}{-12}$ A. $\chi^2_{\text{red.}} = 6.66 \pm 0.12$. The uncertainty of the fit parameters was modified by $\sigma(I_{\text{pulse}}) = \sqrt{\sigma(I_{\text{pulse}})^2 \cdot \chi^2_{\text{red.}}}$ so that the uncertainty value is not misrepresented.

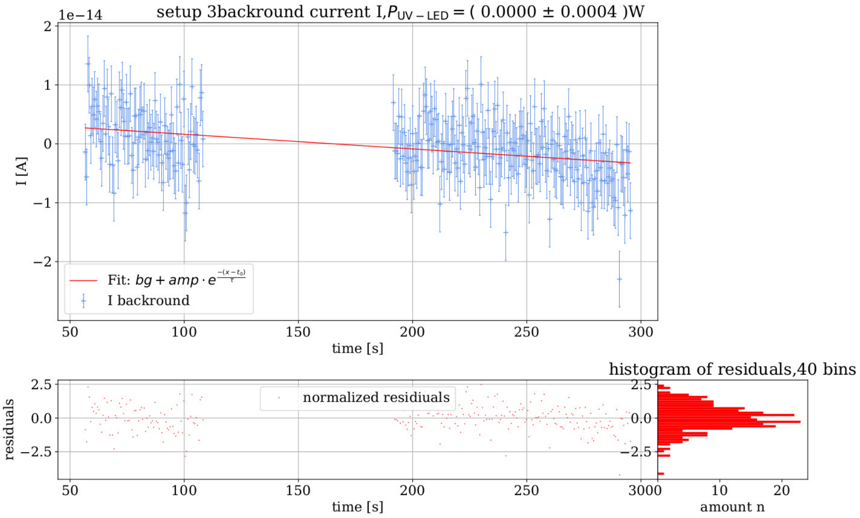

Figure 121: setup 3: background current I for $P_{\text{UV-LED}} = (0.0000 \pm 0.0004)$ W. Fit parameters: $bg = (-54.818 \pm 0.003)\text{e}{-12}$ A, $amp = (21.559 \pm 0.002)\text{e}{-12}$ A, $t_0 = (2.05744 \pm 0.00014)\text{e}6$ s, $\tau = (2.2045 \pm 0.0002)\text{e}6$ s. $\chi^2_{\text{red.}} = 1.00 \pm 0.09$. This fit has already been used to modify the uncertainties of the measured current I to produce a $\chi^2_{\text{red.}} = 1.00$ using formula 16.

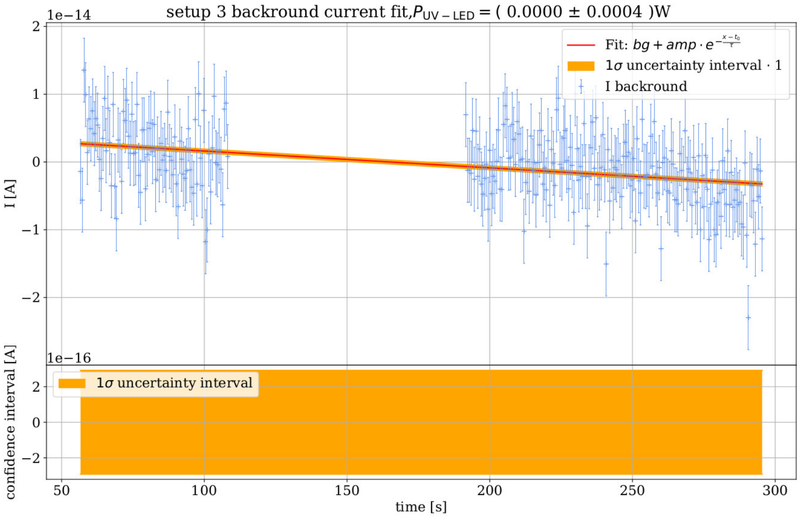

Figure 122: setup 3: background current I for $P_{\mathrm{UV-LED}} = (0.0000 \pm 0.0004)\,\mathrm{W}$. 1 σ confidence of the background fit function.Fit parameters: $bg = (-54.818 \pm 0.003)\mathrm{e}{-12}\,\mathrm{A}$, $amp = (21.559 \pm 0.002)\mathrm{e}{-12}\,\mathrm{A}$, $t_0 = (2.05744 \pm 0.00014)\mathrm{e}6\,\mathrm{s}$, $\tau = (2.2045 \pm 0.0002)\mathrm{e}6\,\mathrm{s}$. $\chi^2_{\mathrm{red.}} = 1.00 \pm 0.09$.

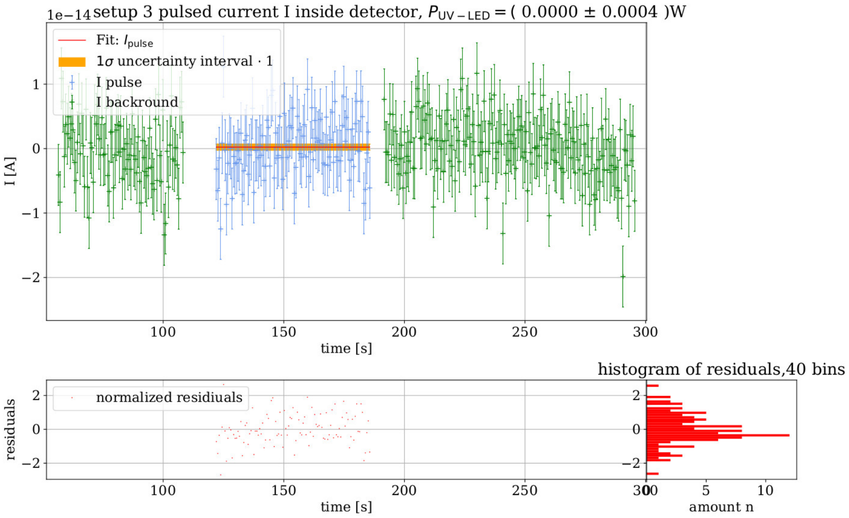

Figure 123: setup 3: background corrected data for the pulse current I_{pulse} with $P_{\mathrm{UV-LED}} = (0.0000 \pm 0.0004)\,\mathrm{A}$. Fit parameters: $I_{\mathrm{pulse}} = (0.2 \pm 0.4)\mathrm{e}{-15}\,\mathrm{A}$. $\chi^2_{\mathrm{red.}} = 0.85 \pm 0.14$. The uncertainty of the fit parameters was modified by $\sigma(I_{\mathrm{pulse}}) = \sqrt{\sigma(I_{\mathrm{pulse}})^2 \cdot \chi^2_{\mathrm{red.}}}$ so that the uncertainty value is not misrepresented.

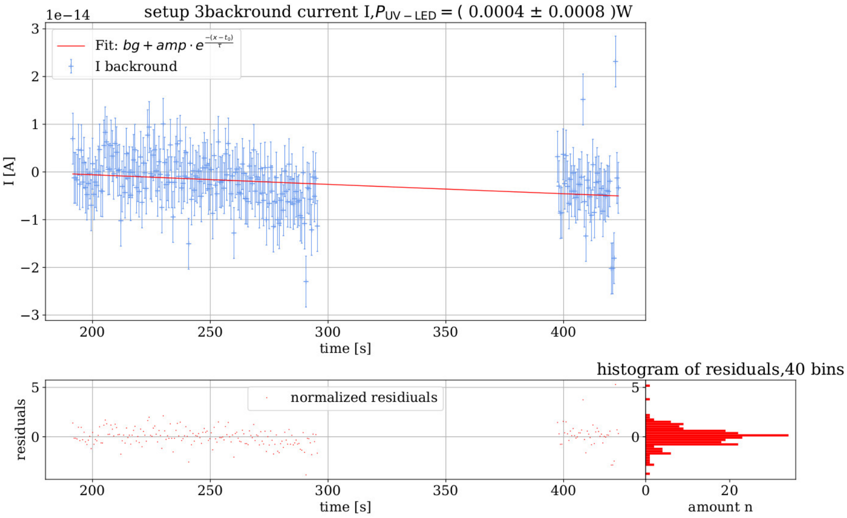

Figure 124: setup 3: background current I for $P_{\mathrm{UV-LED}} = (0.0004 \pm 0.0008)\,\mathrm{W}$. Fit parameters: $bg = (-82.7 \pm 0.7)\mathrm{e}{-15}\,\mathrm{A}$, $amp = (88 \pm 5)\mathrm{e}{-15}\,\mathrm{A}$, $t_0 = (-0.07 \pm 0.13)\mathrm{e}3\,\mathrm{s}$, $\tau = (4.0 \pm 1.4)\mathrm{e}3\,\mathrm{s}$. $\chi^2_{\mathrm{red.}} = 1.00 \pm 0.10$. This fit has already been used to modify the uncertainties of the measured current I to produce a $\chi^2_{\mathrm{red.}} = 1.00$ using formula 16.

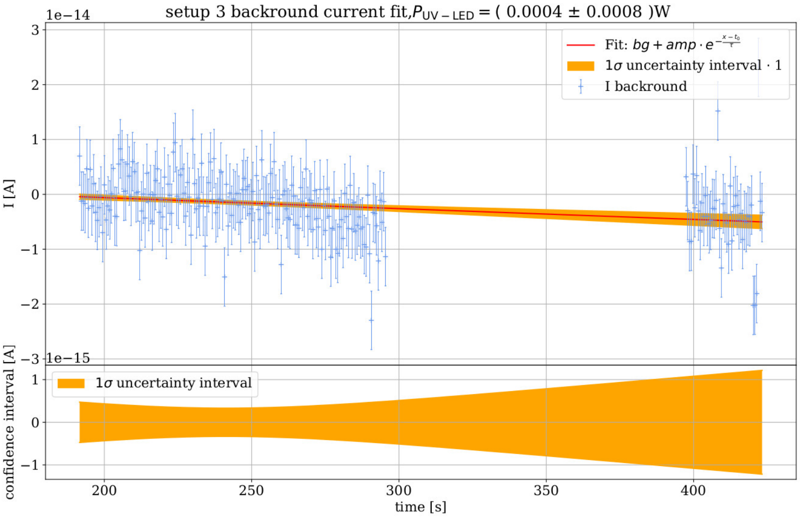

Figure 125: setup 3: background current I for $P_{\mathrm{UV-LED}} = (0.0004 \pm 0.0008)\,\mathrm{W}$. 1 σ confidence of the background fit function.Fit parameters: $bg = (-82.7 \pm 0.7)\mathrm{e}{-15}\,\mathrm{A}$, $amp = (88 \pm 5)\mathrm{e}{-15}\,\mathrm{A}$, $t_0 = (-0.07 \pm 0.13)\mathrm{e}3\,\mathrm{s}$, $\tau = (4.0 \pm 1.4)\mathrm{e}3\,\mathrm{s}$. $\chi^2_{\mathrm{red.}} = 1.00 \pm 0.10$.

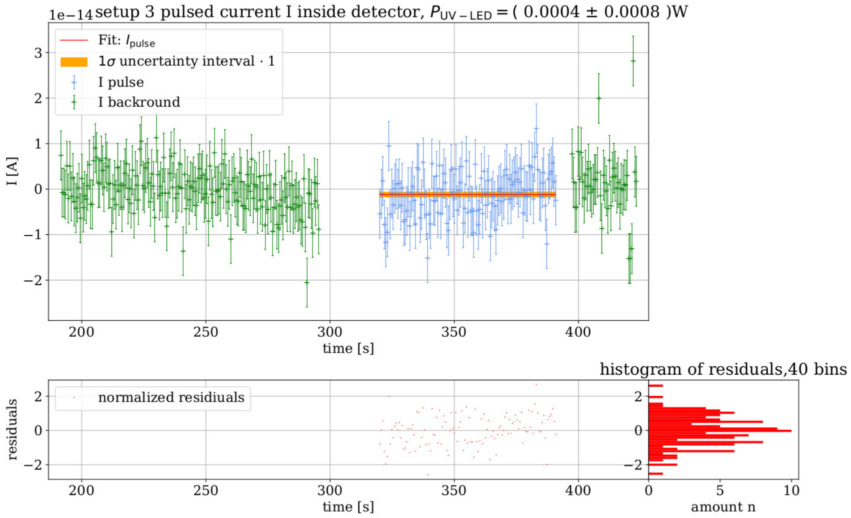

Figure 126: setup 3: background corrected data for the pulse current I_{pulse} with $P_{\text{UV−LED}} = (0.0004 \pm 0.0008)\,\text{A}$. Fit parameters: $I_{\text{pulse}} = (-1.2 \pm 0.4)\text{e}{-15}\,\text{A}$. $\chi^2_{\text{red.}} = 0.82 \pm 0.13$. The uncertainty of the fit parameters was modified by $\sigma(I_{\text{pulse}}) = \sqrt{\sigma(I_{\text{pulse}})^2 \cdot \chi^2_{\text{red.}}}$ so that the uncertainty value is not misrepresented.

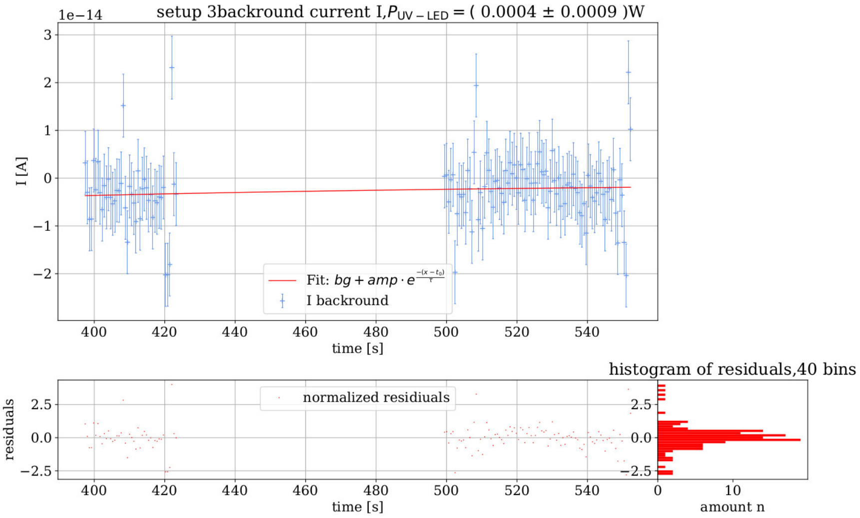

Figure 127: setup 3: background current I for $P_{\text{UV−LED}} = (0.0004 \pm 0.0009)\,\text{W}$. Fit parameters: $bg = (-1 \pm 2)\text{e}{-15}\,\text{A}$, $amp = (-0.04 \pm 0.12)\text{e}{-9}\,\text{A}$, $t_0 = (-1.2 \pm 0.6)\text{e}3\,\text{s}$, $\tau = (160 \pm 60)\,\text{s}$. $\chi^2_{\text{red.}} = 1.00 \pm 0.12$. This fit has already been used to modify the uncertainties of the measured current I to produce a $\chi^2_{\text{red.}} = 1.00$ using formula 16.

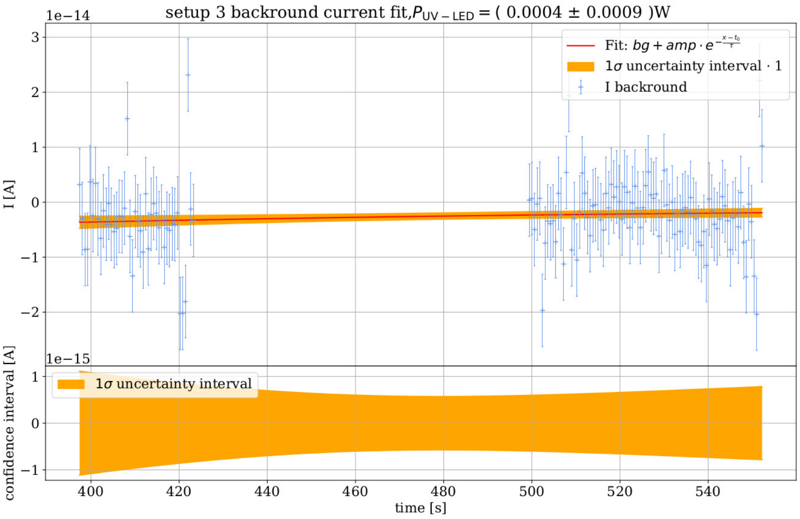

Figure 128: setup 3: background current I for $P_{\mathrm{UV-LED}} = (0.0004 \pm 0.0009)\,\mathrm{W}$. 1 σ confidence of the background fit function.Fit parameters: $bg = (-1 \pm 2)\mathrm{e}{-15}\,\mathrm{A}$, $amp = (-0.04 \pm 0.12)\mathrm{e}{-9}\,\mathrm{A}$, $t_0 = (-1.2 \pm 0.6)\mathrm{e}3\,\mathrm{s}$, $\tau = (160 \pm 60)\,\mathrm{s}$. $\chi^2_{\mathrm{red.}} = 1.00 \pm 0.12$.

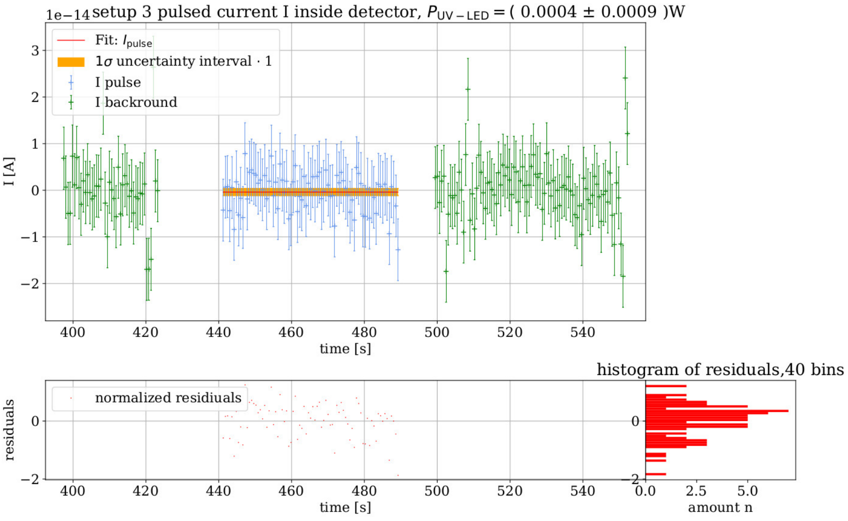

Figure 129: setup 3: background corrected data for the pulse current I_{pulse} with $P_{\mathrm{UV-LED}} = (0.0004 \pm 0.0009)\,\mathrm{A}$. Fit parameters: $I_{\mathrm{pulse}} = (-0.4 \pm 0.4)\mathrm{e}{-15}\,\mathrm{A}$. $\chi^2_{\mathrm{red.}} = 0.3 \pm 0.2$. The uncertainty of the fit parameters was modified by $\sigma(I_{\mathrm{pulse}}) = \sqrt{\sigma(I_{\mathrm{pulse}})^2 \cdot \chi^2_{\mathrm{red.}}}$ so that the uncertainty value is not misrepresented.

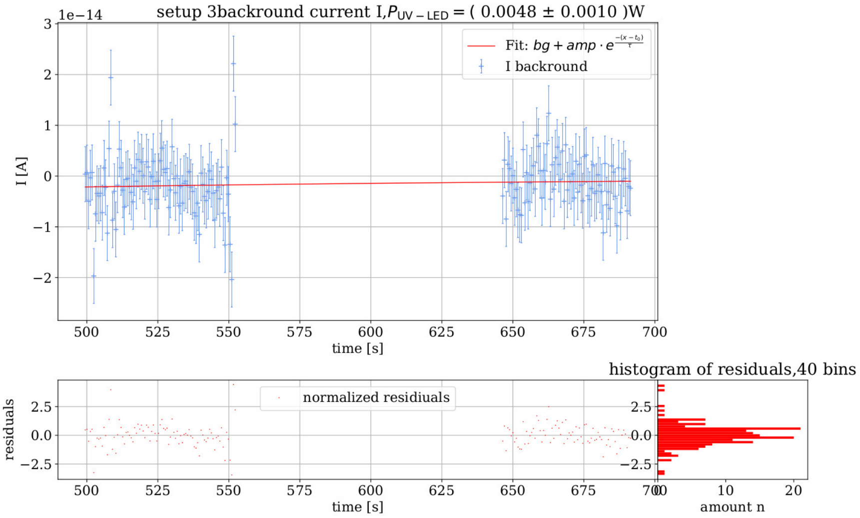

Figure 130: setup 3: background current I for $P_{\mathrm{UV-LED}} = (0.0048 \pm 0.0010)$ W. Fit parameters: $bg = (0 \pm 2)\mathrm{e}{-15}$ A, $amp = (-0.01 \pm 0.02)\mathrm{e}{-12}$ A, $t_0 = (0.2 \pm 0.4)\mathrm{e}3$ s, $\tau = (0.2 \pm 0.2)\mathrm{e}3$ s. $\chi^2_{\mathrm{red.}} = 1.00 \pm 0.11$. This fit has already been used to modify the uncertainties of the measured current I to produce a $\chi^2_{\mathrm{red.}} = 1.00$ using formula 16.

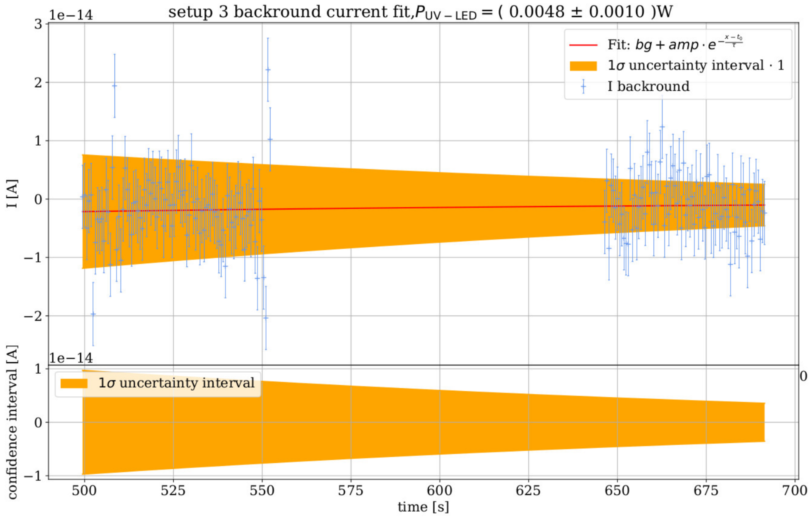

Figure 131: setup 3: background current I for $P_{\mathrm{UV-LED}} = (0.0048 \pm 0.0010)$ W. 1 σ confidence of the background fit function.Fit parameters: $bg = (0 \pm 2)\mathrm{e}{-15}$ A, $amp = (-0.01 \pm 0.02)\mathrm{e}{-12}$ A, $t_0 = (0.2 \pm 0.4)\mathrm{e}3$ s, $\tau = (0.2 \pm 0.2)\mathrm{e}3$ s. $\chi^2_{\mathrm{red.}} = 1.00 \pm 0.11$.

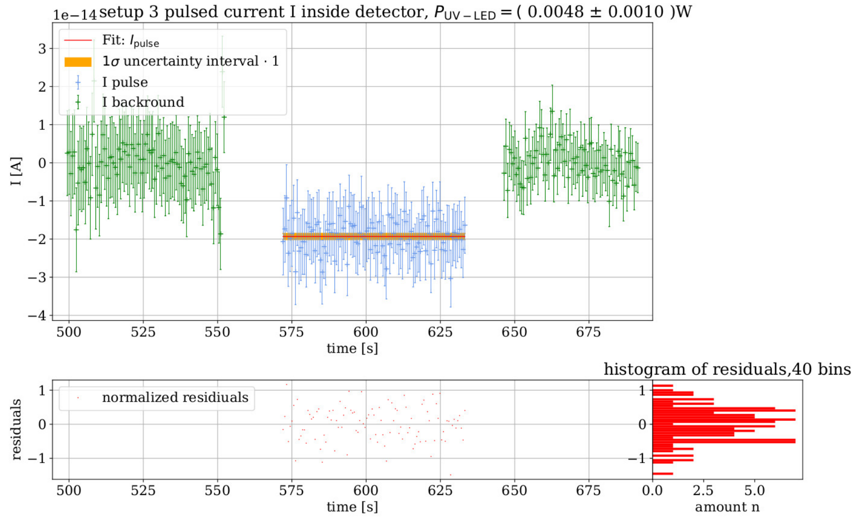

Figure 132: setup 3: background corrected data for the pulse current I_{pulse} with $P_{\mathrm{UV-LED}} = (0.0048 \pm 0.0010)\,\mathrm{A}$. Fit parameters: $I_{\mathrm{pulse}} = (-19.3 \pm 0.4)\mathrm{e}{-15}\,\mathrm{A}$. $\chi^2_{\mathrm{red.}} = 0.26 \pm 0.14$. The uncertainty of the fit parameters was modified by $\sigma(I_{\mathrm{pulse}}) = \sqrt{\sigma(I_{\mathrm{pulse}})^2 \cdot \chi^2_{\mathrm{red.}}}$ so that the uncertainty value is not misrepresented.

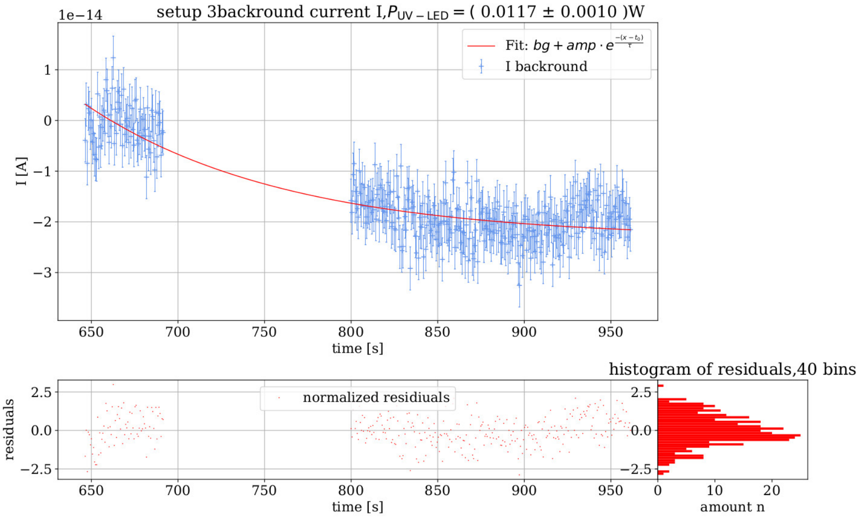

Figure 133: setup 3: background current I for $P_{\mathrm{UV-LED}} = (0.0117 \pm 0.0010)\,\mathrm{W}$. Fit parameters: $bg = (-23.3 \pm 0.2)\mathrm{e}{-15}\,\mathrm{A}$, $amp = (17 \pm 4)\mathrm{e}{-15}\,\mathrm{A}$, $t_0 = (700 \pm 30)\,\mathrm{s}$, $\tau = (115 \pm 7)\,\mathrm{s}$. $\chi^2_{\mathrm{red.}} = 1.00 \pm 0.08$. This fit has already been used to modify the uncertainties of the measured current I to produce a $\chi^2_{\mathrm{red.}} = 1.00$ using formula 16.

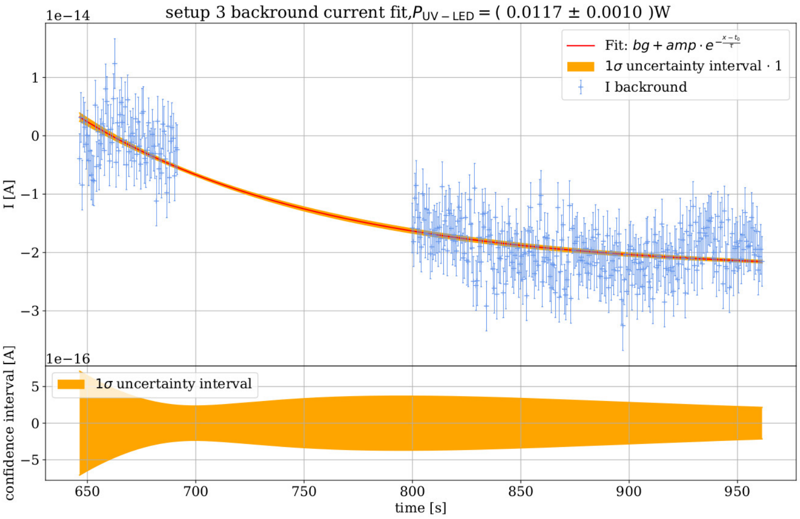

Figure 134: setup 3: background current I for $P_{\mathrm{UV-LED}} = (0.0117 \pm 0.0010)$ W. 1 σ confidence of the background fit function. Fit parameters: $bg = (-23.3 \pm 0.2)\mathrm{e}{-15}$ A, $amp = (17 \pm 4)\mathrm{e}{-15}$ A, $t_0 = (700 \pm 30)$ s, $\tau = (115 \pm 7)$ s. $\chi^2_{\mathrm{red.}} = 1.00 \pm 0.08$.

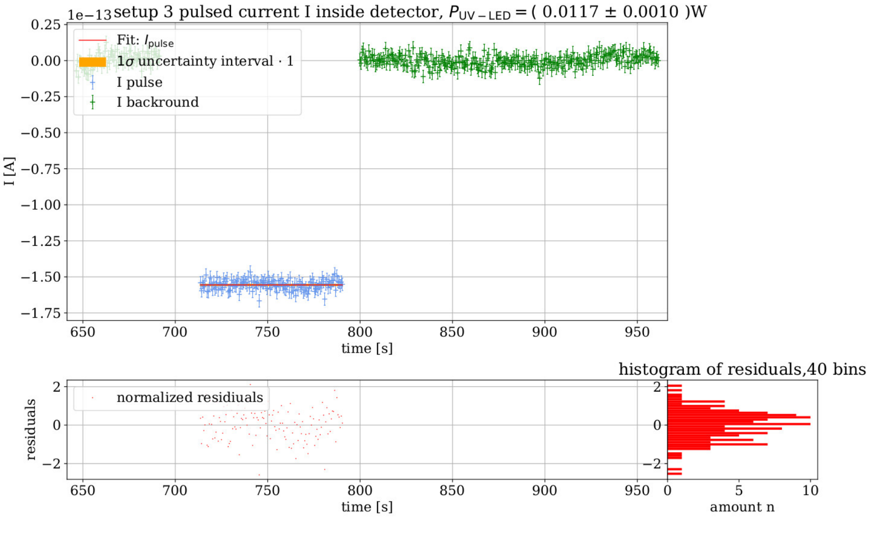

Figure 135: setup 3: background corrected data for the pulse current I_{pulse} with $P_{\mathrm{UV-LED}} = (0.0117 \pm 0.0010)$ A. Fit parameters: $I_{\mathrm{pulse}} = (-155.6 \pm 0.3)\mathrm{e}{-15}$ A. $\chi^2_{\mathrm{red.}} = 0.65 \pm 0.13$. The uncertainty of the fit parameters was modified by $\sigma(I_{\mathrm{pulse}}) = \sqrt{\sigma(I_{\mathrm{pulse}})^2 \cdot \chi^2_{\mathrm{red.}}}$ so that the uncertainty value is not misrepresented.

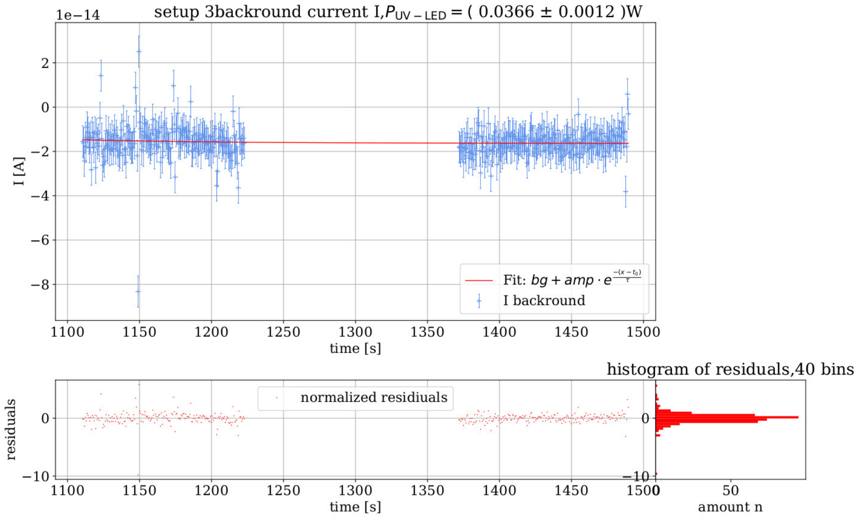

Figure 136: setup 3: background current I for $P_{\mathrm{UV-LED}} = (0.0366 \pm 0.0012)\,\mathrm{W}$. Fit parameters: $bg = (-16.4 \pm 0.5)\mathrm{e}{-15}\,\mathrm{A}$, $amp = (1 \pm 5)\mathrm{e}{-6}\,\mathrm{A}$, $t_0 = (-0.9 \pm 0.7)\mathrm{e}3\,\mathrm{s}$, $\tau = (100 \pm 30)\,\mathrm{s}$. $\chi^2_{\mathrm{red.}} = 1.00 \pm 0.07$. This fit has already been used to modify the uncertainties of the measured current I to produce a $\chi^2_{\mathrm{red.}} = 1.00$ using formula 16.

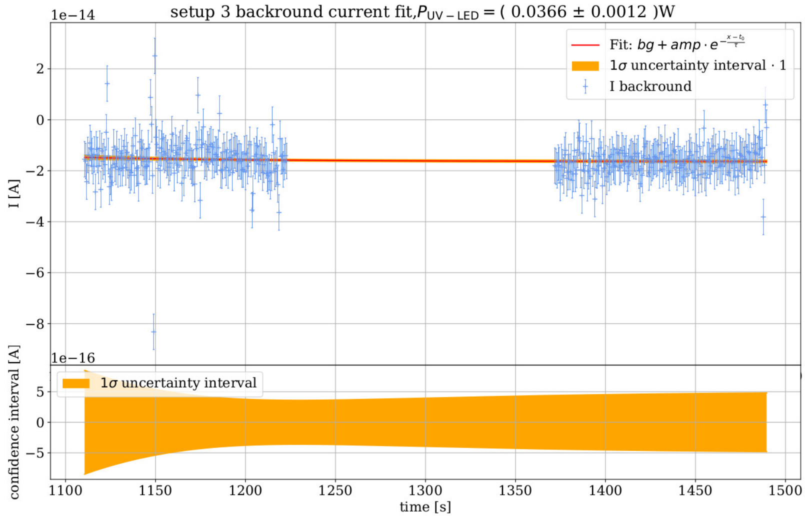

Figure 137: setup 3: background current I for $P_{\mathrm{UV-LED}} = (0.0366 \pm 0.0012)\,\mathrm{W}$. 1 σ confidence of the background fit function. Fit parameters: $bg = (-16.4 \pm 0.5)\mathrm{e}{-15}\,\mathrm{A}$, $amp = (1 \pm 5)\mathrm{e}{-6}\,\mathrm{A}$, $t_0 = (-0.9 \pm 0.7)\mathrm{e}3\,\mathrm{s}$, $\tau = (100 \pm 30)\,\mathrm{s}$. $\chi^2_{\mathrm{red.}} = 1.00 \pm 0.07$.

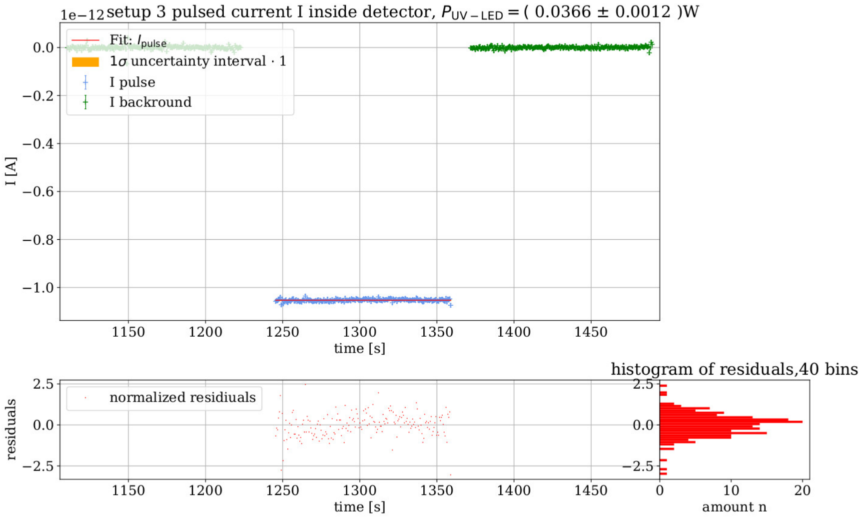

Figure 138: setup 3: background corrected data for the pulse current I_{pulse} with $P_{\text{UV−LED}} = (0.0366 \pm 0.0012)$ A. Fit parameters: $I_{\text{pulse}} = (-1.0530 \pm 0.0004)\text{e}{-12}$ A. $\chi^2_{\text{red.}} = 0.52 \pm 0.10$. The uncertainty of the fit parameters was modified by $\sigma(I_{\text{pulse}}) = \sqrt{\sigma(I_{\text{pulse}})^2 \cdot \chi^2_{\text{red.}}}$ so that the uncertainty value is not misrepresented.

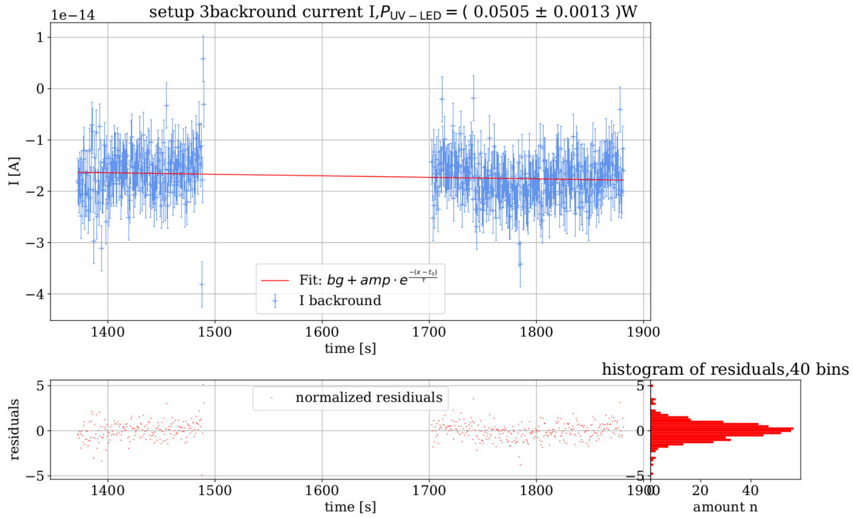

Figure 139: setup 3: background current I for $P_{\text{UV−LED}} = (0.0505 \pm 0.0013)$ W. Fit parameters: $bg = (-2.591 \pm 0.003)\text{e}{-12}$ A, $amp = (52.12 \pm 0.05)\text{e}{-9}$ A, $t_0 = (-8.5922 \pm 0.0009)\text{e}6$ s, $\tau = (866.68 \pm 0.09)\text{e}3$ s. $\chi^2_{\text{red.}} = 1.00 \pm 0.06$. This fit has already been used to modify the uncertainties of the measured current I to produce a $\chi^2_{\text{red.}} = 1.00$ using formula 16.

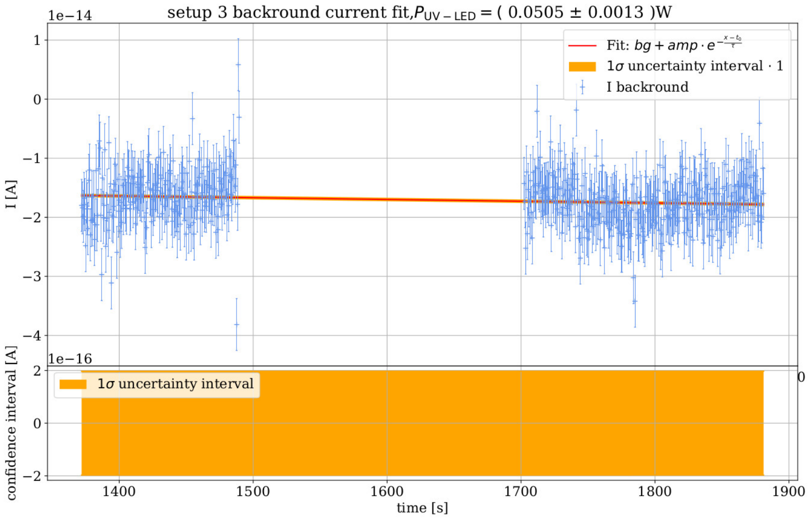

Figure 140: setup 3: background current I for $P_{\mathrm{UV-LED}} = (0.0505 \pm 0.0013)\,\mathrm{W}$. 1 σ confidence of the background fit function. Fit parameters: $bg = (-2.591 \pm 0.003)\mathrm{e}{-12}\,\mathrm{A}$, $amp = (52.12 \pm 0.05)\mathrm{e}{-9}\,\mathrm{A}$, $t_0 = (-8.5922 \pm 0.0009)\mathrm{e}6\,\mathrm{s}$, $\tau = (866.68 \pm 0.09)\mathrm{e}3\,\mathrm{s}$. $\chi^2_{\mathrm{red.}} = 1.00 \pm 0.06$.

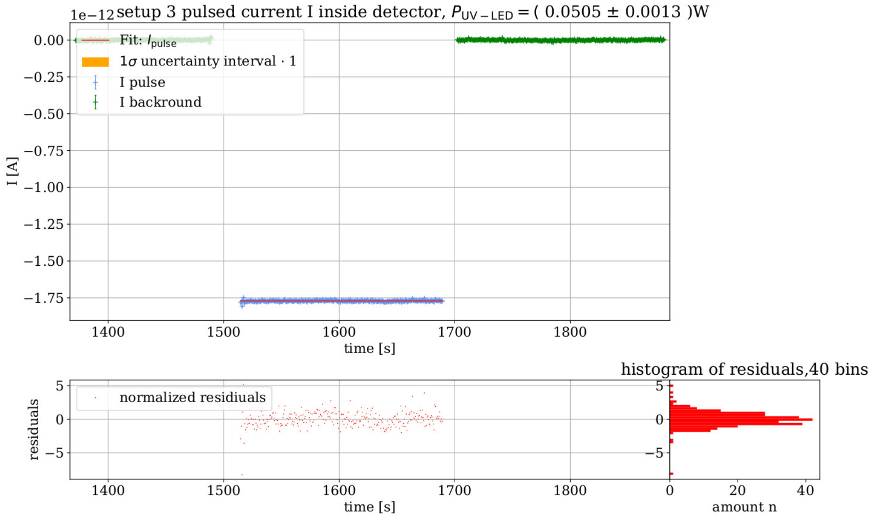

Figure 141: setup 3: background corrected data for the pulse current I_{pulse} with $P_{\mathrm{UV-LED}} = (0.0505 \pm 0.0013)\,\mathrm{A}$. Fit parameters: $I_{\mathrm{pulse}} = (-1.7713 \pm 0.0003)\mathrm{e}{-12}\,\mathrm{A}$. $\chi^2_{\mathrm{red.}} = 1.33 \pm 0.08$. The uncertainty of the fit parameters was modified by $\sigma(I_{\mathrm{pulse}}) = \sqrt{\sigma(I_{\mathrm{pulse}})^2 \cdot \chi^2_{\mathrm{red.}}}$ so that the uncertainty value is not misrepresented.

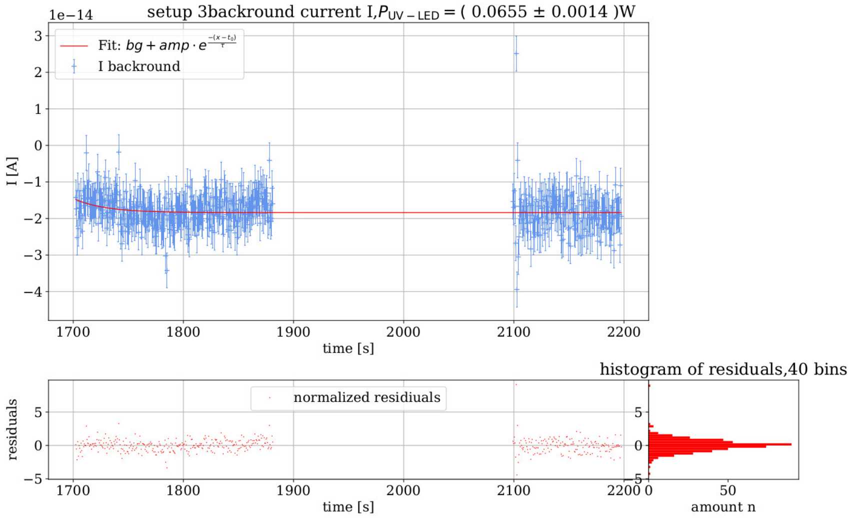

Figure 142: setup 3: background current I for $P_{\mathrm{UV-LED}} = (0.0655 \pm 0.0014)\,\mathrm{W}$. Fit parameters: $bg = (-18.39 \pm 0.06)\mathrm{e}{-15}\,\mathrm{A}$, $amp = (2 \pm 4)\mathrm{e}{-15}\,\mathrm{A}$, $t_0 = (1.71 \pm 0.05)\mathrm{e}3\,\mathrm{s}$, $\tau = (28 \pm 10)\,\mathrm{s}$. $\chi^2_{\mathrm{red.}} = 1.00 \pm 0.07$. This fit has already been used to modify the uncertainties of the measured current I to produce a $\chi^2_{\mathrm{red.}} = 1.00$ using formula 16.

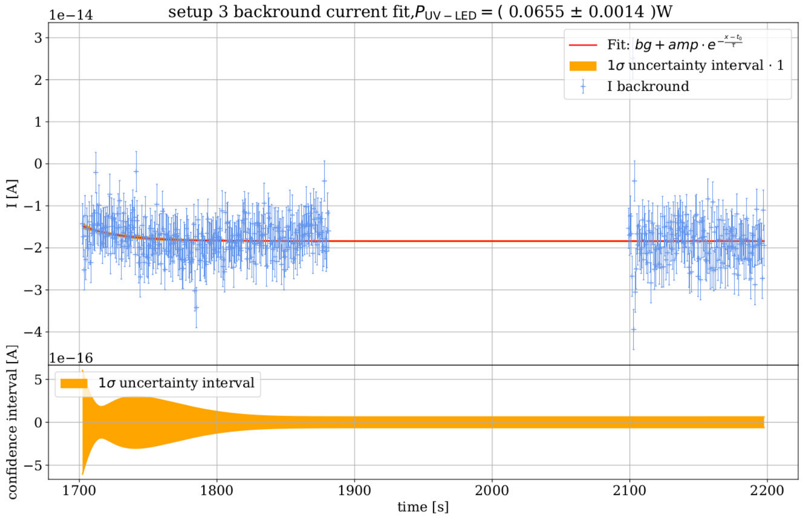

Figure 143: setup 3: background current I for $P_{\mathrm{UV-LED}} = (0.0655 \pm 0.0014)\,\mathrm{W}$. 1 σ confidence of the background fit function. Fit parameters: $bg = (-18.39 \pm 0.06)\mathrm{e}{-15}\,\mathrm{A}$, $amp = (2 \pm 4)\mathrm{e}{-15}\,\mathrm{A}$, $t_0 = (1.71 \pm 0.05)\mathrm{e}3\,\mathrm{s}$, $\tau = (28 \pm 10)\,\mathrm{s}$. $\chi^2_{\mathrm{red.}} = 1.00 \pm 0.07$.

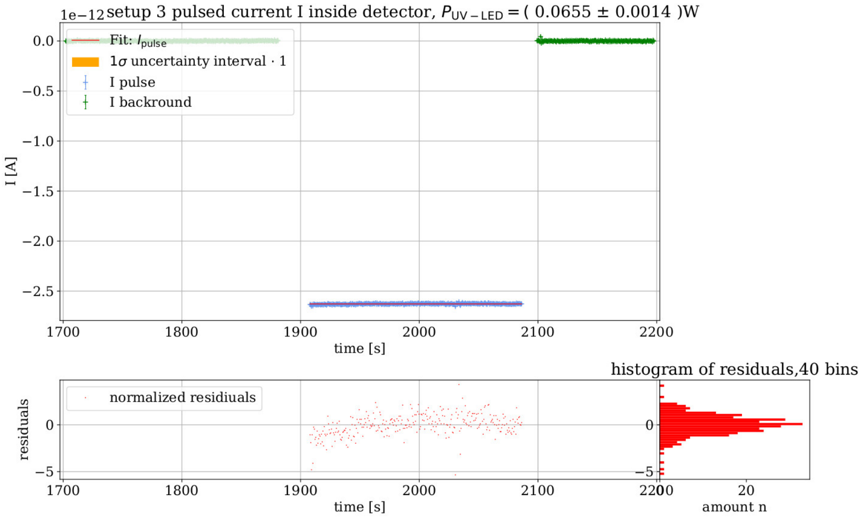

Figure 144: setup 3: background corrected data for the pulse current I_{pulse} with $P_{\text{UV-LED}} = (0.0655 \pm 0.0014)\,\text{A}$. Fit parameters: $I_{\text{pulse}} = (-2.6281 \pm 0.0003)\text{e}{-12}\,\text{A}$. $\chi^2_{\text{red.}} = 1.29 \pm 0.08$. The uncertainty of the fit parameters was modified by $\sigma(I_{\text{pulse}}) = \sqrt{\sigma(I_{\text{pulse}})^2 \cdot \chi^2_{\text{red.}}}$ so that the uncertainty value is not misrepresented.

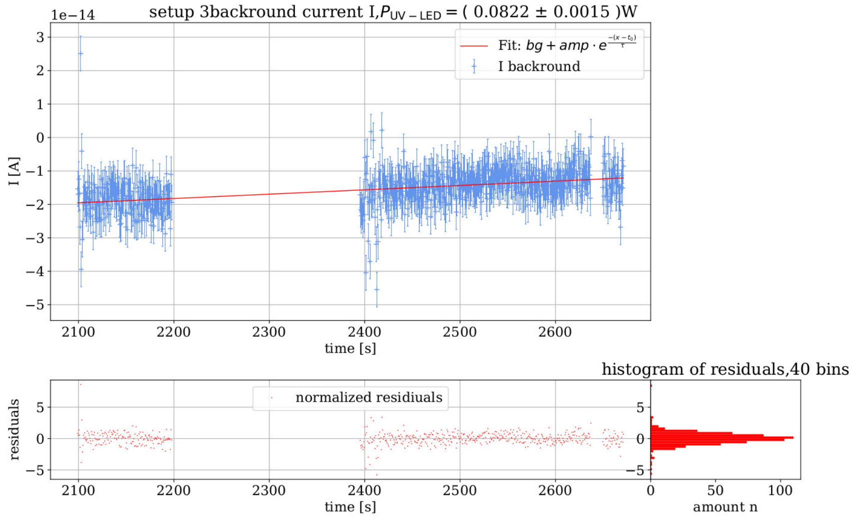

Figure 145: setup 3: background current I for $P_{\text{UV-LED}} = (0.0822 \pm 0.0015)\,\text{W}$. Fit parameters: $bg = (6.441 \pm 0.003)\text{e}{-12}\,\text{A}$, $amp = (-22.35 \pm 0.01)\text{e}{-9}\,\text{A}$, $t_0 = (-4.0472 \pm 0.0002)\text{e}6\,\text{s}$, $\tau = (496.91 \pm 0.03)\text{e}3\,\text{s}$. $\chi^2_{\text{red.}} = 1.00 \pm 0.06$. This fit has already been used to modify the uncertainties of the measured current I to produce a $\chi^2_{\text{red.}} = 1.00$ using formula 16.

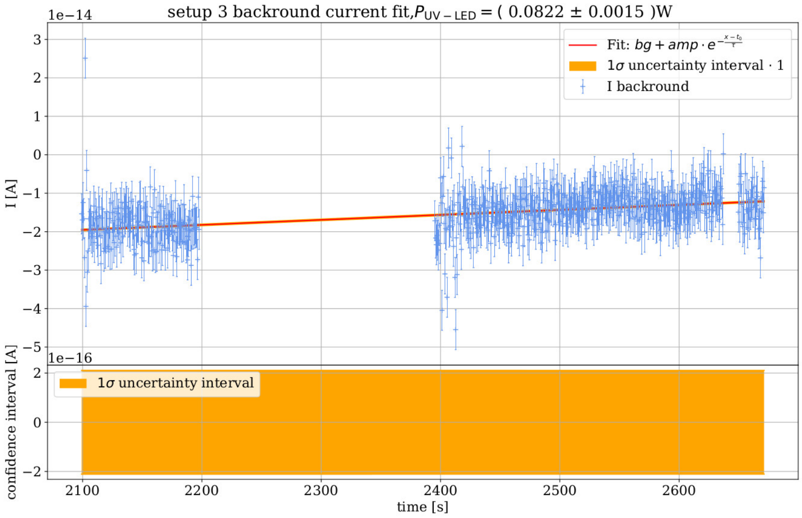

Figure 146: setup 3: background current I for $P_{\mathrm{UV-LED}} = (0.0822 \pm 0.0015)\,\mathrm{W}$. 1 σ confidence of the background fit function. Fit parameters: $bg = (6.441 \pm 0.003)\mathrm{e}{-12}\,\mathrm{A}$, $amp = (-22.35 \pm 0.01)\mathrm{e}{-9}\,\mathrm{A}$, $t_0 = (-4.0472 \pm 0.0002)\mathrm{e}6\,\mathrm{s}$, $\tau = (496.91 \pm 0.03)\mathrm{e}3\,\mathrm{s}$. $\chi^2_{\mathrm{red.}} = 1.00 \pm 0.06$.

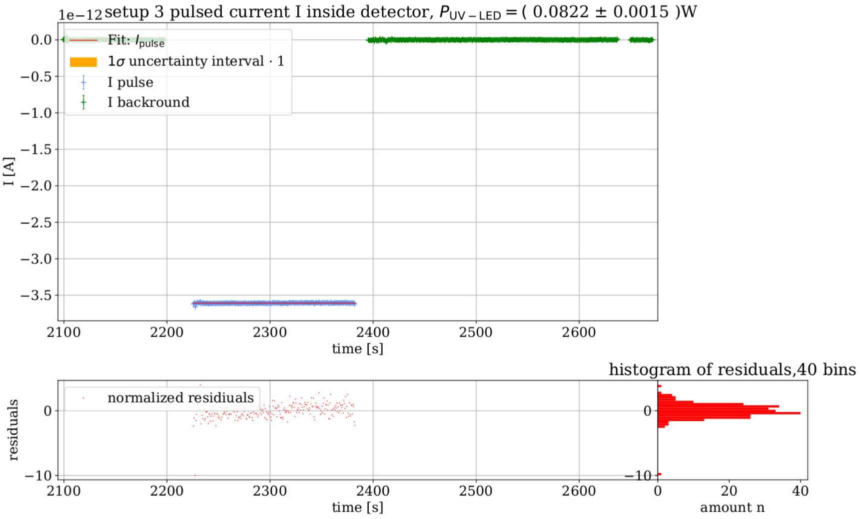

Figure 147: setup 3: background corrected data for the pulse current I_{pulse} with $P_{\mathrm{UV-LED}} = (0.0822 \pm 0.0015)\,\mathrm{A}$. Fit parameters: $I_{\mathrm{pulse}} = (-3.6078 \pm 0.0004)\mathrm{e}{-12}\,\mathrm{A}$. $\chi^2_{\mathrm{red.}} = 1.35 \pm 0.09$. The uncertainty of the fit parameters was modified by $\sigma(I_{\mathrm{pulse}}) = \sqrt{\sigma(I_{\mathrm{pulse}})^2 \cdot \chi^2_{\mathrm{red.}}}$ so that the uncertainty value is not misrepresented.

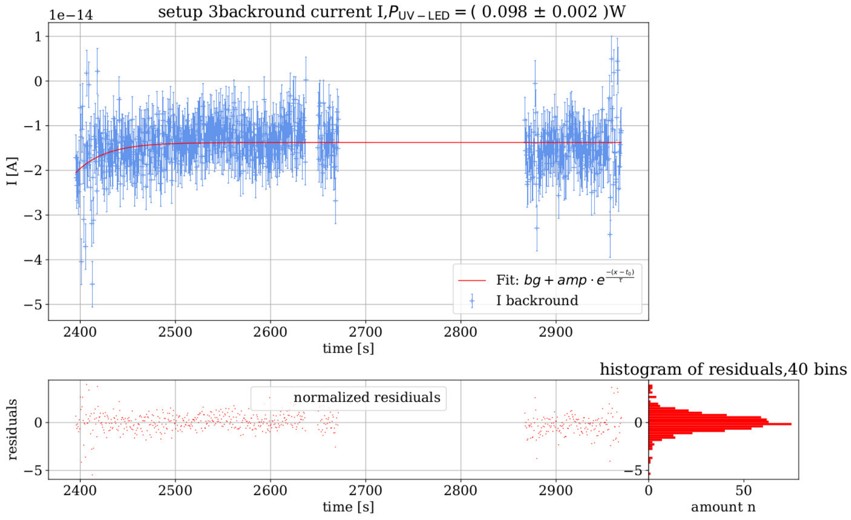

Figure 148: setup 3: background current I for $P_{\mathrm{UV-LED}} = (0.098 \pm 0.002)\,\mathrm{W}$. Fit parameters: $bg = (-13.8 \pm 0.2)\mathrm{e}{-15}\,\mathrm{A}$, $amp = (-0.05 \pm 0.07)\mathrm{e}{-3}\,\mathrm{A}$, $t_0 = (1.69 \pm 0.06)\mathrm{e}3\,\mathrm{s}$, $\tau = (31 \pm 3)\,\mathrm{s}$. $\chi^2_{\mathrm{red.}} = 1.00 \pm 0.06$. This fit has already been used to modify the uncertainties of the measured current I to produce a $\chi^2_{\mathrm{red.}} = 1.00$ using formula 16.

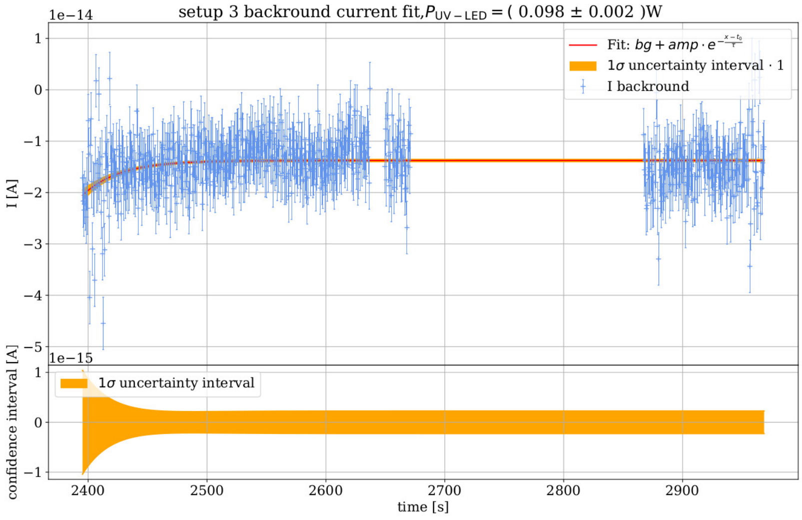

Figure 149: setup 3: background current I for $P_{\mathrm{UV-LED}} = (0.098 \pm 0.002)\,\mathrm{W}$. 1 σ confidence of the background fit function. Fit parameters: $bg = (-13.8 \pm 0.2)\mathrm{e}{-15}\,\mathrm{A}$, $amp = (-0.05 \pm 0.07)\mathrm{e}{-3}\,\mathrm{A}$, $t_0 = (1.69 \pm 0.06)\mathrm{e}3\,\mathrm{s}$, $\tau = (31 \pm 3)\,\mathrm{s}$. $\chi^2_{\mathrm{red.}} = 1.00 \pm 0.06$.

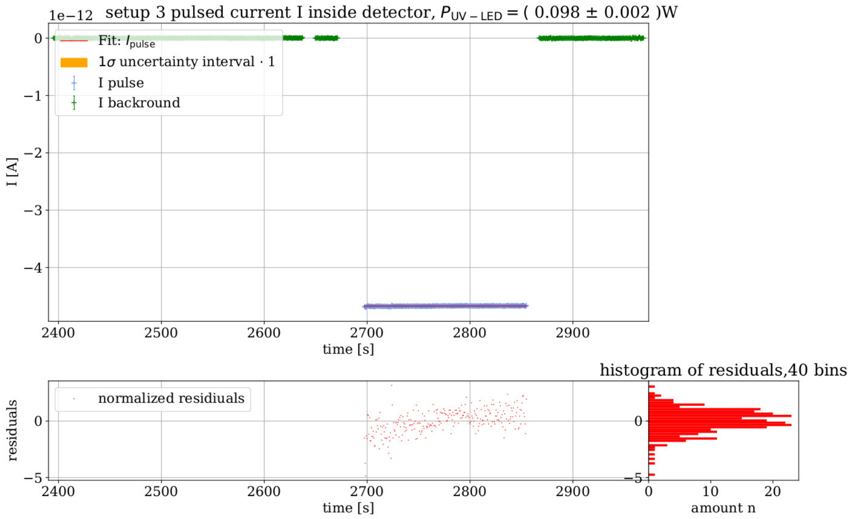

Figure 150: setup 3: background corrected data for the pulse current I_{pulse} with $P_{\text{UV}-\text{LED}} = (0.098 \pm 0.002)\,\text{A}$. Fit parameters: $I_{\text{pulse}} = (-4.6721 \pm 0.0003)\text{e}{-12}\,\text{A}$. $\chi^2_{\text{red.}} = 1.35 \pm 0.09$. The uncertainty of the fit parameters was modified by $\sigma(I_{\text{pulse}}) = \sqrt{\sigma(I_{\text{pulse}})^2 \cdot \chi^2_{\text{red.}}}$ so that the uncertainty value is not misrepresented.

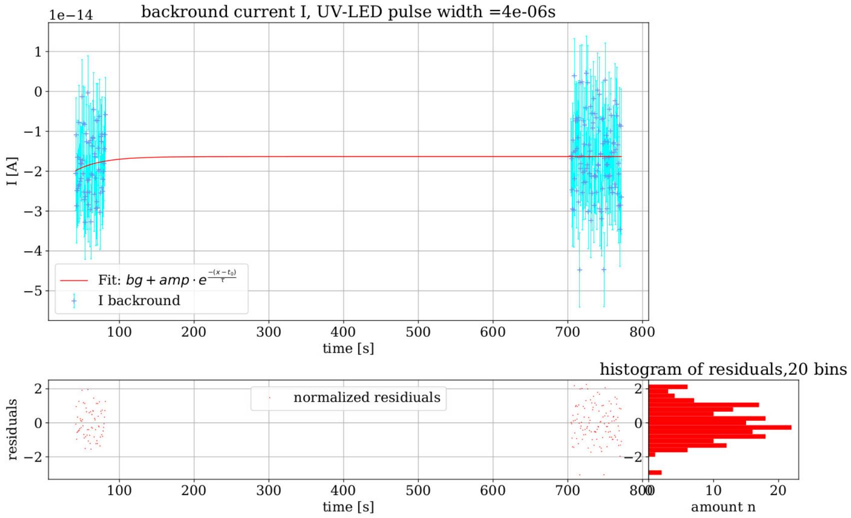

Figure 151: Background current for a pulse width of 4e−6 s. Fit parameters: $bg = (-16 \pm 5)\text{e}{-15}\,\text{A}$, $amp = (-0.01 \pm 0.07)\text{e}{-12}\,\text{A}$, $t_0 = (0.00 \pm 0.12)\text{e}3\,\text{s}$, $\tau = (40 \pm 80)\,\text{s}$. $\chi^2_{\text{red.}} = 1.00 \pm 0.11$.

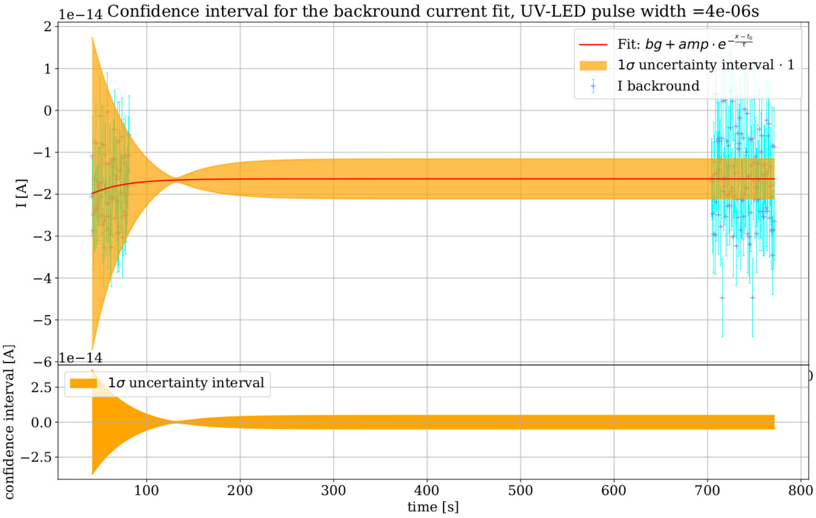

Figure 152: 1σ confidence interval of the background current fit for a pulse width of 4e−6 s. Fit parameters: $bg = (-16 \pm 5)\text{e}{-15}\,\text{A}$, $amp = (-0.01 \pm 0.07)\text{e}{-12}\,\text{A}$, $t_0 = (0.00 \pm 0.12)\text{e}3\,\text{s}$, $\tau = (40 \pm 80)\,\text{s}$. $\chi^2_{\text{red.}} = 1.00 \pm 0.11$.

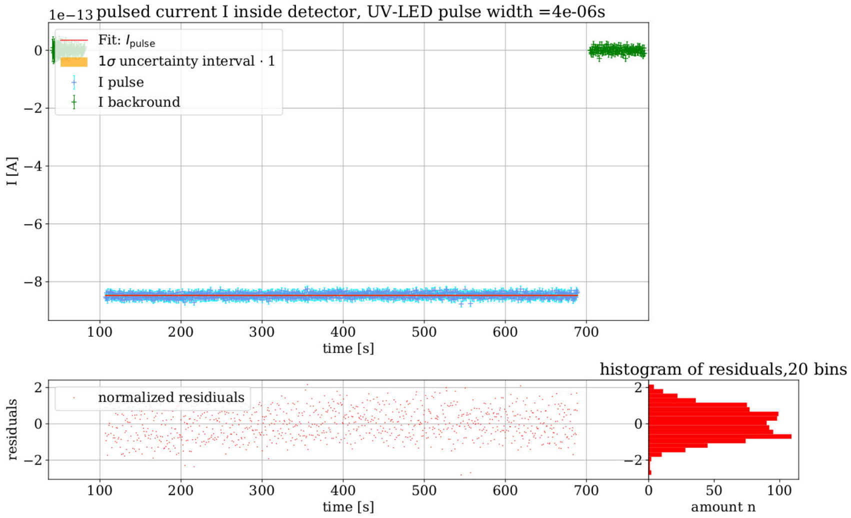

Figure 153: Current I during UV-LED pulses with a pulsewidth of 4e−6 s. Fit parameters: $I_{\text{pulse}} = (-847.3 \pm 0.3)\text{e}{-15}\,\text{A}$. The uncertainty of I_{pulse} has been modified according to formula 16 with $\chi^2_{\text{red.}} = 0.68 \pm 0.05$. This was done in an effort to not misrepresent the uncertainty of the fit.

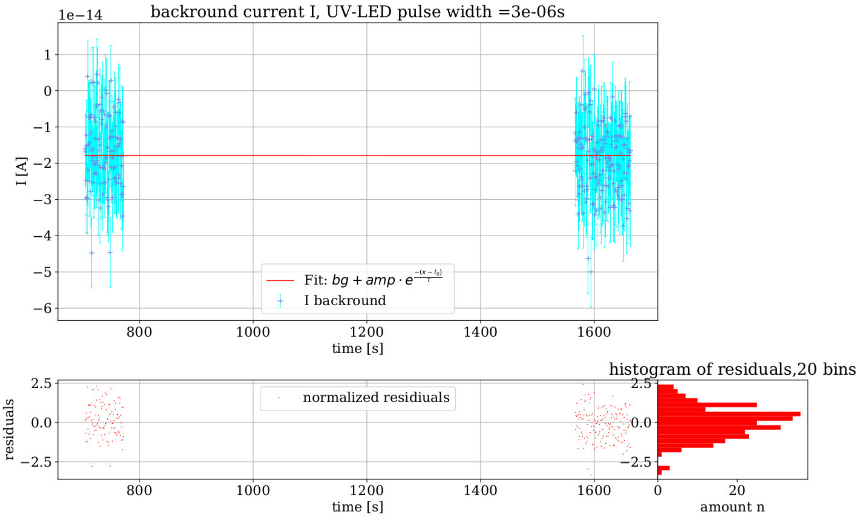

Figure 154: Background current for a pulse width of 3e−6 s. Fit parameters: $bg = (-56.823 \pm 0.007)\text{e}{-12}\,\text{A}$, $amp = (59.094 \pm 0.008)\text{e}{-12}\,\text{A}$, $t_0 = (-211.7 \pm 0.7)\text{e}6\,\text{s}$, $\tau = (5.36 \pm 0.02)\text{e}9\,\text{s}$. $\chi^2_{\text{red.}} = 1.00 \pm 0.09$.

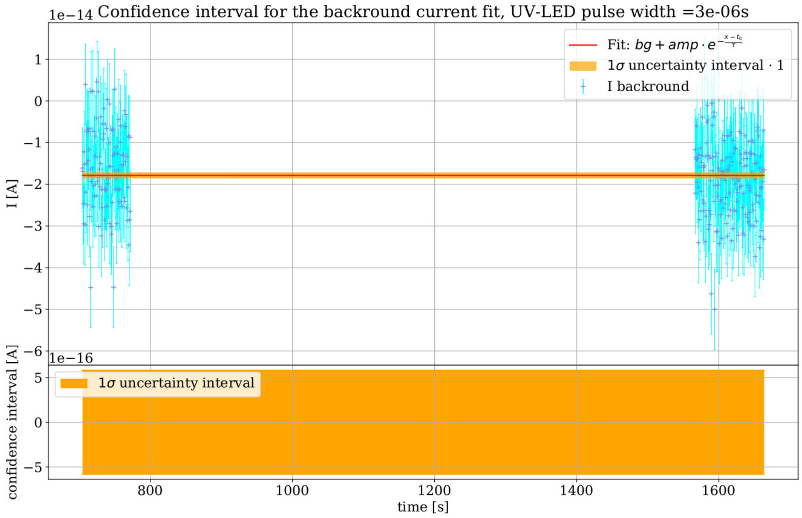

Figure 155: 1σ confidence interval of the background current fit for a pulse width of 3e−6 s. Fit parameters: $bg = (-56.823 \pm 0.007)\text{e}{-12}\,\text{A}$, $amp = (59.094 \pm 0.008)\text{e}{-12}\,\text{A}$, $t_0 = (-211.7 \pm 0.7)\text{e}6\,\text{s}$, $\tau = (5.36 \pm 0.02)\text{e}9\,\text{s}$. $\chi^2_{\text{red.}} = 1.00 \pm 0.09$.

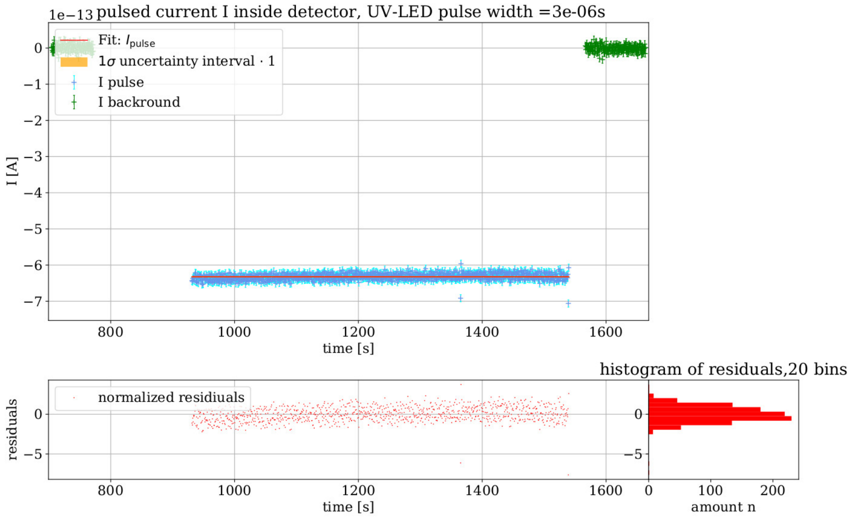

Figure 156: Current I during UV-LED pulses with a pulsewidth of 3e−6 s. Fit parameters: $I_{\text{pulse}} = (-632.4 \pm 0.3)\text{e}{-15}\,\text{A}$. The uncertainty of I_{pulse} has been modified according to formula 16 with $\chi^2_{\text{red.}} = 0.89 \pm 0.04$. This was done in an effort to not misrepresent the uncertainty of the fit.

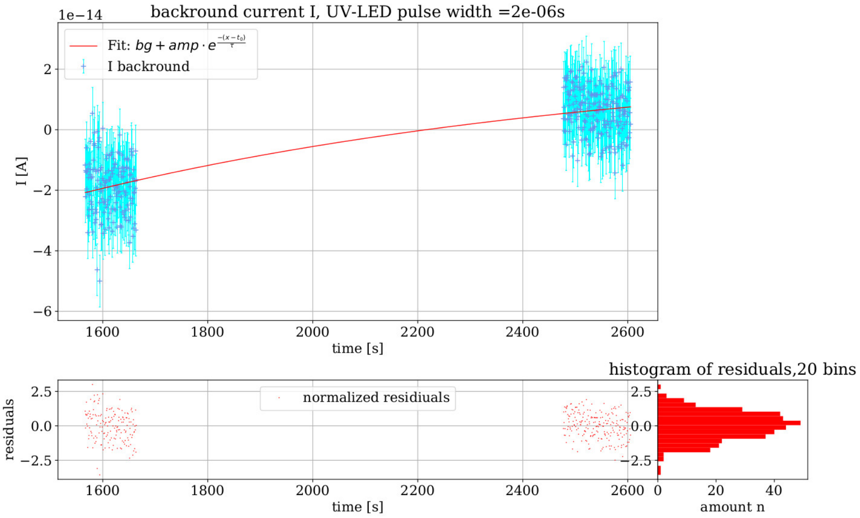

Figure 157: Background current for a pulse width of 2e−6 s. Fit parameters: $bg = (24{\pm}6)\mathrm{e}{-15}\,\mathrm{A}$, $amp = (-43 \pm 5)\mathrm{e}{-15}\,\mathrm{A}$, $t_0 = (1.63 \pm 0.10)\mathrm{e}3\,\mathrm{s}$, $\tau = (1.1 \pm 0.2)\mathrm{e}3\,\mathrm{s}$. $\chi^2_{\mathrm{red.}} = 1.00 \pm 0.07$.

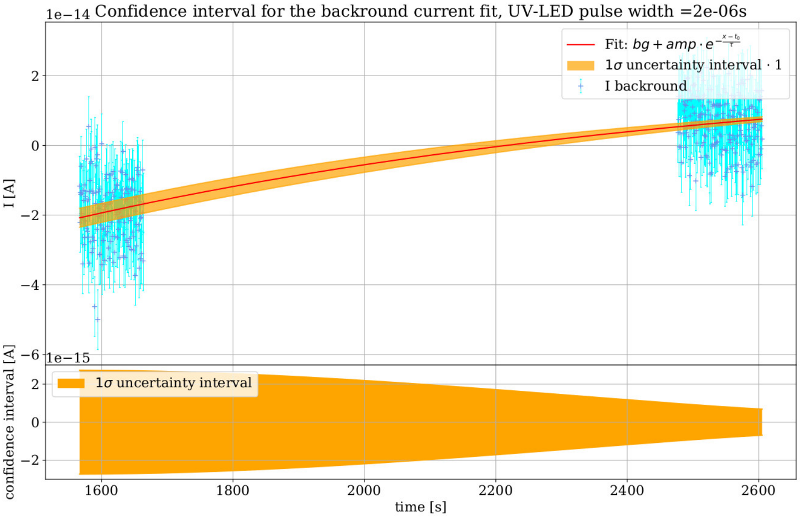

Figure 158: 1σ confidence interval of the background current fit for a pulse width of 2e−6 s. Fit parameters: $bg = (24 \pm 6)\text{e}{-15}\,\text{A}$, $amp = (-43 \pm 5)\text{e}{-15}\,\text{A}$, $t_0 = (1.63 \pm 0.10)\text{e}3\,\text{s}$, $\tau = (1.1 \pm 0.2)\text{e}3\,\text{s}$. $\chi^2_{\text{red.}} = 1.00 \pm 0.07$.

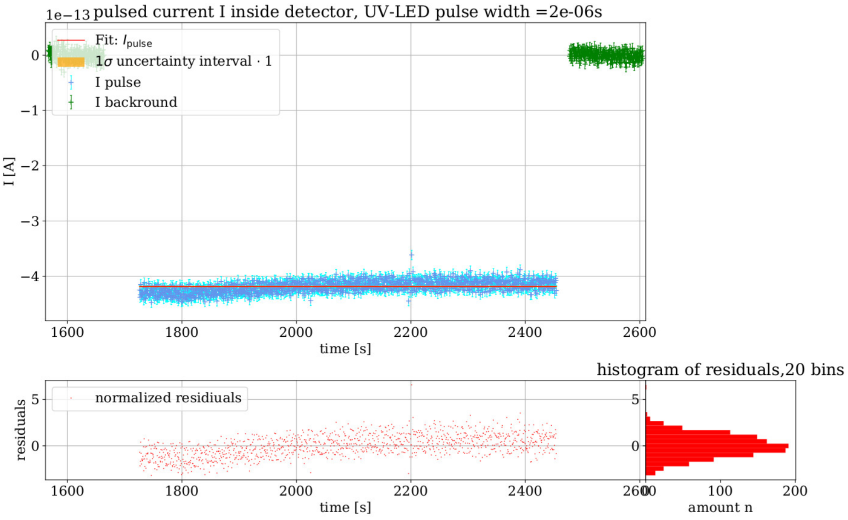

Figure 159: Current I during UV-LED pulses with a pulsewidth of 2e−6 s. Fit parameters: $I_{\text{pulse}} = (-418.7 \pm 0.3)\text{e}{-15}\,\text{A}$. The uncertainty of I_{pulse} has been modified according to formula 16 with $\chi^2_{\text{red.}} = 1.40 \pm 0.04$. This was done in an effort to not misrepresent the uncertainty of the fit.

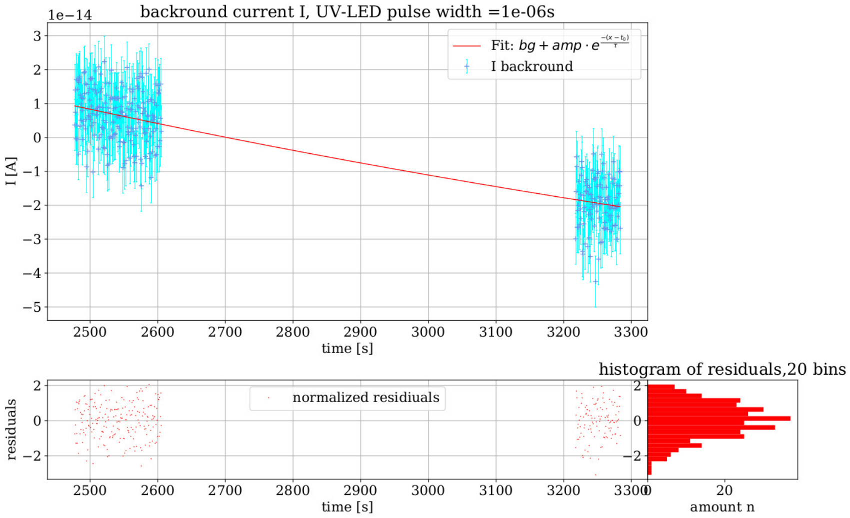

Figure 160: Background current for a pulse width of 1e−6 s. Fit parameters: $bg = (-95 \pm 3)\mathrm{e}{-15}\,\mathrm{A}$, $amp = (9.1 \pm 0.5)\mathrm{e}{-12}\,\mathrm{A}$, $t_0 = (-8.24 \pm 0.11)\mathrm{e}3\,\mathrm{s}$, $\tau = (2.40 \pm 0.03)\mathrm{e}3\,\mathrm{s}$. $\chi^2_{\mathrm{red.}} = 1.00 \pm 0.08$.

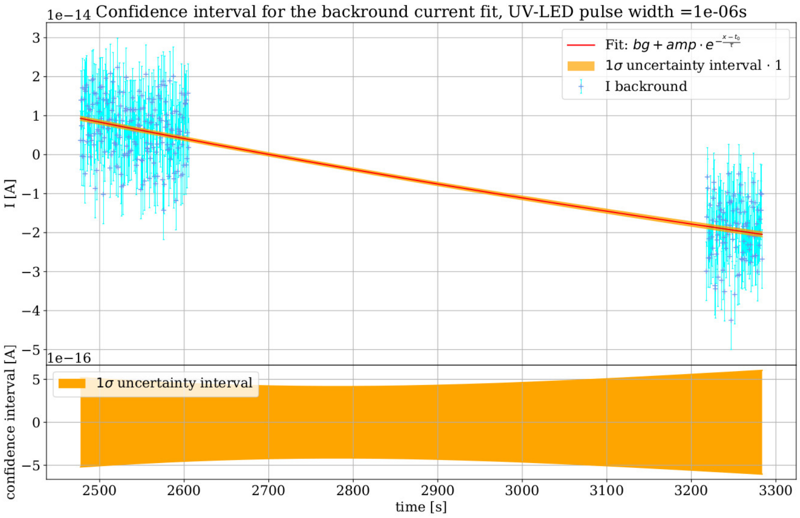

Figure 161: 1σ confidence interval of the background current fit for a pulse width of 1e−6 s. Fit parameters: $bg = (-95 \pm 3)\text{e}{-15}\,\text{A}$, $amp = (9.1 \pm 0.5)\text{e}{-12}\,\text{A}$, $t_0 = (-8.24 \pm 0.11)\text{e}3\,\text{s}$, $\tau = (2.40 \pm 0.03)\text{e}3\,\text{s}$. $\chi^2_{\text{red.}} = 1.00 \pm 0.08$.

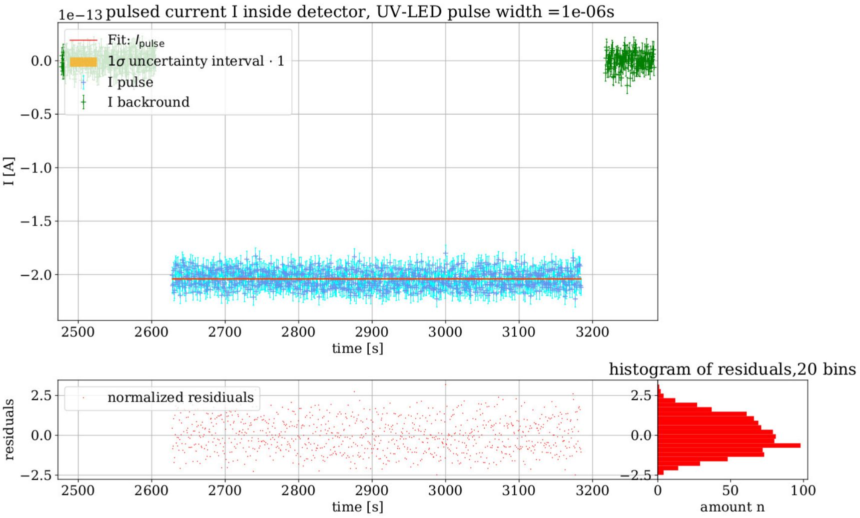

Figure 162: Current I during UV-LED pulses with a pulsewidth of 1e−6 s. Fit parameters: $I_{\text{pulse}} = (-204.0 \pm 0.3)\text{e}{-15}\,\text{A}$. The uncertainty of I_{pulse} has been modified according to formula 16 with $\chi^2_{\text{red.}} = 1.13 \pm 0.05$. This was done in an effort to not misrepresent the uncertainty of the fit.

10.4 Additional figures for the charge measurement in relation to the pulse width of the UV-LED pulse

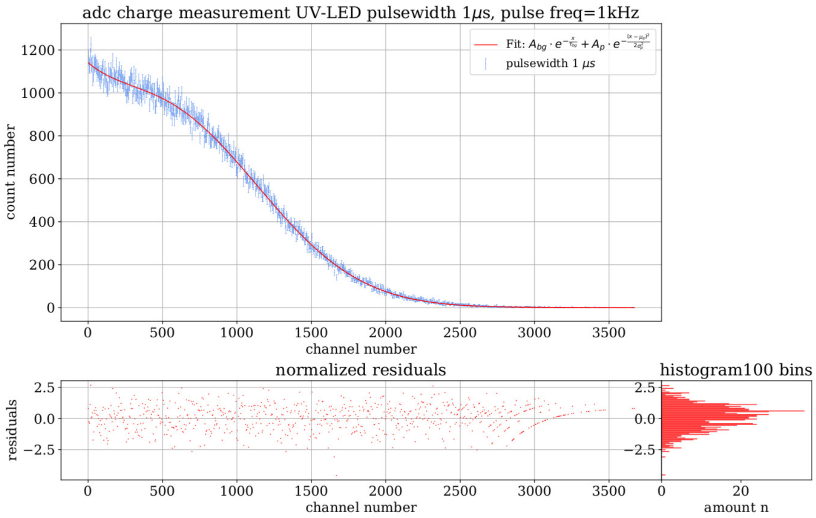

Figure 163: ADC data for the charge measurement for a pulse width of $1e{-}6$ s. UV-LED pulses of $P_{\mathrm{UV-LED}} = (0.419 \pm 0.010)$ W and pulse frequency of $f = (1.0000000000 \pm 0.0000000003)$ kHz. Fit parameters: $A_{bg} = (580 \pm 20)$, $\tau_{bg} = (452 \pm 12)$, $A_p = (783 \pm 12)$, $\mu_p = (541 \pm 12)$, $\sigma_p = (659 \pm 6)$. $\chi^2_{\mathrm{red.}} = 1.02 \pm 0.05$.

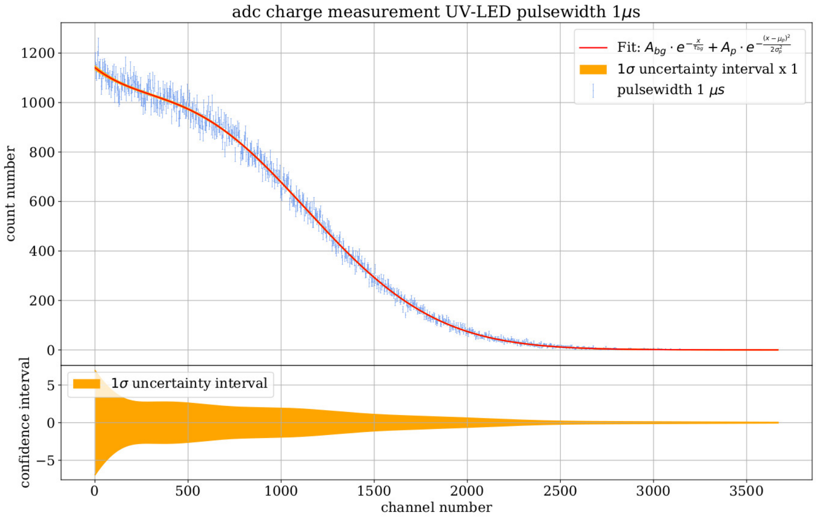

Figure 164: ADC data for the charge measurement for a pulse width of 1e−6 s. UV-LED pulses of $P_{\mathrm{UV-LED}} = (0.419 \pm 0.010)$ W and pulse frequency of $f = (1.0000000000 \pm 0.0000000003)$ kHz and 1σ confidence interval of the fitting function. Fit parameters: $A_{bg} = (580 \pm 20)$, $\tau_{bg} = (452 \pm 12)$, $A_p = (783 \pm 12)$, $\mu_p = (541 \pm 12)$, $\sigma_p = (659 \pm 6)$. $\chi^2_{\mathrm{red.}} = 1.02 \pm 0.05$.

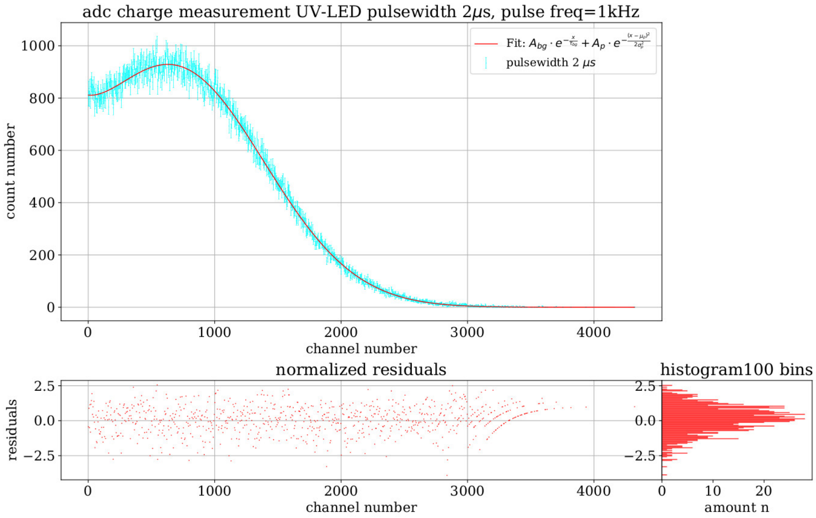

Figure 165: ADC data for the charge measurement for a pulse width of 2e−6 s. UV-LED pulses of $P_{\mathrm{UV-LED}} = (0.419 \pm 0.010)$ W and pulse frequency of $f = (1.0000000000 \pm 0.0000000003)$ kHz. Fit parameters: $A_{bg} = (237 \pm 20)$, $\tau_{bg} = (290 \pm 60)$, $A_p = (904 \pm 14)$, $\mu_p = (682 \pm 14)$, $\sigma_p = (716 \pm 5)$. $\chi^2_{\mathrm{red.}} = 1.01 \pm 0.05$.

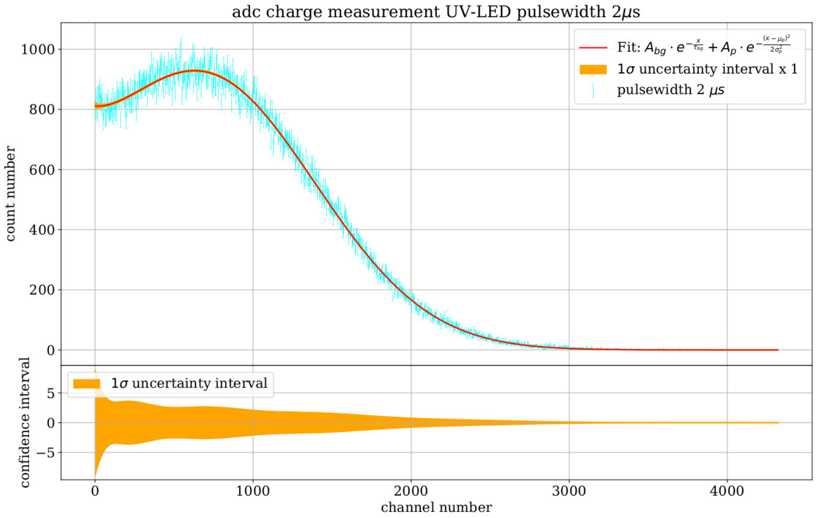

Figure 166: ADC data for the charge measurement for a pulse width of $2e{-}6$ s. UV-LED pulses of $P_{\mathrm{UV-LED}} = (0.419{\pm}0.010)$ W and pulse frequency of $f = (1.0000000000{\pm}0.0000000003)$ kHz and 1σ confidence interval of the fitting function. Fit parameters: $A_{bg} = (237 \pm 20)$, $\tau_{bg} = (290 \pm 60)$, $A_p = (904 \pm 14)$, $\mu_p = (682 \pm 14)$, $\sigma_p = (716 \pm 5)$. $\chi^2_{\mathrm{red.}} = 1.01 \pm 0.05$.

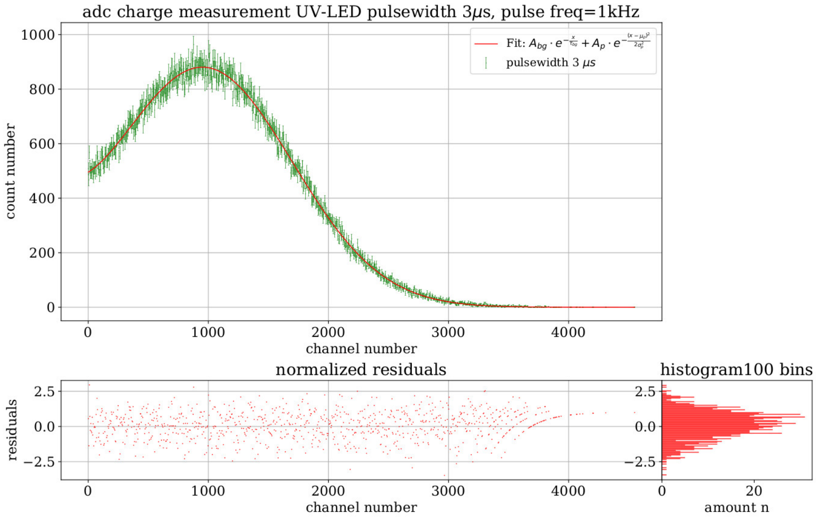

Figure 167: ADC data for the charge measurement for a pulse width of $3e-6$ s. UV-LED pulses of $P_{\mathrm{UV-LED}} = (0.419{\pm}0.010)$ W and pulse frequency of $f = (1.0000000000{\pm}0.0000000003)$ kHz. Fit parameters: $A_{bg} = (118{\pm}9)$, $\tau_{bg} = (300{\pm}70)$, $A_p = (875{\pm}6)$, $\mu_p = (961{\pm}8)$, $\sigma_p = (741{\pm}3)$. $\chi^2_{\mathrm{red.}} = 1.00 \pm 0.05$.

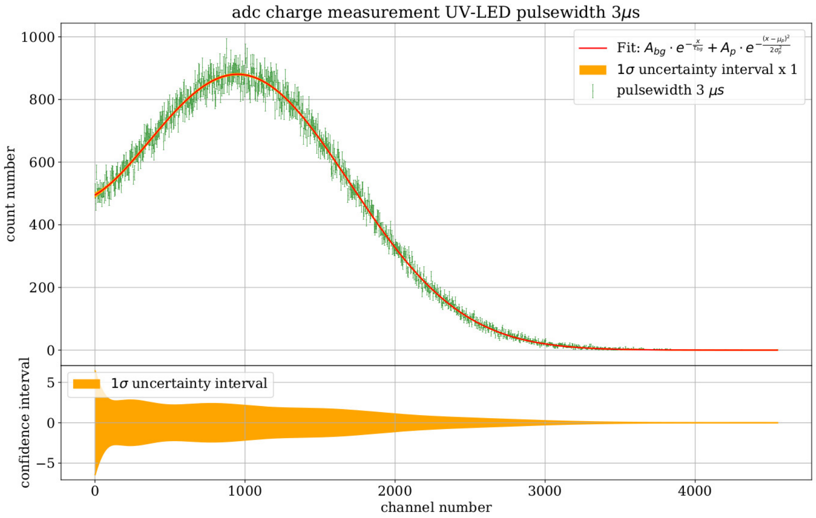

Figure 168: ADC data for the charge measurement for a pulse width of $3e{-}6$ s. UV-LED pulses of $P_{\mathrm{UV-LED}} = (0.419{\pm}0.010)$ W and pulse frequency of $f = (1.0000000000{\pm}0.0000000003)$ kHz and 1σ confidence interval of the fitting function. Fit parameters: $A_{bg} = (118 \pm 9)$, $\tau_{bg} = (300 \pm 70)$, $A_p = (875 \pm 6)$, $\mu_p = (961 \pm 8)$, $\sigma_p = (741 \pm 3)$. $\chi^2_{\mathrm{red.}} = 1.00 \pm 0.05$.

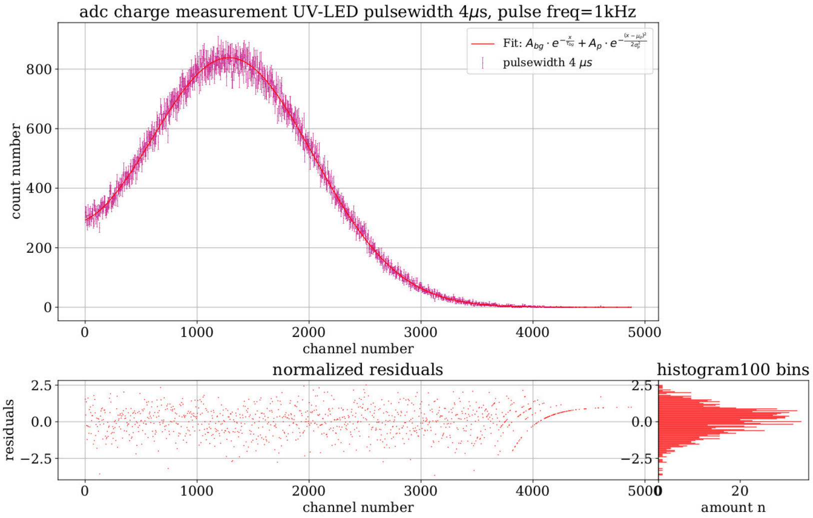

Figure 169: ADC data for the charge measurement for a pulse width of $4e-6$ s. UV-LED pulses of $P_{\mathrm{UV-LED}} = (0.419{\pm}0.010)$ W and pulse frequency of $f = (1.0000000000{\pm}0.0000000003)$ kHz. Fit parameters: $A_{bg} = (101{\pm}5)$, $\tau_{bg} = (370{\pm}80)$, $A_p = (835{\pm}4)$, $\mu_p = (1290{\pm}6)$, $\sigma_p = (753{\pm}3)$. $\chi^2_{\mathrm{red.}} = 0.93 \pm 0.04$.

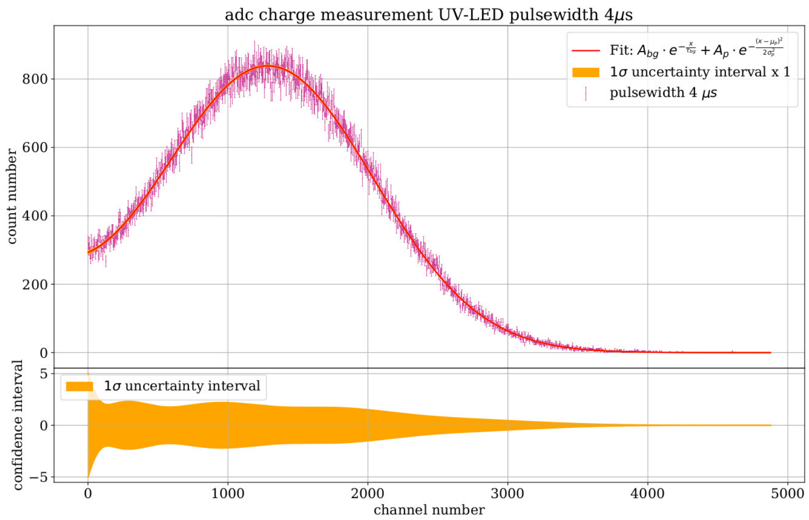

Figure 170: ADC data for the charge measurement for a pulse width of $4e{-}6$ s. UV-LED pulses of $P_{\mathrm{UV-LED}} = (0.419{\pm}0.010)$ W and pulse frequency of $f = (1.0000000000{\pm}0.0000000003)$ kHz and 1σ confidence interval of the fitting function. Fit parameters: $A_{bg} = (101 \pm 5)$, $\tau_{bg} = (370 \pm 80)$, $A_p = (835 \pm 4)$, $\mu_p = (1290 \pm 6)$, $\sigma_p = (753 \pm 3)$. $\chi^2_{\mathrm{red.}} = 0.93 \pm 0.04$.

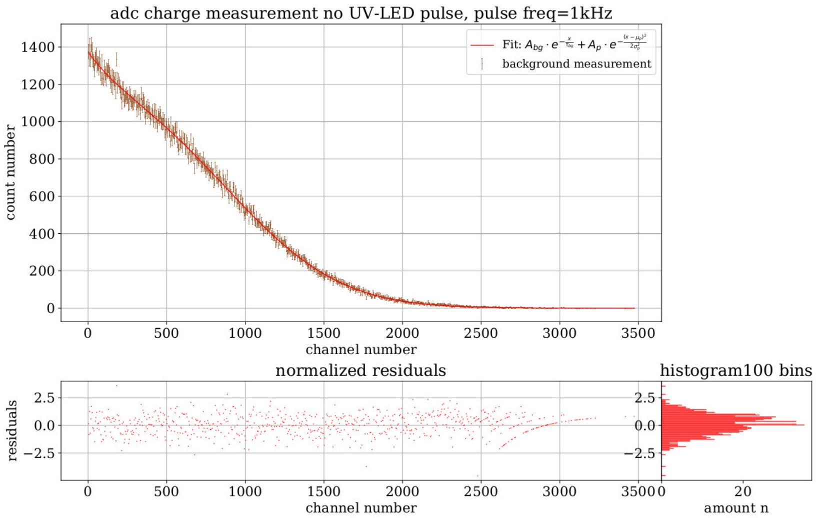

Figure 171: ADC data for the charge measurement with no UV-LED pulse. Fit parameters: $A_{bg} = (710 \pm 40)$, $\tau_{bg} = (416 \pm 10)$, $A_p = (770 \pm 20)$, $\mu_p = (360 \pm 20)$, $\sigma_p = (650 \pm 8)$. $\chi^2_{\mathrm{red.}} = 0.88 \pm 0.05$.

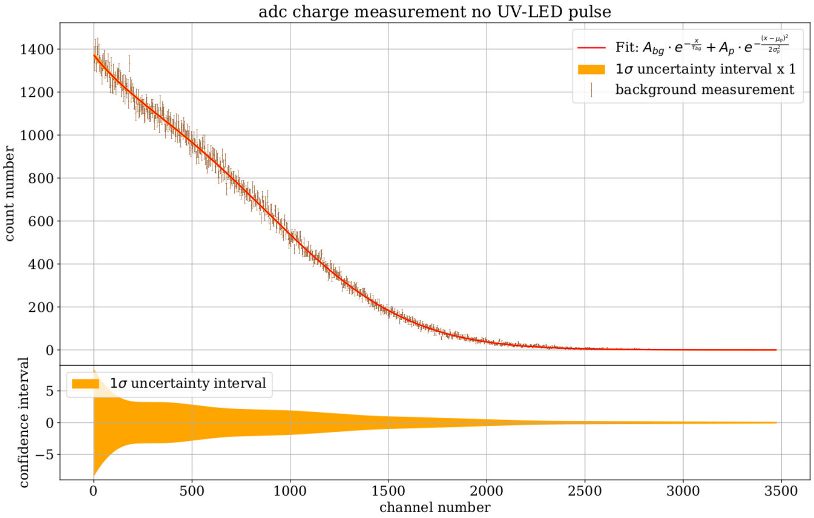

Figure 172: ADC data for the charge measurement with no UV-LED pulse. The 1σ confidence interval of the fitting function is shown as well. Fit parameters: $A_{bg} = (710 \pm 40)$, $\tau_{bg} = (416 \pm 10)$, $A_p = (770 \pm 20)$, $\mu_p = (360 \pm 20)$, $\sigma_p = (650 \pm 8)$. $\chi^2_{\text{red.}} = 0.88 \pm 0.05$.